Localized Dissipation in Fermionic Quantum Wires

Inaugural-Dissertation

zur

Erlangung des Doktorgrades

der Mathematisch-Naturwissenschaftlichen Fakultät

der Universität zu Köln

vorgelegt von

Heinrich Filon Fröml

aus Bergisch Gladbach

Köln 2020

Berichterstatter: Prof. Dr. Sebastian Diehl
Prof. Dr. Achim Rosch

Tag der mündlichen Prüfung: 26. Juni 2020

Abstract

Localized dissipation in many-body quantum systems represents an emergent focal point of non-equilibrium physics. In recent experiments, localized particle losses were realized in ultracold atomic gases, thus opening up new avenues for investigating the interplay between many-body and non-equilibrium effects. The main focus of this work is the theoretical study of collective phenomena in one-dimensional systems of interacting spinless fermions subject to a localized loss. This model constitutes a non-equilibrium counterpart of the paradigmatic Kane-Fisher potential barrier problem. In particular, strong interaction effects emerge due to the gapless nature of the system.

We show that the loss and transport properties of the quantum wire in the presence of a localized loss are drastically modified by interactions as a result of the interplay between coherent and incoherent processes. In experiments with localized losses, a manifestation of the quantum Zeno effect is encountered, which can be described exhaustively in terms of local, microscopic physics. In contrast, we demonstrate that the interplay of gapless quantum fluctuations and particle interactions with the localized dissipation leads to an instance of the quantum Zeno effect of genuine many-body nature.

After the localized losses are switched on, a non-equilibrium steady state emerges in the quantum wire. We derive exact results for the properties of this steady state in the non-interacting limit and formulate a theoretical description of the depletion processes by introducing the momentum-dependent loss probability of modes. Remarkably, we find that coherence properties of the initial state persist, leading to the formation of Friedel oscillations near the loss site.

The presence of interactions between the fermions modifies the dynamics in the wire and leads to an energy-dependent renormalization of loss processes. We find that the loss probability is strongly renormalized for modes with an energy close to the Fermi energy, leading to the suppression of losses at the Fermi level. In the case of repulsive interactions, the suppression of losses is accompanied by the loss site becoming completely opaque, which establishes a fluctuation-induced quantum Zeno effect. For attractive interactions, instead, the localized loss becomes fully transparent to particles at the Fermi level, resulting accordingly in the suppression of losses as a fluctuation-induced transparency.

The strong modifications of the loss properties are reflected in observables such as the momentum distribution in the wire, exhibiting an increased occupation at the Fermi momentum. In addition, we study the influence of self-thermalization effects on the renormalization of the effective dissipation strength. Here, we identify regimes where the generation of an effective temperature is sufficiently weak to achieve significant renormalization. Furthermore, the microscopic quantum Zeno effect affects the spectral properties of the non-Hermitian Hamiltonian associated with a localized loss for a lattice model. Here, a sharp reorganization of the spectrum is encountered at a critical dissipation strength, causing a characteristic signature in the response properties of the wire.

We investigate the interplay of interactions in the wire and localized dissipation within three complementary approaches. In a microscopic real-space renormalization group analysis the physical mechanisms behind the modified depletion properties are particularly transparent. Within a dynamical Hartree-Fock approximation the resulting effects on observables such as the momentum distribution in the non-equilibrium steady states can be studied. Finally, an effective Luttinger liquid description demonstrates the universality of the findings and enables the investigation of mode-coupling effects.

Kurzzusammenfassung

Lokalisierte Dissipation in Vielteilchen-Quantensystemen stellt einen aufkommenden Schwerpunkt der Nichtgleichgewichtsphysik dar. In aktuellen Experimenten wurden lokalisierte Teilchenverluste in ultrakalten atomaren Gasen realisiert und damit neue Wege für die Untersuchung des Zusammenspiels von Vielteilchen- und Nichtgleichgewichtseffekten eröffnet. Das Hauptaugenmerk dieser Arbeit liegt auf der theoretischen Untersuchung kollektiver Phänomene in eindimensionalen Systemen wechselwirkender spinloser Fermionen, die einem lokalisierten Teilchenverlust unterliegen. Dieses Modell stellt ein Pendant der Nichtgleichgewichtsphysik zum paradigmatischen Kane-Fisher-Problem einer Potentialbarriere dar. Insbesondere treten aufgrund der masselosen Fluktuationen des Systems starke Wechselwirkungseffekte auf. Wir zeigen, dass die Verlust- und Transporteigenschaften des Quantendrahtes in Gegenwart eines lokalisierten Teilchenverlustes durch Wechselwirkungseffekte erheblich verändert werden, als Resultat des Zusammenspiels von kohärenten und inkohärenten Prozessen. In Experimenten mit lokalisierten Teilchenverlusten tritt eine Erscheinungsform des Quanten-Zeno-Effekts auf, die sich durch lokale, mikroskopische Physik vollständig beschreiben lässt. Im Gegensatz dazu stellen wir fest, dass das Zusammenspiel von masselosen Quantenfluktuationen und Wechselwirkungseffekten mit der lokalisierten Dissipation zu einer Manifestation des Quanten-Zeno-Effekts führt, welche sich grundlegend als ein Vielteilcheneffekt auffassen lässt.
Nach dem Einsetzen der lokalisierten Teilchenverluste tritt im Quantendraht ein stationärer Nichtgleichgewichtszustand auf. Wir leiten exakte Ergebnisse für die Eigenschaften dieses stationären Zustands im Grenzfall verschwindender Wechselwirkung her und formulieren eine theoretische Beschreibung der Verlustprozesse mittels der Definition einer impulsabhängigen Verlustwahrscheinlichkeit. Kohärenzeigenschaften des Anfangszustands bestehen bemerkenswerterweise fort, was zum Auftreten von Friedel-Oszillationen in der Umgebung der Verluststelle führt.
Die Wechselwirkungen zwischen den Fermionen modifizieren die Dynamik des Quantendrahts und führen zu einer energieabhängigen Renormierung der Verlustprozesse. Wir zeigen, dass die Verlustwahrscheinlichkeit für Moden mit einer Energie nahe der Fermi-Energie stark renormiert wird, was zu einer Unterdrückung der Teilchenverluste an der Fermi-Kante führt. Bei repulsiven Wechselwirkungen geht die Unterdrückung der Verluste damit einher, dass die Verluststelle völlig undurchlässig wird, was einen fluktuationsinduzierten Quanten-Zeno-Effekt begründet. Bei attraktiven Wechselwirkungen wird stattdessen der lokalisierte Teilchenverlust für Teilchen am Fermi-Niveau vollständig transparent, was dementsprechend zur Unterdrückung von Verlusten als eine fluktuationsinduzierte Transparenz führt.
Die starke Modifizierung der Verlusteigenschaften spiegelt sich in Observablen wie der Verteilung der Impulszustände im Quantendraht wider, welche eine erhöhte Besetzung am Fermi-Impuls aufweist. Des Weiteren untersuchen wir den Einfluss von Selbstequilibrierungseffekten auf die Renormierung der effektiven Dissipationsstärke. Dabei bestimmen wir Regime, in denen die Generierung einer effektiven Temperatur hinreichend schwach ist, sodass eine signifikante Renormierung erreicht werden kann. Darüber hinaus wirkt sich der mikroskopische Quanten-Zeno-Effekt auf die spektralen Eigenschaften des nicht-hermiteschen Hamiltonians aus, der mit einem lokalisierten Teilchenverlust in einem Gittermodell assoziiert ist. Hier findet eine Reorganisation des Spektrums bei einer kritischen Dissipationsstärke statt, die eine charakteristische Signatur in den Antwortfunktionen des Quantendrahtes bewirkt.
Wir untersuchen das Zusammenspiel von Wechselwirkungen im Quantendraht und lokalisierter

Dissipation unter Verwendung von drei komplementären Methoden. In einer mikroskopischen Analyse mittels einer Realraum-Renormalisierungsgruppe werden die physikalischen Mechanismen hinter den modifizierten Verlusteigenschaften in besonderem Maße deutlich. Im Rahmen einer dynamischen Hartree-Fock Näherung können die sich daraus ergebenden Effekte auf Observablen wie die Impulsverteilung im stationären Nichtgleichgewichtszustand untersucht werden. Abschließend verdeutlicht eine effektive Beschreibung als Luttinger-Flüssigkeit die Universalität der Ergebnisse und ermöglicht die Untersuchung von Modenkopplungseffekten.

CONTENTS

CHAPTER 1

INTRODUCTION AND KEY RESULTS

1.1. Introduction

The notion of non-equilibrium can be quickly defined: the absence of equilibrium. In fact, the majority of the phenomena we experience in our daily lives are out of equilibrium [1], which illustrates the generality of the field of non-equilibrium physics. What is true in the macroscopic world is even more severe on the scale of quantum systems, which are generically very susceptible to influences by their environment. Shielding quantum systems completely from environmental perturbations is generally a difficult task and not feasible in many situations [2]. Therefore, the natural consequence is to include environmental effects in the description. On the one hand, the abandonment of restrictions such as the requirement of equilibrium can lead to a complication of the methods [2–6], but on the other hand, it can also pave the way to a potentially rich field of novel physics. Hence, the occurrence of dissipation by a coupling to the environment is not necessarily an undesired effect, but it may instead represent a resource for engineering quantum states beyond the limitations of equilibrium physics [7]. In a natural way, the novel effects that emerge in open quantum systems out of equilibrium can be utilized as a source for physical insights – or in Landauer's words: "The noise is the signal" [8].

The endeavor to characterize non-equilibrium in a positive way, beyond the absence of equilibrium, is particularly challenging since non-equilibrium dynamics is a vast field, reflecting its generality. Many ways are imaginable to drive a quantum system out of equilibrium: the realization of a quantum quench in a closed system [9–13], the application of a coherent drive via external driving fields [6, 14], or the incoherent coupling to a bath [6, 7], leading to an exchange of energy or particles with the system. Moreover, the question of whether and how a quantum system approaches equilibrium, i.e., the problem of quantum thermalization, is itself far from trivial [15]. In particular, combinations of external drive and dissipation enable far-reaching ways to engineer driven-dissipative quantum systems [6]. Driven-dissipative systems are characterized by the equal importance of coherent and dissipative dynamics in contrast to considering dissipative effects as a weak perturbation. Accordingly, the time evolution is not solely generated by a Hamiltonian but originates from several sources. This leads to non-unitary

dynamics and a loss of fluctuation-dissipation relations familiar in equilibrium, reflecting the independence of reversible and irreversible dynamics [16].

A major goal is the design of quantum states by engineering the coupling to an external reservoir [6, 7, 17–25]. The coupling of a system to an environment leads to dissipative processes and, as a result, non-equilibrium many-body steady states and time evolution without immediate counterpart in equilibrium condensed matter systems can be achieved. Here, the analog of the equilibrium ground state is a non-equilibrium (quasi-)steady state (NESS), whose study is of particular interest if it is non-thermal, i.e., its properties differ from those accessible in canonical ensembles with fixed temperature [10]. Indeed, the interplay of many-body physics and open quantum systems has proven to be a source of numerous novel effects, thanks to advances in controlling both coherent and dissipative processes. Novel universal phenomena and universality classes have been described [26–28], e.g., the universality classes of Kardar–Parisi–Zhang (KPZ) [29] and directed percolation [6], as well as new tools to probe universal scaling such as the Kibble-Zurek mechanism [30]. Order in many-body states has been achieved by engineering the coupling to a bath, where, e.g., topological properties [18, 19, 31] and long-range order in driven-dissipative BECs [32] were revealed. Additional examples include driven-dissipative phase transitions [33–36], among them the paradigmatic superradiant phase transition in the Dicke model [37]. The extension to non-stationary situations enables phenomena such as prethermalization [38] or dynamical quantum phase transitions where observables become non-analytic at critical times [39]. Moreover, exotic states like time crystals in periodically driven systems have been proposed [39].

In recent years, research on localized dissipation in many-body quantum systems has been one of the emergent focal points of non-equilibrium physics, both experimentally [24, 40–44] and theoretically [22, 24, 25, 45–65]. In this thesis, we study the elementary problem of a single dissipative impurity in one-dimensional systems of interacting fermions. In this context, we encounter a rich interplay between non-equilibrium and many-body physics. In the following, we outline the three main pillars of our motivation that underlie the exploration of this problem.

As a first motivation, the theoretical study of localized dissipation provides insights into the dynamics and control of open quantum systems. Localized dissipation may be either engineered [24, 40–42] or intrinsically present as an unavoidable feature due to the manipulation of the system [43, 44]. Beyond regarding localized dissipation as an unwanted feature, it provides a suitable tool for the design of quantum states [22–25, 40, 65, 66]. Here, particle losses that occur in a localized spatial subregion of a system provide a common instance for such manipulations. As discussed below, localized losses are accessible in current experiments, e.g., in ultracold atoms by a simple implementation using a focused electron beam created with an electron microscope [40]. The state of a quantum system subject to localized losses is far from equilibrium due to the violation of particle number and energy conservation. Additionally, currents are induced by the presence of localized particle losses, directed towards the loss site [41], as illustrated in Fig. 1.1 (upper panel). Moreover, the lower panel of Fig. 1.1 illustrates the mechanism by which a NESS can be realized in a quantum wire with localized losses. The outer parts of the wire act effectively as reservoirs, residing at the initial thermal state of the wire. The central part of the system then establishes a NESS with steady currents flowing towards the loss site. The systematic characterization of the dynamics leading to the NESS in a fermionic quantum wire, its properties, and emerging interaction effects will be studied in the course of this thesis.

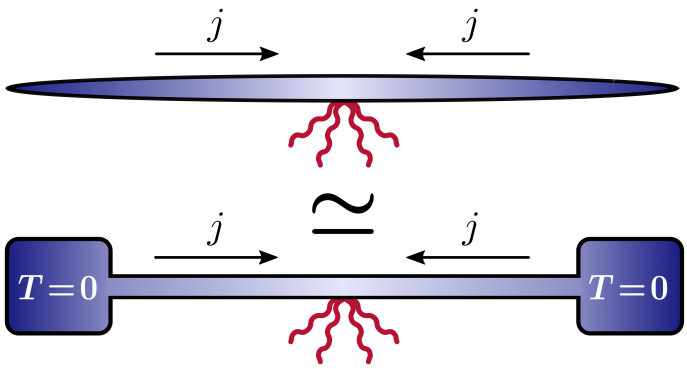

Fig. 1.1. Sketch of a fermionic wire subject to a localized loss. Before emptying out completely, a non-equilibrium (quasi-)stationary state occurs characterized by constant currents j flowing towards the loss site, analogous to a wire connected to reservoirs at its far ends.

As a second motivation, localized losses were implemented in recent experiments [40–44] in systems of ultracold atomic gases. Besides demonstrating the experimental practicality of localized dissipation, remarkable dynamical properties were found, such as a manifestation of the quantum Zeno effect [67–71].

The experimental platform of ultracold atoms allows the precise control of both the dissipation and the interaction processes between particles while exhibiting strong quantum effects [72–74]. Designed to establish nearly closed systems, ultracold atomic gases can be opened in a controlled way to achieve the intended dissipative processes [44]. Here, the use of optical traps and lattices provides suitable methods for controlling systems of ultracold atoms [72, 73]. Furthermore, the interaction strength can be widely modified by exploiting Feshbach resonances, which allows the engineering of both repulsive and attractive interactions [72, 73]. Accordingly, ultracold atoms provide a suitable platform for the investigation of interaction effects in the presence of localized losses, in which we are particularly interested. Localized losses were experimentally realized in Refs. [40–42] by directing a focused electron beam onto the system. Collisions between the electrons and the atoms excite the latter, which leads to their escape from the trap. Moreover, in Refs. [43, 44] localized losses were induced by a near-resonant so-called optical tweezer, which similarly leads to losses by photon scattering at the atoms. Both bosonic [40–42] and fermionic [43, 44] ultracold atomic gases with localized losses were experimentally investigated. The accompanying theoretical works mainly focused on bosonic systems [45, 48–52, 54–56, 58]. Recently, also fermionic systems have been considered [25, 59].

The quantum Zeno effect was originally formulated [67, 68] as the inhibition of the decay of an unstable quantum system due to a frequent measurement of its state. In more general terms, the quantum Zeno effect entails that a frequent measurement of a quantum state decouples its dynamics from all other states [69–71, 75]. In the context of open quantum systems, the coupling to the many degrees of freedom of a bath acts as a continuous measurement [69–71, 75, 76]. In experiments with localized losses, the quantum Zeno effect then manifests itself as a prominent non-monotonic dependence of the particle loss rate on the dissipation strength [40, 41]. This results from the fact that the dissipation acts as both the measurement and the loss mechanism. For strong dissipation strengths, the dissipative region decouples from the remaining wire due to the quantum Zeno effect, resulting in the suppression of losses. Figure 1.2 shows the particle loss rate which was measured in the experiment of Ref. [40], where localized losses are induced

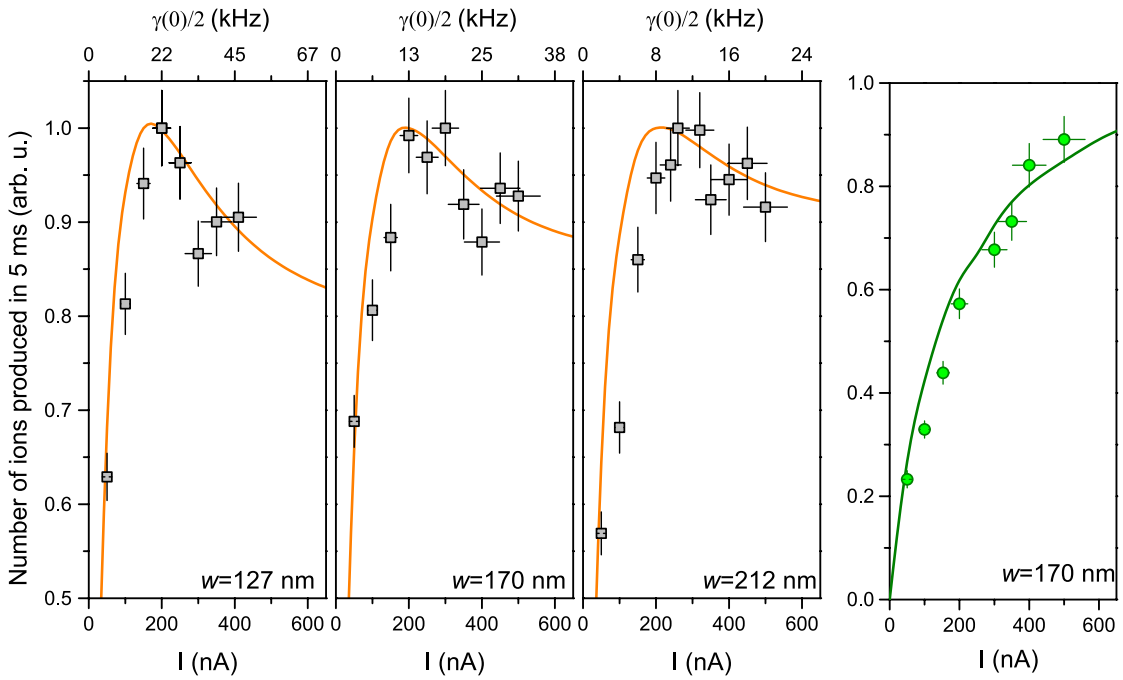

Fig. 1.2. The three panels on the left depict the number of atoms (squares) emitted from the BEC (within the first 5 ms of dissipation), as a function of the current I of the electron beam, acting as a dissipation strength γ. The data depicted in the three different panels are obtained for different widths w of the electron beam. The right panel shows the same observable (dots) but measured for a classical gas. The solid lines indicate the comparison to a theoretical model, respectively. (Figures taken from Ref. [40] with minor adaptations.)

by shining a focused electron beam on a BEC (three leftmost panels). Here, the particle loss rate is depicted as a function of the dissipation strength γ, determined, in turn, by the current I of the electron beam (for three different widths of the beam). At small dissipation strengths, the loss rate increases with γ as naively expected, whereas it decreases for large γ, as a manifestation of the quantum Zeno effect [40]. The rightmost panel depicts the same observable but obtained for a classical gas, where a simple monotonic behavior is revealed, demonstrating the quantum nature of the effect.

The interplay between the quantum Zeno effect and the particle loss rate in these cases can be understood solely in terms of local, single-body physics. In contrast, we consider the question of the interplay between the quantum Zeno effect and many-body physics as a guiding principle of this thesis and set it apart from the microscopic manifestations of the quantum Zeno effect. Experimentally, in Ref. [77] an exemplary instance of such an effect was observed where strong inelastic collisions in an ultracold molecular gas lead to a strongly-correlated state that is protected from decay [78].

These considerations lead us, as our third motivation, to the identification of one-dimensional interacting fermions as a promising platform to reveal a rich interplay of interactions in the wire and non-equilibrium effects induced by localized dissipation, such as the quantum Zeno effect. This expectation is based on the fact that impurities in interacting fermionic quantum wires generically give rise to drastic effects due to the presence of gapless fluctuations [79–82].

Here, the Luttinger liquid model constitutes the infrared fixed point of a large class of interacting one-dimensional models in their gapless metallic phase, thus establishing a Luttinger liquid universality class [10, 82–84]. Hence, the Luttinger liquid has a similar stand for one-dimensional interacting quantum systems as the Fermi liquid theory provides for higher-dimensional interacting gapless systems [82, 84]. Consequently, the consideration of a Luttinger liquid with localized losses enables us to conduct a study with a corresponding degree of universality.

A peculiarity of Luttinger liquids lies in the fact that its elementary low-energy excitations correspond to collective bosonic degrees of freedom, in contrast to the fermionic quasi-particles of the Fermi liquid theory [84]. In simple words, this feature can be rationalized by noting that in one dimension particles cannot circumvent each other. Hence, any single-particle excitation leads to a collective one, similar to a "traffic jam" phenomenon. This observation leads to an effective description in terms of new bosonic degrees of freedom via the method of bosonization, enabling the exact computation of the low-energy properties of interacting quantum wires.

A hallmark of Luttinger liquids is their strong susceptibility to spatial inhomogeneities. In fact, the density-density response function diverges as $|q - 2k_F|^{2(g-1)}$ [10], with k_F the Fermi momentum, for Luttinger parameters $g < 1$, which corresponds to any repulsive microscopic interaction [84]. Therefore, even a weak impurity acts as a strong perturbation as it leads to backscattering with a momentum transfer $q \sim 2k_F$. This strong susceptibility to backscattering originates from the restricted phase space available in one-dimension and is thus a general property of gapless interacting quantum wires [84]. In the view of the "traffic jam" simile stressed earlier, it is intuitive that an impurity can strongly affect a one-dimensional system since particles cannot evade it.

The effects of coherent impurities on the transport properties of Luttinger liquids have been studied in the paradigmatic works of Kane and Fisher [79, 80] by mapping the problem via the bosonization technique to a local sine-Gordon model. The effect of an impurity at long wavelength is then described by a renormalization group (RG) flow of the effective impurity strength, which grows to infinity in the case of repulsive interactions, leading, in turn, to a suppression of conductance. Not less remarkably, in the case of attractive interactions, the impurity is instead completely masked by the gapless fluctuations and the conductance of the interacting system is restored as if the impurity was not present. In the course of this thesis, we encounter the fact that the barrier created by a localized loss likewise induces backscattering. Hence, a localized dissipation is expected to provoke a strong response in a one-dimensional system of interacting fermions. Accordingly, the problem of localized losses in a Luttinger liquid constitutes a non-equilibrium counterpart of the paradigmatic Kane-Fisher problem [79–81].

Furthermore, the drastic renormalization effects of impurities in interacting quantum wires can be understood from a microscopic approach [81, 85, 86]. In fact, impurities in fermionic systems induce Friedel oscillations [87, 88] of the density profile, which in one dimension decay particularly slowly with $|x|^{-1}$ in the distance of the impurity [89, 90]. These density modulations provide an effective barrier in the presence of interactions for particles traversing the impurity region [81, 85, 86]. In addition, the wavenumber of Friedel oscillations is related to the Fermi momentum. As a result, particles with a matching wavenumber, i.e., those near the Fermi level, are particularly susceptible to this effective barrier. We will discover that the NESS in presence of a localized loss likewise supports Friedel oscillations and hence provides the mechanism for strong renormalization effects of the scattering and loss properties for particles

near the Fermi momentum. This provides an instance of the competition between coherent and dissipative processes in an interacting quantum wire subject to a localized loss.

For these reasons, we identify localized dissipation in interacting fermionic quantum wires as a promising field of study, where a rich interplay between many-body physics and non-equilibrium effects can be expected. In particular, we chose a one-dimensional realization because of the strong impurity effects typically revealed in these systems. Moreover, we focus on fermions, since these effects are most prominent in fermionic systems. Finally, the setup is experimentally realizable it ultracold atomic gases with localized losses.

In the following, we give a brief synopsis of several main findings of this thesis. The key results are presented systematically in the following section, which concludes with an overview of the structure of this thesis. The key results have been published in:

- H. Fröml, A. Chiocchetta, C. Kollath, and S. Diehl, *'Fluctuation-Induced Quantum Zeno Effect'*, Phys. Rev. Lett. 122, 040402 (2019)
- H. Fröml, C. Muckel, C. Kollath, A. Chiocchetta, and S. Diehl, *'Ultracold quantum wires with localized losses: Many-body quantum Zeno effect'*, Phys. Rev. B 101 (Editors' Suggestion), 144301 (2020)

The study of collective phenomena in a fermionic interacting quantum wire driven out of equilibrium by a localized loss reveals a variety of novel effects. The approach of this problem within several complementary methods reveals a low-energy collective behavior due to the interplay of the localized dissipation with the strong correlations and gapless modes of the wire. The transport and loss properties of modes near the Fermi level are found to be strongly modified by interactions. This establishes a fluctuation-induced quantum Zeno effect for repulsive interactions as a genuine many-body incarnation of the quantum Zeno effect. Instead, for attractive interactions, the impurity is completely masked by fluctuations and a fluctuation-induced transparency is established for modes near the Fermi energy. These effects influence the time evolution of observables in a characteristic way reflecting the suppression of losses near the Fermi level for both attractive and repulsive interactions.

A synthesis of several main findings is illustrated in the conceptual Fig. 1.3, as explained in the following. The quantum wire in the presence of a localized loss establishes a well-defined NESS (cf. Fig. 1.1). The depletion dynamics in this NESS can be quantified by the loss probability of modes. In the absence of interactions, it is then described by the black curve as a function of the dissipation strength γ. Here, the typical non-monotonic behavior for a dissipative impurity is encountered as a manifestation of the quantum Zeno effect (cf. Fig. 1.2), which at this level is exhaustively described by single-particle physics. The microscopic value of the loss probability (with an exemplary realization marked by the white dot) for modes near the Fermi level is then strongly modified (black dots) by interactions, as indicated by the arrows. For repulsive interactions, the dissipation strength γ is effectively increased (red arrows) and the loss of particles for $k \sim k_F$ is suppressed as a many-body incarnation of the quantum Zeno effect. For attractive interactions, instead, the effective dissipation strength is reduced (blue arrows) and the loss of particles for $k \sim k_F$ is likewise suppressed, as the dissipative impurity becomes effectively transparent. The underlying analysis leading to the here described picture as well as additional findings are summarized in the following section.

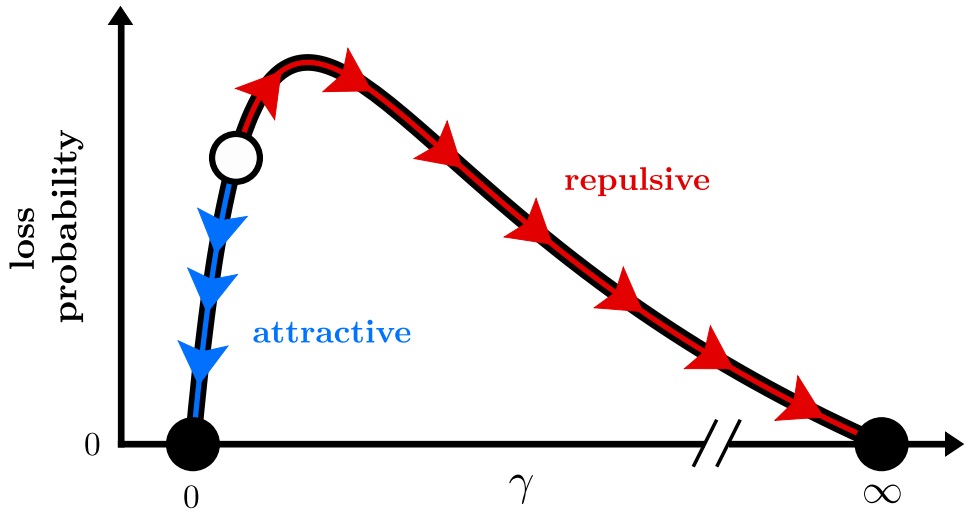

Fig. 1.3. Non-monotonic behavior of the loss probability as a function of the dissipation strength. For momenta close to k_F, gapless fluctuations renormalize the loss probability, reaching the Zeno (rightmost black dot) or transparent (leftmost black dot) fixed points for repulsive or attractive interactions, respectively.

1.2. Key results

Exact solution of the single-particle problem — The non-interacting system is studied both numerically and analytically, yielding a systematic description of the dynamics after the quench of a localized loss. Here, we consider a quantum wire of spinless fermions which is initially prepared in its zero-temperature ground state. The obtained characterization of the dynamics provides the basis for the subsequent investigation of the full interacting problem. Within a first numerical study, the time evolution is found to subdivide into three temporal regimes. Here, the extensively long second regime establishes a non-equilibrium (quasi-)steady state (NESS), which provides a well-defined setting for analytical approaches. To this end, we investigate the properties of the NESS in the non-interacting limit by exactly solving the single-particle problem. We obtain exact results for observables such as the density profile, loss rate, and currents, revealing the microscopic quantum Zeno effect for large dissipation strengths. Remarkably, the density profile around the loss site exhibits robust Friedel oscillations. The occurrence of Friedel oscillations is related to the discontinuity of the initial Fermi distribution which is found to persist in the NESS. Friedel oscillations are known as a key ingredient for severe interaction effects for modes close to the Fermi momentum. Moreover, the solution of the single-particle problem yields crucial insights into the physical mechanisms of depletion processes. Here, the loss probability η_k for particles with momentum k is identified as the key quantity to describe the depletion dynamics of the system. The loss rate is characterized by a Landauer-like formula depending on the loss probability η_k, the group velocity v_k and the initial momentum distribution $n_{0,k}$. These insights pave the way for an energy-resolved study of depletion processes, which can be achieved by considering the dynamics of the momentum distribution, carrying a direct signature of η_k. Finally, we consider the modifications of the dynamics due to a finite-temperature of the initial state.

Real-space renormalization group approach — We study the interplay between interparticle interactions in the NESS and the presence of a localized loss. To this end, we apply a microscopic

approach formulated in terms of the scattering and loss probabilities of the barrier established by a localized loss. Here, the Friedel oscillations in the vicinity of the loss site provide an additional effective scattering barrier in the presence of interactions. As a consequence, strong modifications of the scattering and loss probabilities are revealed for modes near the Fermi level within a real-space renormalization group (RG) analysis perturbative in the interaction strength. Remarkably, a suppression of the loss probability η_k is obtained for $k \sim k_F$ for both repulsive and attractive interactions. In addition, the transport properties are greatly modified, with the transmission vanishing for repulsive interactions, while being completely restored for attractive interactions despite the presence of a barrier. These results are understood as a fluctuation-induced quantum Zeno effect of genuine many-body character for repulsive interactions and a fluctuation-induced transparency for attractive interactions. Moreover, the RG flow reveals a novel logarithmic scaling in the approach to the fixed points for attractive interactions, with no counterpart in the RG flow of a coherent potential barrier. This scaling translates into the physics in the vicinity of the Fermi points and observables scale logarithmically with, e.g., temperature, instead of the more common algebraic behavior. The renormalization of the loss probability is reflected by observables such as the momentum-resolved loss rate and the momentum distribution, where the latter exhibits an increased occupation of modes near the Fermi level due to the suppression of losses.

Dynamical Hartree-Fock study — Within a dynamical Hartree-Fock approximation we investigate the influence of interactions on the time evolution in the presence of a localized loss. The classification of the dynamics in terms of three temporal regimes remains well-defined, supporting the notion of the NESS. The Friedel oscillations in the vicinity of the loss site persist, with a wavelength independent of the interaction strength. Moreover, the total particle loss rate increases for repulsive interactions while it is reduced for attractive ones. The momentum distribution is numerically evaluated within this approximation and exhibits a peak close to the Fermi momentum, in accordance with the predictions of the real-space RG approach, which we therefore interpret as a signature of the fluctuation-induced quantum Zeno effect.

Luttinger liquid approach — As the effective low-energy description of the considered microscopic models, we study a Luttinger liquid subject to localized losses. Since the quantum wire is driven out of equilibrium, a suitable functional description can be formulated within the Keldysh field theory. This formulation allows one to conduct an RG analysis perturbative in the dissipation strength γ. Moreover, a dual formulation perturbative in γ^{-1} is feasible, where the strong dissipation effectively separates the wire into two parts weakly connected by a dissipative link. At first order, gapless fluctuations strongly renormalize the effective dissipation strength. For repulsive interactions, γ is enhanced indefinitely, thus suppressing losses as a fluctuation-induced quantum Zeno effect. For attractive interactions, γ vanishes and backscattering is correspondingly suppressed, resulting in a fluctuation-induced transparency. Hence, in both cases, losses are suppressed at the Fermi level, consistently with the results of the real-space RG. Moreover, a reparametrization of the real-space RG flow by an effective dissipation strength enables a comparison of the RG scaling near the fixed points for both approaches. The analysis is extended to second order, where mode-coupling effects lead to the generation of a local effective temperature, which effectively cuts off the RG flow. Here, different regimes can be identified in which either the first-order renormalization qualitatively persists or in which self-thermalization effects dominate the RG flow of the effective dissipation strength.

Spectral properties of localized dissipation — We investigate the spectral properties of the effective non-Hermitian Hamiltonian and retarded Green's function associated with a localized loss in the non-interacting lattice model. At a threshold value of the dissipation strength, the complex spectrum of the non-Hermitian Hamiltonian is found to exhibit a sharp reorganization. Beyond the transition point, a single distinct mode emerges whose eigenvalue acquires an imaginary part much larger than all other modes. This distinct mode is localized at the dissipation site and can be interpreted as a spectral incarnation of the microscopic quantum Zeno effect. In addition, the spectral transition point constitutes an exceptional point of the non-Hermitian Hamiltonian. We consider the observability of the transition in the spectral function and within a related protocol with a localized pump, where it is signaled by an instability. Moreover, the description is extended by including a coherent potential superimposed on the localized loss, revealing remarkable spectral properties such as a spectral flow phenomenon for a variation of the complex impurity potential.

Outline of the thesis

The remainder of this thesis is structured as follows. In Chapter 2, the physical concepts and methods underlying the discussion are introduced. In Chapter 3, the microscopic model for a fermionic wire with localized losses is formulated, and its properties are studied in the absence of interparticle interactions. The obtained description of the dynamics provides the basis for further studies. In Chapter 4, we extend the model by the inclusion of interactions in the wire. The interplay of interactions and the localized loss is then investigated within a microscopic real-space RG approach. In Chapter 5, we present a numerical study of the interacting model based on a Hartree-Fock approximation of the dynamics in the wire. In Chapter 6, we develop a Luttinger theory description including localized losses within a Keldysh framework. A perturbative RG analysis is performed up to second order in the dissipation strength. In Chapter 7, we study the spectral properties of the effective non-Hermitian Hamiltonian and associated retarded Green's function in the presence of localized dissipation. Finally, in Chapter 8, the main results are summarized and future directions are discussed.

CHAPTER 2

PHYSICAL BACKGROUND AND METHODS

The goal of this thesis is the study of localized dissipation in interacting quantum wires. In this chapter, we discuss the physical principles and methods underlying the formulation and motivation of this problem. First, we introduce the concept of open quantum systems and suitable methods to describe their physics. We focus on the Markovian quantum master equation and Keldysh field theory, both of which find many applications in the course of this work. Subsequently, we discuss the quantum Zeno effect as a fascinating effect encountered in open quantum systems, that occurs in the study of dissipative impurities. We then turn towards the characteristics of one-dimensional interacting quantum systems and formulate a description in terms of the Luttinger model using the framework of bosonization. This sets the stage for approaching the remarkable physics of impurities in Luttinger liquids. As a synthesis of the presented concepts, we discuss recent research on dissipative impurities in low dimensions, with a special focus on experiments with localized losses in ultracold atomic gases. We conclude the chapter with a warm-up study of the non-Hermitian Schrödinger equation in the presence of an imaginary delta potential, which constitutes a toy model of a localized dissipation.

2.1. Open quantum systems and non-equilibrium physics

In the remainder of this thesis, we consider quantum wires subject to localized dissipation, which constitutes systems that are both open and out of equilibrium. In this section, we introduce two fundamental methods capable to describe non-equilibrium physics, which are used throughout this thesis: the quantum master equation and the Keldysh field theory.

One of the driving concepts of condensed matter physics is the identification of the fundamental degrees of freedom most suitable to formulate the intended theory. A careful choice of the degrees of freedom enables an accessible description and highlights the underlying physical mechanisms. Given a closed system, one may often introduce a bipartition of the system by identifying a part of it as the system of interest and the remaining part as environmental degrees of freedom. The complete dynamical description in terms of the microscopic degrees of freedom of both system and environment is often intractable and undesirable. The former is a consequence of the typically many degrees of freedom and potentially complicated interaction

between system and environment, and the latter reflects the fact that such a description would include unnecessary and thus obscuring information. Instead, one can obtain an effective description of the system by tracing out the environmental degrees of freedom. As the constituents are generally coupled to each other, the resulting dynamics of the system's degrees of freedom then establishes an open quantum system. As a consequence of the coupling to the environment, open quantum systems are typically driven out of equilibrium, which requires methodological descriptions not bound to the assumption of equilibrium. This entails that the steady state ρ_{SS} of the system is not described by a canonical Gibbs ensemble $\rho_{\mathrm{SS}} \not\sim \exp(-\beta H_S)$ (or its generalizations), with $\beta^{-1} = k_B T$ the inverse temperature and H_S the Hamiltonian of the system. We will discuss in the following both an operatorial description established by the Markovian quantum master equation in Lindblad form and a functional formalism given by the Keldysh field theory. Both methods are indeed equivalent; a further equivalent method is established by the quantum Langevin formalism, a stochastic differential equation for the system operators.

2.1.1. Quantum master equation

The quantum master equation is a suitable tool to describe the time evolution of open quantum systems out of equilibrium. We introduce the concept of the quantum master equation with a focus on Markovian dynamics and derive the quantum master equation in Lindblad form. We use the Lindblad equation in Chapter 3 to formulate the microscopic model of a localized loss in an interacting quantum wire.

Open quantum systems generally cannot be described by unitary time evolution, as it is achieved by the Schrödinger or von Neumann equation. Moreover, as the coupling with the environment may transform an initially pure state into a mixed one, a description in terms of density matrices is required. The quantum master equation then constitutes the non-unitary equation of motion for the density matrix of an open quantum system. Under certain assumptions it can be cast in a simple form: the quantum master equation in Lindblad form (or Lindblad equation). The Lindblad equation is a first-order linear differential equation for the reduced density matrix [2], that incorporates the effective action of the environment on the system in terms of so-called Lindblad operators. Its derivation relies on three approximations which are referred to as the Born, Markov, and rotating-wave approximations, whose validity is mainly controlled by a separation of time scales between system and bath, as discussed in the following.

As a starting point, we consider a closed system, $S + B$, which is constituted by the system of interest S and the environment B. We will also refer to the environment as a bath as we assume it contains many degrees of freedom. The full Hilbert space is thus given by $\mathcal{H} = \mathcal{H}_S \otimes \mathcal{H}_B$. The dynamics of the full system is generated by a Hamiltonian [2]

$$H_{\mathrm{full}} = H_S \otimes I_B + I_S \otimes H_B + H_I, \tag{2.1}$$

with $H_{S,B}$ the respective Hamiltonians of S and B, and $I_{S,B}$ the identities on $\mathcal{H}_S$ and $\mathcal{H}_B$. Further, H_I describes a coupling Hamiltonian acting on both constituents, which couples S and B. The goal is then to obtain an effective description for the system S by tracing out the degrees of freedom of the environment B, yielding the reduced density matrix of S

$$\rho_S = \mathrm{tr}_B\, \rho, \tag{2.2}$$

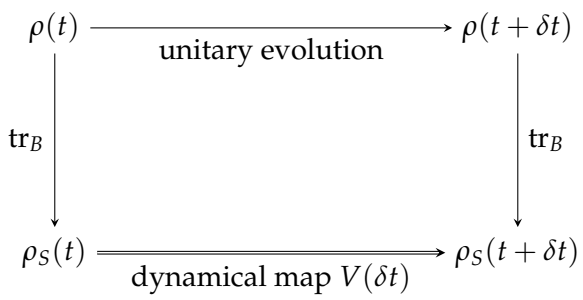

Fig. 2.1. Relationship between the dynamics of the full density matrix ρ and the one of the reduced representation ρ_S, defining a dynamical map V that describes the non-unitary evolution of the reduced system.

where tr_B denotes the partial trace over the degrees of freedom of B. By starting from the von Neumann equation

$$\partial_t \rho(t) = -i\,[H_{\mathrm{full}}, \rho(t)] \tag{2.3}$$

(we set $\hbar = 1$ here and in the remainder of the thesis), the reduced dynamics of S is most-generally described by

$$\partial_t \widetilde{\rho}_S(t) = -i\,\mathrm{tr}_B\,[H_I(t), \widetilde{\rho}(t)]\,, \tag{2.4}$$

where $\widetilde{\rho}(t)$ denotes the density matrix in the interaction picture. Here, operators $\widetilde{A}(t)$ in the interaction picture are related to the representation in the Schrödinger picture, A, via

$$\widetilde{A}(t) = \mathrm{e}^{iH_0 t} A \mathrm{e}^{-iH_0 t}. \tag{2.5}$$

With this preparation done, we aim to derive an effective equation for the time evolution of the reduced dynamics, solely formulated in degrees of freedom of the reduced system S. We mainly follow the derivation presented in Ref. [2]. As an alternative point of view, the derivation can also be formulated in terms of quantum trajectories [91, 92].

The underlying concept is depicted schematically in Fig. 2.1. The full density matrix ρ evolves unitarily according to the von Neumann equation. The reduced description can be obtained at any point in time by tracing out the environmental degrees of freedom. However, it would be impractical and not particularly instructive to actually follow this approach. Instead, we aim for a description describing the time evolution of $\rho_S(t)$ intrinsically, corresponding to the dynamical map $V(t)$ in Fig. 2.1. The external degrees of freedom do not enter this description but modify the time evolution of $\rho_S(t)$, effectively acting as dissipation, hence rendering the dynamics non-unitary. The differential form of the dynamical map constitutes the quantum master equation for the reduced density matrix. The description can then be simplified by assuming that the dynamics is Markovian, resulting in a semi-group structure $V(t_1 + t_2) = V(t_1)V(t_2)$ for the dynamical map. The associated generator of the dynamical group, the so-called Liouvillian superoperator $\mathcal{L}$, can be defined via $V(t) = \exp(\mathcal{L}t)$[1], leading, in turn, to the differential form $\partial_t \rho_S(t) = \mathcal{L}\rho_S(t)$. Here, the term *super*operator refers to the fact that the Liouvillian acts from both sides on the density matrix, as elaborated below.

We now derive the quantum master equation in Lindblad form starting from the microscopic Hamiltonian (2.1). The derivation relies on three approximations, on which we direct particular

[1]The mathematical assumptions underlying the existence of such a representation are discussed, e.g., in Ref. [2].

attention: the Born, Markov (or Born-Markov), and rotating wave (or secular) approximation. The formal solution of the von Neumann equation (2.3) in the interaction picture is given by

$$\widetilde{\rho}(t) = \widetilde{\rho}(0) - i \int_0^t ds\ [H_I(s), \widetilde{\rho}(s)]\,. \tag{2.6}$$

By inserting this expression into the von Neumann equation (2.4) for the reduced density matrix, corresponding to a perturbative expansion to second order, we obtain

$$\partial_s \widetilde{\rho}_S(t) = -\int_0^t ds\, \mathrm{tr}_B\,[H_I(t), [H_I(s), \widetilde{\rho}(s)]]\,, \tag{2.7}$$

where we assumed that the initial state fulfills $\mathrm{tr}_B\,[H_I(t), \rho(0)] = 0$, i.e., system and environment are initially uncorrelated. To simplify this integro-differential equation for $\widetilde{\rho}_S$ we apply the *Born approximation*, by which is assumed that the state of the environment remains unchanged during the time evolution. This assumption allows one to factorize $\widetilde{\rho}(s) = \widetilde{\rho}_S(s) \otimes \widetilde{\rho}_B$ in Eq. (2.7), with $\widetilde{\rho}_B \equiv \widetilde{\rho}_B(0)$. The approximation is valid when the effect on the environment B induced by the coupling to S can be neglected because excitations of the environment decay on a time scale τ_B much smaller than the characteristic time scale τ_S for the time evolution of S. Therefore, by this assumption, we commit to an effectively coarse-grained description, not able to resolve the fast-decaying excitations in the environment.

As a second approximation, we apply the *Markov approximation*, which assumes a rapidly decaying memory kernel of the system. This enables us to replace $\widetilde{\rho}_S(s)$ by $\widetilde{\rho}_S(t)$ in the right-hand side of Eq. (2.7), by which we obtain a time-local master equation for $\widetilde{\rho}_S(t)$, called the Redfield equation:

$$\partial_s \widetilde{\rho}_S(t) = -\int_0^t ds\, \mathrm{tr}_B\,[H_I(t), [H_I(s), \widetilde{\rho}_S(t) \otimes \widetilde{\rho}_B]]\,. \tag{2.8}$$

The time evolution described by the Redfield equation is non-ergodic and thus does not describe true Markovian dynamics. To this end, we additionally assume that the integrand vanishes sufficiently fast for $s \gg \tau_B$, which allows us to substitute $s \to t - s$ in the integrand and to extend the upper limit of the integration to infinity. This yields the Markovian quantum master equation

$$\partial_t \widetilde{\rho}_S(t) = -\int_0^\infty ds\, \mathrm{tr}_B\,[H_I(t), [H_I(t-s), \widetilde{\rho}_S(t) \otimes \widetilde{\rho}_B]]\,. \tag{2.9}$$

Note that the approximations applied here rely on related assumptions and are sometimes combined as the Born-Markov approximation [93].

We now rewrite the quantum master equation in a form suitable for implementing a final approximation given by the rotating wave approximation. Starting from the most generic form of the interaction Hamiltonian $H_I = \sum_\alpha A_\alpha \otimes B_\alpha$, we aim to rewrite this expression in terms of eigenoperators of the system Hamiltonian H_S. In this expression, the operators A_α describe physical processes in the system induced by the coupling to the environment. These operators will play a crucial role in the effective description obtained after integrating out the environment. On the contrary, we are not interested in the dynamics of the environment and hence the operators B_α will be traced out and do not enter explicitly the final description. The construction yields in the interaction picture $H_I(t) = \sum_{\alpha,\omega} \mathrm{e}^{-i\omega t} A_\alpha(\omega) \otimes B_\alpha(t)$ (for details see

Ref. [2]). By plugging this expression back into the master equation (2.9), one obtains

$$\partial_t \widetilde{\rho}_S(t) = \sum_{\omega,\omega'} \sum_{\alpha,\beta} \mathrm{e}^{i(\omega-\omega')t} \Gamma_{\alpha,\beta}(\omega) \left(A_\beta(\omega) \widetilde{\rho}_S(t) A_\alpha^\dagger(\omega') - A_\alpha^\dagger(\omega') A_\beta(\omega) \widetilde{\rho}_S(t) \right) + \text{h.c.}, \quad (2.10)$$

by which we therefore completed the task to trace out the environmental degrees of freedom. Here, we defined

$$\Gamma_{\alpha,\beta}(\omega) = \int_0^\infty \mathrm{d}s\, \mathrm{e}^{i\omega s} \left\langle B_\alpha^\dagger(t) B_\beta(t-s) \right\rangle_B, \quad (2.11)$$

the Fourier transform of the reservoir correlation functions

$$\left\langle B_\alpha^\dagger(t) B_\beta(t-s) \right\rangle_B = \mathrm{tr}_B \left[B_\alpha^\dagger(t) B_\beta(t-s) \widetilde{\rho}_B \right]. \quad (2.12)$$

Finally, one can apply the so-called *rotating wave approximation* (or secular approximation). The approximation is based on the assumption that the bath correlation function decay on a time scale τ_B much smaller than the relaxation time scale of the open system. This assumption requires typically a large environment with a continuum of modes. Moreover, let τ_S be the typical time scale of the intrinsic system dynamics, and let us assume that this time scale is much larger than the typical time scale of coupling processes between system and environment, i.e., $\tau_S \gg |\omega - \omega'|^{-1}$ in Eq. (2.10). This assumption implies that during the time τ_S the oscillating (non-secular) terms in Eq. (2.10) average out, and the only contribution originates from terms with $\omega = \omega'$. This construction effectively corresponds to a coarse-graining of the time evolution $\sim \int_t^{t+\tau_S} \mathrm{d}s$. Hence, we arrive at

$$\partial_t \widetilde{\rho}_S(t) = \sum_{\omega} \sum_{\alpha,\beta} \Gamma_{\alpha,\beta}(\omega) \left(A_\beta(\omega) \widetilde{\rho}_S(t) A_\alpha^\dagger(\omega) - A_\alpha^\dagger(\omega) A_\beta(\omega) \widetilde{\rho}_S(t) \right) + \text{h.c.} \quad (2.13)$$

At this point, it is instructive to decompose $\Gamma_{\alpha,\beta}$ as

$$\Gamma_{\alpha,\beta}(\omega) = \gamma_{\alpha,\beta}(\omega) + i S_{\alpha,\beta}(\omega), \quad (2.14)$$

where $S_{\alpha,\beta}(\omega)$ is Hermitian and $\gamma_{\alpha,\beta}(\omega)$ positive, given explicitly by

$$\gamma_{\alpha,\beta}(\omega) = \int_{-\infty}^\infty \mathrm{d}s\, \mathrm{e}^{i\omega s} \left\langle B_\alpha^\dagger(s) B_\beta(0) \right\rangle_B. \quad (2.15)$$

Finally, we obtain the quantum master equation in the interaction picture in the form

$$\partial_t \widetilde{\rho}_S(t) = -i \left[H_{\mathrm{LS}}, \widetilde{\rho}_S(t) \right] + D[\widetilde{\rho}_S(t)]. \quad (2.16)$$

Here, H_{LS} is a Hermitian operator that entails corrections to the Hamiltonian of the system, leading to a Lamb-type shift of the energy levels due to environmental fluctuations. Further, the so-called dissipator $D[\widetilde{\rho}_S(t)]$ contains the non-unitary part of the dynamics of S induced by the coupling to B, reading

$$D[\widetilde{\rho}_S(t)] = \sum_{\omega} \sum_{\alpha,\beta} \gamma_{\alpha,\beta}(\omega) \left(A_\beta(\omega) \widetilde{\rho}_S(t) A_\alpha^\dagger(\omega) - \frac{1}{2} \left\{ A_\alpha^\dagger(\omega) A_\beta(\omega), \widetilde{\rho}_S(t) \right\} \right). \quad (2.17)$$

Equation (2.17) can be diagonalized by choosing new operators L_α as linear combinations of the set of operators A_α. Further, the summation over ω can be absorbed in a redefinition of the sum over α by reinterpreting each ω as an individual process, thus enlarging the set of L_α.

After incorporating these considerations, we return to the Schrödinger picture and write $\rho \equiv \rho_S$ since we eliminated all other degrees of freedom from the description. As the central result presented in this section, we arrive at the quantum master equation in Lindblad form, given by [2, 5, 6]

$$\partial_t \rho = \mathcal{L}\rho = -i\,[H, \rho] + \sum_\alpha \gamma_\alpha \left(L_\alpha \rho L_\alpha^\dagger - \frac{1}{2} \left\{ L_\alpha^\dagger L_\alpha, \rho \right\} \right). \tag{2.18}$$

Here, the dissipative processes are describes by the Lindblad operators L_α (also called jump operators) and quantified by the respective rates γ_α, which have the dimension of an inverse time (provided the Lindblad operators are dimensionless). The Lindblad operators can be understood as the effective action of the bath on the system, e.g., the destruction of particles to incorporate losses. The generator of the coherent part of the dynamics is given by the Hamiltonian $H = H_S + H_{LS}$. The right-hand side of Eq. (2.18) defines the Liouvillian superoperator $\mathcal{L}[\rho]$. The time evolution generated by the Liouvillian superoperator is trace-preserving and establishes a completely positive map [2].

We conclude with a brief discussion of the structure of the Lindblad equation (2.18). Its first term describes unitary dynamics in full analogy to the von Neumann equation. The non-unitary part of the dynamics is entailed in the dissipator, describing the effective action of the environment on the system. It is itself composed of an anti-commutator term and a term where the Lindblad operators act from both sides on the density matrix, the so-called jump or recycling term. This structure can be interpreted as follows. The anti-commutator term describes dissipation as one could naively guess by adding an effective imaginary potential term, quadratic in the Lindblad operator, to the Hamiltonian. Indeed, the resulting effective non-Hermitian Hamiltonian provides in some cases a useful effective description, where it governs the dynamics of observable in which fluctuations average out. However, by considering only this term in Eq. (2.18), one would violate the conservation of probability, i.e., not preserve the trace of ρ. Indeed, in the quantum master equation the additional jump term restores the preservation of the trace and can be interpreted as the fluctuations associated with the dissipation [6]. The conservation of probability is readily confirmed by taking the trace on both sides of Eq. (2.18) and by making use of the cyclicity of the trace. Finally, we remark that the description by a quantum master equation is equivalent to the one established by a quantum Langevin equation or Keldysh field theory [6].

2.1.2. Keldysh field theory

Functional descriptions have proven as powerful methods for the study of many-body systems [1]. The Keldysh field theory [3] (also called Keldysh-Schwinger field theory) is applicable in non-equilibrium contexts, while more conventional field theories are limited by their construction to equilibrium partition functions corresponding to a thermal state. In particular, the Keldysh method allows for a field-theoretic treatment of the Markovian quantum master equation introduced in the previous section and opens up the powerful toolbox of field theory for the application to open quantum systems out of equilibrium. In the remainder of this thesis, the Keldysh formalism is frequently used.

We outline the derivation of the Keldysh field theory by starting from the non-unitary dynamics of the density matrix described by a quantum master equation in Lindblad form. Subsequently, we discuss the Green's functions and several further important properties of the Keldysh action [4, 16, 94].

Trotterization of the quantum master equation

In the following, we discuss the derivation of the Keldysh functional integral starting from a quantum master equation [4, 6, 95]. A Trotter decomposition [1] of the dynamical map $\exp(\mathcal{L}t)$ (cf. Sec. 2.1.1) leads to a description by a functional integral which is equivalent to the quantum master equation. We present here a derivation for bosonic degrees of freedom, while the procedure can be adapted straightforwardly to fermions [4], resulting in an analogous Grassmann functional integral. In this thesis, the fermionic Keldysh theory is used to analyze the single-particle problem of a localized loss in Chapter 3 while the bosonic counterpart is encountered in a bosonized description of localized losses applied in Chapter 6.

As a key difference to its equilibrium counterparts, the Keldysh field theory includes a doubling of the degrees of freedom. This can be understood by noting that in the case of thermal equilibrium it is sufficient to apply the Trotter decomposition to a *single* operator $\exp(-\beta H)$, which is the imaginary-time analog of the time-evolution operator in the construction of the Feynman path integral [1]. In contrast, also in a closed system, a generic mixed state cannot be described by a single wave function but, instead, a description by a density matrix is required. The time evolution is then determined by the von Neumann equation (2.3), with the formal solution

$$\rho(t) = U(t, t_0)\rho(t_0)U^\dagger(t, t_0), \tag{2.19}$$

where *two* time-evolution operators $U(t, t') = \exp[-iH(t - t')]$ appear, acting from both sides on the density matrix. As the formulation of the functional integral then proceeds by a Trotter decomposition [1] of the time-evolution operators, the action on the density matrix from both sides results in a doubling of the degrees of freedom [6].

The central object of interest in the functional description is the partition function

$$Z = \operatorname{tr}\rho(t), \tag{2.20}$$

which allows for the computation of correlation functions (by the inclusion of source terms, see below). The partition function obeys the normalization condition $Z = 1$, originating from the conservation of probability. If we focus on the stationary state of the system, corresponding to the limit $t \to \infty$, due to the cyclicity of the trace, the evolution of the density matrix can be interpreted to take place on a closed time contour [4, 6].

We now outline the derivation of the Keldysh functional integral obtained by a Trotter decomposition of the partition function, where the time evolution of $\rho(t)$ is described by the Lindblad equation (2.18). Hence, the constructed field theory is capable to describe the dissipative dynamics of generic mixed states. For the technical steps of the derivation we mainly follow Ref. [6]. The formal solution of the Lindblad equation (2.18) is given by

$$\rho(t) = \mathrm{e}^{\hat{\mathcal{L}}(t-t_0)}\rho(t_0), \tag{2.21}$$

with $\rho(t_0)$ the density matrix of the initial state. Here, we emphasize that the superoperator $\exp(\hat{\mathcal{L}}t)$ acts from both sides on the density matrix, similar to the time-evolution operators in Eq. (2.19). Moreover, $\hat{\mathcal{L}}$ includes operator-valued coefficients, i.e., the Lindblad operators, which we emphasize in the notation by introducing a hat. In order to perform the Trotter decomposition, we write the generator of the dynamics evolving from the initial time t_0 to the time t as the limit of a sequence of N time steps:

$$\mathrm{e}^{\hat{\mathcal{L}}(t-t_0)} = \lim_{N\to\infty} \left(1 + \delta_t \hat{\mathcal{L}}\right)^N, \tag{2.22}$$

where $\delta_t = (t - t_0)/N$ is the duration of each time step. In analogy to the construction of the equilibrium functional integral, we can make use of a resolution of the identity $\mathbb{I}$ in terms of coherent bosonic states [6]

$$\mathbb{I} = \frac{1}{\pi} \int \mathrm{d}\phi\, \mathrm{d}\bar{\phi}\, \mathrm{e}^{-\bar{\phi}\phi}\, |\phi\rangle\, \langle\phi| \,. \tag{2.23}$$

This allows one to trade the bosonic creation and annihilation operators for complex fields by using the fact that the coherent states are eigenstates of the annihilation operator, i.e., $a\,|\phi\rangle = \phi\,|\phi\rangle$ and $\langle\phi|\, a^\dagger = \langle\phi|\,\bar{\phi}$, with $\phi \in \mathbb{C}$. We can understand the decomposition (2.22) as an iterative time evolution where after the n-th step, at time $t_n = t_0 + \delta_t n$, we obtain

$$\rho(t_{n+1}) = \left(1 + \delta_t \hat{\mathcal{L}}\right) \rho(t_n) + \mathcal{O}(\delta_t^2). \tag{2.24}$$

In each step, we now insert two resolutions of the identity (2.23) left and right next to $\rho(t_n)$. Here, we label the fields appearing in the integral (2.23) with an index (n) for the insertion in the n-th time step, and an index $+$ for the insertion to the left, or $-$ for the insertion to the right of $\rho(t_n)$. This procedure yields after a single iteration

$$\rho(t_{n+1}) = \int D_n \mathrm{e}^{-\bar{\phi}_+^{(n)}\phi_+^{(n)} - \bar{\phi}_-^{(n)}\phi_-^{(n)}}\, \langle\phi_+^{(n)}|\rho(t_n)|\phi_-^{(n)}\rangle\, (1 + \delta_t\hat{\mathcal{L}})\, |\phi_+^{(n)}\rangle\, \langle\phi_-^{(n)}| \,, \tag{2.25}$$

where we introduced the shorthand notation for the measure $D_n \equiv \mathrm{d}\bar{\phi}_+^{(n)}\mathrm{d}\phi_+^{(n)}\mathrm{d}\bar{\phi}_-^{(n)}\mathrm{d}\phi_-^{(n)}/\pi^2$, and used the linearity of $\hat{\mathcal{L}}$ to factor out the matrix element of $\rho(t_n)$.

We can now explicitly evaluate $(1 + \delta_t\hat{\mathcal{L}})\, |\phi_+^{(n)}\rangle\, \langle\phi_-^{(n)}|$ and by using the coherent state properties, $a\,|\phi\rangle = \phi\,|\phi\rangle$, $\langle\phi|\, a^\dagger = \langle\phi|\,\bar{\phi}$, trade the operators in $\hat{\mathcal{L}}$ for fields, in full analogy to the construction of a path integral [1]. This step relies on the normal ordering of all constituents of the quantum master equation, i.e., the Hamiltonian H, L, and $L^\dagger L$ (the latter might be non-trivial [6, 96]). As a result of this procedure we obtain [97]

$$(1 + \delta_t\hat{\mathcal{L}})\, |\phi_+^{(n)}\rangle\, \langle\phi_-^{(n)}| = (1 + \delta_t\mathcal{L}_n)\, |\phi_+^{(n)}\rangle\, \langle\phi_-^{(n)}| \,, \tag{2.26}$$

with the now field-valued element

$$\begin{aligned}
\mathcal{L}_n \equiv & -i \left(H[\bar{\phi}_+^{(n+1)}, \phi_+^{(n)}] - H[\bar{\phi}_-^{(n+1)}, \phi_-^{(n)}] \right) \\
& - \frac{1}{2} \sum_\alpha \Big(L_\alpha^\dagger L_\alpha[\bar{\phi}_+^{(n+1)}, \phi_+^{(n)}] + L_\alpha^\dagger L_\alpha[\bar{\phi}_-^{(n+1)}, \phi_-^{(n)}] \\
& + 2 L_\alpha[\bar{\phi}_+^{(n+1)}, \phi_+^{(n)}]\, L_\alpha^\dagger[\bar{\phi}_-^{(n+1)}, \phi_-^{(n)}] \Big),
\end{aligned} \tag{2.27}$$

where the notation $X[\bar{\phi}, \phi]$ entails that bosonic creation and annihilation operators in X are replaced by $\bar{\phi}$ and ϕ, respectively. Hence, the Liouvillian expressed in the fields at time step n takes on a form analogous to the one of its operator-valued counterpart $\hat{\mathcal{L}}$, where operators acting from the left on the density matrix translate into $+$ fields, and operators acting from the right into $-$ fields. Remarkably, the jump term in the quantum master equation couples the $+$ and $-$ fields. In analogy to the action of the time-evolution operators in Eq. (2.19), describing evolution forward (backward) in time when acting from the left (right) on the density matrix, we can thus refer to the $+$ $(-)$ fields to reside on the forward (backward) time branch of the Keldysh contour. By implementing these considerations into Eq. (2.25), we arrive at

$$\rho(t_{n+1}) = \int D_n \mathrm{e}^{-\bar{\phi}_+^{(n)}\phi_+^{(n)} - \bar{\phi}_-^{(n)}\phi_-^{(n)}} \mathrm{e}^{\delta_t \mathcal{L}_n} \left|\phi_+^{(n)}\right\rangle \left\langle\phi_+^{(n)}\right|\rho(t_n)\left|\phi_-^{(n)}\right\rangle \left\langle\phi_-^{(n)}\right| . \tag{2.28}$$

The procedure can now be iterated recursively. In the next iteration, i.e., using the corresponding decomposition for $\rho(t_n)$ in Eq. (2.28), the following overlaps between coherent states are produced [6]

$$\left\langle\phi_+^{(n)}|\phi_+^{(n-1)}\right\rangle = \mathrm{e}^{\bar{\phi}_+^{(n)}\phi_+^{(n-1)}}, \qquad \left\langle\phi_-^{(n-1)}|\phi_-^{(n)}\right\rangle = \mathrm{e}^{\bar{\phi}_-^{(n-1)}\phi_-^{(n)}}. \tag{2.29}$$

These factors can be combined with the exponential factors in Eq. (2.28) of the previous step, originating from the resolution of the identity. As a result, one obtains the expressions $\exp[-\bar{\phi}_+^{(n)}(\phi_+^{(n)} - \phi_+^{(n-1)})]$ and $\exp[-(\bar{\phi}_-^{(n)} - \bar{\phi}_-^{(n-1)})\phi_-^{(n)}]$, which in the continuum limit, $N \to \infty$, entail a time derivative upon the identification $\partial_t \phi_\pm^{(n)} \equiv (\phi_\pm^{(n)} - \phi_\pm^{(n-1)})/\delta_t$. Additionally, in this continuum limit, the distinction between $(n+1)$ and (n) fields in Eq. (2.27) can be neglected [6].

The Keldysh field integral can now be constructed by starting from the partition function $\mathrm{tr}\,\rho(t_N)$, iterating recursively the decomposition described by Eq. (2.28) until the initial time t_0 is reached, and then taking the continuum limit $N \to \infty$. In the following, we restrict the description to a stationary state by taking additionally the limits $t_0 \to -\infty, t \to \infty$. The construction yields the Keldysh functional integral representation of the partition function reported below in Eq. (2.31) [6].

In principle, in this construction, two additional matrix elements occur which have not been discussed so far, which originate from the Trotter decomposition steps $n = 0$ and $n = N$, and read (using the cyclic property of the trace)

$$\left\langle\phi_+^{(0)}\right|\rho(t_0)\left|\phi_-^{(0)}\right\rangle , \qquad \left\langle\phi_-^{(N)}|\phi_+^{(N)}\right\rangle . \tag{2.30}$$

Here, the first element depends on the density matrix of the initial state and is, in general, demanding to compute. The second matrix element connects the $+$ and $-$ contour of the functional integral, even in the case of purely coherent dynamics where a jump term in the quantum master equation is absent. Although in the continuum limit these two terms only represent a domain of zero measure, they are, in fact, important for providing both a regularization and the information about the properties of the initial state [4]. However, these matrix elements are usually not explicitly considered in the formulation of the Keldysh action (2.31) but instead are implicitly included via a regularization of the action [4]. This becomes most clear in a time-discretized discussion which, e.g., can be found in Ref. [4]. Finally, we remark that in the case of fermions, particular attention must be paid to the ordering of the Grassmann fields due to their anti-commuting properties [98].

Keldysh partition function

The construction yields the following Keldysh functional integral [4, 6, 98], which we report here for the case of fermions, where the functional integration involves Grassmann variables [4]. In fact, in case of a quadratic bosonic quantum master equation, the same form of the action is obtained [4, 6, 98], with the functional integration given by complex fields. The Keldysh partition function reads

$$Z = \int \mathcal{D}[\psi_+, \psi_+^*, \psi_-, \psi_-^*] e^{iS[\psi_+, \psi_+^*, \psi_-, \psi_-^*]}, \tag{2.31}$$

with the Keldysh action

$$S[\psi_+, \psi_+^*, \psi_-, \psi_-^*] = \int_{-\infty}^{\infty} dt \left(\psi_+^* i\partial_t \psi_+ - \psi_-^* i\partial_t \psi_- - i\mathcal{L}[\psi_+, \psi_+^*, \psi_-, \psi_-^*] \right), \tag{2.32}$$

where the field analog of the Liouville superoperator, is given by

$$\begin{aligned} \mathcal{L}[\psi_+, \psi_+^*, \psi_-, \psi_-^*] = &- i \left(H[\psi_+, \psi_+^*] - H[\psi_-, \psi_-^*] \right) \\ &+ \sum_\alpha \gamma_\alpha \left[L_{\alpha,-}^* L_{\alpha,+} - \frac{1}{2} \left(L_{\alpha,+}^* L_{\alpha,+} + L_{\alpha,-}^* L_{\alpha,-} \right) \right]. \end{aligned} \tag{2.33}$$

Thus, the form of the action closely reflects the form of the corresponding Lindblad equation (2.18).

Green's functions, Keldysh rotation and causality structure

We briefly discuss some important properties of the Keldysh action that are relevant for the further discussion. Most importantly, we point out a useful representation by a change from the $\pm$-basis to the so-called c, q-basis, whereby the latter indices stand for "classic" and "quantum". This terminology is motivated by the fact that classic Keldysh fields can acquire a finite expectation value, whereas quantum Keldysh fields cannot. In addition, this representation is instructive as it allows the Green's functions to be interpreted in terms of response and correlation properties.

First, in order to obtain a non-trivial partition function, the insertion of external sources $j_\pm$ is required, which can be simply added to the Hamiltonian on each Keldysh contour, resulting in a term in the action of the form [6]

$$\int_{t,x} \left(j_+^\dagger \psi_+ - j_-^\dagger \psi_- \right). \tag{2.34}$$

Correlation functions are then computed as functional derivatives with respect to these sources [4, 6]. This allows one to evaluate the correlation functions in the $\pm$-basis, formally related to Green's functions obtained from the action as [4]

$$\begin{pmatrix} \langle \psi_+ \psi_+^* \rangle & \langle \psi_- \psi_+^* \rangle \\ \langle \psi_+ \psi_-^* \rangle & \langle \psi_- \psi_-^* \rangle \end{pmatrix} = i \begin{pmatrix} G^T & G^> \\ G^< & G^{\tilde{T}} \end{pmatrix}, \tag{2.35}$$

where the average is defined as

$$\langle X \rangle = \int \mathcal{D}\left[\psi_+, \psi_+^*, \psi_-, \psi_-^*\right] X \, e^{iS[\psi_+, \psi_+^*, \psi_-, \psi_-^*]}. \tag{2.36}$$

Here, the notation G^T ($G^{\widetilde{T}}$) refers to the (anti-)time-ordering operator T ($\widetilde{T}$) and is inspired by the fact that in the connection to the operator formalism particular care has to be given to the time-ordering of the correlation functions. The reason is that in the construction of the Keldysh action an (anti-)time ordering [i.e., time arguments increase from right to the left] was assumed on the $+(-)$ contour. In turn, the notation $G^<, G^>$ is motivated by the fact that the $+$ field occurs before the $-$ field on the Keldysh contour and vice versa. However, the Green's functions (2.35) corresponding to the $\pm$ basis are not independent, since they fulfill the relation [4]

$$G^T(t,t') + G^{\widetilde{T}}(t,t') - G^>(t,t') - G^<(t,t') = 0. \tag{2.37}$$

This condition reflects the fact that the Green's functions in the $\pm$ representation contain redundancies. These redundancies can be made explicit by a change of basis, yielding a minimal description which contains all information, as discussed in the following. For these reasons, we will not consider the Green's functions (2.35) in the $\pm$-basis in the following.

By means of the so-called Keldysh rotation, the Keldysh action is transformed to its c, q or Retarded-Advanced-Keldysh (RAK) representation. To this end, the Keldysh rotation is given by the unitary transformation

$$\psi_c = \frac{1}{\sqrt{2}}\left(\psi_+ + \psi_-\right), \qquad \psi_q = \frac{1}{\sqrt{2}}\left(\psi_+ - \psi_-\right), \tag{2.38}$$

and analogously for $\psi_{c/q}^*$. We remark that, in the case of fermions, it is possible to choose a different convention for the transformations of the conjugate fields $\psi_\pm^*$, since the Grassmann fields are not related by complex conjugation to $\psi_\pm$ and hence can be chosen independently [4]. Nevertheless, we use in this thesis the analog of the transformation (2.38) for $\psi_\pm^*$ also for fermions, leading to the same form of the action for bosons and fermions.

After performing the Keldysh rotation, the quadratic part of the action is obtained as

$$S[\psi_c, \psi_c^*, \psi_q, \psi_q^*] = \int_t \begin{pmatrix} \psi_c^* & \psi_q^* \end{pmatrix} \begin{pmatrix} 0 & P_A \\ P_R & P_K \end{pmatrix} \begin{pmatrix} \psi_c \\ \psi_q \end{pmatrix}, \tag{2.39}$$

which in turn yields the retarded, G_R, advanced, G_A, and Keldysh, G_K, Green's functions via

$$\begin{pmatrix} G_K & G_R \\ G_A & 0 \end{pmatrix} = \begin{pmatrix} -P_R^{-1} P_K P_A^{-1} & P_R^{-1} \\ P_A^{-1} & 0 \end{pmatrix}. \tag{2.40}$$

From this, correlation functions in the c, q representation can be obtained via [6]

$$\begin{pmatrix} \langle \psi_c \psi_c^* \rangle & \langle \psi_c \psi_q^* \rangle \\ \langle \psi_q \psi_c^* \rangle & \langle \psi_q \psi_q^* \rangle \end{pmatrix} = i \begin{pmatrix} G_K & G_R \\ G_A & 0 \end{pmatrix}. \tag{2.41}$$

Here, G_R and G_A are related by Hermitian conjugation, while G_K is anti-Hermitian:

$$G_A = G_R^\dagger, \qquad G_K^\dagger = -G_K. \tag{2.42}$$

Additionally, the retarded and advanced Green's function obey the equal-time identity [4]

$$G_R(t,t) + G_A(t,t) = 0, \tag{2.43}$$

while, in contrast, their difference is finite

$$G_R(t,t) - G_A(t,t) = -i. \tag{2.44}$$

The appearance of only three finite Green's function in Eq. (2.40) reflects the reduction of the redundancy present in Eq. (2.35). Moreover, the RAK representation yields an instructive form of the action which can be physically interpreted in terms of response and correlations properties [6]. Here, the retarded and advanced Green's functions describe response (as anticipated in their name), while the Keldysh Green's function contains the information about correlations. Finally, we report the Dyson equation in the Keldysh formalism, given by [6]

$$\begin{pmatrix} G_K & G_R \\ G_A & 0 \end{pmatrix}^{-1} = \begin{pmatrix} 0 & G_0^A - \Sigma^A \\ G_0^R - \Sigma^R & -\Sigma_K \end{pmatrix}, \tag{2.45}$$

where the self-energies $\Sigma_{R,A,K}$ denote the corrections to the bare Green's functions $G_0^{R,A,K}$ and $G^{R,A,K}$ the full Green's functions.

The Keldysh action exhibits a so-called causality structure with the defining property [6]

$$S[\psi_c, \psi_c^*, \psi_q = 0, \psi_q^* = 0] = 0, \tag{2.46}$$

which implies that terms of the form $\psi_c^* \psi_c$ cannot appear in the Keldysh action. This causality structure is a consequence of the conservation of probability, which can be inferred as follows. The act of setting the quantum fields to zero in Eq. (2.46) corresponds to setting $\psi_+ = \psi_-$ (cf. Eq. (2.38)). This transformation resembles taking the trace of the quantum master equation, since due to the cyclicity of the trace the notion of acting from the left or the right on the density matrix is lost and with it the distinction of the $\pm$ contours. While the identity (2.46) is obvious on a single-particle level (see Eq. (2.39)), it can also be proven for the full theory [6].

As a last remark, in thermal equilibrium, fluctuation-dissipation relations connect fluctuations and dissipation which are hence not independent players. As the simplest example of such a relation, a resistor in an electric circuit always introduces noise [1]. We report here the fluctuation-dissipation theorem of the Keldysh action for bosonic degrees of freedom, given by

$$G_K(\omega) = \coth\left(\frac{\omega - \mu}{2T}\right)\left(G_R(\omega) - G_A(\omega)\right), \tag{2.47}$$

with μ the chemical potential, T the temperature of the thermal state, and the coth entailing the Bose distribution function. Further, it is always possible, in particular away from equilibrium, to parametrize the Green's functions according to

$$G_K = G_R \circ F - F \circ G_A, \tag{2.48}$$

where F is Hermitian and $\circ$ denotes convolution. Here, F represents the distribution function of (quasi-)particles in the (non-)equilibrium state.

2.2. Quantum Zeno effect

> "He [Zeno of Elea] says that if everything when it occupies an equal space is at rest, and if that which is in locomotion is always in a now, the flying arrow is therefore motionless." (Aristotle Physics [99])

The quantum Zeno effect was named after Zeno's arrow paradox (see quotation at the beginning of this section), where the evolution of a quantum system constitutes a "quantum arrow" whose dynamics is stopped by a frequent observation [67]. When first (explicitly) formulated in Ref. [67], the quantum Zeno effect was regarded as a paradoxical result, questioning the completeness of quantum mechanics. However, the quantum Zeno effect was soon realized to be far from an artifact of a flawed description but physically relevant. Nowadays, it is not considered as a paradox but as a fascinating effect of quantum mechanics.

The essence of the quantum Zeno effect can be understood as follows [40, 67–71, 75–77]. Let us assume a quantum system is coupled with external degrees of freedom that act as a measurement apparatus. The measurement can distinguish certain states of the system. In the limit of strong coupling to the measurement apparatus, the transition between these states is then suppressed, strongly affecting the dynamics of the system. As a special case, if the measurement can probe the initial state, the dynamics is stopped.

We now develop this perspective on the quantum Zeno effect as the generalization of its initial formulation [67]. Beside theoretical arguments, the discussion of experimental observations highlights instructively several important aspects of the quantum Zeno effect. Throughout this thesis, the quantum Zeno effect is revealed in many observables and is therefore of importance in all following chapters.

2.2.1. Basic formulation

The quantum Zeno effect was originally formulated in the following minimalist way. An unstable quantum system is frequently probed by projective measurements to see whether it has already decayed [67]. For an infinitely fast measuring rate, the decay of the unstable system is then stopped, leaving the unstable system "frozen" in its initial state. Hence, the effect results from a competition between the frequent measurements and the infinitesimal unitary evolution of the system taking place in between. A measurement according to von Neumann's projection postulate [69] projects a quantum system onto the state of the measurement outcome. After only a short time, the unstable system is most likely found in its initial state. Crucially, the short-time dynamics of Schrödinger's equation entails that for any quantum system the transition probability grows initially *quadratic* in time [67, 70, 71], before typically an exponential decay sets in for an unstable system. Now, if measurements are performed in short intervals δt, the "reset" to the initial state $\sim \delta t$ dominates over the infinitesimal evolution $\sim \delta t^2$ and the dynamics of the system is "frozen".

A simple derivation of the effect proceeds as follows [70, 71]. For simplicity, we assume a system prepared in a pure state $|\psi_0\rangle$, which evolves unitarily between measurements, $|\psi(t)\rangle = \mathrm{e}^{-iHt}|\psi_0\rangle$. The survival probability $p(t)$ of the initial state is then defined as

$$p(t) = |\langle\psi_0|\mathrm{e}^{-iHt}|\psi_0\rangle|^2. \tag{2.49}$$

After a short time δt has passed, the survival probability reads [71]

$$p(\delta t) = 1 - \frac{\delta t^2}{\tau_Z^2} + \ldots, \qquad \tau_Z^{-2} \equiv \langle \psi_0 | H^2 | \psi_0 \rangle - \langle \psi_0 | H | \psi_0 \rangle^2, \tag{2.50}$$

revealing a quadratic behavior on a characteristic time scale τ_Z. Now, consider a protocol where N measurements are performed up to a time t during the evolution, and $\delta t \equiv t/N$. Each measurement ascertains whether the system still remains in the initial state $|\psi_0\rangle$ and, according to von Neumann's theorem, the state $|\psi(t)\rangle$ is projected "back" on the initial state $|\psi_0\rangle$ for a positive measurement outcome. The survival probability $p^{(N)}(t)$ of the undecayed state for $N \gg 1$ measurements interrupting the evolution up to time t is then given by

$$p^{(N)}(t) = p^N(\delta t) \simeq \left[1 - \left(\frac{t}{N\tau_Z}\right)^2\right]^N \simeq \mathrm{e}^{-t^2/(N\tau_Z^2)}. \tag{2.51}$$

Hence, when the decay is monitored with an infinite measurement rate, $N \to \infty$, the probability to find the system in its initial state is one, thus the system remains in its initial state. This perhaps surprising results was dubbed the quantum Zeno effect.

The simple derivation presented above calls for several improvements. First, the generalization to mixed states described by a density matrix ρ is straightforward [69] since the projective measurement removes any coherences between subspaces of the Hilbert space corresponding to different measurement outcomes [70]. Second, a more rigorous mathematical treatment of the expansion for short times leads to a confirmation of the previous reasoning [67, 70].

The quantum Zeno effect was initially considered paradoxical because of the following seeming contradiction [67]. The predicted "freezing" of the transition is not observed in certain unstable systems that are apparently continuously monitored, e.g., an unstable particle in a bubble chamber, which nevertheless decays. The paradox stated above is resolved in a simple way, by noting that the limit $N \to \infty$ is normally not physically realizable [70, 75], leading rather to a slowing down than a complete stopping of the dynamics for large N. We discuss below how a rather natural description can be formulated in terms of continuous measurements, i.e., by explicitly including the coupling to the environment in the description.

2.2.2. Generalization

The concept of the quantum Zeno effect can be generalized beyond the hitherto developed description. First, we discuss the generalization to higher-dimensional Hilbert spaces, where the frequent measurements allow dynamics within certain subspaces, in turn, defined by the measurements. Hence, the dynamics is strongly affected but not necessarily "frozen" in its initial state [69, 76]. Second, the notion of projective measurements can be relaxed to continuous measurements, which are realized by a coupling of the system to external degrees of freedom providing the measurement apparatus.

A measurement is naturally associated with a projection operator P [70]. In turn, this operator defines a generally multidimensional subspace $\mathcal{H}_P = P\mathcal{H}$ of a Hilbert space $\mathcal{H}$, where the measurement acts by distinguishing whether the state of the system is inside or outside this subspace. One can then show [70] that transitions between $\mathcal{H}_P$ and its complement are

suppressed by a frequent measurement rate, establishing a generalized instance of the quantum Zeno effect.[2] In the derivation of the previous section, we encountered a one-dimensional projector, $P = |\psi_0\rangle \langle\psi_0|$, leading to a restriction of the system to its initial state. However, $\mathcal{H}_P$ and its complement can exhibit a higher dimension, allowing for dynamics within these subspaces, respectively. Remarkably, in the limit of an infinite measurement rate, this dynamics is found to be unitary, despite the presence of projective measurements, generated by an effective Hamiltonian reduced to the subspace [70]. We encounter an instance of emergent unitarity associated with an incarnation of the quantum Zeno effect in Chapters 4 and 6. Moreover, if frequent measurements are performed on a spatial segment of a system to ascertain the presence of a particle therein (thus defining a spatial subspace of the system), this region effectively acquires rigid walls, constituting Dirichlet boundary conditions for the wave function of a particle [70]. From this observation we can anticipate that in the case of a localized dissipation, acting effectively as a measurement (see discussion below), a particle will rather be reflected back from the dissipative region than experiencing the dissipation within. This behavior is indeed observed experimentally (see Sec. 2.4) and a recurring aspect in the remainder of this thesis.

As a second generalization, the description of a measurement can be generalized from projective measurements to continuous measurements, as outlined in the following. While the quantum Zeno effect can be derived in a simple way in terms of projective measurements on a quantum system, one can consider, however, the projection due to a measurement rather as a simple picture summarizing the effect of the complicated physical processes underlying a quantum measurement [70]. Hence, it is natural to generalize the pulsed projective measurements to an explicit coupling to environmental degrees of freedom, providing the measurement apparatus. Such a coupling can be interpreted as a measurement if it is suitable to encode information on the state of the observed system in the external degrees of freedom. The experiment in Ref. [100] provides both an example and a counterexample of this fact, as discussed in Sec. 2.2.4. One can show [70, 71, 76] that a continuous measurement in this sense induces the quantum Zeno effect in analogy to projective measurements. From this generalized viewpoint, the quantum Zeno effect entails that a strong coupling to an environment leads to the inhibition of transitions between internal quantum states, specified by the details of this coupling. Here, a characteristic time scale of the coupling between system and environment, e.g., a response time or interaction rate, replaces the measurement interval δt of the pulsed measurement.

A simple example of an open quantum system exhibiting a quantum Zeno effect due to a continuous coupling to a bath is described by the following non-Hermitian Hamiltonian [71]:

$$\widetilde{H} = \begin{pmatrix} 0 & \Omega \\ \Omega & -i2\Gamma \end{pmatrix}. \tag{2.52}$$

This non-Hermitian Hamiltonian entails an effective description for a two-level system that exhibits Rabi oscillations with a frequency Ω, whereby additionally the second level decays at a rate Γ. Along the lines of the discussion in Sec. 2.2.1, we consider the survival probability at time t for a preparation of the system in the first level, which is obtained, for a large coupling to the environment, by expanding in small Ω/Γ as [71]

$$p(t) \sim \mathrm{e}^{-\Omega^2 t/\Gamma}. \tag{2.53}$$

[2] The description may be further generalized to a collection of projectors.

As expected, the dissipation leads to an exponential loss of probability. However, the initial state decays with an effective rate $\gamma_{\text{eff}} = \Omega^2/\Gamma$ which counter-intuitively *decreases* with increasing dissipation rate Γ. The comparison to the effective decay rate for the pulsed measurement in Eq. (2.51) yields the relation $\Gamma = \delta t^{-1}$ [71]. Therefore, the presence of the dissipation Γ has a similar effect on the dynamics as pulsed projective measurements in intervals δt^{-1}. We can understand the stabilization of the first level as a consequence of the quantum Zeno effect: the transition to the dissipative second level is suppressed by the strong continuous (null) measurement of the transition $1 \to 2$.

Moreover, the description via an effective Hamiltonian with a large imaginary potential as in Eq. (2.52) allows an alternative rationalization of the quantum Zeno effect [77]. In classical optics, a large imaginary refraction index, quantifying the absorption of a medium, leads to the asymptotically perfect reflection of incoming electromagnetic waves, analogous to a large real-valued refraction index. Consequently, given the wave nature of quantum mechanics, it is not surprising that a dissipative potential leads to the reflection of a quantum particle.

2.2.3. Anti-Zeno effect

In Sec. 2.2.1 we encountered the quantum Zeno effect as a slowing down in the decay of an unstable quantum system. While a total inhibition of the decay is obtained in the limit of an infinite measuring rate, a slowing down is already evident for a sufficiently large measuring rate (see Eq. (2.51)), rendering the onset of the quantum Zeno effect a continuous process. Besides, even an increase of the effective decay rate can be achieved in some systems by tuning the measurement interval, which creates the anti-Zeno effect [75, 100] (or inverse Zeno effect [70]).

To this end, let us consider the probability $p^{(N)}(t)$ to find a generic unstable system at time t in its initial state, where N measurements in intervals δt interrupt the dynamics [70] (cf. Sec. 2.2.1):

$$p^{(N)}(t) = p^N(\delta t) = \mathrm{e}^{N \ln p(\delta t)} = \mathrm{e}^{-\gamma_{\text{eff}}(\delta t) t}, \tag{2.54}$$

where we defined the effective decay rate

$$\gamma_{\text{eff}}(\delta t) = -\frac{1}{\delta t} \ln p(\delta t). \tag{2.55}$$

In Eq. (2.51), we considered the limit $\delta t \to 0$, which lead to $\gamma_{\text{eff}}(\delta t) \sim \delta t/\tau_Z^2 \to 0$. In contrast, for large δt, one expects to recover the decay rate γ obtained in the absence of any measurement. For an intermediate choice of δt, it is found that the effective decay rate can also be *larger* than γ, if $p(\delta t)$ is sufficiently large in a domain between the initial quadratic and eventual exponential regime [70, 75]. In Sec 2.2.4, we discuss an experiment [100] where the emergence of the anti-Zeno effect and its relation to the Zeno effect is instructively illustrated. The anti-Zeno effect may be observed even in systems where the large measurement rates required to obtain the slowing down in the quantum Zeno regime are physically not feasible [75]. Whether a Zeno or Anti-Zeno effect is observed for a given measurement rate is generally a non-trivial question depending on the form factors governing the coupling between the system and the measurement apparatus [75]. The existence of the anti-Zeno regime highlights that the quantum Zeno effect is not simply an "on/off switch" of the dynamics, but is a gradual process of dominating the dynamics of a quantum system due to frequent measurements of a subsystem.

2.2.4. Experimental realizations

The quantum Zeno effect was observed in a variety of experimental setups [40, 68, 77, 100]. Beyond providing the experimental proof of the effect, the discussion of the experimental realizations highlights several important aspects of the quantum Zeno effect.

Quantum Zeno effect: experiment by Itano et al.

We first discuss the paradigmatic experiment in Ref. [68], providing an early experimental confirmation of the quantum Zeno effect. Here, the quantum Zeno effect was observed in transitions between hyperfine levels of cold trapped ions.

The system can be modeled by three levels $1, 2, 3$, as illustrated in Fig. 2.2 (right panel). A transition between the levels $1, 2$ is induced by the application of a radio pulse P_T with a controlled duration, whereas spontaneous decay $2 \to 1$ is assumed to be negligible. Level 3 is utilized to probe the occupation of level 1 by the application of a second, optical pulse P_M. If the ion is in state 1, during a pulse P_M it cycles between the states $1, 3$ emitting a series of photons that can be detected. In contrast, if the ion is in state 2, no photons are emitted. Therefore, the application of a pulse P_M constitutes an ideal measurement of the quantum states 1 and 2, in the latter case via a null measurement. Initially, all ions are prepared in state 1 and after the application of a pulse P_T, the state of the ion is measured with a pulse P_M to infer the transition probability. Now, in order to probe the quantum Zeno effect, additionally, n short pulses P_M can be applied while the pulse P_T is active, establishing a pulsed measurement of the transition progress at intermediate times.

The measured transition probability of the transition $1 \to 2$, during which n measurement pulses are applied, is reported in Fig. 2.2 (left panel). A single measurement run involves an ensemble average of many ions in parallel where mutual interactions can be neglected. With an increasing number of interrupting measurements n, the transition probability is found to decrease, in accordance with the quantum Zeno effect. Moreover, when the system is initially prepared in state 2, the transition probability $2 \to 1$ can be probed. In this case, also a null measurement, where during pulses P_M no photons are emitted, is found to suppress the decay of level 2 with increasing measurement rate, signaling the inhibition of transitions between the subspaces defined by the measurement (cf. Sec. 2.2.2).

(Anti)-Zeno effect: experiment Fischer et al.

A further instructive experiment was performed in Ref. [100], providing insights on both the Zeno and Anti-Zeno effect. Here, ultracold atoms are trapped in an optical lattice which is accelerated for a controlled duration, accelerating the atoms in the ground state along with the lattice. In particular, an acceleration sequence is applied, consisting of slow and fast phases, which on the one hand induces decay of the atom population, and on the other hand is used as a measurement of the time of decay events, as explained in the following. During the slow phases atoms are simply accelerated along with the lattice, whereas during the fast phase, they can additionally tunnel out of the lattice via an excitement to untrapped states. In the process, atoms acquire a velocity proportional to the duration they were accelerated together with the lattice, as depicted in Fig. 2.3 (left panel). Eventually, the trapping potential is switched off and the

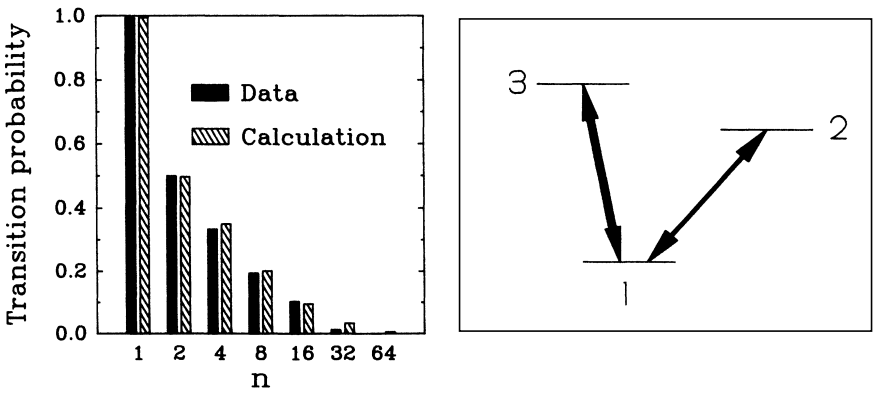

Fig. 2.2. Left panel: Measured transition probability (black bars) of the transition $1 \rightarrow 2$ as a function of the number n of interrupting measurements. Right panel: Energy-level diagram of the three-level system. The black arrows indicate induced transitions. (Figures taken from Ref. [68] with minor adaptions.)

velocity distribution is measured by the time-of-flight method, as shown in Fig. 2.3 (right panel). Atoms that stay in the lattice until the end of the sequence acquire a maximal velocity. In turn, particles that are lost from the lattice earlier during a fast acceleration phase possess a lower velocity. If the fast acceleration phase is now interrupted repeatedly by slow phases, particles lost during each of the resulting short fast acceleration phases possess a distinct velocity, as illustrated by the blue arrows in Fig. 2.3. Therefore, each interruption of the fast acceleration phase corresponds to a measurement of whether particles have already decayed at that time.

From the final population, the survival probability can be inferred. In Fig. 2.4 (left panel) the survival probability is shown as a function of the tunneling time (sum of the fast acceleration intervals). The lower curve corresponds to an uninterrupted fast acceleration phase. In contrast, the upper curve corresponds to a fast acceleration phase with frequent interruptions every $1\mu s$, acting as measurements. The frequently measured protocol has a larger survival probability, corresponding to a slowing down of the decay due to the quantum Zeno effect. Indeed, the survival probability of the uninterrupted system decreases slowly in the initial regime up to time $\sim 1\mu s$, resulting in a slowing down of the decay if the evolution is repeatedly "reset" by a measurement after that time.

Moreover, as an interesting feature, the uninterrupted survival probability exhibits a steeply declining domain for tunneling times $\sim (1-5)\mu s$. If the measuring interval is increased to $5\mu s$, the in this way interrupted system is found to decay *faster* than the uninterrupted one, as shown in Fig. 2.4 (right panel). Here, the lower curve corresponds to the interrupted system and the upper curve to the uninterrupted one. The measurements "reset" the time evolution in a way that this fast domain dominates the decay, thus revealing an instance of the Anti-Zeno effect.

A further insightful aspect of this experiment is the interpretation of the coarse-graining of the velocity distribution (cf. Fig. 2.4, right panel) as a measurement of tunneling events. In turn, if the intermediate slow acceleration intervals are chosen too short to resolve different peaks in the velocity distribution, only incomplete information on the time of the tunneling events is acquired, thus not performing an ideal measurement. In this case, the (Anti-)Zeno effect is diluted, and the survival probability is found to approach the unperturbed curve.

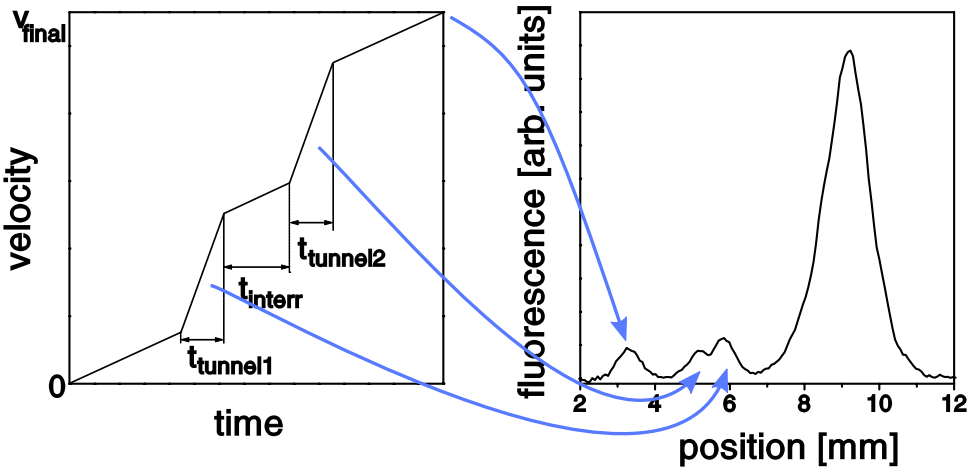

Fig. 2.3. Left panel: Schematic acceleration sequence in time with alternating phases of slow and fast acceleration. Right panel: Typical spatial distribution of atoms measured in Ref. [100] after switching off the trapping potential, allowing the reconstruction of the particle velocity. The blue arrows indicate the origin of the observed peaks in the distribution. The large peak on the right corresponds to particles initially untrapped by the optical lattice (irrelevant for the discussion). The leftmost peak corresponds to undecayed particles. The two peaks in between are constituted of particles that decayed in one of the two fast acceleration phases, respectively. (Figures taken from Ref. [100] with minor adaptions; annotations added.)

Quantum Zeno effect and many-body physics: experiment by Syassen et al.

Finally, we briefly discuss an experiment [77] where the quantum Zeno effect was observed in a strongly correlated open many-body system. In contrast, the instances of the quantum Zeno effects discussed so far are exhaustively described by single-particle physics. Here, a one-dimensional gas of ultracold bosons is considered. A molecule state was formed for which strong inelastic interactions between the molecules lead to losses. On the other hand, strong inelastic interactions are found to increase the correlations in the system [78], leading, in turn, to a reduction of the loss rate according to [77]

$$\frac{\mathrm{d}n}{\mathrm{d}t} \sim g^{(2)} n, \tag{2.56}$$

where $g^{(2)} < 1$ for a correlated state, with $g^{(2)} = \langle n^2 \rangle \,/\, \langle n \rangle^2$ the pair-correlation function, and n the particle density.

The effect of strong inelastic interactions thus bears parallels to the quantum Zeno effect: the initial state is protected against losses and does not decay. Moreover, the very fact that strong inelastic collisions result in strong correlations rather than strong losses can be related to the reasoning of the quantum Zeno effect in the following way [77]. Bosons interacting with a large imaginary scattering length are almost perfectly reflected off each other, in analogy to a classical absorbing potential. The resulting constraints on the many-body wave function result in a strongly correlated state. This provides an example of the interplay between many-body physics and the quantum Zeno effect, which acts as a guiding principle for the remainder of this thesis.

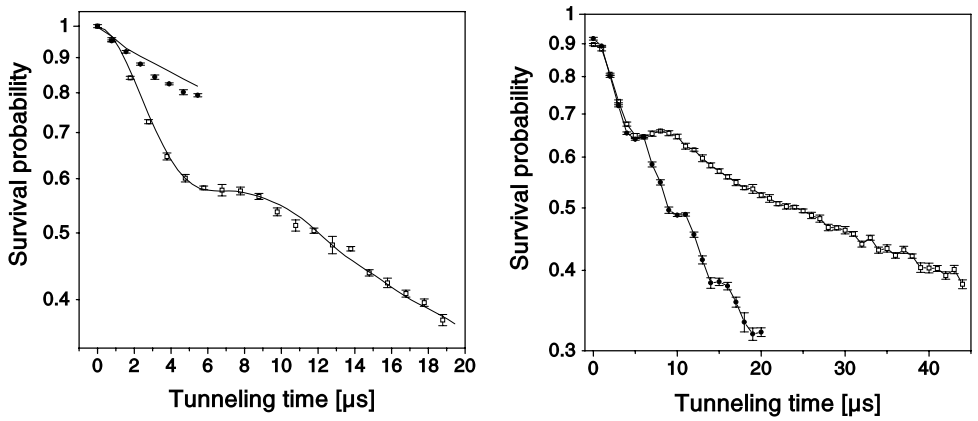

Fig. 2.4. Survival probability of atoms in the accelerated lattice as a function of the total duration of the fast acceleration phases (tunneling time). Left panel: Hollow squares (lower curve) show the non-interrupted sequence, solid circles (upper curve) show the sequence with interruptions acting as measurements. The measurement interval is $1\mu s$, leading to a quantum Zeno effect. Right panel: Hollow squares (upper curve) show the non-interrupted sequence, solid circles (lower curve) show the sequence with interruptions acting as measurements. The measurement interval is $5\mu s$, leading to an anti-Zeno effect. (Figures taken from Ref. [100] with minor adaptions.)

Moreover, the experiment [77] provides an example of the Zeno effect in a dissipative system where dissipation plays a double role: it provides the mechanism for both losses and measurements. In such systems, a characteristic suppression of the loss rate is typically encountered (cf. Eq. 2.56), as losses take place via states that are continuously monitored [78] and to which transitions are consequently suppressed by the quantum Zeno effect. Therefore, the quantum Zeno effect in systems with a lossy subspace reveals itself in a non-monotonic dependence of the dissipation, e.g., quantified by a particle loss rate $\dot{N}$, on a dissipation strength Γ, for large Γ [40]:

$$\frac{\mathrm{d}\dot{N}}{\mathrm{d}\Gamma} < 0. \tag{2.57}$$

We encounter this effect in the discussion of experiments with localized dissipation in Sec. 2.4 below and in the further analysis of this thesis.

2.3. Luttinger liquids and bosonization

The physics of one-dimensional interacting fermions exhibits several peculiarities which we highlight in this section. In doing so, we characterize the concept of a Luttinger liquid as the effective model for interacting quantum systems in one dimension by setting it apart from the Fermi liquid behavior found for interacting fermions in higher dimensions. To this end, we first give a conceptional introduction to Luttinger liquid physics. Subsequently, in a more technical discussion, we introduce the method of bosonization which allows one to derive exact solutions in the low-energy limit for interacting one-dimensional systems [84, 101]. Here, the interacting model can be mapped to the quadratic Luttinger Hamiltonian. The in this way constructed Luttinger liquid model describes the universal low-energy behavior of many fermionic (and bosonic) one-dimensional interacting models [84, 102]. It is found to describe accurately the low-energy properties of both condensed matter and ultracold atomic systems of fermions

in one dimension [82]. This fact expresses that the construction is deeply connected to the dimensionality of the system and its restricted phase space, and not specific to any particular model. Experimental realizations in condensed matter include carbon nanotubes [103] and edges of higher-dimensional systems [101, 104]. We make use of the bosonization mapping in the study of dissipative impurities in Luttinger liquids, presented in Chapter 6 of this thesis.

2.3.1. Luttinger liquids versus Fermi liquids

In the following, we discuss the nature of low-energy excitations in one-dimensional interacting fermionic systems, in contrast to their higher-dimensional counterparts, to motivate the subsequent analysis. In a free system, at $T = 0$, all states below the Fermi energy are occupied. Excitations then correspond to adding particles with momentum k and a well-defined energy ϵ_k on top of this ground state, which possess an infinite lifetime since they are eigenstates of the Hamiltonian. Remarkably in dimensions $d > 1$, interactions change relatively little compared to free fermions [84]. Interacting systems for $d > 1$ constitute Fermi liquids, in which the elementary, low-energy excitations are given by fermions dressed by density fluctuations. Thus, the excitations are collective but still of fermionic character. These excitations can be described by fermionic quasi-particles with a renormalized mass which, however, exhibit a finite lifetime due to scattering between quasi-particles. The identification of excitations as quasi-particles can be made more precise by considering the spectral function where a quasi-particle reveals itself as a peak at a well-defined energy with a width corresponding to its inverse lifetime. For the understanding of many properties of a Fermi liquid it is then sufficient to consider these quasi-particles themselves as approximately free [84]. This is in contrast to the microscopic fermions, which are strongly coupled. Upon switching on interactions adiabatically, the Fermi momentum[3] coincides with the one of the free system for a given filling, which can be proven as a consequence of the Luttinger theorem, stating that the volume enclosed by the Fermi surface is invariant under this protocol [84].

The nature of the excitations leaves a signature in the momentum distribution of the system. The momentum distribution n_k of the free system exhibits a discontinuity at the Fermi momentum of height one, as depicted in Fig. 2.5 (upper left panel). In a Fermi liquid, a discontinuity at the Fermi momentum is still present but diminished to a factor $Z < 1$, as shown in Fig. 2.5 (upper right panel). One can interpret Z as the fraction of excitations which are of sharp quasi-particle character (Z can be related to the weight of the quasi-particle peaks in the spectral function), while the remaining part of excitations forms a continuous background [84]. Near the Fermi energy, the sharp excitations then dominate the physical properties. Crucially, the validity of the Fermi liquid description is not restricted to weak interactions as the formation of fermionic quasi-particles is robust also for fairly strong interactions [84]. In $d = 1$, instead, interacting quantum systems reveal a Luttinger liquid behavior, fundamentally different from a Fermi liquid, as discussed in the following. To complete the triptych of qualitatively different momentum distributions in Fig. 2.5, we anticipate the fermionic momentum distribution obtained for a Luttinger liquid, which is shown in the lower panel of Fig. 2.5. Here, the distribution is continuous at the Fermi momentum ($Z = 0$), but non-analytic corresponding to a so-called

[3] We assume rotational symmetry and thus a spherical Fermi surface.

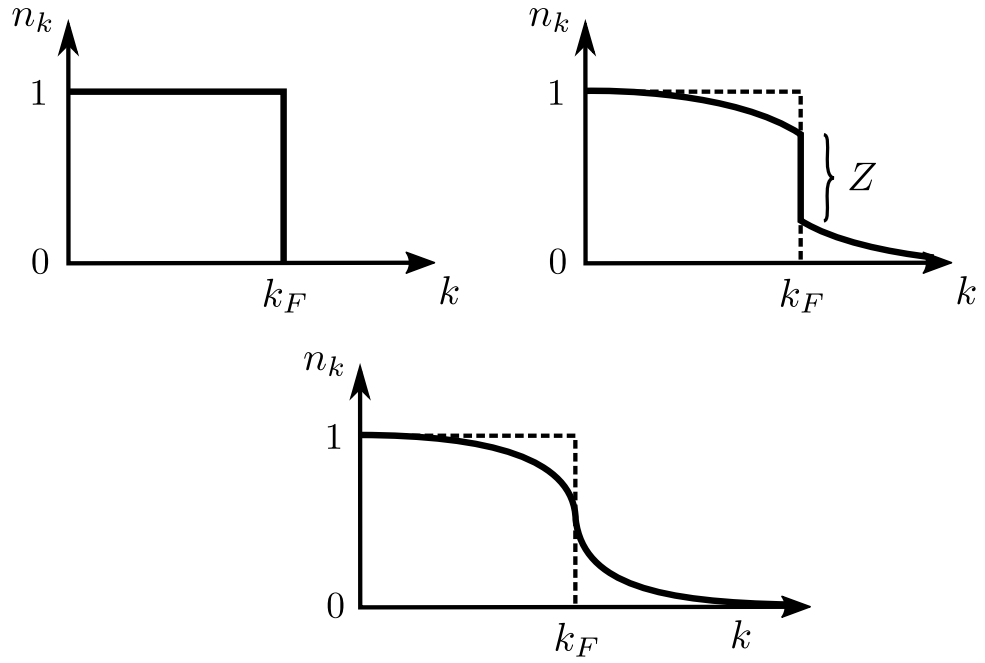

Fig. 2.5. Schematic momentum distributions (solid) for fermionic systems without interactions (upper left panel), a Fermi liquid (upper right panel) and a Luttinger liquid (lower panel) [84]. The dashed lines indicate the comparison to the distribution of the non-interacting system, respectively.

essential power law singularity at k_F [84], given by

$$n_k \sim |k - k_F|^{(g+g^{-1})/2-1}, \tag{2.58}$$

where g is the Luttinger parameter introduced below. Therefore, the notion of a Fermi surface persists. In the sense of the previous discussion, the absence of a discontinuity in the momentum distribution can be interpreted as the absence of sharp single-particle excitations. In fact, it can be assumed that the situation in a one-dimensional interacting system must differ strongly from a Fermi liquid. In one dimension, no individual motion is possible since a propagating fermion is forced to collide with its neighbors, and hence single-particle excitations decay rapidly into collective ones, as substantiated in the following.

Moreover, in one-dimensional fermionic systems a failure of perturbation theory is encountered, hinting towards the fact that interactions pose a severe modification of the free theory. The susceptibility associated with the response to a density perturbation, relevant for the perturbation theory in the interactions, behaves as [84]

$$\chi(q,\omega) \sim \int_k \frac{f_F(\zeta_k) - f_F(\zeta_{k+q})}{\omega + \zeta(k) - \zeta(k+q) + i\delta}, \tag{2.59}$$

where $\zeta(k) = \epsilon_k - \mu$, with ϵ_k the dispersion relation and μ the chemical potential, f_F is the Fermi distribution, and $\delta > 0$ is an infinitesimal quantity to ensure causality. The zero-frequency contribution ($\omega = 0$) of the susceptibility is divergent for certain combinations of k and q. In particular, a strong singularity is encountered for any q such that $\zeta(k) - \zeta(k+q) = 0$, for all k (or a finite domain). For small q, this property defines the so-called nesting property of the Fermi surface. In higher dimensions, the required matching of the angle and modulus leads typically

to a nesting only at isolated k, and the divergence is smoothed out by other contributions in the integration of k [84]. In contrast, in one-dimensional systems, the Fermi surface is *totally* nested. By linearizing the dispersion relation close to the Fermi surface, one finds the nesting vector $q = 2k_F$, at which consequently the susceptibility (2.59) exhibits a severe divergence, signaling a breakdown of perturbation theory even for weak interactions. This indicates that the ground state of the interacting system can be expected to differ greatly from the ground state of the non-interacting system. (Similar divergences are encountered, e.g., in the BCS theory for pair susceptibilities, indicating the superconducting transition [84].)

As a further peculiarity in one dimension, particle-hole excitations are well-defined bosonic quasi-particles at low-energies, as discussed in the following [84]. To create a particle-hole excitation, a particle residing below the Fermi energy, at a momentum k, is excited to an unoccupied state, at momentum $k + q$, with an energy above the Fermi surface. Given the momentum q of the excitation, in higher dimensions, the corresponding energy generally depends on both k and q, leading to a continuum of arbitrarily low energies (for $q < 2k_F$) of particle-hole excitations. In one-dimension, on the contrary, only $q \simeq 0$ and $q \simeq 2k_F$ are possible low-energy excitations. If one linearizes the dispersion at k_F (cf. Fig. 2.6), this fact results in a unique relation between the momentum q and energy $E(q)$ of a particle-hole excitation, given by $E(q) = v_F q$, with v_F the Fermi velocity. Because particle-hole excitations are of bosonic nature, as they are quadratic in the fermionic operators, this observation suggests that fundamental, low-energy excitations of one-dimensional fermionic systems are given by bosonic excitations.

Summarizing, we highlighted two properties that are peculiar of one-dimensional fermionic systems. First, the perturbation theory in the interactions breaks down and indicates that the ground state of the interacting system differs strongly from the non-interacting one. Second, we identified bosonic particle-hole excitations as well-defined quasi-particles. While the first observation highlights that a description different from a Fermi liquid must be developed, the second fact can be actually leveraged to achieve this goal, which is the essence of the bosonization technique discussed in the following.

2.3.2. Bosonization

In the previous section, we highlighted the obstacles encountered when trying to incorporate interactions in a fermionic language based on a perturbation of the non-interacting ground state. Instead, the problem can be elegantly solved by making use of the fundamental bosonic excitations. This approach is accordingly referred to as bosonization and allows one to obtain non-perturbative results in interacting quantum wires. The road map towards bosonization proceeds as follows [79–81, 84, 102, 105–107]. Having identified the peculiarities of one-dimensional systems, we formalize the description of particle-hole excitations as the fundamental quasi-particles. We can then utilize this description to rewrite the interacting Hamiltonian in a basis of bosonic degrees of freedom. To this end, we focus on the low-energy properties, which allows us to linearize the fermionic dispersion near the Fermi energy, yielding an effective description in terms of the Tomonaga-Luttinger model [108, 109]. An exact representation of the Tomonaga-Luttinger model in terms of bosonic fields is then constructed, in which the interacting Hamiltonian becomes quadratic, significantly simplifying the analysis. The inclusions of deviations from the Tomonaga-Luttinger model leads only to minor modifications of the resulting theory, as discussed in the subsequent section. The main steps of the presented

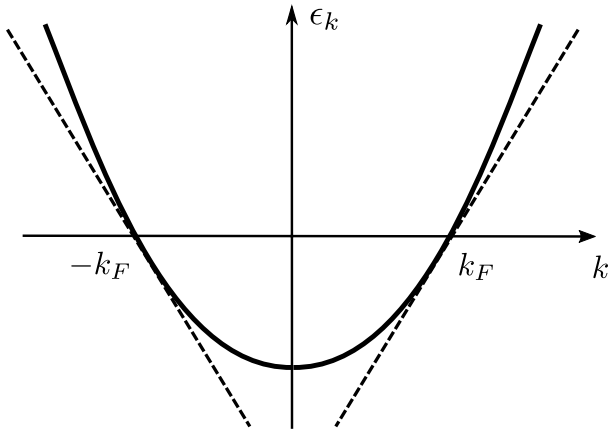

Fig. 2.6. Linearization (dashed) of the dispersion relation ϵ_k (solid) at the Fermi points $k = \pm k_F$.

derivation follow Ref. [84]. The notation used in the bosonization scheme varies rather strongly among different authors. In this thesis, we mainly follow the notation used in the study of impurity problems in Refs. [79–81].

Linearization of the kinetic term: bosonic representation

As a starting point, we consider a generic Hamiltonian describing the dynamics of a one-dimensional system of spinless fermions

$$H = \int_k \psi^\dagger(k)\epsilon_k\psi(k) + \int_{x,y} V(x-y)n(x)n(y), \tag{2.60}$$

with ϵ_k the dispersion relation, $V(x-y)$ a short-ranged interaction potential, and $n(x) = \psi^\dagger(x)\psi(x)$ the fermionic density operator. First, we focus on its kinetic part, which we can linearize at the Fermi points, as illustrated in Fig. 2.6. This procedure yields an effective description by the Tomonaga-Luttinger model given by the Hamiltonian [84, 108, 109]

$$H = \sum_r \int_k v_F(\xi_r k - k_F)\psi^\dagger_{r,k}\psi_{r,k}, \tag{2.61}$$

where $r = R, L$ labels left- and right-moving fermions with fermionic operators $\psi^\dagger_r, \psi_r$, $\xi_{R,L} = \pm 1$, and $v_F \equiv \partial_k\epsilon_k|_{k=k_F}$ is the Fermi velocity. Since all states below the Fermi energy $\epsilon_F \equiv \epsilon_{k_F}$ are occupied, the infinitely many states with negative energy do not affect the low-energy properties of the theory, in the usual sense of a Dirac sea.[4] From the linearized dispersion relation, in turn, the dispersion relation of particle-hole excitations is obtained as

$$E_{r,k}(q) = v_F(\xi_r k + q) - v_F\xi_r k = v_F q. \tag{2.62}$$

In order to utilize the anticipated bosonic nature of the relevant low-energy excitations, we aim to rewrite the Hamiltonian in a basis of bosonic operators $b, b^\dagger$, which, in turn, can be constructed from density fluctuations as well-defined excitations. As a starting point, we

[4] However, particular care has to be taken to treat these states, e.g., in the computation of expectation values, which can be achieved by considering normal ordered operators with respect to the ground state of the non-interacting system [84].

consider the creation operator of left- and right-moving density fluctuations

$$\rho_r^\dagger(q) = \sum_k c_{r,k+q}^\dagger c_{r,k}, \tag{2.63}$$

which corresponds to a superposition of particle-hole excitations (the summation indicates that a finite system size L was reinstated). The commutation relations of the creation operators (2.63) are found as [84]

$$\left[\rho_r^\dagger(k), \rho_r^\dagger(k')\right] = -\delta_{r,r'}\delta_{k,-k'}\frac{\xi_r pL}{2\pi}. \tag{2.64}$$

These commutation relations are indeed analogous to canonical bosonic commutation relations with an additional momentum-dependent normalization factor. Moreover, one can define the corresponding annihilation operators by realizing that

$$\rho_L^\dagger(k>0)\,|0\rangle = 0, \qquad \rho_R^\dagger(k<0)\,|0\rangle = 0, \tag{2.65}$$

with $|0\rangle$ the ground state of the non-interacting Hamiltonian, where we rely on the fact that all states below the Fermi energy are occupied while those above are unoccupied. With this construction, we can define the following bosonic creation and annihilation operators with respect to the vacuum state $|0\rangle$:

$$b_k^\dagger = \sqrt{\frac{2\pi}{L|k|}} \sum_{r=L,R} \Theta(\xi_r\, k)\, \rho_r^\dagger(k), \tag{2.66a}$$

$$b_k = \sqrt{\frac{2\pi}{L|k|}} \sum_{r=L,R} \Theta(\xi_r\, k)\, \rho_r^\dagger(-k), \tag{2.66b}$$

with $\Theta(x)$ the Heaviside step function, and valid for $k \neq 0$. As a first major achievement, by means of these operators, the Hamiltonian (2.61) can be rewritten in the bosonic representation

$$H = \sum_{k\neq 0} v_F\,|k|\, b_k^\dagger b_k + \sum_r \frac{\pi v_F}{L} N_r^2, \tag{2.67}$$

where the last term originates from the $k = 0$ contribution, with N_r the total number of left- and right-moving fermions. Remarkably, the kinetic energy remains quadratic in the bosonic operators $b^\dagger, b$, although it is also quadratic in the fermionic operators.

A more convenient representation, which also allows the simple inclusion of interactions below, can be achieved by introducing the bosonic fields

$$\theta(x) = -\left(N_R + N_L\right)\frac{\pi x}{L} - \frac{i\pi}{L}\sum_k \sqrt{\frac{L|k|}{2\pi}}\frac{1}{k} \mathrm{e}^{-\alpha|k|/2 - ikx}\left(b_k^\dagger + b_{-k}\right), \tag{2.68a}$$

$$\phi(x) = \left(N_R - N_L\right)\frac{\pi x}{L} + \frac{i\pi}{L}\sum_k \sqrt{\frac{L|k|}{2\pi}}\frac{1}{|k|} \mathrm{e}^{-\alpha|k|/2 - ikx}\left(b_k^\dagger - b_{-k}\right), \tag{2.68b}$$

which is valid in the limit $\alpha \to 0$. One may keep a finite α, which acts as a cutoff mimicking a finite bandwidth [84]. The bosonic fields θ, ϕ fulfill the commutation relations

$$[\theta(x), \phi(y)] = i\frac{\pi}{2}\mathrm{sgn}(y-x), \qquad \left[\theta(x), \partial_y\phi(y)\right] = i\pi\delta(y-x), \tag{2.69}$$

valid in the limits $\alpha \to 0$ and $L \to \infty$. The latter identity defines canonical commutation relations between θ and the corresponding conjugate momentum $\Pi = \partial_x \phi / \pi$. The fields can be related to the left- and right-moving densities

$$\partial_x \theta(x) = -\pi \left(\rho_R(x) + \rho_L(x)\right), \qquad \partial_x \phi(x) = \pi \left(\rho_R(x) - \rho_L(x)\right), \tag{2.70}$$

respectively, which is valid in the thermodynamic limit $L \to \infty$. Finally, the kinetic part of the Hamiltonian, given in Eq. (2.67), can be rewritten in terms of the bosonic fields in the simple form [84]

$$H = \frac{1}{2\pi} \int_x v_F \left[(\partial_x \phi)^2 + (\partial_x \theta)^2\right]. \tag{2.71}$$

The fields ϕ and θ can be interpreted in terms of phase and density fluctuations, in the following way. As can be inferred from Eq. (2.70), $\partial_x \theta / \pi$ describes the density fluctuations related to the left- and right moving excitations. Instead, $\partial_x \phi$ is related to the current in the system, established by the difference of left- and right moving excitations and, in turn, related to phase fluctuations. Moreover, the field $\theta(x)$ can be understood as counting the number of excitations up to point x since its derivative describes their density. Note that such a mapping from real space to a particle number is uniquely defined only in one dimension where the single spacial axis imposes a natural way to label positions [84]. Hence, the appearance of a labeling field highlights the deep connection between the developed bosonization scheme and the dimension of the system.

Bosonization of the interaction term

We now consider interactions between the fermions described by the interacting part of the Hamiltonian (2.60):

$$H_{\text{int}} = \int_{x,y} V(x-y) n(x) n(y). \tag{2.72}$$

The application of the bosonization scheme developed above yields a quadratic representation of H_{int} in terms of the fields ϕ, θ. To this end, one can decompose the fermionic operators in the Hamiltonian (2.72) in their left- and right-moving parts [84]

$$\psi(x) \simeq \psi_R(x) + \psi_L(x). \tag{2.73}$$

The classification of all low-energy interaction processes between the left- and right-moving fermions is referred to as g-ology, and yields the processes shown in Fig. (2.7) [84]. Here, three low-energy interaction processes at the Fermi surface can be identified, quantified by coefficients g_1, g_2, g_4, which are related to the $q \sim 0$ and $q \sim 2k_F$ components of the Fourier transform of the microscopic interaction potential $V(x)$, respectively [84]. In the case of spinless fermions, the g_1 and g_2 processes are equivalent as a result of the indistinguishability of particles, and hence, we can focus in the description on the g_2 and g_4 processes. These processes can be represented in the bosonic fields with the use of the identities (2.70). In doing so, the g_4 processes yield two terms originating from the left and right Fermi surface, respectively:

$$g_4 \psi^\dagger_{R,L} \psi_{R,L} \psi^\dagger_{R,L} \psi_{R,L} = \frac{g_4}{2} \rho_{R,L} \rho_{R,L} = \frac{g_4}{2} \frac{1}{(2\pi)^2} \left(\partial_x \theta \mp \partial_x \phi\right)^2, \tag{2.74}$$

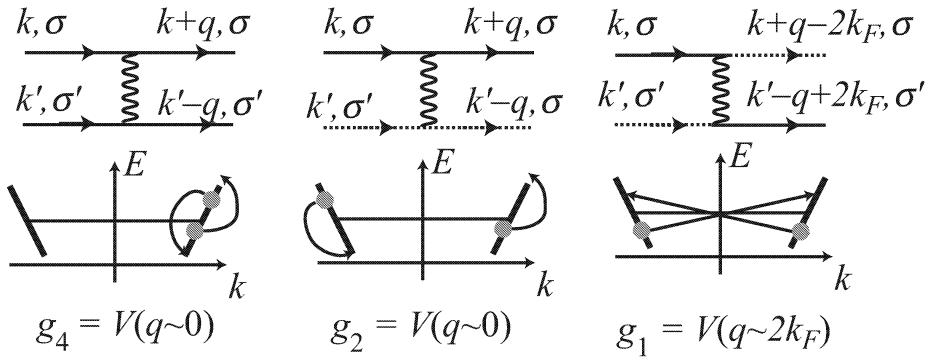

Fig. 2.7. Classification of low-energy interaction processes in a fermionic quantum wire. Three types of processes can be identified, quantified by coupling constants g_1, g_2, g_4, respectively. Here, $V(q)$ denotes the Fourier transform of the microscopic interaction potential $V(x)$. (Figure taken from Ref. [84] with minor adaptions.)

which yields a total contribution to the Hamiltonian of the form

$$\frac{g_4}{(2\pi)^2}\int_x \left[(\partial\theta)^2 + (\partial\phi)^2\right]. \tag{2.75}$$

Analogously, the g_2 processes contribute to the Hamiltonian with a term

$$g_2\psi_R^\dagger\psi_R\psi_L^\dagger\psi_L = g_2\rho_R\rho_L = g_2\frac{1}{(2\pi)^2}\left[(\partial\theta)^2 - (\partial\phi)^2\right]. \tag{2.76}$$

Crucially, all contributions are found to be *quadratic* in the bosonic fields θ, ϕ, therefore greatly simplifying the description, which was initially formulated by a term quartic in the fermionic operators. Finally, by combining the bosonic representations of the kinetic and interacting parts of the Hamiltonian, we arrive at the Luttinger Hamiltonian [84]

$$H = \int_x \frac{v}{2\pi}\left[g(\partial_x\phi)^2 + g^{-1}(\partial_x\theta)^2\right], \tag{2.77}$$

which represents the central result presented in this section. This Hamiltonian describes the low-energy physics of the microscopic Hamiltonian (2.60) and defines the Luttinger liquid theory. The Hamiltonian (2.77) is fully characterized by only two parameters g and v. Here, v has the dimension of a velocity while the so-called Luttinger parameter g is dimensionless. The two parameters are related to the microscopic parameters by the mapping

$$g = \sqrt{\frac{1 + g_4/2\pi v_F - g_2/2\pi v_F}{1 + g_4/2\pi v_F + g_2/2\pi v_F}}, \tag{2.78a}$$

$$v = v_F\sqrt{(1 + g_4/2\pi v_F)^2 - (g_2/2\pi v_F)^2}. \tag{2.78b}$$

Since the signs of g_2 and g_4 are directly determined by the sign of the interaction potential $V(x)$, for repulsive interactions ($V(x) > 0$), we always obtain $g < 1$, while for attractive interactions ($V(x) < 0$), we obtain $g > 1$, independent of the microscopic realization of the interaction potential. The non-interacting case ($g_2 = 0 = g_4$) is described by the Luttinger parameter $g = 1$. Remarkably, the Luttinger Hamiltonian (2.77) is quadratic, corresponding to a free theory of the

bosonic excitations. Hence, by identifying the fundamental degrees of freedom (and finding a suitable representation), exact results in the low-energy limit can be obtained for the interacting problem via the bosonization mapping.

Representation of the fermionic operator

The single-particle fermionic operators $\psi, \psi^\dagger$ can likewise be represented in the bosonic fields, which enables the analysis of observables formulated in the fermionic degrees of freedoms. The mapping can be found by noticing the commutation relations of the left- and right-moving fermions ψ_r with the density fluctuation (2.63), yielding

$$\left[\rho_r^\dagger(k), \psi_r(x)\right] = -\mathrm{e}^{ikx}\psi_r(x), \tag{2.79}$$

from which one can infer the representation [84]

$$\psi_r = U_r \exp\left[\sum_k \frac{2\pi\xi_r}{Lp}\mathrm{e}^{ikx}\rho_r^\dagger(-k)\right]. \tag{2.80}$$

Here, additionally the so-called Klein factors U_r appear. These fermionic operators are formally required to change the number of fermions of the state (which is preserved by $\rho_r^\dagger$). While in principle it makes the above operator identity rigorous, it often can be safely neglected, e.g., in the calculation of correlation functions, as it contains no space-time dependence [84]. For these reasons, we will not consider Klein factors in the following.

A more convenient representation for the fermionic operators is obtained in terms of the Luttinger fields ϕ, θ as

$$\psi_{R/L}(x) \simeq \mathrm{e}^{\pm ik_F x}\mathrm{e}^{i(\phi(x)\pm\theta(x))}. \tag{2.81}$$

With this mapping, we obtain the bosonic representation of the fermionic operator according to

$$\psi(x) \simeq \psi_R(x) + \psi_L(x) \simeq e^{ik_F x}e^{i\Phi_R(x)} + e^{-ik_F x}e^{i\Phi_L(x)}, \tag{2.82}$$

where we defined $\Phi_{R/L} = \phi \pm \theta$. Here, Φ_R and Φ_L commute with each other, and further fulfill the so-called Kac-Moody commutation relations

$$\left[\Phi_R(x), \Phi_R(x')\right] = -\left[\Phi_L(x), \Phi_L(x')\right] = i\pi\,\mathrm{sgn}(x - x'). \tag{2.83}$$

One can interpret the representation of the fermionic operators (2.81) in the following way. Since θ and $\partial_x\phi$ are conjugate variables, $e^{i\phi(x)}$ creates a kink in $\theta(x)$ at position x, corresponding to a particle at x [84], as θ describes a counting field. The remaining factor can be understood as a Jordan-Wigner string, required for the fermionic commutation relations [80].

2.3.3. Generalizations

Remarkably, the Luttinger Hamiltonian (2.77) is found to also capture accurately the low-energy properties of models with a non-linear dispersion, highlighting the deep rooting of the discussion on dimensional arguments [82, 84]. Hence, the Luttinger liquid provides a universal low-energy theory for one-dimensional interacting quantum systems irrespective of the precise

nature of the microscopic Hamiltonian. This fact expresses the irrelevance of band curvature terms in a renormalization group sense [110]. When a non-linear dispersion is considered, the effective Luttinger parameters g and v generally can not be derived in a simple way from the microscopic parameters, as it was the case for the Tomonaga-Luttinger model in Eq. (2.78). Instead, they can be obtained numerically or via a mapping to integrable models [110, 111], e.g., for spinless fermions on a lattice to an anisotropic Heisenberg (XXZ) model, where exact solutions are available via the Bethe ansatz [83, 84, 110]. Further, in some cases, the mapping to the Luttinger Hamiltonian breaks down, e.g., for strongly interacting spinless fermions on a lattice at half-filling, where additional interaction processes (so-called Umklapp processes) become important and a gapped phase is entered [84, 111].

Moreover, while the mapping of the fermionic operator (2.82) is exact for the linear dispersion relation of the Tomonaga-Luttinger model, deviations from the linear dispersion result in corrections to the representation of the fermionic operators [84, 112], leading to the appearance of higher harmonics

$$\psi(x) \simeq [k_F/\pi - \partial_x\theta(x)/\pi]^{1/2} \sum_{m\,\mathrm{odd}} e^{im(k_F x+\theta(x))} e^{i\phi(x)}, \tag{2.84}$$

where the summation over odd integers ensures the fermionic statistics. However, the fundamental existence of such a mapping is independent of the dispersion relation and deeply bound to the dimensionality, where it can be mathematically cast as a coherent state expansion of the electron operator [107]. In case of impurity problems, the additional terms appearing in Eq. (2.84) are usually less relevant under RG [79–81], and Eq. (2.82) yields the leading behavior.

With the help of the Luttinger model, several exact properties in the low-energy limit for interacting one-dimensional quantum systems can be computed. Typically, non-universal power laws, depending only on the Luttinger parameter g, are encountered in the correlation functions [84]. The parameter g is also encountered in the linear conductance, which is given by $G = ge^2/h$ [84, 113, 114].[5]

Interacting bosons

Interacting bosons in one-dimension can also be mapped to the Luttinger model (2.77) [84, 115], which further highlights the generality of the latter. This fact implies, that in one dimension interaction effects can be described independently of the statistics, as fundamental excitations are always of bosonic nature. We emphasize, that this does not mean that correlations functions are necessarily identical to those obtained for fermions [84].

In the case of bosons, repulsive interactions are required in order to obtain a stable theory. In the mapping process, the Luttinger parameter g is related to the microscopic interactions differently compared to the case of fermions. For purely local interactions, characterizing the Lieb–Liniger model [116], the Luttinger parameter is always obtained as $g > 1$, whereas $g = 1$ corresponds to infinitely strong interactions and $g \to \infty$ to the weak-interaction limit. In the Tonks–Girardeau limit [84, 115, 117] of infinitely strong interactions, one obtains $g = 1$ and the system behaves analogously to free spinless fermions, i.e., as hard-core bosons. Moreover, for

[5] However, the conductance may be dominated by the attachment of non-Luttinger leads, by which the conductance of a non-interacting wire is restored [113, 114].

long-ranged interactions, a Luttinger parameter $g < 1$ can be achieved. As for fermions on a lattice, peculiarities occur for commensurate bosons on a lattice, which can give rise to Mott transitions [84].

Spinful fermions: decoupling of charge and spin excitations

In this thesis, we focus on spinless fermions, as in this way a minimal description is obtained which nevertheless provides the most important underlying physical mechanisms to study the interplay of a localized loss and interaction effects. In order to complement the present discussion of Luttinger liquid physics, we briefly comment on the bosonization mapping obtained in the case of spin-1/2 fermions. As stressed before, the excitations in one-dimensional interacting systems are necessarily of collective, bosonic nature. Consequently, single-particle excitations carrying a spin and a charge are required to transform into collective excitations, by which a decoupling of the charge and spin properties of the excitations is encountered [84]. This decoupling of charge and spin excitations constitutes another hallmark of the physics of Luttinger liquids. The resulting charge and spin excitations generally do not propagate at the same speed, but independently of each other.

The Luttinger model for spinful fermions is obtained by applying the bosonization mapping to each species of fermions and then decoupling charge and spin degrees of freedoms by the transformation

$$\theta_\rho = \theta_\uparrow + \theta_\downarrow, \qquad \theta_\sigma = \theta_\uparrow - \theta_\downarrow, \tag{2.85a}$$

$$\phi_\rho = \frac{\phi_\uparrow + \phi_\downarrow}{2}, \qquad \phi_\sigma = \frac{\phi_\uparrow - \phi_\downarrow}{2}. \tag{2.85b}$$

Thus, the number of Luttinger fields is doubled compared to the spinless case. The in this way obtained Hamiltonian in the bosonic representation reads

$$H = H_{0,\rho} + H_{0,\sigma} + H_\sigma, \tag{2.86}$$

where $H_{0,\rho/\sigma}$ denotes the quadratic Luttinger Hamiltonian (2.77), respectively, with independent Luttinger parameters $g_{\rho/\sigma}, v_{\rho/\sigma}$. Additionally, in the mapping of the microscopic interaction processes, now contributions given by g_1-processes become important (cf. Fig. 2.7). This results in an additional sine-Gordon-type term $H_\sigma \sim g_{1\perp} \int_x \cos 2\sqrt{2}\theta_\sigma$ in the Hamiltonian [84]. As a consequence, correlation function cannot be calculated exactly but can be computed perturbatively in the coefficient $g_{1\perp}$ via renormalization group arguments [84].

2.3.4. Coherent impurities in Luttinger liquids

In this section, we give a concise overview of the physics of coherent impurities in Luttinger liquids, where many concepts are again encountered in more detail in the remainder of this thesis during the study of incoherent impurities. Coherent impurities, established by localized real potentials, induce strong effects in interacting quantum wires due to their interplay with the gapless modes described by the Luttinger Hamiltonian (2.77). This is a consequence of the strong response inhomogeneities provoke in these systems, as discussed below Eq. (2.59). The strong effects encountered for coherent impurities in Luttinger liquids motivate the investigation

of dissipative impurities. In Chapter 6, we study localized losses within a Luttinger liquid approach. In particular, we revise some results for coherent potential impurities in Sec. 6.3.2 in a more technical approach.

The hallmark result of impurity physics in Luttinger liquids is the suppression of linear conductance even by a weak impurity for repulsive interactions at $T = 0$, which has been studied in the paradigmatic works of Kane and Fisher [79, 80]. Here, an impurity Hamiltonian for spinless fermions is considered,

$$H_{\text{imp}} = \int_x u\delta(x)\psi^\dagger(x)\psi(x), \tag{2.87}$$

quantified by a real coefficient u. Within the framework of bosonization, via the bosonic mapping in Eq. (2.82), the following representation is obtained:

$$H_{\text{imp}} = 2u \int_x \delta(x)\cos(2\theta). \tag{2.88}$$

By an RG analysis perturbative in u, an RG flow equation for the effective barrier strength at low energies can be derived as

$$\frac{\mathrm{d}u}{\mathrm{d}\ell} = (1-g)u, \tag{2.89}$$

where the dimensionless parameter ℓ parametrizes the RG flow. This RG equation entails, that u constitutes a relevant perturbation for repulsive interactions ($g < 1$), while being irrelevant for attractive interactions ($g > 1$). As a result, the linear conductance in the presence of a weak impurity is found to be strongly modified. This fact leads to a power law behavior at finite temperature T or voltage V of the conductance G and $I - V$ characteristics, according to

$$G(T) = \frac{e^2}{h}(g - \text{const.} \times T^{2g-2}), \qquad I(V) = V\frac{e^2}{h}(g - \text{const.} \times V^{2g-2}). \tag{2.90}$$

Remarkably, for attractive interactions ($g > 1$), in the limits of small temperature or voltage, the corrections due to the impurity vanish and the transport properties are not affected by the impurity at all. In contrast, for repulsive interactions ($g < 1$), the corrections actually diverge in these limits, and perturbation theory breaks down. However, a perturbative analysis is also feasible for a large impurity potential resulting in a weak link between the effectively disconnected parts of the wire. By assuming, that the fixed points of a fully connected and fully disconnected wire are the only ones of the theory, the RG flow can be interpolated in between. Therefore, even a microscopically weak impurity potential creates effectively a weak link for repulsive interactions. The analysis for a weak link then yields the power law behavior

$$G(T) = \frac{e^2}{h}(\text{const.} \times T^{2g^{-1}-2}), \qquad I(V) = V\frac{e^2}{h}(\text{const.} \times V^{2g^{-1}-2}). \tag{2.91}$$

Hence, a power law suppression of transport is encountered for repulsive interactions. Impurity problems for spinless fermions have been further studied with different methods and within different contexts, as outlined in the following.

A microscopic approach was performed in Refs. [85, 86], which is adapted in Chapter 4 to the study of a dissipative impurity. The approach is based on the presence of density modulations induced by the impurity potential, so-called Friedel oscillations [87, 88], which establish an effective scattering barrier in the presence of interactions.

The amplitude of Friedel oscillations exhibits a spatial decay $|x|^{-d}$ in the non-interacting system (for the impurity situated at $x = 0$), with d the dimension of the system [89, 90]. Therefore, Friedel oscillations are peculiar in dimension $d = 1$ due to their slow spatial decay, given by $|x|^{-1}$. In interacting systems of spinless fermions in $d = 1$ the asymptotic decay is modified according to $|x|^{-g}$ [89, 90]. Moreover, the Friedel oscillations exhibit a period π/k_F and are thus deeply linked to the presence of a Fermi surface and, in turn, to the strong response for perturbations with a $2k_F$ wave vector [84] (cf. Sec. 2.3.1). We encounter Friedel oscillations also in the vicinity of a localized loss, as presented in Chapter 3.

Another microscopic approach was conducted by the functional renormalization group (FRG) method [118–121]. Here, the scaling connecting the weak and strong impurity limits was further investigated. We comment on generalizations of this method to dissipative impurities in Sec. 4.6.

Moreover, non-equilibrium effects for coherent impurities in Luttinger liquids were studied [9, 11, 122, 123], where, e.g., a quench of interactions was considered in order to drive the system out of equilibrium. Here, self-thermalization effects are encountered due to the non-linear coupling of modes induced by the impurity. These studies are of particular importance, as discussed in Sec. 6.4, for the investigation of dissipative impurities, since the latter intrinsically drive the system out of equilibrium.

Related to impurity problems, wire junctions of Luttinger liquids have been studied in Refs. [57, 124–128], revealing similar effects as induced by impurity potentials. Furthermore, the impurity problem (2.87) can be mapped to the so-called Schmidt transition [129] which is useful to study the universality class of the transition between the cases $g < 1$ and $g > 1$.

As pointed out in Sec. 2.3.3, bosonic systems can likewise be mapped to the Luttinger model for spinless fermions, and impurities can lead to strong effects in these systems [115, 117, 130, 131]. For strong interactions, also in bosonic systems Friedel-type density oscillations occur near an impurity [117, 131], where $2\pi\rho_0$ takes over the role of $2k_F$, with ρ_0 the mean density. For example, a quantum phase transition at $g = 1$ between a superfluid ($g > 1$) and non-superfluid phase ($g < 1$) was shown in Ref. [130], revealing analogies to the Kane-Fisher transport properties across a single impurity.

2.4. Localized dissipation in low dimensions

Recently, quantum systems with localized dissipation have been investigated in numerous studies. Here, we focus on the experimental realizations [24, 40–44] of localized losses in ultracold quantum wires. We conclude the discussion by a brief overview of the many theoretical works on localized dissipation in low-dimensional systems accompanying these experiments.

2.4.1. Experimental realizations of localized dissipation

Experiment by Barontini et al.

In Ref. [40] a localized dissipation was experimentally realized in an atomic Bose-Einstein condensate (BEC) in an optical trap by shining a focused electron beam [132] onto the system, acting as a fully controllable, environmentally induced dissipative potential. Collisions between

the high-energy electrons ($\sim$ 6 keV) and the atoms of the condensate cause the excitation or ionization of atoms, which leads, in turn, to their escape from the trap, hence establishing losses. The strength of the dissipation can be controlled by the intensity of the electron beam. The latter is technically realized via an electron microscope and exhibits a Gaussian profile, thus resulting in a purely dissipative potential

$$\gamma(x) = \frac{I\sigma}{2\pi e w^2} \mathrm{e}^{-\frac{x^2+y^2}{2w^2}}, \tag{2.92}$$

with I the current of the electron beam, σ the electron-BEC scattering cross section, w the width of the spatial electron distribution, and e the elementary charge. The particle loss was shown here and in other experiments [40–44] to be conveniently modeled by a Lindblad master equation (2.18).

The particle loss rate can be measured by detecting the ions emitted from the trap and is shown in Fig. 1.2 (three leftmost panels) as a function of the intensity of the electron beam, for three different widths of the beam. The measured loss rate (squares) then reveals a perhaps surprising non-monotonic behavior: If the dissipation strength exceeds a critical limit, the number of atoms lost from the BEC decreases. This decrease of the loss rate for large dissipation strengths can be interpreted in terms of the quantum Zeno effect (cf. Sec. 2.2). The localized loss constitutes a continuous measurement of the local density, which for strong dissipation inhibits the transitions of atoms from the surrounding BEC into the loss region, resulting in an effective decrease of the loss rate. The occurrence of the quantum Zeno effect reflects the quantum nature of the BEC. If instead, an analogous experiment is performed in which a focused electron beam is directed at a classical thermal gas, a simple monotonic dependence of the loss rate on the dissipation strength is measured, as shown in Fig. 1.2 (right panel). The solid orange lines in Fig. 1.2 (three leftmost panels) indicate the comparison to a numerical description based on a Lindblad master equation and show good agreement with the experimental data.

Experiments by Labouvie et al. and Müllers et al.

In a one-dimensional system, a localized loss was experimentally realized in Ref. [41] for a weakly interacting BEC in an optical lattice. A similar setup was realized in Ref. [42]. Here, the dissipation is implemented analogously to Ref. [40] by shining a focused electron beam onto a single lattice site. After the switching on of the localized loss, a non-equilibrium quasi-steady state is observed, characterized by steady currents flowing towards the loss site, where bosons are lost from the wire. In Fig. 2.8 the measured current (red squares) is shown as a function of the dissipation strength, for a system prepared initially in a homogeneous state. Again, a non-monotonic behavior for increasing dissipation strength is visible, as a consequence of the quantum Zeno effect. The blue squares in Fig. 2.8 depict the current measured for different initial conditions, with an initially empty loss site, where a similar non-monotonic behavior is observed. Additionally, a bistability region is revealed by comparing both curves, as a result of the interplay between superfluid response and depletion in the considered system.

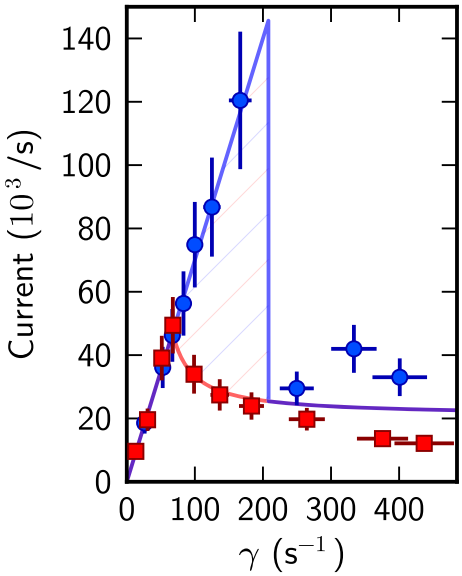

Fig. 2.8. Current directed towards the loss site corresponding to the particle loss rate, as a function of the dissipation strength γ. The red squares correspond to a system initially prepared with a homogeneous density (solid lines are a guide to the eye). The blue dots correspond to different initial conditions, revealing a bistability for the system realized in Ref. [41]. (Figure taken from Ref. [41] with minor adaptations.)

Experiments by Lebrat et at. and Corman et al.

While so far bosonic systems were considered, a localized dissipation was experimentally realized in Refs. [43] and [44] for an ultracold atomic gas of weakly-interacting fermions. An initially three-dimensional cloud of atoms is shaped by optical potentials into two reservoirs connected by a quasi-one-dimensional region. The transport properties of the effective quantum wire are then controlled by the application of a near-resonant optical tweezer, imposing an effective spin-dependent potential in the wire. Beyond providing an effective potential barrier, the optical tweezer induces losses of atoms due to photon scattering, thus establishing a localized loss. Within the wire, the shape of the optical light beam exhibits a Gaussian profile which is shaped by digital micromirror devices, with a width smaller than the length of the wire and the typical Fermi wavelength.

The analysis then focuses on realizing a microscopic spin filter by tuning the optical tweezers in a way that both species of fermions experience a different effective complex-valued potential. Two hyperfine states establish the ground states of both species of fermions, where the transition to the next excited state, respectively, occurs at different frequencies. By tuning the light frequency close to these transitions, strongly state-dependent polarizabilities are obtained, which in turn lead to an effective spin-dependent localized potential with an imaginary part controlled by a scattering rate

$$\Gamma_{\uparrow,\downarrow} \sim I \,\mathrm{Im}\, \vec{\epsilon} \cdot \alpha_{\uparrow,\downarrow} \cdot \vec{\epsilon}. \tag{2.93}$$

Here, I is the intensity of the light, $\vec{\epsilon}$ the light polarization, and α the complex polarizability tensor, related to the dipole matrix elements of the transitions induced by the near-resonant light. The effective dissipative potential can be varied via the detuning of the optical tweezer.

The setting with two reservoirs then allows the study of transport properties, revealing a spin-dependent quantized conductance even in the presence of dissipation.

The loss mechanism realized by the optical tweezer is as follows. An atom scattering a near-resonant photon acquires a large kinetic energy via the absorption and spontaneous reemission of the photon. The recoil energy is sufficiently large for the atom to escape from the trapping potential. Before leaving the trap, the atom can principally scatter with other atoms and deposit energy within the system. However, the estimated scattering rates even for moderate interactions indicate that only a small fraction $\sim 0.4\%$ of the atoms scatters within the wire, and hence such scattering events can be neglected, leading to an accurate description by irreversible losses of particles.

Experiment by Lapp et al.

Finally, we remark that in Ref. [24] a controlled, localized single-particle loss was experimentally implemented in a synthetic lattice of momentum-states. Here, localized losses are realized via a localized coupling to a reservoir with a large number of unoccupied degrees of freedom, effectively leading to irreversible losses. A good agreement of the dynamics with a non-Hermitian description was shown. In synthetic lattices, lattice sites are mimicked by non-spatial degrees of freedom of a quantum system, which are coupled to each other such that a description of tunneling along an effective dimension emerges.

2.4.2. Overview of theoretical works on localized dissipation

We give a brief overview of the numerous theoretical works dealing with localized dissipation in low-dimensional many-body systems. A variety of many-body platforms was considered, with a large focus on bosonic systems via Bose-Hubbard dynamics [48, 51, 54, 55] and BECs [45, 49, 50, 52, 56, 58]. Moreover, fermionic systems were recently discussed [25, 59], as well as synthetic lattices [24] and chaotic systems [59, 60].

In these systems, different types of localized dissipation were studied, with a focus on single-body losses [25, 48–52, 55, 58, 60]. Moreover, the coupling to a large empty reservoir [24] effectively leads to irreversible losses of particles. In contrast, phase noise impurities preserve the particle number, corresponding to Lindblad operators $\mathrm{L} \sim n$ with n the density operator [49, 61, 64]. In Ref. [54], localized dissipation was induced by a "hot needle", realized by the local coupling to a thermal reservoir at a large temperature. Further, a localized pump was recently analyzed in fermionic [62] and bosonic [63] one-dimensional systems. The studies revealed a variety of remarkable effects ranging from non-equilibrium quasi-steady states [25, 48, 50, 55, 56, 58, 60] over the engineering of entanglement [48, 52] and dissipation-free subspaces [51] to the characteristic reduction of dissipative effects for strong dissipation strengths as a consequence of the quantum Zeno effect [25, 48–50, 54].

Furthermore, localized dissipation was discussed in higher dimensional many-body systems [22, 53, 57, 65] and in the context of few level dynamics [46, 47, 52]. As a related setup, one can consider the study of junctions of quantum wires [57, 124–128]. Here the description is typically Hermitian, however, in a three-wire junction, for example, one of the wires can be regarded as a

loss channel to the main wire formed by the two remaining wires, resulting in similarities to the effects of a localized loss (cf. Sec. 3.3.3).

2.5. Schrödinger equation with a dissipative delta potential

As a toy model of localized dissipation, we conclude this introductory chapter with a brief study of the following non-Hermitian Schrödinger equation in the presence of a localized dissipative barrier for a particle in an infinite continuous system:

$$i\partial_t \psi = -\partial_x^2 \psi - i\gamma\delta(x)\psi. \tag{2.94}$$

In Chapter 3, the relationship of this non-Hermitian model to the quantum master equation (2.18) becomes clear. With the use of the ansatz $\psi(x,t) = f(x)g(t)$ we perform a separation of variables leading to

$$-\partial_x^2 f - i\gamma\delta(x)f(x) = \kappa^2 f(x), \tag{2.95}$$

with a constant κ and $g(t) = \mathrm{e}^{-i\kappa^2 t}$. Integrating this equation reveals that $f(x)$ is continuous everywhere, whereas its derivative $f'(x)$ is discontinuous at $x = 0$, with a discontinuity described by

$$f'(0_+) - f'(0_-) = -i\gamma f(0). \tag{2.96}$$

Since the solutions away from $x = 0$ are given by plane waves, we infer the following piecewise solution for $f(x)$:

$$f(x) = \begin{cases} A_+ \mathrm{e}^{i\kappa x} + B_+ \mathrm{e}^{-i\kappa x}, & \text{for } x > 0, \\ A_- \mathrm{e}^{i\kappa x} + B_- \mathrm{e}^{-i\kappa x}, & \text{for } x < 0. \end{cases} \tag{2.97}$$

As a boundary condition, we choose a plane wave incoming from the left and accordingly set $B_+ = 0$. By requiring the continuity of the wave function at $x = 0$ and by using Eq. (2.96), we find the conditions for the amplitudes as

$$A_+ = \frac{2\kappa}{2\kappa + \gamma} A_-, \quad B_- = -\frac{\gamma}{2\kappa + \gamma} A_-. \tag{2.98}$$

The dissipative nature of the system is then revealed by noticing that the probability is not conserved, but given by

$$P(\kappa,\gamma) = \left|\frac{A_+}{A_-}\right|^2 + \left|\frac{B_-}{A_-}\right|^2 = \frac{4\kappa^2 + \gamma^2}{(2\kappa+\gamma)^2} \leqslant 1. \tag{2.99}$$

Moreover, $P(\kappa,\gamma)$ exhibits a non-monotonic behavior as a function of γ, as depicted in Fig. 2.9. This fact can be interpreted as a consequence of the quantum Zeno effect, leading to an effective decrease of dissipation for large γ (cf. Sec 2.2). We discuss the scattering problem associated with a loss barrier in more detail in Chapter 3, where we take a more rigorous approach in terms of the retarded Green's function instead of a wave function, yielding crucial insights for the description of the many-body problem.

Since the analog of the Schrödinger equation (2.94) for a real-valued delta potential features a bound state, we finally check for localized solutions of Eq. (2.94). Localized solutions are

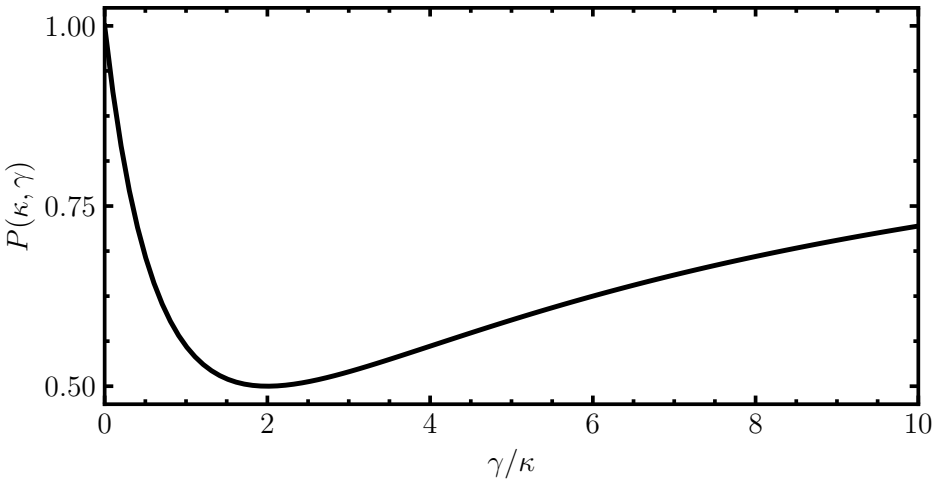

Fig. 2.9. Probability $P(\kappa, \gamma)$ as a function of the dissipation strength γ.

characterized by complex κ, corresponding to a spatially decaying wave function in Eq. (2.97), where normalization requires $A_+ = 0$ and $B_- = 0$. By plugging this ansatz into Eq. (2.96) we obtain the condition $\kappa = \gamma/2$. This identity does not admit an imaginary solution for real γ and hence we conclude that localized solutions are absent. In contrast, in Chapter 7, we disclose the presence of localized solutions for the analog of Eq. (2.94) on a lattice, emerging for a threshold value of the dissipation strength γ, which leads to remarkably rich spectral properties of the associated eigenvalue problem.

CHAPTER 3

NON-INTERACTING FERMIONS WITH LOCALIZED LOSSES

A localized particle loss was implemented in recent experiments with ultracold atoms either by shining a focused electron beam onto the system [40–42] or by using a near-resonant optical tweezer [43, 44], thus locally exciting atoms resulting in their escape from the trapping potential. Once escaped, atoms are unlikely to return to the trap and the particle loss has been shown to be conveniently described by Markovian single-particle loss [40–44]. As a starting point, we formulate a model of spinless fermions in one dimension subject to a localized loss. To this end, we model the loss as a localized coupling to an empty Markovian bath in terms of a quantum master equation in Lindblad form, describing the irreversible loss of atoms from the wire. The presence of a localized loss generates particle currents, thus driving the system out of equilibrium. We then study the effects of a localized loss in the non-interacting model. The detailed discussion of the non-interacting problem is motivated as follows. On the one hand, this approximation results in a solvable model that allows us to identify the key physical mechanisms and observable quantities of the present problem. On the other hand, it is actually relevant for experiments with ultracold atoms, where the effective particle interaction can be tuned via Feshbach resonances and made negligible [43, 44]. The effects of interaction are studied in subsequent chapters. The present chapter can be considered as preliminary to any further study which requires a profound understanding of the dynamics in the presence of a localized loss.

We focus on systems initialized in a thermal ground state before switching on the localized loss at time $t = 0$ and letting the system evolve in its presence. The analysis of the remarkably complex dynamics in the presence of a localized loss is performed based on a numerical and analytical description. A first numerical study yields a description of the dynamics in terms of three temporal regimes, among which the second one establishes a non-equilibrium steady state (NESS). Due to its extensive duration and correlation properties, it is identified as the relevant temporal regime for further studies. Based on the insights of this numerical study, an analytical solution of the correlation properties of the NESS is developed, which enables us to exactly compute a variety of observables in the NESS. Having established both a numerical and analytical description of the dynamics, we can apply these methods to investigate several important aspects of the dynamics in the presence of a localized loss.

The key findings reported in this chapter are as follows. i) The particle loss rate displays a non-monotonic behavior as a signature of the quantum Zeno effect. ii) Depletion processes can be described transparently in terms of a loss probability η_k. iii) The density profile supports Friedel oscillations near the loss site. iv) The momentum distribution can be studied as a dynamical object providing a momentum-resolved description of depletion processes.

The main results of this chapter have been published in publications [133] and [134]. We present here a more detailed discussion which is complemented by a variety of additional results. [1]

3.1. Microscopic model of a localized loss

We consider spinless fermions with mass m moving in a wire of length L described by the non-interacting Hamiltonian

$$H = -\int_x \psi^\dagger(x)\frac{\partial_x^2}{2m}\psi(x). \tag{3.1}$$

Here, $\psi^\dagger, \psi$ are fermionic creation and annihilation operators, and $\int_x = \int_{-L/2}^{L/2} \mathrm{d}x$. We set $\hbar = 1$ here and in the rest of this thesis.

The dynamics of the system can then be described by a quantum master equation [5] (cf. Sec. 2.1.1)

$$\partial_t \rho = -i[H,\rho] + \int_x \Gamma(x)\left[2\mathrm{L}\rho\mathrm{L}^\dagger - \{\mathrm{L}^\dagger\mathrm{L},\rho\}\right], \tag{3.2}$$

with $\mathrm{L}(x) = \psi(x)$ the Lindblad operators and $\Gamma(x) = \gamma\delta(x)$, entailing that the loss acts locally at $x = 0$ (cf. Fig. 1.1), and where γ quantifies the dissipation strength. We consider the system to be initialized in a thermal state defined by the Hamiltonian (3.1) and characterized by a temperature T and a chemical potential μ. At time $t = 0$, the localized loss is switched on at position $x = 0$, consequently driving the system out of equilibrium.

In addition to the continuum model (3.1), we also consider a lattice model described in the absence of interparticle interactions by the Hamiltonian

$$H = -J\sum_j \left(\psi_{j+1}^\dagger\psi_j + \mathrm{h.c.}\right), \tag{3.3}$$

with $\psi_j, \psi_j^\dagger$ the fermionic annihilation and creation operators on site j, and $\sum_j = \sum_{j=j_{\min}}^{j_{\max}}$. Here, the summation index runs from $j_{\min} = \lfloor -(L-1)/2 \rfloor$ to $j_{\max} = \lfloor (L-1)/2 \rfloor$, with $\lfloor x \rfloor$ the floor function. Periodic boundary conditions are assumed, i.e., $\psi_{j_{\max}+1} = \psi_{j_{\min}}$ and ${\psi^\dagger}_{j_{\max}+1} = {\psi^\dagger}_{j_{\min}}$. The dynamics is still defined by Eq. (3.2), where the integral is replaced by a sum over the lattice sites, $\mathrm{L}(x)$ is replaced by $\mathrm{L}_j = \psi_j$, and $\Gamma(x)$ is replaced by $\Gamma_j = \gamma\delta_{j,0}$, with $\delta_{i,j}$ the Kronecker delta, yielding the quantum master equation on a lattice:

$$\partial_t \rho = -i\,[H,\rho] + \sum_j \Gamma_j\left[2\mathrm{L}_j\rho\mathrm{L}_j^\dagger - \left\{\mathrm{L}_j^\dagger\mathrm{L}_j,\rho\right\}\right]. \tag{3.4}$$

We set the lattice constant to unity in the rest of the thesis. The reason for considering the lattice Hamiltonian (3.3) is twofold: first, it can be regarded as an approximation to the continuum

[1] Sections 3.6.2, 3.7.1 and 3.7.2 can be found with minor adaptions in publication [134]. Other sections may contain paragraphs and sentences that appear verbatim in publication [134].

Hamiltonian (3.1), useful for numerical investigations; second, it represents an interesting model per se, which can be experimentally realized [72–74].

The consideration of an interaction-free Hamiltonian and Lindblad operators linear in the fermionic operators leads to a quadratic quantum master equation (3.2) (respectively Eq. (3.4)) which is exactly solvable. In subsequent chapters, we extend this model by including interparticle interactions in the Hamiltonian, cf. Sec. 4.1.

3.2. Dynamics and temporal regimes

As a starting point, we investigate the time-evolution of several observables in the interaction-free lattice model after the quench of a localized loss. On the one hand, this approach yields insights into the remarkable rich dynamics in the presence of a dissipative impurity, interesting in itself, and on the other hand, it provides the foundation of any further numerical and analytical analysis. The study is based on the time-evolution of the equal-time correlations $\langle \psi_i^\dagger(t)\psi_j(t)\rangle$ for which we derive a closed-form expression. As the central building block, we identify the emergence of a non-equilibrium (quasi-)stationary state (NESS) that lasts up to a time scale extensive in the system size. The density profile in this NESS approaches a constant background density with Friedel oscillations in the vicinity of the loss site.

3.2.1. Time evolution of the correlation matrix

In order to investigate the dynamics of the lattice model (3.4) after switching on the localized loss, we study the time evolution of the equal-time correlations

$$C_{ij}(t) = \langle \psi_i^\dagger(t)\psi_j(t)\rangle. \tag{3.5}$$

In this section, we derive a closed-form expression for $C_{ij}(t)$ which enables us to study conveniently a variety of observables in the following.

Based on the quantum master equation on a lattice (3.4) with the Hamiltonian (3.3), the equation of motion in the Heisenberg picture for the operator $A(t)$ reads [2]

$$\frac{\mathrm{d}A(t)}{\mathrm{d}t} = i\left[H, A(t)\right] + \gamma\left[2\mathrm{L}^\dagger A(t)\mathrm{L} - \left\{\mathrm{L}^\dagger\mathrm{L}, A(t)\right\}\right], \tag{3.6}$$

also referred to as adjoint quantum master equation since the right-hand side of Eq. (3.6) is generated by the adjoint of the Liouville superoperator (2.18). For $A(t) = \psi_i^\dagger(t)\psi_j(t)$ and by taking the expectation value of Eq. (3.6) we obtain the equation of motion for the equal-time correlations

$$\frac{\mathrm{d}}{\mathrm{d}t}C_{ij}(t) = i\sum_l \left(\widetilde{H}_{il}^\dagger C_{lj}(t) - C_{il}(t)\widetilde{H}_{lj}\right). \tag{3.7}$$

Eq. (3.7) takes on the form of a non-Hermitian Heisenberg equation of motion with the dynamics being generated by the non-Hermitian effective Hamiltonian $\widetilde{H}$ associated with the master equation (3.2):

$$\widetilde{H}_{kl} = -J\left(\delta_{k,l+1} + \delta_{k+1,l}\right) - i\gamma\delta_{k,0}\delta_{l,0}. \tag{3.8}$$

The solution of Eq. (3.7) is found straightforwardly in terms of the closed-form expression

$$C_{ij}(t) = \sum_{k,l} G^{\dagger}_{ik}(t) G_{jl}(t) C_{kl}(0), \tag{3.9}$$

with $G(t) = \exp[-i\tilde{H}t]$ the retarded Green's function and $C_{ij}(0)$ the correlation matrix of the initial state at time $t = 0$. Here, the initial correlations $C_{ij}(0)$ are obtained from

$$C_{jl}(0) = \langle \psi^{\dagger}_j(0)\psi_l(0)\rangle = \frac{1}{L^2}\sum_{k,k'} \mathrm{e}^{-ikj}\mathrm{e}^{ik'l}\langle \psi^{\dagger}_k(0)\psi_{k'}(0)\rangle, \tag{3.10}$$

where k are the lattice momenta $k = 2\pi n/L$, with $n \in \{j_{\min}, j_{\min}+1, \ldots, j_{\max}\}$ (periodic boundary conditions). Assuming a thermal initial state, the momentum correlations $\langle \psi^{\dagger}_k(0)\psi_{k'}(0)\rangle$ are given by

$$\langle \psi^{\dagger}_k(0)\psi_{k'}(0)\rangle = \delta_{k,k'}\frac{1}{1+\mathrm{e}^{(\epsilon_k-\mu)/T}}, \tag{3.11}$$

with T the temperature, μ the chemical potential and $\epsilon_k = -2J\cos(k)$ the lattice dispersion. The availability of a closed-form solution (3.9) of Eq. (3.7) is a consequence of considering a quadratic quantum master equation and permits us to compute observables derived from $C_{jl}(t)$ efficiently at arbitrary large times and for relatively large system sizes. In Chapter 5 we consider a generalization of Eq. (3.7) which includes interparticle interactions within a Hartree-Fock approximation.

3.2.2. Loss rate and temporal regimes

The total particle loss rate $|\mathrm{d}N/\mathrm{d}t|$ is a natural observable to characterize the dynamics in the presence of a localized loss and its study allows us to identify three temporal regimes following the quench. The total particle loss rate is obtained as the time derivative of the average total particle number $N(t)$, which is in turn evaluated from the time evolution of the correlation matrix (3.9) as $N(t) = \sum_j C_{jj}(t)$. As the initial state (3.10), we assume the system to be prepared in its zero-temperature ground state characterized by a Fermi momentum $k_F = \pi n_0$, with n_0 the initial density.

In Fig. 3.1 the total particle loss rate is shown as a function of time elapsed from the quench, for different system sizes L. Three different temporal regimes can be distinguished:

i) In the first temporal regime, for times $0 < t < t_{\mathrm{I}} \sim \gamma^{-1}$, a rapid drop in the particle number occurs, signaled by an increased loss rate. This regime corresponds to a fast local depletion of the density close to the position of the localized loss (cf. discussion of the density dynamics in Sec. 3.2.3). The loss rate in this regime is independent of the system size.

ii) In the second temporal regime, for times $t_{\mathrm{I}} < t < t_{\mathrm{II}}$, the particle loss rate is constant. In this regime, the local loss of particles is balanced with steady currents directed towards the impurity (cf. Sec. 3.5), feeding on particles of the regions far away from the impurity. The perturbation induced by the loss impurity spreads ballistically with a speed v, defining a light cone separating regions affected by the impurity ($|x| < vt$) from those still unaffected ($|x| > vt$) (cf. also Fig. 3.2, upper panel). The regions affected by the loss are characterized

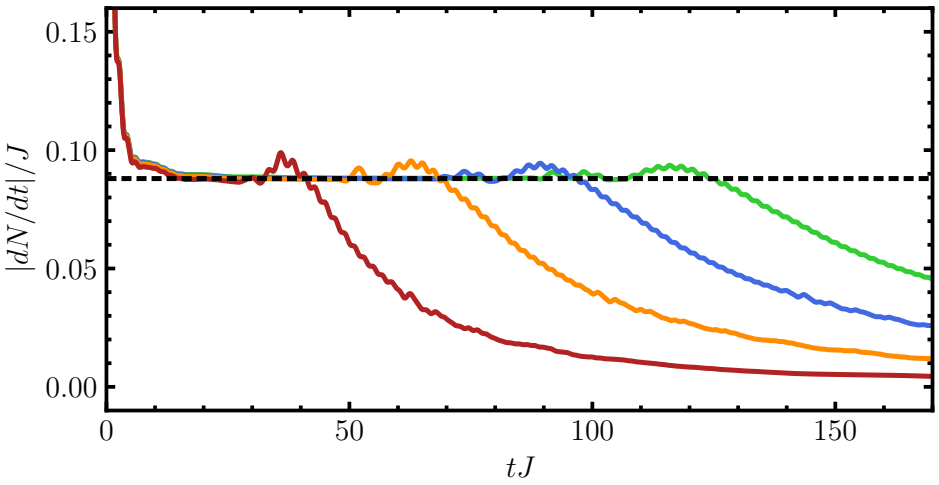

Fig. 3.1. Particle loss rate for the lattice model as a function of time elapsed from the quench, for increasing system sizes, $L = 61, 101, 141, 181$ (leftmost to rightmost curve, respectively). The dashed line indicates the constant loss rate (3.64) obtained analytically for $L \to \infty$. For all curves, $\gamma = J, N(0)/L = 0.25$.

by a drop of the density and the presence of currents. During this regime, every particle scatters at most once against the impurity. The boundaries of the system remain outside the light cone, rendering the properties of this regime independent of the boundary conditions. At the time $t_{\mathrm{II}} = L/(2v)$ the perturbation arrives at the boundary, signaling the end of the second regime, which is thus extensive in the system size L. We elaborate more on the light-cone speed v in Sec. 3.2.4

iii) In the third temporal regime, for times $t > t_{\mathrm{II}} = L/(2v)$, the perturbation reaches the boundaries and the entire system experiences the presence of the loss. In this regime, particles scatter repeatedly against the loss after returning from the boundaries, consequently rendering the boundary conditions relevant. Due to these multiple scattering events the density depletes further, resulting in a decrease of the particle loss rate, as observed in Fig. 3.1. Eventually, the system fully empties out. Under certain conditions [51], however, the system can exhibit a dissipationless subspace of modes decoupled from the loss, preventing the system from completely emptying. The fulfillment of these conditions is fragile against, e.g., interactions, boundary conditions, or finite size of the impurity. Moreover, in Sec. 3.8 we show that the properties of the second temporal regime are indeed independent of the presence of a dissipationless subspace.

We remark that similar aspects of the dynamics have been found also in interacting bosonic systems with a localized loss [45, 48, 51, 53, 55, 60], thus suggesting the generality of the described dynamical regimes. The stationary regime within the light-cone for times $t_{\mathrm{I}} < t < t_{\mathrm{II}}$ can be understood as a non-equilibrium (quasi-) stationary state (NESS) characterized by a balance between the losses at the impurity site and the currents maintained from the particles of the regions outside the light cone (cf. Fig. 1.1).

Providing the generality of the second regime and that it lasts up to times extensive in the system size L, we identify the NESS as the relevant regime for further analytical studies.

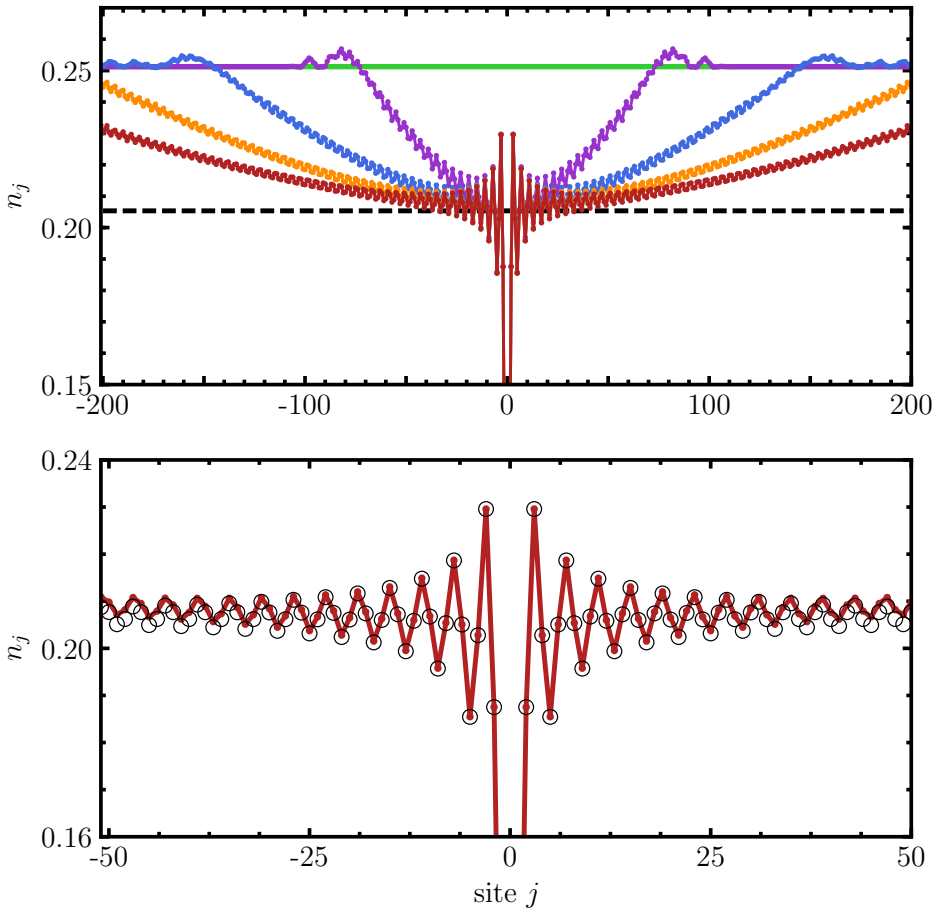

Fig. 3.2. Density profile for the non-interacting lattice model (3.4). Upper panel: Density profiles for different times elapsed from the quench ($tJ = 0, 50, 100, 150, 200$) and analytical average density n_{bg} (dashed line). Lower panel: Friedel oscillations around the impurity at time $tJ = 200$ obtained numerically (solid line) and analytically (hollow circles). For all curves $L = 601, \gamma = 2J, N(0)/L = 0.25$. For this filling, the period of the Friedel oscillations corresponds to $\pi/k_F = 4$ sites.

3.2.3. Density profile and Friedel oscillations

Further insight on the dynamical regimes and the properties of the NESS can be disclosed by inspecting the dynamics of the density profile. In Fig. 3.2 (upper panel) the density profile is shown for different times elapsed from the quench: the density at the loss site is strongly depleted, while inside the light cone ($|x| \lesssim vt$) the density approaches a stationary profile, exhibiting spatial oscillations around a mean value lower than the initial value. Outside the light cone, the density remains at its initial value. An analytical expression for this profile is provided in Sec. 3.4. In Fig. 3.2 (lower panel) the comparison between the density profile at the latest time in Fig. 3.2 (upper panel) to the analytical density profile (3.56) is shown: the density relaxes to its stationary value proceeding from the sites near the loss. The density oscillations are characterized by a period of π/k_F, with k_F the Fermi momentum of the initial state. A further numerical inspection discussed below, supported by an analytical solution (see Sec. 3.4), shows that the oscillation amplitude decays in space as $\sim 1/x$. The density oscillations can thus be regarded as Friedel oscillations [89]. Since these oscillations are characteristic of Fermi systems at $T = 0$, their presence and robustness in a non-equilibrium steady state is remarkable and can

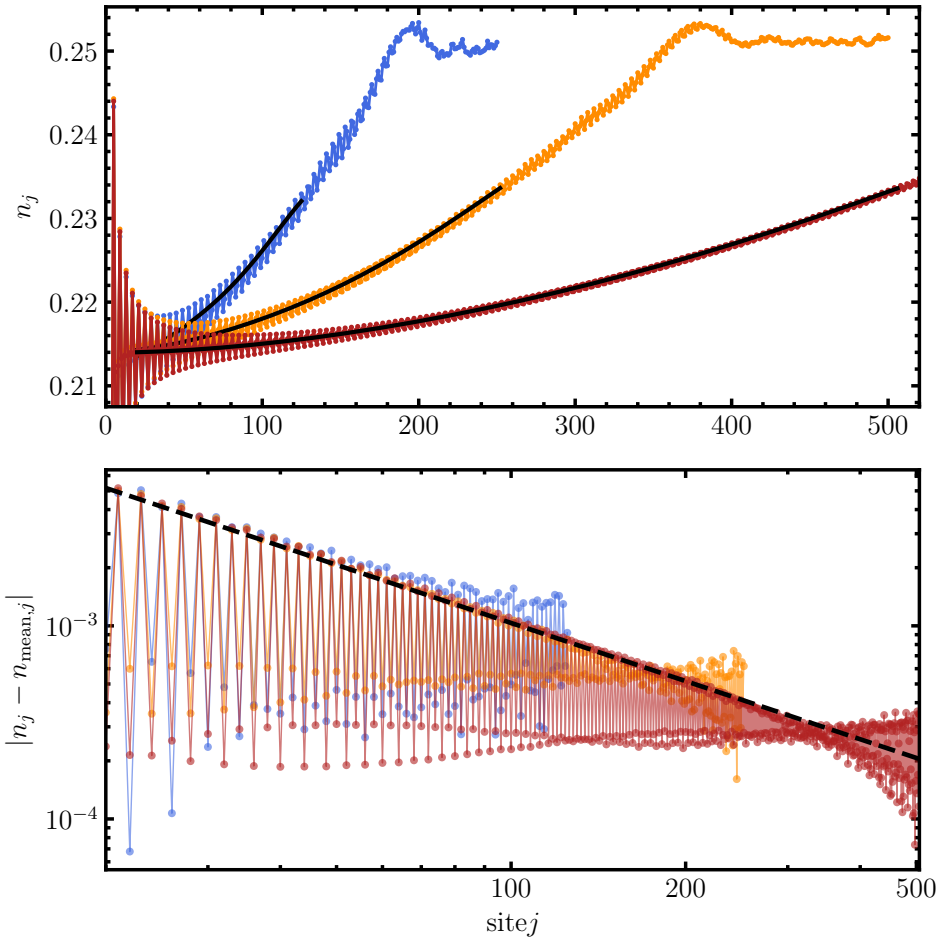

Fig. 3.3. Upper panel: Density profile right to the loss site for increasing system sizes, $L = 501, 1001, 2001$ (leftmost to rightmost curve), at times $t = L/4 < t_{II}$ in the second temporal regime. For all curves $\gamma = 3, \nu = 0.25$. The solid black lines indicate polynomial fits in a spatial segment $j \in [20, vt - L/10]$ within the light cone (cf. main text) to determine the local mean value $n_{\mathrm{mean},j}$ of the oscillating profile. Lower panel: Absolute value of the amplitude of the Friedel oscillations with respect to the local mean value $n_{\mathrm{mean},j}$, for the same parameters as in the upper panel. The dashed black line indicates an algebraic decay as $1/j$.

be traced back to the dynamics of the particle momentum distribution, which is analyzed in detail in Sec. 3.6.

In order to clarify the asymptotic behavior of the density oscillations, in Fig. 3.3 (upper panel) the density profile is shown in a segment of the wire right to the loss site, for different system sizes L at rescaled times $tJ = L/4$ within the second regime. The amplitude of the density oscillations with respect to the local mean density $n_{\mathrm{mean},j}$ (black solid lines, see discussion below) is then given by $|n_j - n_{\mathrm{mean},j}|$ and depicted in Fig. 3.3 (lower panel). The envelope of the oscillation amplitude decays as $1/|j|$ (indicated by the dashed black line) in a large region around the loss site, whose size increases with the system size. Finite-size effects are visible near the interface between the depleted and undepleted regions at the light-cone. Hence, the asymptotic behavior of the density oscillations indeed corresponds to the one expected for Friedel oscillations, decaying algebraically $\sim 1/|j|$.

Here, we extract the amplitude of the density oscillations with respect to the local mean value $n_{\mathrm{mean},j}$ of the density which at finite times is described by a slightly arched profile (see black solid lines in Fig. 3.3, upper panel) due to the incomplete relaxation of the density. At large times, the mean density flattens to a uniform value n_{bg} (cf. Fig. 3.2 and analytical analysis in Sec. 3.4). We determine the local mean density $n_{\mathrm{mean},j}$ by a polynomial fit for which the oscillations average out. The fit is performed in a spatial segment sufficiently deep inside the light-cone where the Friedel oscillations had sufficient time to build up after the quench and excluding the further depleted region close to the loss site.

The emergence of Friedel oscillations in the second temporal regime provides a further motivation to focus in the following on the properties of the quasi-stationary steady state.

3.2.4. Light-cone speed

The interface between the depleted and undepleted regions propagates ballistically with a constant speed v, hence defining the light-cone dynamics described in Sec. 3.2.2. The speed v hereby corresponds to the one of the fastest particles available in the system. In the continuum model this speed corresponds to the Fermi velocity, i.e., $v = v_F$. In the lattice model, due to the non-monotonic group velocity $v_k = 2J\sin(k)$, the fastest speed is given by $v = v_F$ below half filling, while for larger fillings it saturates at $v = 2J$, i.e.,

$$v = \begin{cases} v_F = 2J|\sin(k_F)|, & k_F \leq \pi/2, \\ v_{k=\pi/2} = 2J, & k_F > \pi/2. \end{cases} \tag{3.12}$$

This is substantiated in Fig. 3.4, where we show the light-cone speed as a function of the filling (black dots) in comparison to the corresponding Fermi velocity (red dashed curve). Here, the light-cone speed is determined numerically by tracking the boundary between depleted and undepleted regions in the density profile, with the depleted region identified by a decrease of the density below 98% of its initial value.

Additionally, small density perturbations propagating slightly faster than the boundary of the depleted region can be observed in Fig. 3.2 (upper panel). For fillings above half-filling, such density perturbations are absent (see App. A.1). We explain this effect as follows. The quench can lead to a small occupation of states with momentum $k > k_F$ (cf. Sec. 3.6). Due to the non-monotonic group velocity of the lattice model, below half-filling, these modes can propagate faster compared to the initially occupied modes which dominate the depletion. As a consequence, these perturbations can travel faster than the depleted region, with a maximal speed $2J$.

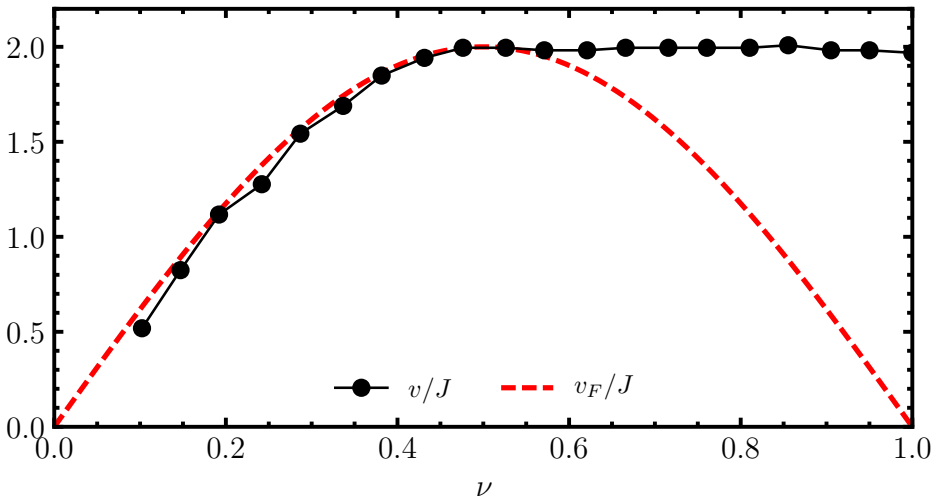

Fig. 3.4. Speed v of the light cone (dots) separating depleted and unperturbed regions as a function of the initial filling factor $\nu = N(0)/L$, obtained numerically in the lattice system, with $L = 401, \gamma = 3J$. The dashed line indicates the Fermi velocity v_F as a function of the filling factor.

3.3. Analytical solution in the stationary regime

Having identified the temporal regime of interest, we substantiate and extend the results discussed in the previous section with exact analytical results. In the present section, we provide the main steps of the derivation, while the discussion of observables and the interpretation of the results will be given in subsequent sections. To this end, we solve exactly the single-particle problem for the continuum model (3.2) using the Green's function formalism. This approach yields an exact solution of the correlations in the second temporal regime, fully characterizing observables in the Gaussian model. The physical mechanism underlying these results can be highlighted by the formulation of a non-unitary scattering problem for a loss impurity. This approach yields a description in terms of the loss probability η_k, which is identified in the remainder of this thesis as the key quantity to describe depletion processes.

3.3.1. Retarded Green's function

In order to evaluate the retarded Green's function for the non-interacting continuum model, we map the quantum master equation (3.2) onto a Keldysh action $S = S_0 + S_{\text{loss}}$ [4, 6], with (see Sec. 2.1.2)

$$S_0 = \int_{x,t} \left[i\psi_+^* \partial_t \psi_+ - H(\psi_+^*, \psi_+) - i\psi_-^* \partial_t \psi_- + H(\psi_-^*, \psi_-) \right], \tag{3.13}$$

and

$$S_{\text{loss}} = -i \int_{x,t} \Gamma(x) \left[2\mathrm{L}_-^* \mathrm{L}_+ - (\mathrm{L}_+^* \mathrm{L}_+ + \mathrm{L}_-^* \mathrm{L}_-) \right], \tag{3.14}$$

where $\mathrm{L}_\pm(x) = \psi_\pm(x)$. Note that for $\mathrm{L} = \psi$ all terms appearing in the quantum master equation (3.2) are normal ordered. After performing the Keldysh rotation (2.38), we obtain

$$S_{\text{loss}} = -i \int_{x,t} \Gamma(x) \left[-2\psi_q^* \psi_q + \left(\psi_c^* \psi_q - \psi_q^* \psi_c \right) \right]. \tag{3.15}$$

The retarded Green's function is defined as (cf. Sec. 2.1.2)

$$G(x,y,t) = -i\theta(t)\langle\{\psi(x,t),\psi^\dagger(y,0)\}\rangle = -i\langle\psi_c(x,t)\psi_q^*(y,0)\rangle. \tag{3.16}$$

Since $G(x,y,t)$ only depends on the time difference, it is convenient to consider its Fourier transform $G(x,y,\omega)$ in frequency ω. Throughout this thesis, we use the following convention for the Fourier transformation of space and time arguments:

$$f(x,t) = \int_\omega \int_k f(k,\omega)e^{ikx-i\omega t}, \tag{3.17}$$

with $\int_\omega \equiv \frac{1}{2\pi}\int_{-\infty}^{\infty} d\omega$ and $\int_k \equiv \frac{1}{2\pi}\int_{-\infty}^{\infty} dk$. We can then evaluate the retarded Green's function of the non-interacting system with a localized loss exactly using a Dyson equation [4] (2.45):

$$G(x,x',\omega) = G_0(x,x',\omega) + \int_y G_0(x,y,\omega)\Sigma(y)G(y,x',\omega). \tag{3.18}$$

Here, $\Sigma(y)$ is the self-energy associated with the localized loss and G_0 is the retarded Green's function of the homogeneous system, i.e., in the absence of the dissipative impurity:

$$G_0(x,x',\omega) = \int_q (\omega+i\delta-\epsilon_q)^{-1}\mathrm{e}^{iqx} = \frac{\sqrt{2m}}{2i\sqrt{\omega}}\mathrm{e}^{i\sqrt{2m\omega}|x-x'|}, \tag{3.19}$$

where δ is an infinitesimal dissipation whose presence ensures causality. Due to the quadratic structure of S_{loss} (3.14) the self-energy is field independent and reads $\Sigma(y) = -i\gamma\delta(y)$, and the Dyson equation can be written as

$$G(x,x',\omega) = G_0(x,x',\omega) - i\gamma G_0(x,0,\omega)G(0,x',\omega). \tag{3.20}$$

We obtain an expression for $G(0,x',\omega)$ at the right-hand side of this equation by evaluating Eq. (3.20) for $x=0$ and arrive at

$$G(x,x',\omega) = G_0(x,x',\omega) - i\gamma\frac{G_0(x,0,\omega)G_0(0,x',\omega)}{1+i\gamma G_0(0,0,\omega)}. \tag{3.21}$$

From this, we readily find the solution of the retarded Green's functions as

$$G(x,x',\omega) = \frac{\sqrt{2m}}{2i\sqrt{\omega}}\left[\mathrm{e}^{i\sqrt{2m\omega}|x-x'|} + r(\omega)\,\mathrm{e}^{i\sqrt{2m\omega}(|x|+|x'|)}\right], \tag{3.22}$$

with

$$r(\omega) = \frac{-\gamma}{\sqrt{2\omega/m}+\gamma}. \tag{3.23}$$

We also report the solution of Eq. (3.21) in a mixed momentum and real-space representation

$$G(x,q,\omega) = G_0(q,\omega)\left[\mathrm{e}^{iqx} + r(\omega)\,\mathrm{e}^{i\sqrt{2m\omega}|x|}\right], \tag{3.24}$$

where $G_0(q,\omega) = (\omega+i\delta-\epsilon_q)^{-1}$.

3.3.2. Analytical solution via Green's function method

With the retarded Green's function in presence of a localized loss at hand, we now derive an exact expression for the two-time one-particle correlation functions

$$C(x,x',t,t') = \langle \psi^\dagger(x,t)\psi(x',t')\rangle. \tag{3.25}$$

Since in the present section we neglect interactions, the fluctuations of the system are Gaussian and, therefore, the knowledge of $C(x,x',t,t')$ is sufficient to determine any observable. For the sake of brevity, calculations are presented for the continuum system described by the Hamiltonian (3.1). The adaptation to the lattice case is straightforward and presented in Sec. 3.3.4.

A major simplification arises when the thermodynamic limit $L \to \infty$ is considered. However, this limit has to be implemented with care since it does not commute with the limit $t \to \infty$, as the timescale t_{II}, characterizing the end of the second regime, scales itself with L (cf. Sec. 3.2.2). In fact, if the limit $L \to \infty$ is taken *after* $t \to \infty$, the system will be in the trivial vacuum state. In contrast, if the limit $L \to \infty$ is taken *before* $t \to \infty$, the system will never reach the end of the second regime, which becomes thus a true stationary state. Therefore, we will focus on the latter case.

The system is assumed to be prepared in a homogeneous state characterized by a momentum distribution $n_{0,k}$, and the localized loss is switched on at time t_0. Since no particles are injected in the system, the dynamics of the one-particle correlation functions $C(x,x',t,t')$ can be determined as a propagation of the initial correlations, as in Eq. (3.9),

$$C(x,x',t,t') = \int_{y,y'} G^*(x,y,t-t_0)G(x',y',t'-t_0)C(y-y',t_0,t_0), \tag{3.26}$$

where $G(x,y,t)$ is the retarded Green's function (3.16) and $C(x-x',t_0,t_0)$ is the correlation function of the initial state. With the initial correlations $C(x,x',t_0,t_0)$ given by

$$C(x,x',t_0,t_0) = \int_k \mathrm{e}^{ik(x'-x)} n_{0,k}, \tag{3.27}$$

and by using the retarded Green's function $G(x,x',t)$ (3.22), we obtain

$$C(x,x',t,t') = \int_k G^*(x,-k,t-t_0)G(x',-k,t'-t_0)n_{0,k}. \tag{3.28}$$

Having provided an explicit form of the retarded Green's function $G(x,k,t)$ in Eq. (3.24), we can then evaluate Eq. (3.28) analytically in the stationary regime by taking the limit $t,t' \to +\infty$, while $t-t'$ remains finite. To this end, the integrand in Eq. (3.28) can be evaluated as follows:

$$G^*(x,-k,t-t_0)G(x',-k,t'-t_0) = \int_{\omega,\omega'} \frac{\mathrm{e}^{i\omega(t-t_0)}\mathrm{e}^{-i\omega'(t'-t_0)} f^*(\omega,k,x)f(\omega',k,x')}{(\omega - i\delta - \epsilon_k)(\omega' + i\delta - \epsilon_k)}, \tag{3.29}$$

where we defined $f(\omega, k, x) = \mathrm{e}^{-ikx} + r(\omega)\mathrm{e}^{i\sqrt{2m\omega}|x|}$ and $\epsilon_k = k^2/2m$ is the dispersion relation of the continuum model. Further progress can be achieved by recasting

$$(\omega + i\delta - \epsilon_q)^{-1} = -i \int_{t''} \theta(t'')\mathrm{e}^{i(\omega-\epsilon_q)t''}, \tag{3.30}$$

which allows us to make use of the crucial identity

$$\mathrm{e}^{i\omega' t_0}\, \mathrm{e}^{-i\omega t_0} \int_{t''} \theta(t'')\mathrm{e}^{i(\omega'-\epsilon_k)t''} \int_{t'''} \theta(t''')\mathrm{e}^{-i(\omega-\epsilon_k)t'''} \tag{3.31a}$$

$$= \int_{t''} \theta(t''-t_0)\mathrm{e}^{i(\omega'-\epsilon_k)t''} \int_{t'''} \theta(t'''-t_0)\mathrm{e}^{-i(\omega-\epsilon_k)t'''} \tag{3.31b}$$

$$= (2\pi)^2\delta(\omega-\epsilon_k)\delta(\omega'-\epsilon_k). \tag{3.31c}$$

Here, in the last equality we took the limit $t_0 \to -\infty$ in order to obtain the expression in the stationary regime. We can now evaluate Eq. (3.28) and arrive at the central result

$$C(x, x', t, t') = \int_k f^*(\epsilon_k, k, x) f(\epsilon_k, k, x')\mathrm{e}^{i\epsilon_k(t-t')} n_{0,k}. \tag{3.32}$$

Notice that the right-hand side of Eq. (3.32) only depends on the difference $t - t'$ as a consequence of stationarity in time. From the previous equation, a number of exact results can be obtained, which will be discussed in later sections.

3.3.3. Scattering problem: Loss probability

Beyond providing the technical foundation of the further analysis, the derivation in the previous section illuminates the physical mechanisms underlying the results. To this end, the retarded Green's function in Eq. (3.22) can be interpreted in terms of a non-Hermitian scattering problem in the following way. If a particle with momentum $k > 0$ and energy $\omega = \epsilon_k$ is injected at $y \ll x$, $G(x, y, \omega)$ describes the probability amplitude of finding the particle at position x:

$$G(x, y \ll x, \omega) \propto \begin{cases} \mathrm{e}^{ikx} + r(\omega)\mathrm{e}^{-ikx} & x < 0, \\ t(\omega)\mathrm{e}^{ikx} & x > 0, \end{cases} \tag{3.33}$$

with $t(\omega) = 1 + r(\omega)$ fixed by the continuity condition at $x = 0$. Equivalently, we can understand Eq. (3.33) as the response to a plane wave perturbation incoming from the left with momentum k and energy $\omega = \epsilon_k$. This interpretation becomes evident by considering the retarded Green's function $G(x, q, \omega)$ in a mixed momentum and real-space representation (3.24). Note that $G(x, q, \omega)$ has the same asymptotic behavior as reported in Eq. (3.33). In fact, $G(x, q, \omega)$ corresponds to the response to an external perturbation $V = \int_x \left(h(x,t)\psi^\dagger(x) + \text{h.c.}\right)$ with $h(x,t) = h_0 \exp\left[iqx - i\omega t\right]$, describing the injection of a free particle (described by a plane wave) incoming from the left, i.e.,

$$G(x, q, \omega) = \left.\frac{\partial\langle\psi(x)\rangle_{h_0}}{\partial h_0}\right|_{h_0=0}. \tag{3.34}$$

Therefore, $G(x, y \ll x, \omega)$ describes a one-dimensional scattering problem. From its asymptotic form (3.33) one can read off the transmission and the reflection amplitudes, $t_k \equiv t(\omega = \epsilon_k)$ and $r_k \equiv r(\omega = \epsilon_k)$, respectively:

$$t_k = \frac{|v_k|}{|v_k| + \gamma}, \quad r_k = -\frac{\gamma}{|v_k| + \gamma}, \tag{3.35}$$

with $v_k = \partial\epsilon_k/\partial k = k/m$ the group velocity. In contrast to the case of a coherent delta potential barrier, these amplitudes are real-valued and violate probability conservation as $|r_k|^2 + |t_k|^2 \neq 1$: a loss impurity acts as a non-unitary scatterer. The study of this scattering problem yields crucial insights to characterize the losses in the system.

In order to quantify the loss of unitarity (cf. discussion below), it is then convenient to introduce the *loss probability* η_k as

$$\eta_k = 1 - |r_k|^2 - |t_k|^2, \tag{3.36}$$

corresponding to the probability of a particle with momentum k and energy ϵ_k to be absorbed by the localized loss. By using the definition (3.36) and Eq. (3.35), the loss probability of the non-interacting system reads

$$\eta_k = \frac{2\gamma\,|v_k|}{(\gamma + |v_k|)^2}. \tag{3.37}$$

From Eq. (3.37) it can be thus inferred that η_k is a non-monotonic function of the ratio γ/v_k, corresponding to a manifestation of the quantum Zeno effect. We emphasize that this is not a many-body quantum Zeno effect, but rather a single-particle property. In Fig. 3.5 the transmission and reflection probabilities

$$\mathcal{T}_k = |t_k|^2, \qquad \mathcal{R}_k = |r_k|^2, \tag{3.38}$$

and the loss probability η_k are depicted as a function of momentum k for both the continuum and the lattice model (see Sec. 3.3.4 for the latter). The loss probability is non-monotonic as a function of the momentum k as a consequence of the quantum Zeno effect: more precisely, η_k becomes negligible for $|v_k| \ll \gamma$, indicating that particles are rather reflected than lost from the system. The appearance of the group velocity as the relevant scale is reasonable since to estimate the efficiency of the dissipation one should compare the time a particle spends in the loss region to the dissipation rate it experiences within. Note that in the limit of a delta-shaped loss γ has the dimension of a velocity. The loss probability η_k plays a central role in our analysis: it appears ubiquitously in the observables discussed in the following sections and represents a directly observable quantity itself (see Sec. 3.6). In addition, η_k can be strongly affected by interactions, resulting in a universal behavior at low momenta (see Chapter 4).

Moreover, we remark that the scattering solutions (3.33) can be equivalently obtained by solving a single particle Schrödinger equation with a non-Hermitian Hamiltonian (cf. Sec. 2.5). This equivalence carries over to the lattice system, see Sec. 3.3.4. On the lattice, the eigenfunctions of the non-Hermitian Hamiltonian include, besides scattering solutions, a localized state, whose presence is, however, irrelevant to the effects discussed in this work. Remarkably, the emergence of the localized state is related to an exceptional point [135] of the non-Hermitian Hamiltonian. The nature of this localized state and further spectral properties of the effective non-Hermitian Hamiltonian are discussed in Chapter 7.

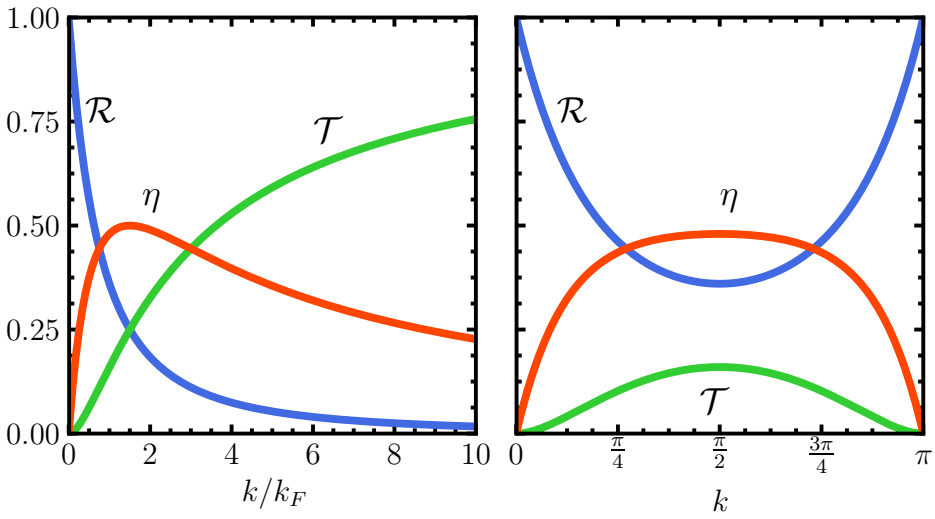

Fig. 3.5. Transmission probability $\mathcal{T}_k$, reflection probability $\mathcal{R}_k$ and loss probability η_k as a function of momentum k for the continuum (left panel, $\gamma/v_F = 1.5$) and lattice model (right panel, $\gamma = 3J$).

Finally, we briefly comment on the absence of unitarity in the above considered non-Hermitian scattering problem. Indeed, we can understand a non-vanishing η as a way to quantify the breaking of unitarity in presence of the loss barrier. To this end, we consider a scattering matrix S connecting the in- and outgoing solutions (cf. Eq. (3.33)) scattering off a barrier

$$S = \begin{pmatrix} r & t \\ t & r \end{pmatrix}, \tag{3.39}$$

where we assume a symmetric barrier and omitted the momentum index for now. If the scattering matrix is unitary, i.e., $S^\dagger S = \mathbb{I}$, the following conditions are imposed:

$$|t|^2 + |r|^2 = 1, \qquad r^* t + t r^* = 2\mathrm{Re}(r^* t) = 0. \tag{3.40}$$

The first condition is straightforwardly interpreted as the conservation of probability by considering the conservation of the probability current. The second identity can be interpreted as an additional requirement of time-reversal symmetry, which can be seen as follows. In the present section we considered a plane wave incoming from the left $\psi_{\mathrm{in}} = \mathrm{e}^{ikx}$ which is scattered to an outgoing solution $\psi_{\mathrm{out}} = t\mathrm{e}^{ikx} + r\mathrm{e}^{-ikx}$. The corresponding time-reversed solution is given by an incoming solution $\psi_{\mathrm{in,TR}} = \psi^*_{\mathrm{out}} = t^*\mathrm{e}^{-ikx} + r^*\mathrm{e}^{ikx}$ [136] which, in turn, is mapped by S to an outgoing solution $\psi_{\mathrm{out,TR}} = (t^* r + r^* t)\mathrm{e}^{ikx} + (r^* r + t^* t)\mathrm{e}^{-ikx}$. Time-reversal symmetry then requires $\psi_{\mathrm{out,TR}} = \psi^*_{\mathrm{in}}$, which implies $t^* r + r^* t = 0$ and $|t|^2 + |r|^2 = 1$; these conditions correspond exactly to the two unitarity conditions reported in Eq. (3.40).

For the case of a loss barrier, S is not unitary and both conditions (3.40) are indeed violated by the explicit expressions of t and r (3.35). The first identity (3.40), reflecting the conservation of probability, has been utilized in Eq. (3.36) to define the loss probability η (3.36). Additionally, from the explicit forms of the scattering amplitudes t, r (3.35) we find

$$2rt + \eta = 0. \tag{3.41}$$

This expression is the analog (t, r are real-valued) of the second identity in Eq. (3.40) for a non-unitary scatterer, for which $r^*t + t^*r \neq 0$. Even though η was defined only with regard to the loss of probability, the loss of time-reversal symmetry due to the loss barrier is equally quantified by η.

The specific appearance of η in Eq. (3.41) has a straightforward interpretation in terms of the unitarity conditions of a three-wire configuration [126, 127]. A three-wire junction resembles a single wire with a localized loss where two of the wires constitute the main wire and the third wire resembles the loss channel. The corresponding scattering matrix reads [126, 127]

$$S = \begin{pmatrix} r & t & \tau \\ t & r & \tau \\ \tau & \tau & \rho \end{pmatrix}, \tag{3.42}$$

with τ the transmission into the loss channel (and ρ the backscattering in the loss channel). The unitarity conditions for this three-wire configuration read[2]

$$|r|^2 + |t|^2 + |\tau|^2 = 1, \qquad r^*t + t^*r + |\tau|^2 = 0. \tag{3.43a}$$

With the identification $|\tau|^2 = \eta$ in Eq. (3.43) we recover Eqs. (3.41) and (3.37) of the loss barrier. For a non-unitary 2×2 scattering matrix describing scattering off a localized loss, the second unitarity condition (3.40) is thus violated exactly by an amount quantifying the probability to escape from the wire. A further analysis shows that Eq. (3.41) (generalized to complex-valued t, r) holds also for a composite scatterer of coherent and incoherent delta barrier, but in general breaks down for barriers with a finite width [137].

3.3.4. Generalization to the lattice model

We derive the retarded Green's functions for the non-interacting lattice model (3.4) with a dissipative loss at site $j = 0$. The results of Sec. (3.3.2) obtained for the continuum model can then be straightforwardly adapted for the lattice model. In analogy to the continuum case in Sec. 3.3.1 we obtain the retarded Green's function as

$$G_{i,j}(\omega) = G_{0i-j}(\omega) - \frac{i\gamma G_{0i}(\omega) G_{0j}(\omega)}{1 + i\gamma G_{0j=0}(\omega)}, \tag{3.44}$$

where $G_{0j}(\omega)$ is the retarded Green's function of the homogeneous system ($\gamma = 0$) in real space:

$$G_{i,j}(\omega) = \frac{1}{L} \sum_k (\omega + i\delta - \epsilon_k)^{-1}, \tag{3.45}$$

with $\delta \to 0^+$ an infinitesimal dissipation which guarantees causality and $\epsilon_k = -2J\cos(k)$ the dispersion relation for the lattice model. Thus, in order to evaluate Eq. (3.44), we need to compute the retarded Green's function of the homogeneous system G_{0j} in a real-space representation, where we focus on the case of infinitely many lattice sites, $L \to \infty$, and periodic boundary conditions. To this end, we express the Green's function of the homogeneous system

[2] Additionally, the conditions $2|\tau|^2 + |\rho|^2 = 1$ and $r^*\tau + t^*\tau + \tau^*\rho = 0$ including reflection in the loss channel are obtained.

as

$$G_{0i-j,\omega} = \lim_{\delta\to 0^+} \mathrm{I}(\omega + i\delta, i-j), \tag{3.46}$$

where we defined

$$\mathrm{I}(z,j) = \int_{-\pi}^{\pi} \frac{dk}{2\pi} \frac{\mathrm{e}^{ikj}}{z-\epsilon_k}. \tag{3.47}$$

The integral $I(z,j)$ can be mapped to an integration over the unit circle S^1 in the complex plane by the parametrization $u = \mathrm{e}^{ik}$:

$$\mathrm{I}(z,j) = \oint_{S^1} \frac{du}{2\pi i} \frac{u^{|j|}}{u^2 + zu + 1} = \oint_{S^1} \frac{du}{2\pi i} \frac{u^{|j|}}{(u-u_+)(u-u_-)}, \tag{3.48}$$

with $u_\pm$ the roots of the denominator:

$$u_\pm(z) = -\frac{z}{2} \pm i\sqrt{1-\frac{z^2}{4}}. \tag{3.49}$$

For all z with $\mathrm{Re}\, z > 0$, we find that u_+ lies inside the unit circle and u_- outside. With the use of the residue theorem we can perform the integration and obtain

$$\mathrm{I}(z,j) = \frac{u_+^{|j|}}{u_+ - u_-}, \qquad \text{for Re } z > 0. \tag{3.50}$$

With this solution at hand, we obtain from Eq. (3.46) the retarded Green's function of the homogeneous system:

$$G_{0i-j,\omega} = \frac{\left(-\frac{\omega}{2J} + i\sqrt{1-\frac{\omega^2}{4J^2}}\right)^{|i-j|}}{2Ji\sqrt{1-\frac{\omega^2}{4J^2}}}. \tag{3.51}$$

From Eq. (3.44), we obtain by using Eq. (3.51) the retarded Green's function $G_{i,j}(\omega)$:

$$G_{i,j}(\omega) = \frac{1}{i\sqrt{4-\frac{\omega^2}{J^2}}} \left[\mathrm{e}^{if(\omega)|i-j|} + r(\omega)\mathrm{e}^{if(\omega)(|i|-|j|)}\right], \tag{3.52}$$

where

$$f(\omega) = -i\ln\left(-\frac{\omega}{2J} + i\sqrt{1-\frac{\omega^2}{4J^2}}\right), \tag{3.53}$$

and

$$r(\omega) = -\frac{\gamma}{v(\omega)+\gamma}, \tag{3.54}$$

with the group velocity $v(\omega) = J\sqrt{4-\omega^2/J^2}$. In a mixed real-space and momentum representation, we obtain

$$G_j(k,\omega) = G_0(k,\omega)\left[\mathrm{e}^{ikj} + r(\omega)\mathrm{e}^{if(\omega)|j|}\right]. \tag{3.55}$$

As discussed in Sec. 3.3.1, we can use the mixed representation to quantify the response to a plane wave perturbation with frequency $\omega = \epsilon_k$. In this case, we obtain the concise expression $f(\omega) = |k|$, in analogy to Eq. (3.24). Exactly as for the continuum model, the Green's function (3.52) exhibits the structure of a scattering problem and we can identify $r_k = r(\omega = \epsilon_k)$ (3.54) and $t_k = 1 + r_k$ as the reflection and transmission amplitudes. The similar

form of the lattice Green's function and scattering coefficients in comparison to the continuum case allows one to adapt the results of Sec. 3 straightforwardly by replacing the dispersion relation (and consequently the group velocity) with the one of the lattice model and integrals with their lattice counterparts.

In contrast to the continuum system, the non-monotonic dependence of the lattice group velocity as a function of k results in perfect reflection for modes at the upper band edge ($k = \pi$), which is accompanied by vanishing η_k and t_k, as seen in Fig. 3.5 (right panel).

3.4. Density profile

We now turn to the study of observables. The density profile in the stationary state is defined as $n(x) = C(x, x, t, t)$ (note that the time dependence drops out due to the time-translational invariance), and using Eq. (3.32) it reads

$$n(x) = \int_k \left[1 + r_k^2 + r_k + r_k \cos(2k|x|)\right] n_{0,k} \equiv n_{\mathrm{bg}} + \delta n(x). \tag{3.56}$$

The density profile thus consists of a homogeneous background density n_{bg}, corresponding to the mean density in the stationary state, with density modulations $\delta n(x)$.

Assuming the system to be prepared at $T = 0$, so that $n_{0,k} = \theta(k_F^2 - k^2)$, the asymptotic behavior of these modulations for $|x| \gg k_F^{-1}$ can be derived in the following way. The non-translational-invariant term in Eq. (3.56) reads

$$\delta n(x) \equiv \int_0^{k_F} \frac{\mathrm{d}k}{\pi} r_k \cos(2k|x|), \tag{3.57}$$

where we used that r_k is an even function of k. Integrating this expression twice by parts yields:

$$\delta n(x) = r_k \frac{\sin(2k|x|)}{2\pi|x|}\bigg|_0^{k_F} + r_k^{(1)} \frac{\cos(2k|x|)}{\pi(2|x|)^2}\bigg|_0^{k_F} - \int_0^{k_F} \frac{\mathrm{d}k}{\pi} r_k^{(2)} \frac{\cos(2k|x|)}{(2|x|)^2}, \tag{3.58}$$

with $r_k^{(n)} \equiv \mathrm{d}^{(n)} r_k / \mathrm{d}k^{(n)}$. By noting that the derivatives of the reflection coefficient scale as $r_{k_F}^{(n)} \sim k_F^{-n}$ (cf. Eq. (3.35)) we can conclude that further iterations of this procedure only generate terms of at least order $\mathcal{O}(k_F^2 x^2)$. Therefore, in the limit $|x| \gg k_F^{-1}$, we obtain the leading behavior

$$\delta n(x) \simeq r_{k_F} \frac{\sin(2k_F|x|)}{2\pi|x|}. \tag{3.59}$$

As a result, the modulations are identified as Friedel oscillations of the fermionic density, characterized by a period π/k_F and spatial decay of $\sim 1/x$, confirming the numerical results discussed in Sec. 3.2. The background density n_{bg} is readily obtained from the homogeneous part of Eq. (3.56) and can be expressed in terms of η_k in a closed form:

$$n_{\mathrm{bg}} = \int_k \left(1 - \frac{\eta_k}{2}\right) n_{0,k}, \tag{3.60}$$

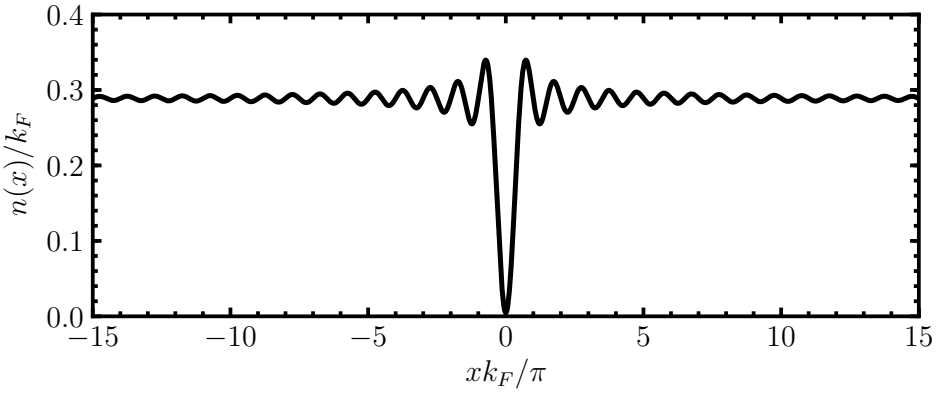

Fig. 3.6. Density profile of the continuum model from the analytical solution (3.56) exhibiting Friedel oscillations around the constant background density, centered at the loss site, for $\gamma/v_F = 4$.

where we identified $\eta_k = -2r_k(1 + r_k)$ (3.41). The density profile entailed in Eq. (3.56) is depicted in Fig. 3.6, revealing that the periodicity of the Friedel oscillations (3.59) of π/k_F is observed even at a short distance from the loss site.

In addition, the expression for the density at the impurity site $n_{\text{imp}} = n(x = 0)$ can be derived from Eq. (3.56) and reads

$$n_{\text{imp}} = \frac{1}{2\gamma} \int_k |v_k| \, \eta_k n_{0,k}. \tag{3.61}$$

The values of n_{bg} and n_{imp} for $T = 0$ can be found analytically and are shown in Fig. 3.7 (left panel) as functions of the dissipation strength γ. The background density n_{bg} exhibits a non-monotonic behavior representing a manifestation of the quantum Zeno effect. On the other hand, the density n_{imp} exhibits a monotonically decreasing behavior, as the loss site remains directly affected by the dissipation for any value of γ.

For the case of the continuum model, we can perform the integrations in Eqs. (3.60) and (3.61) explicitly and obtain by using the identities (A.1) and (A.2):

$$n_{\text{imp}} = \frac{k_F}{\pi} \left[1 + \frac{\gamma/v_F}{1 + \gamma/v_F} - \frac{2\gamma}{v_F} \log\left(1 + \frac{v_F}{\gamma} \right) \right], \tag{3.62}$$

$$n_{\text{bg}} = \frac{k_F}{\pi} \left[1 - \frac{\gamma}{v_F} \left(\log\left(1 + \frac{v_F}{\gamma} \right) - \frac{1}{1 + \gamma/v_F} \right) \right]. \tag{3.63}$$

3.5. Loss rate and currents

The total particle loss rate $|\mathrm{d}N/\mathrm{d}t|$ is determined by the density at the loss site n_{imp} via the equation

$$\frac{\mathrm{d}N}{\mathrm{d}t} = -2\gamma n_{\text{imp}}, \tag{3.64}$$

which can be readily obtained by calculating the equation of motion for the average number of particles $N = \langle \hat{N} \rangle$ from Eq. (3.6). Its analytical expression in the non-equilibrium steady state

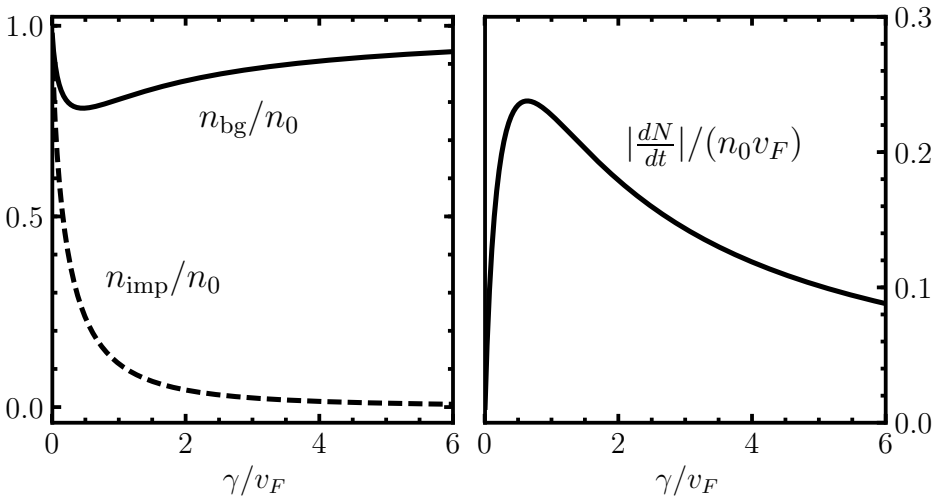

Fig. 3.7. Left panel: Background density n_{bg} (solid) and density at the loss site n_{imp} (dashed) in the second temporal regime as a function of the dissipation strength γ in the continuum model. Right panel: Particle loss rate $|dN/dt|$ in the second regime as a function of the dissipation strength γ in the continuum model.

can be directly inferred from n_{imp} (3.61). The particle loss rate as a function of γ is depicted in Fig. 3.7 (right panel) and exhibits a non-monotonic dependence, reflecting the typical behavior of the loss rate due to the quantum Zeno effect [40]: for small dissipation strength γ compared to v_F, the loss rate increases as $\sim \gamma$, while at large γ it is found to decrease as $\sim \gamma^{-1}$. The non-monotonic dependence of the loss rate on the dissipation strength γ can be interpreted as an incarnation of the quantum Zeno effect [40, 67, 68] since one can understand the localized loss as a continuous measurement of the occupation at the loss site (cf. Sec. 2.2). At large dissipation strength, the loss rate is reduced because n_{imp} decreases as $\sim \gamma^{-2}$, signaling the suppression of the transition of particles from the wire into the loss site.

The stationary regime is further characterized by steady currents which originate at the far ends of the wire and flow towards the loss site (cf. Fig. 1.1). These steady currents are calculated as follows. Starting from the definition

$$j(x) = \frac{1}{2m}(-i)\left\langle \psi(x)^\dagger \partial_x \psi(x) - (\partial_x \psi(x)^\dagger)\psi(x) \right\rangle = \frac{1}{m}\mathrm{Im}\partial_y C(x,y)|_{y=x}, \tag{3.65}$$

we evaluate this expression with the use of the two-point correlations $C(x,y) \equiv C(x,y,t,t)$ in the stationary regime which can be obtained from Eq. (3.32):

$$\mathrm{Im}\partial_y C(x,y)|_{y=x} = \mathrm{Im}\partial_y \int_{-k_F}^{k_F} \frac{dq}{2\pi} f^*(\epsilon_q, q, x) f(\epsilon_q, q, y)|_{y=x}. \tag{3.66}$$

We obtain via a straightforward calculation (see App. A.3)

$$\mathrm{Im}\partial_y C(x,y)|_{y=x} = \mathrm{sgn}(x) \int_k k \left[|r_k|^2 + \mathrm{Re}(r_k) \right] n_{0,k}. \tag{3.67}$$

Here, using Eq. (3.35) we can identify $|r_k|^2 + \mathrm{Re}(r_k) = -\frac{\eta_k}{2}$ and obtain

$$j(x) = -\mathrm{sgn}(x)\gamma\, n_{\mathrm{imp}}, \tag{3.68}$$

with n_{imp} given in Eq. (3.61). Note that in the case of a potential barrier (i.e., by replacing $\gamma \to iu, u \in \mathbb{R}$), the expression $|r_k|^2 + \text{Re}(r_k)$ vanishes, consistently with the fact that no currents are expected for a coherent impurity. The sign function entails that the currents are flowing towards the loss site, as expected (we chose, as a convention, $j(x) > 0$ corresponding to a current flowing to the right). Notice that Eq. (3.64) can also be straightforwardly derived by integrating the continuity equation

$$\frac{\partial n(x,t)}{\partial t} = \partial_x j(x,t) - 2\gamma\, n(x,t)\delta(x), \tag{3.69}$$

in the stationary state. The continuity equation (3.69) can be proven directly by evaluating $\partial n(x,t)/\partial t$ from the adjoint master equation (3.6).

The loss rate $\mathrm{d}N/\mathrm{d}t$ exhibits a characteristic maximum separating the increasing regime for small γ from the decreasing "Zeno regime" for large γ. The dissipation strength γ/v_F at which this maximum occurs takes on a universal value in the case of the continuum model. For the lattice model, it depends additionally on the filling factor ν. With the explicit expression of the loss rate for the continuum model obtained from Eqs. (3.62) and (3.64), one can find the position of the maximum γ/v_F from the condition ($\mathrm{d}N/\mathrm{d}t \equiv \dot{N}$)

$$d\dot{N}/d(\gamma/v_F) = v_F k_F h(\gamma/v_F) \stackrel{!}{=} 0, \tag{3.70}$$

where we defined

$$h(\gamma/v_F) = -\frac{2}{\pi}\left[\frac{\left(4(\gamma/v_F)^2 + 6\gamma/v_F + 1\right)}{(\gamma/v_F + 1)^2} - 4\gamma/v_F \log\left(\frac{1}{\gamma/v_F} + 1\right)\right]. \tag{3.71}$$

The condition (3.70) hence imposes $h(\gamma/v_F) = 0$ which can be solved numerically yielding $\gamma/v_F \simeq 0.638$, in agreement with the position of the maximum in Fig. 3.7. The generality of this result relies on the structure of Eq. (3.70), as a consequence of the quadratic dispersion relation, imposing a condition only in terms of the dimensionless parameter γ/v_F. This fact could possibly be utilized to calibrate the dissipation strength γ in relation to the experimental control parameter, e.g., the current of the electron beam in Ref. [40].

3.6. Momentum distribution dynamics

In the presence of a localized loss, particles which scatter against the impurity can either remain in the wire or get lost. Consequently, one expects the momentum distribution of particles in the wire to bear a characteristic signature of the losses. In this section, we analyze the dynamics of the momentum distribution and show that it is closely related to the loss probability η_k defined in Eq. (3.36). Since the momentum distribution is experimentally accessible, e.g., in time-of-flight measurements with cold atoms, it provides a direct way of measuring η_k. Remarkably, the momentum distribution is found to deplete for all momenta while preserving the discontinuity of the initial zero-temperature Fermi distribution at the *initial* k_F, separating occupied from unoccupied states.

In the following, we will focus on two different momentum distributions: the distribution $n_k(t)$ for a finite size L of the system and evaluated at a finite time t elapsed from the quench, and

the one for the NESS discussed in Sec. 3, which we dub $n_{\text{ness}}(k)$. In particular, $n_k(t)$ describes the momentum distribution of the *entire* system, including the regions outside the light cone (see Sec. 3.2) and therefore dynamical effects. In contrast, $n_{\text{ness}}(k)$ describes the momentum distribution only in the region inside the light cone. These two different cases do not simply coincide in the $L, t \to \infty$ limit as a consequence of the limiting procedure (cf. discussion in Sec. 3.3.2), but they effectively correspond to two different physical quantities.

In this section, we drive analytical expressions for the considered momentum distribution in the thermodynamic limit. We then benchmark the analytical results numerically by taking the Fourier form of the correlations in Eq. (3.9) which allows us to monitor exactly the depletion of the momentum distribution of a finite-size wire.

3.6.1. Analytical derivation

In this section, we analytically derive the stationary momentum distribution of an infinitely long wire at large times. The momentum distribution $n_k(t)$ can be evaluated from

$$n_k(t) = \frac{2\pi}{L}\langle \psi^\dagger(k,t)\psi(k,t)\rangle, \tag{3.72}$$

with $\psi^\dagger(k)$ and $\psi(k)$ the fermionic creation and annihilation operators for a particle with momentum k and L the volume of the system. We aim to compute $n_k(t)$ in the second temporal regime at large times and system sizes. Again, particular care must be taken to the applied limiting scheme: In a real-space representation, considered in Sec. 3.3.2, the order of the space and time limits, first, $L \to \infty$ and, second, $t \to \infty$, leads to a well-defined description since, first, at finite times the system establishes a local NESS which then, second, is extended to infinity. Contrary, in a momentum-space representation, the depletion takes place globally at all momenta. In order to perform the limits it is then convenient to specify the aspect ratio $v_a = L/t$ between space and time, such that $v_a \leq v$ with v the light-cone velocity in order to remain in the second temporal regime, i.e., $t \leq t_{II}$.

To make progress, we express Eq. (3.72) as the propagation of the initial distribution by taking the Fourier transform of Eq. (3.28)

$$\langle \psi^\dagger(k,t)\psi(k,t)\rangle = \int_q G^*(k,-q,t-t_0)G(k,-q,t-t_0)n_{0,q}, \tag{3.73}$$

with $n_{0,q}$ the initial Fermi distribution before switching on the localized loss at time t_0 and $G(k,q,t)$ the Fourier transform of the retarded Green's function (3.21). Alternatively, one could obtain the momentum distribution in the NESS by taking the Fourier transform of Eq. (3.32). The momentum distribution is then obtained from

$$\begin{aligned}\langle \psi^\dagger(k,t)\psi(k,t)\rangle = \int_q n_{0,q}\Big\{ &|G_0(k,t-t_0)|^2(2\pi)^2\delta^2(k+q) \\ &+ 2\pi\delta(k+q)2\text{Re}\left[G_0^*(k,t-t_0)\widetilde{G}(k,-q,t-t_0)\right] + |\widetilde{G}(k,-q,t-t_0)|^2\Big\},\end{aligned} \tag{3.74}$$

where

$$\widetilde{G}(k,k',\omega) = \widetilde{r}(\omega)G_0(k,\omega)G_0(k',\omega), \tag{3.75}$$

with $\widetilde{r}(\omega) = i|v(\omega)|r(\omega)$ and $r(\omega)$ given in Eq. (3.23), $v(\omega)$ the group velocity, and $G_0(k,\omega)$ the Fourier transform of Eq. (3.19). One can evaluate Eq. (3.74) in the stationary limit $t_0 \to -\infty$ analogously to the computation of the correlation functions in Sec. 3.3.2 using identity (3.31), yielding

$$\int_q |G_0(k, t-t_0)|^2 (2\pi)^2 \delta^2(k+q) n_{0,q} = 2\pi\delta(k=0) n_{0,k}, \tag{3.76a}$$

$$\int_q 2\pi\delta(k+q) 2\mathrm{Re}\left[G_0^*(k,t-t_0)\widetilde{G}(k,-q,t-t_0)\right] n_{0,q} = 2\pi\delta(\omega=0) 2|v_k| r_k n_{0,k}, \tag{3.76b}$$

$$\int_q |\widetilde{G}(k,-q,t-t_0)|^2 n_{0,q} = 2\pi\delta(\omega=0) 2|v_k| r_k^2 n_{0,k}. \tag{3.76c}$$

Collecting these results, we obtain from Eq. (3.74)

$$\langle \psi^\dagger(k,t)\psi(k,t)\rangle = 2\pi n_{0,k}\left[\delta(k=0) + \delta(\omega=0)|v_k|\, 2(r_k + r_k^2)\right]. \tag{3.77}$$

Here, we can identify the loss probability η_k (3.41) and write $\delta(x=0) \equiv \delta(0)$ to keep track of the physical dimension of the argument. The delta functions evaluated at zero account for a factor diverging as the system size in the definition of the momentum distribution (3.72). This fact can be made clear by noting $\delta(\omega) \simeq \frac{1}{2\pi}\int_{t_0}^{t} \mathrm{e}^{i\omega t'}\mathrm{d}t'$, valid in the limit $t_0 \to -\infty$ while keeping the aspect ratio between space and time constant, i.e., $t - t_0 = L/v_a$ (cf. discussion above), yields $\delta(\omega=0) = L/v_a$. Analogously, we obtain $\delta(k=0) = L/2\pi$ and find the momentum distribution

$$n(k) = n_0(k)\left[1 - \frac{|v_k|}{v_a}\eta_k\right], \tag{3.78}$$

where the parameter v_a with the dimension of a velocity remains to be specified. This fact can be actually leveraged to capture either the momentum distribution in the NESS or a finite-sized system at time t, as discussed in the following. In order to eliminate any doubt possibly originating from the transformations with divergent factors, we carefully benchmark the obtained result in Secs. 3.6.2 and 3.6.3, confirming it captures precisely the momentum distribution dynamics of the wire.

3.6.2. Momentum distribution for finite L and t

We now consider the momentum distribution $n_k(t)$ of a finite-sized system within the second temporal regime. From Eq. (3.78) we obtain

$$n_k(t) = n_{0,k}\left[1 - \frac{|v_k|t}{L}\eta_k\right], \tag{3.79}$$

where we identified $v_a = t/L$. Equation (3.79) is valid up to order $\mathcal{O}(L^{-1})$ and in the second temporal regime, i.e., for $t < t_{\mathrm{II}}$ (cf. Sec. 3.2). Hence, for all time it holds $|v_k|t/L < 1$, ensuring a positive distribution. The linear depletion in time of the modes described by Eq. (3.79) has a transparent physical interpretation. The density of particles lost, $n_{0,k} - n_k(t)$, is proportional to three factors: the original number of particles $n_{0,k}$, the fraction of particles which have reached the impurity at a given time $|v_k|t/L$, and the loss probability η_k. As a consistency check, we notice that Eq. (3.79) renders, after integrating over all momenta k, the expected result for the

total number of particles, i.e., $N(t) = N(0) + (\mathrm{d}N/\mathrm{d}t)t$, with

$$\frac{\mathrm{d}N}{\mathrm{d}t} = -\int_k |v_k|\, \eta_k n_{0,k}, \tag{3.80}$$

in agreement with $\mathrm{d}N/\mathrm{d}t$ obtained from Eqs. (3.61) and (3.64). Equation (3.80) then illustrates how each mode contributes to the depletion of the system. Particles initially present in the system (or incoming from a reservoir) with a distribution $n_{0,k}$ impinge on the loss barrier with a velocity v_k and are lost from the system with a probability η_k. We note in passing that Eq. (3.80) takes on the form of a Landauer formula for the loss current [4, 43, 44].

From Eq. (3.79) it becomes evident that, in the case of a $T = 0$ initial state, the discontinuity of the distribution at the initial Fermi surface persists at finite times at the same value of k_F. The presence of this discontinuity thus rationalizes the emergence of π/k_F-periodic Friedel oscillations in the density profile (cf. Eq. (3.59) and Sec. 3.2). Further, Eq. (3.79) established a useful relation to probe the loss probability η_k.

Equation (3.79) can be adapted straightforwardly for the lattice model by using the appropriate v_k and η_k. This allows us to further benchmark Eq. (3.79) with the full numerical solution for the lattice model (3.4) and to explore finite-size deviations. The comparison to the numerical simulations for a system prepared at $T = 0$ is shown in Fig. 3.8 (upper panel), indicating the depletion of $n_k(t)$ with a constant rate in the presence of a localized loss (solid lines). A very good agreement with Eq. (3.79) (dashed lines) is found, except for small discrepancies at $k \approx 0$ and $k \approx \pm k_F$, due to finite-size effects.

In order to quantify these finite-size effects, we considered the same momentum distribution for different system sizes; in each case we rescale the time elapsed from the quench as $t = L/2v$, with v the light-cone velocity, corresponding to the end of the second regime t_{II}, thus rendering Eq. (3.79) independent of L:

$$n_k(t_{II}) = n_0(k)\left[1 - \frac{v_k}{2v}\eta_k\right]. \tag{3.81}$$

The results are displayed in Fig. 3.8 (lower panel) and reveal that the momentum distribution approaches the value predicted by Eq. (3.79) upon increasing the system size.

3.6.3. Momentum distribution of the non-equilibrium steady state

The momentum distribution of the NESS, $n_{\mathrm{ness}}(k)$, can be computed by taking the Fourier transform of Eq. (3.32) in the limit of $L, t \to \infty$, resulting in

$$n_{\mathrm{ness}}(k) = n_{0,k}\left[1 - \frac{\eta_k}{2}\right]. \tag{3.82}$$

As mentioned above, Eq. (3.82) cannot be simply obtained as a limit of Eq. (3.79): in fact, it describes the momentum distribution *inside* the light cone, where the system reaches a NESS continuously replenished by the currents originating from outside the light cone. Here, we present an alternative derivation based on Eq. (3.78) with the use of the following semiclassical picture. At time t, the density of particles with momentum k and group velocity v_k is depleted within a segment of size $L_k = 2v_k t$, centered at the loss site. Moreover, at later times $t' > t$, the outer regions are constantly refilling particles with momentum k within this segment and

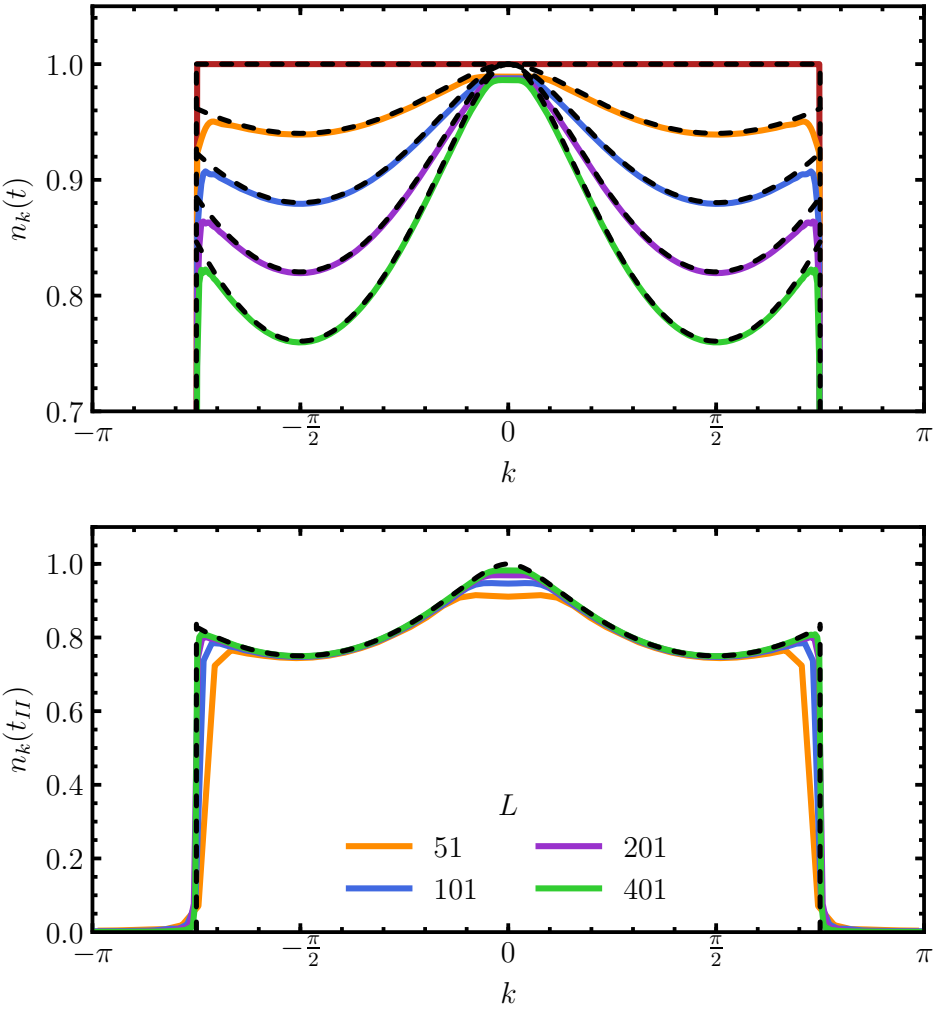

Fig. 3.8. Momentum distribution $n_k(t)$ for the lattice model after the quench with solid lines indicating numerical simulations and dashed lines the analytical results. Upper panel: Momentum distribution in the second regime for different times elapsed from the quench, $tJ = 0, 25, 50, 75, 100$. For all curves $L = 401, \gamma = 3J, N(0)/L = 0.75, T/J = 0$. Lower panel: Momentum distribution at the end of the second regime for different system sizes, for a fixed aspect ratio $t_{\mathrm{II}} = L/(2v)$. For all curves, $\gamma = 2J, N(0)/L = 0.75, T/J = 0$. For $N(0)/L = 0.75$, $v = 2J$.

therefore the occupation in this region cannot drop further. Consequently, the occupation in the NESS of each mode is obtained from Eq. (3.78) by taking $v_a = L_k/t$, yielding Eq. (3.82).

The factor $1/2$ in Eq. (3.82) comes from the fact that only half of the particles within the light cone have scattered off the impurity. This can be understood as follows: particles with momentum $k > 0$, i.e., traveling rightward, are initially uniformly distributed along the wire. When the impurity is switched on, only the fraction of these particles at the left of the impurity will scatter on it within the second regime, while the fraction on its right side will not. Therefore, only half of the particles with momentum $k > 0$ will experience losses. The same argument holds for particles with $k < 0$.

In a finite-size system, Eq. (3.82) is expected to describe the momentum distribution of a segment of the system within the light cone, up to finite-size effects. Experimentally, this quantity could

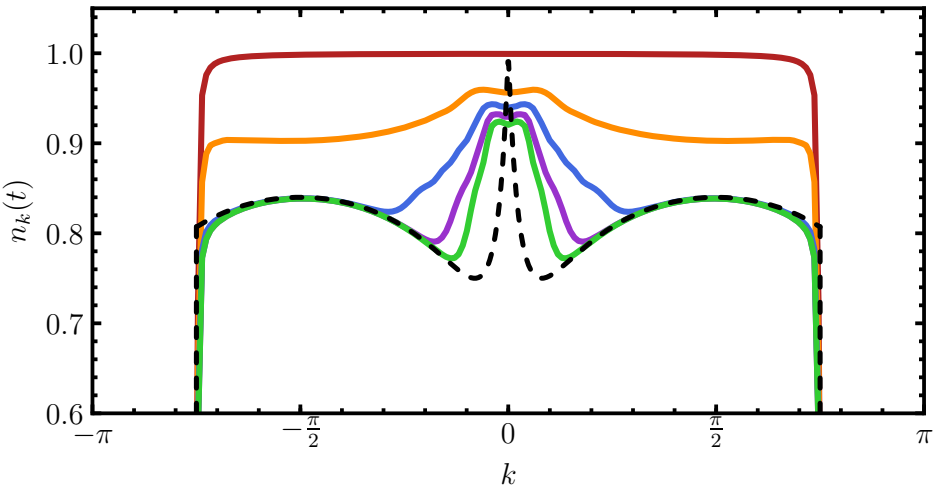

Fig. 3.9. Momentum distribution $n_k(t)$ from the numerical simulations (solid) in the lattice model approaching a stationary value within the spatial segment $j \in [-100, 100]$ of a system with $L = 501$ sites, for different times elapsed from the quench in the second regime, $tJ = 0, 30, 60, 90, 120$. The dashed line, indicating the stationary distribution $n_{\rm ness}(k)$, is approached asymptotically in time. For all curves $\gamma = 0.5J, N(0)/L = 0.75, T/J = 0$.

be obtained in a time-of-flight measurement where the parts of the system not belonging to this segment are shielded from the detectors. We report in Fig. 3.9 (upper panel) the asymptotic approach of $n_k(t)$ to the stationary distribution $n_{\rm ness}(k)$ for a segment of size L_s centered around the loss site, obtained from the numerical simulations of the lattice model (3.4), where $n_k(t)$ is computed from the Fourier transform of the correlations (3.9) restricted to this segment. For the finite times shown, slow modes with $|v_k|t < L_s/2$ have not yet relaxed to their stationary value in the considered segment, while the occupation of sufficiently fast modes approaches accurately the value predicted by Eq. (3.82). The slightly different shapes of the momentum distribution in Fig. 3.8 and Fig. 3.9 can be understood in the following way. In Eq. (3.82), the loss probability η_k of the lattice model is a monotonic function of $|k|$ for $\gamma \geq 2$ while for $\gamma < 2$ it is non-monotonic. In contrast, the product $|v_k|\eta_k$ appearing in Eq. (3.79) is always a monotonic function of $|k|$. Finally, as a consistency check, the comparison of Eq. (3.82) with Eq. (3.60) reveals that the average density of the NESS given by $n_{\rm bg}$ is indeed obtained by summing over the momentum distribution in the NESS $n_{\rm ness}(k)$.

In addition, we consider the momentum distribution of a segment of the system created by an asymmetric shielding, which is shown in Fig. 3.10. More specifically, the momentum distribution is computed from a segment of the wire situated to the right of the impurity, within the light cone. Consequently, particles with $k < 0$ have not scattered against the loss barrier yet and are uniformly distributed. In contrast, all particles with $k > 0$ have been scattered at the loss site and the distribution is described by

$$n_k = \begin{cases} n_{0,k}\,[1 - \eta_k] & \text{for } k > 0, \\ n_{0,k} & \text{for } k < 0. \end{cases} \tag{3.83}$$

Hence, the consideration of an asymmetric shielding is useful to separate the outgoing contributions to n_k, which bear the maximal signature of depletion, from the incoming ones, which are

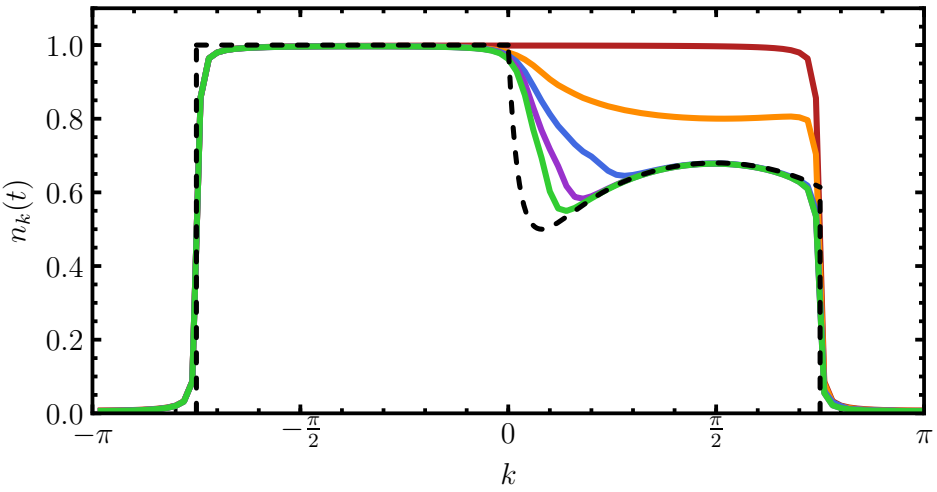

Fig. 3.10. Momentum distribution $n(k)$ from the numerical simulations (solid) in a segment $j \in [0, 100]$ of the system right to the impurity, for different times elapsed from the quench in the second regime, $tJ = 0, 30, 60, 90, 120$. Left movers are uniformly distributed (dashed line for $k < 0$), whereas right moving modes approach a stationary distribution (3.83) (dashed line for $k > 0$). For all curves $\gamma = 0.5$, $L = 501$, $v = 0.75$.

not depleted. We will make use of this construction in Chapter 5 when we consider interaction effects in the momentum distribution of the wire within a Hartree-Fock approximation of the dynamics.

3.7. Finite temperature of the initial state

So far we focused on the analysis of systems prepared at zero temperature before switching on the localized loss. However, the presence of a finite temperature of the initial state is unavoidable in any experimental platform. In fact, the analytical results derived in the previous sections also apply to an initial state characterized by a Fermi distribution $n_{0,k}$ with a finite temperature T. In this section, we consider the effect of a finite-temperature initial state on the dynamics of the momentum distribution and the total particle loss rate. In Sec. 4.4.3, we will further comment on the effect of temperatures in the presence of interactions.

3.7.1. Momentum distribution dynamics

In Fig. 3.11 (lower panel) the evolution of $n_k(t)$ in the presence of a localized loss is shown for a system prepared at a finite temperature T, obtained from the numerical simulations of the lattice model (3.4). The comparison to Eq. (3.79) (dashed lines) with a thermal $n_{0,k}$ indicates a very good agreement with the numerical curves (solid lines). Beside of the smearing effect of temperature, already present in the initial state, the same effect as for $T = 0$ is observed, namely the depletion of the momentum distribution due to the losses. Moreover, because of the smearing, we expect the Friedel oscillations in the density profile to be damped out at distances larger than the thermal wavelength corresponding to the initial temperature.

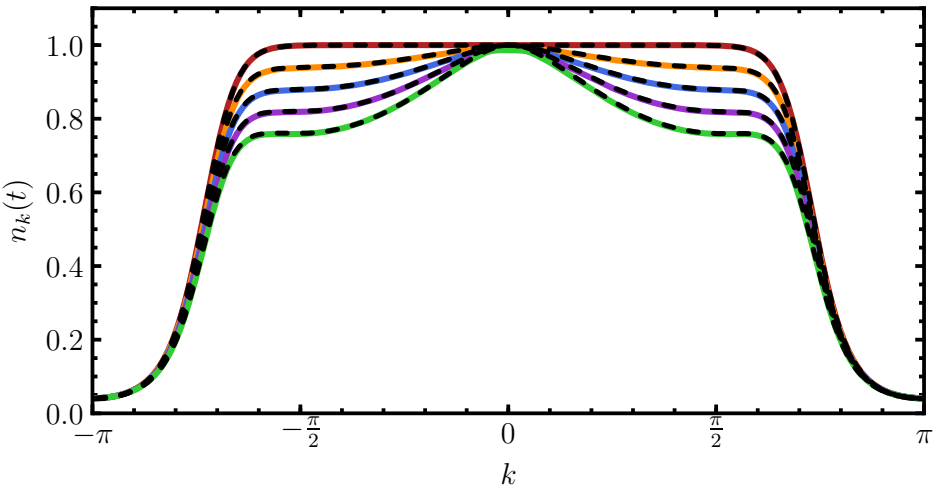

Fig. 3.11. Momentum distribution $n_k(t)$ from the numerical simulations (solid) in the lattice model initialized with a finite temperature $T/J = 0.2$ for different times after the quench in the second regime, $tJ = 0, 25, 50, 75, 100$. The dashed lines indicate analytical results. For all curves $L = 401, \gamma = 3J, N(0)/L = 0.75$.

3.7.2. Loss rate

Further, we investigate how the interplay of temperature and filling of the initial state affects the total particle loss rate $|\mathrm{d}N/\mathrm{d}t|$ in the second regime. In Fig. 3.12 (upper panel) we display $|\mathrm{d}N/\mathrm{d}t|$ as a function of the temperature for different fillings, comparing the loss rates obtained from numerically simulating the lattice model (3.4) (dots) with the analytical expression (3.80) (solid lines), indicating very good agreement. The loss rate exhibits a strong dependence on the initial particle filling. Below half filling, a higher temperature leads to a larger loss rate, while above half filling, a higher temperature leads to a lower loss rate. At half filling and at maximal filling, the loss rate is independent of the temperature. Moreover, for large temperatures T, the loss rate becomes independent of the temperature: in Fig. 3.12 (lower panel) the curves indicating the loss rate rescaled by the initial filling indeed collapse for large T. A simple explanation for this behavior relies on the fact that the particle loss rate increases parametrically with the particle group velocity (cf. Eqs. (3.80) and (3.37)), as faster particles scatter more frequently with the impurity. Since the group velocity on the lattice is non-monotonic in k (i.e., $v_k = 2J \sin k$), thermal fluctuation can increase or decrease the average particle group velocity, depending on the filling. In particular, the average particle velocity increases with the temperature below half filling (as states with higher group velocity are available to populate), while it decreases with the temperature above half filling (as only states with lower group velocity are available). When temperatures are high enough, the average particle velocity saturates to a finite value as every mode is occupied with the same probability, thus leading to a saturation of the particle loss rate as well.

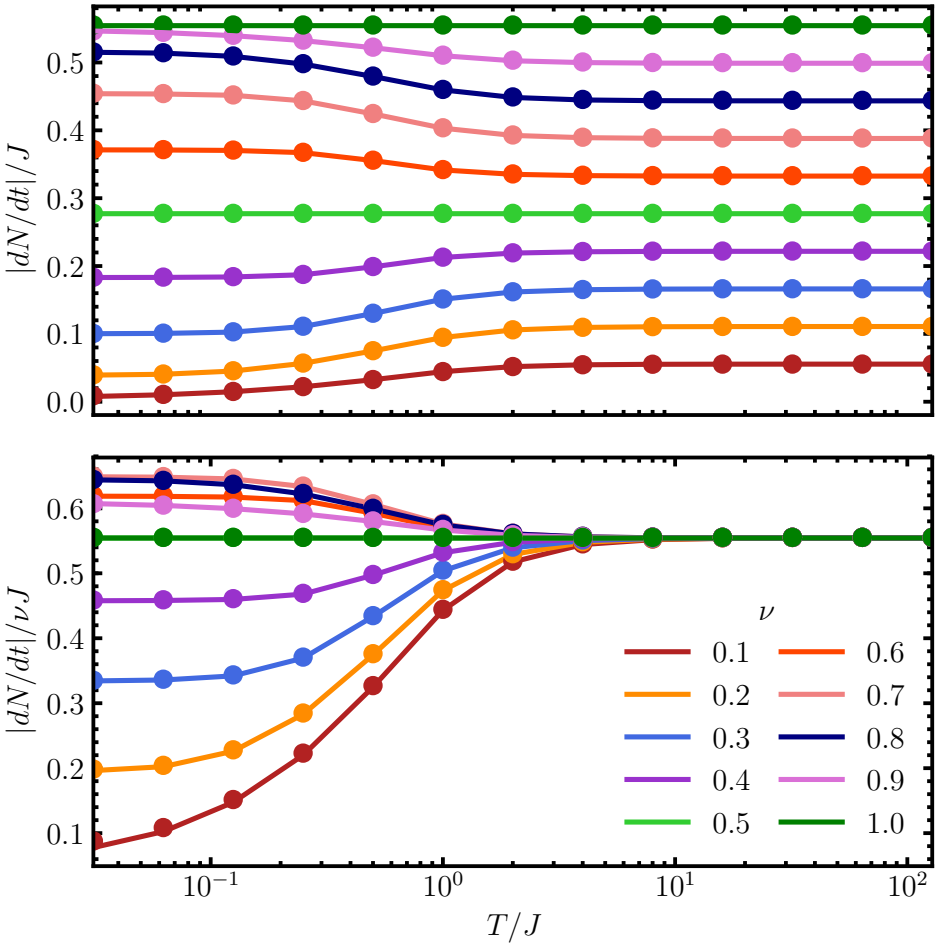

Fig. 3.12. Particle loss rate $|\mathrm{d}N/\mathrm{d}t|$ (upper panel) and rescaled particle loss rate $|\mathrm{d}N/\mathrm{d}t|/\nu$ (lower panel) of the lattice model in the second regime as a function of the temperature T ($k_\mathrm{B} = 1$), for different initial filling factors $\nu = N(0)/L$. Dots indicate the results of numerical simulations, lines the analytical prediction. For all curves $\gamma = 3J$, $L = 101$.

3.8. Third temporal regime and dissipation-free subspace

In experimental realizations eventually the third temporal regime is reached due to the finite size of the system (cf. Sec. 3.2), characterized by the arrival of the light cone at the boundaries of the system thus rendering the boundary conditions important. In this section, we clarify the onset and properties of the third temporal regime and substantiate the universality of the second temporal regime for different geometries of the system where we focus on the lattice model (3.4). Hereby, the geometry is characterized by the boundary conditions, periodic or open, and the number of sites L to be even or odd, the latter determining the existence of a true center site. In the case of open boundary conditions, also the precise position of the loss site is relevant. The study of different geometries is of special importance due to the possible presence of a dissipation-free subspace (cf. Sec. 3.2.2) whose existence is highly geometry-dependent. For this reason, the properties of the third temporal regime are likewise sensitive to the geometry of the system. In contrast, for the second temporal regime, we elaborate that the effects of a dissipation-free subspace are indeed irrelevant. In fact, its presence is found to modify only the asymptotic value of the occupation number $N(t)$ but not the rate with which it is approached

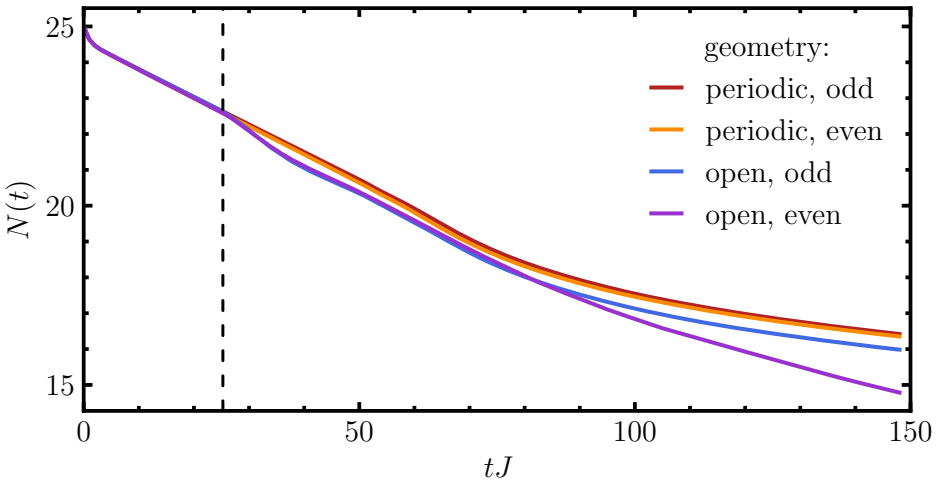

Fig. 3.13. Comparison of the loss rate for different geometries of systems (see main text), with $L = 101$ for an odd and $L = 100$ for an even number sites. For all curves $\gamma = 2, \nu = 0.25$. The dashed vertical line marks the end of the second temporal regime.

in the second temporal regime. In the system under consideration, such a subspace is always present for periodic boundary conditions, whereas for open boundary conditions it depends additionally on the precise position of the impurity with respect to the boundaries.

In Chapter 7 we study the eigenfunctions of the effective Hamiltonian (3.8) and find an incarnation of the dissipation-free subspace in terms of modes [3] with an infinite lifetime.

3.8.1. Loss rate

In Fig. 3.13 the particle number $N(t)$ is depicted for different geometries of the system as a function of time for all three temporal regimes. The vertical dashed line indicates the end of the second temporal regime. Clearly, in the second regime, the particle number decays with a constant loss rate which is independent of the chosen geometry. In contrast, in the third regime, the loss rate is geometry-dependent. Remarkably, for geometries supporting a dissipation-free subspace, the occupation number $N(t)$ approaches asymptotically a finite value, observed in Fig. 3.13 for curves representing periodic boundary conditions and for open ones with an odd number of sites. Therefore, in these cases, the final state is not the vacuum but occupied with a fraction of the initial number of particles corresponding to the fraction of protected modes (cf. Sec. 3.2.2). In Fig. 3.13, this asymptotic occupation number is given by $N(t \to \infty) = 12$, which can be obtained by evaluating Eq. (3.9) for $t \to \infty$, and corresponds to approximately half of the initial particles $N(0) = 25$.

The existence of a dissipation-free subspace has been reported in Ref. [51] for a one-dimensional gas of bosons in presence of a localized loss, where it was shown to be fragile against the geometry of the system as well as interactions. In the presence of interactions, protected modes can be converted into unprotected ones, resulting in an eventual decay towards the vacuum [51].

[3] Not to be confused with the plane wave scattering states labeled by k considered in the present discussion.

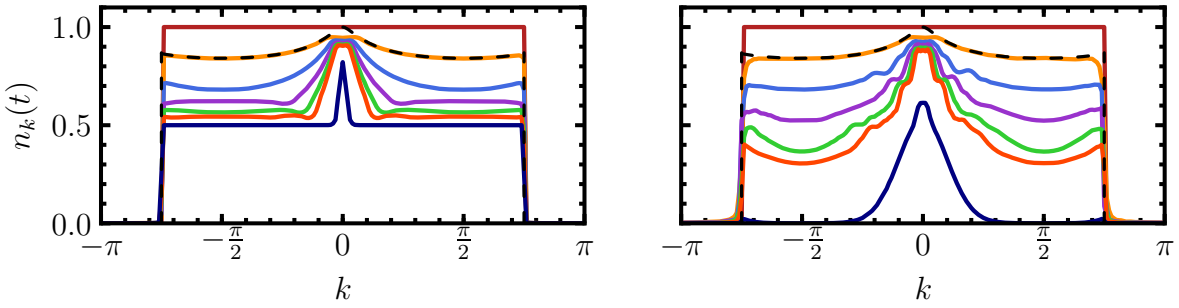

Fig. 3.14. Momentum distribution $n_k(t)$ from the numerical simulations (solid) for different geometries of the system. The distribution is shown for different times after the quench in the second and third temporal regime, $tJ = 0, 50, 100, 150, 200, 250, 2000$. Left Panel: Periodic boundary conditions and odd number of sites, $L = 201$. Right panel: Open boundary conditions and even number of sites, $L = 200$. For all curves $\gamma = 0.5, v = 0.75$. The dashed lines indicate the comparison with the analytical results in the second regime which lasts up to time $t_{II}J = 50$.

3.8.2. Momentum distribution dynamics

In Fig. 3.14 the momentum distribution dynamics in the second and third temporal regime is shown for two different geometries of the system, one supporting a dissipation-free subspace (left panel, periodic boundary conditions) and one without (right panel, open boundary conditions with an odd number of sites). In App. A.4 we present the momentum distribution dynamics for the remaining geometries discussed in the previous Section 3.8.1 (cf. Fig 3.13), which behave similarly to the one in the left panel of Fig. 3.14.

For both geometries realized in Fig. 3.14, the depletion of the momentum distribution $n_k(t)$ in the second temporal regime is described by Eq. (3.79) indicated by the dashed lines. This is consistent, with the geometry-independence of the total particle loss rate in the second regime found in Sec. 3.8.1. In the third regime, the behavior is different for both geometries. In the case where a dissipation-free subspace is present (left panel), the occupation of each mode approaches asymptotically a finite value of $1/2$. In contrast, in the case where a dissipation-free subspace is absent (right panel), each mode asymptotically empties out completely. For the times shown, fast particles (large $|k|$) are already maximally depleted, while slow particles (small $|k|$) are not. As a consequence, a peak in the occupation near $k \sim 0$ is seen in Fig. 3.14 at the largest time shown.

As a final remark, we point out an additional effect observed in the third temporal regime in the density profile for periodic boundary conditions. The exact antipodal point, $j = L/2$, of the loss site depletes below the average value of the density in the remaining system, as shown in Fig. A.3 in the appendix, similar to the drop of the density at the loss site itself.

3.9. Variation of the loss profile

In experiments featuring localized loss, the electron beam used to induce the losses usually exhibits a Gaussian profile [40]. For a continuum system, a delta function is expected to be

a good approximation of the localized loss as long as the width of the latter is smaller than the Fermi wavelength, as experimentally realized in Ref. [43]. Moreover, in experiments with cold atoms on a lattice, localized loss on a single lattice site has been realized [42], where the focused electron beam is actually scanned rapidly over the extension of an effective lattice site. In this thesis, we focus on a loss region with the spatial profile of a delta function which establishes a model of localized loss with minimal intrinsic structure. However, the barrier shape can be generalized to richer structures which introduces additional parameters in the model. As a simple extension, one can consider a finite width of the barrier specified, e.g., by a Gaussian or box profile. Further, asymmetric barrier shapes can lead to asymmetric scattering properties. Even more complicated barrier shapes support effects such as resonant scattering, resulting in non-monotonic scattering amplitudes with a strong momentum dependence at certain resonant values of k [80, 81]. Additionally, the loss barrier can be superimposed with a real-valued potential.

In this section, we briefly discuss some future directions based on the generalization of the barrier shape. The scattering properties of generally shaped barriers have been studied separately in Ref. [138] via the transfer matrix formalism.

3.9.1. Complex-valued delta barrier

The simplest extension of a delta loss barrier can be considered a localized loss superimposed with a localized potential described by the Hamiltonian term $H_{\text{imp}} = \int_x u\delta(x)\psi^\dagger(x)\psi(x)$. In the resulting effective non-Hermitian Hamiltonian (cf. Sec. 3.2.1), this establishes a complex-valued delta barrier with an amplitude $u - i\gamma \equiv g$, where $u \in \mathbb{R}$ and $\gamma > 0$. [4] Following the lines of Sec. 3.3, one obtains straightforwardly the scattering amplitudes

$$r_k = \frac{-ig}{|v_k| + ig}, \qquad t_k = 1 + r_k, \tag{3.84}$$

and the loss probability

$$\eta_k = \frac{2\gamma|v_k|}{(|v_k| + \gamma)^2 + u^2}. \tag{3.85}$$

Remarkably, the presence of a potential with an amplitude u suppresses losses regardless of the sign of u.

3.9.2. Asymmetric loss profiles

Non-reciprocal effects in non-Hermitian system have been in the focus of recent studies [20, 21], motivating the consideration of asymmetric loss profiles. As an example of an asymmetric loss barrier, we consider two delta impurities in a lattice model situated at sites $j = \pm a$. This setup can be modeled by a quantum Master equation (3.4) with $\Gamma_j = \gamma_L\delta_{j,-a} + \gamma_R\delta_{j,a}$.

The description of the time evolution of the correlation matrix C_{ij} derived in Sec. 3.2.1 can be readily adapted to include generalized barrier shapes which results in a complex-valued

[4] $\gamma < 0$ cannot be achieved for fermions even including gain, as can be readily checked from the corresponding quantum master equation. However, it is in principle accessible for bosons, where additionally the stability of the pumped system can be ensured, e.g., by adding homogeneous losses, cf. Sec. 7.3.2.

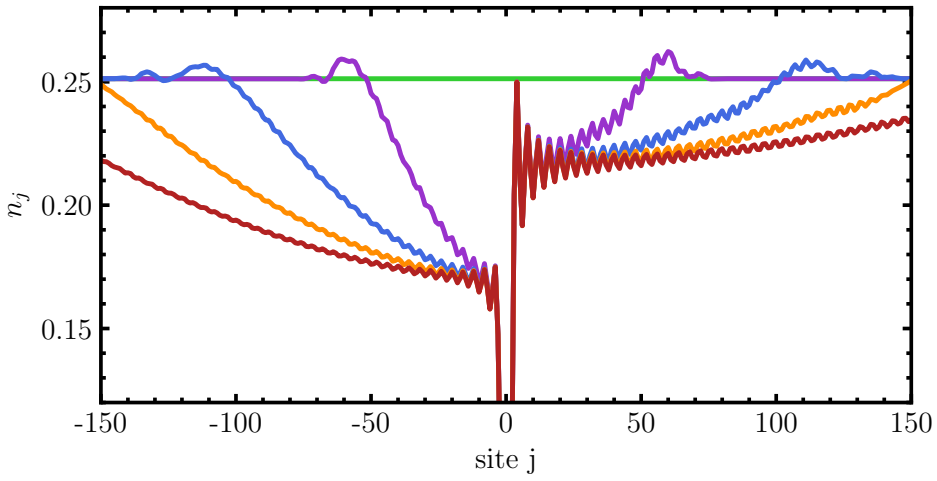

Fig. 3.15. Density profile in the vicinity of an asymmetric double impurity, specified by $\gamma_L = J$ at $j = -1$ and $\gamma_R = 4J$ at $j = 1$, at different times in the second regime, $tJ = 0, 35, 70, 105, 140$. For all curves $\nu = 0.25$, $L = 601$.

scattering potential in the effective non-Hermitian Hamiltonian (3.8). From this we numerically evaluate the density profile of an asymmetric double loss impurity which we report in Fig. 3.15. A NESS is approached characterized by a background density asymmetric in the regions left and right of the impurity. This fact reflects that the loss probability for a particle impinging from the left, η_k, is different from the respective loss probability experienced from the right, η'_k. For an asymmetric scatterer, generally $r_k \neq r'_k$ and $t_k = t'_k$ [136] and we define $\eta'_k = 1 - |t'_k| - |r'_k|$. The background density is then described by the corresponding generalization of Eq. (3.60), i.e., with η_k replaced by η'_k for the density to the right of the impurity. As a result, the value of the mean density jumps at the loss site possibly giving rise to additional effects in the presence of interaction.

Further, the density profile exhibits Friedel oscillations (see Fig. 3.15) whose amplitude is different on both sides of the loss and described by $|r_{k_F}|$ to the left and $|r'_{k_F}|$ to the right of the impurity, as a generalization of Eq. (3.59) [86].

Beyond the asymmetric scattering properties, the double barrier profile leads to resonant tunneling effects resulting in a rapid variation of η_k, η'_k as a function of k. This effect can be clearly observed in the momentum distribution (cf. Sec. 3.6) in presence of a double-delta-shaped loss depicted in Fig. 3.16 in form of complexly shaped depletion of the distribution, reflecting resonances of η_k. Further, due to the asymmetric loss probabilities, $\eta_{k<0} \neq \eta_{k>0}$, positive and negative momenta deplete differently. Figure 3.16 illustrates how a localized loss can be used to engineer a non-equilibrium momentum distribution [66]. Resonant tunneling effects for dissipative barriers are studied in more detail in a separate work in Ref. [137].

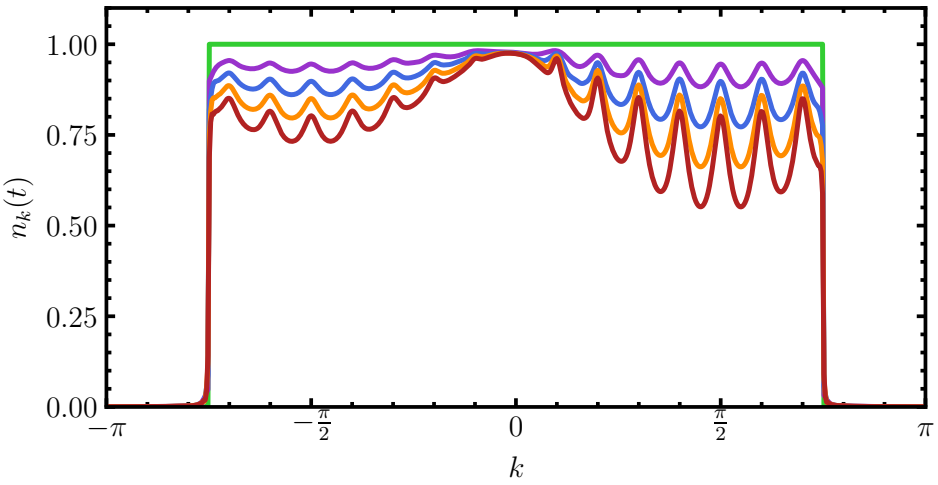

Fig. 3.16. Momentum distribution in the wire for an asymmetric double impurity, specified by $\gamma_1 = J$ at $j_1 = -5$ and $\gamma_2 = 4J$ at $j_2 = 5$, at different times in the second regime, $tJ = 0, 35, 70, 105, 140$. For all curves $\nu = 0.75$, $L = 601$.

3.10. Conclusion and outlook

In summary, we formulated the model of a fermionic quantum wire subject to localized losses in terms of a Lindblad master equation. Based on both an analytical and numerical approach, we provided a systematic analysis of the dynamics after a quench of the localized loss in systems prepared in a thermal state. Crucially, the dynamics can be characterized in terms of three temporal regimes, of which the second one constitutes a NESS for a duration extensive in the system size, which was therefore identified as the relevant dynamical regime. An exact solution of the correlation properties in the NESS was derived analytically, yielding an instructive description of the depletion dynamics considering several observables in terms of the loss probability η_k. The momentum distribution $n_k(t)$ was shown to reflect directly the properties of the loss probability η_k and hence proves as a convenient observable to study depletion processes in a momentum-resolved way. Remarkably, the coherence properties of the initial equilibrium state are not completely lost after the system is driven out of equilibrium by the localized loss but the momentum distribution preserves a discontinuity at the initial Fermi momentum. As a result, the density profile in the NESS supports algebraically decaying Friedel oscillations in the vicinity of the loss site.

Friedel oscillations are known to give rise to strong effects in the presence of interactions: they constitute an effective barrier strongly affecting the scattering probabilities of a barrier [85, 86]. Hence, the presence of a stationary regime supporting Friedel oscillations calls for a study of the scattering and loss probabilities in the presence of interactions, which is performed in the subsequent Chapter 4. The properties of the NESS are also relevant for the construction of an effective description which will be performed in terms of a Luttinger liquid approach in Chapter 6. In Chapter 5, the characterization of the time evolution by three temporal regimes including the NESS, developed here in the non-interacting limit, is further strengthened by a study of the dynamics incorporating interactions within a Hartree-Fock approximation. Moreover, the non-Hermitian effective Hamiltonian is itself an interesting object of study as it supports an exceptional point, which is investigated in Chapter 7.

The methods developed in this Chapter are easily generalized to non-Hermitian scattering potentials with a richer internal structure, as outlined in Sec. 3.9, thus calling for further studies, e.g., aiming for non-Hermitian effects such as non-reciprocity [20, 21], the control and engineering of states [66] or the generalization to time-dependent loss impurities [139]. A preliminary study on time-dependent loss impurities is reported in Appendix E.

CHAPTER 4

REAL-SPACE RENORMALIZATION GROUP APPROACH

A peculiarity of impurities in one-dimensional fermionic systems is the emergence of slowly decaying Friedel oscillations [89]. In the presence of interactions, the Friedel oscillations provide an additional effective scattering potential for particles impinging on the loss site. In the case of a coherent potential barrier, it has been shown that the scattering properties of the emerging effective barrier are dramatically altered [81, 85, 86]. We now consider the interplay between interparticle interactions in the wire and the presence of a localized loss using a microscopic approach. To this end, we include short-range interactions in the model introduced in the previous chapter. The subsequent analysis is built on the description of the dynamics in the non-interacting system presented in Chapter 3. In particular, we will focus on interaction effects in the NESS for an infinitely long wire (see Sec. 3.2).

In Chapter 3, we investigated the dynamics after switching on a localized loss and identified a NESS in which the loss barrier induces Friedel oscillations in its vicinity. By making use of the properties of the NESS, we describe the effects of the interaction in terms of a renormalization of the scattering probabilities (cf. Sec. 3.3.3). The analysis is based on the real-space renormalization group (RG) approach initially developed for a coherent impurity at equilibrium [85, 86]. This approach is perturbative in the microscopic interaction strength V, and valid for arbitrary dissipation strengths γ. For the case of a loss barrier, the open nature of the system gives rise to new phenomena as the renormalization of loss processes. Due to its prominent role in the present analysis, we focus especially on the renormalization of the loss probability η_k, which is found to vanish for modes near the initial Fermi momentum, for both repulsive and attractive interactions. Moreover, transmission and reflection probabilities near the Fermi level are strongly modified, leading to perfect reflection for repulsive interactions, and perfect transmission for attractive interactions, in analogy to the case of a coherent barrier. The scaling behavior of the RG flow near the stable fixed point for attractive interactions exhibits a novel behavior compared to the equilibrium counterpart. We then work out the observability of the renormalized loss probability in energy-resolved observables such as the momentum-resolved loss rate and the momentum distribution of particles in the system. We conclude this chapter with an outlook on the effects of generalized loss profiles on the RG flow, as well as a discussion of the functional renormalization group (FRG) and its applications to coherent and dissipative impurity problems.

The main results of this chapter have been published in publications [133] and [134]. In this chapter, we provide a more detailed discussion and derivation of the results and point out forward directions.[1]

4.1. Microscopic interacting model

The non-interacting model defined in Sec. 3.1 can be straightforwardly generalized to include interparticle interactions. As before, we consider spinless fermions with mass m moving in a wire of length L, but particles now interact via a short-range potential $V(x)$, either repulsively or attractively. The system is thus described by the Hamiltonian

$$H = -\int_x \psi^\dagger(x)\frac{\partial_x^2}{2m}\psi(x) + \int_{x,y} V(x-y)n(x)n(y), \tag{4.1}$$

with $\psi^\dagger, \psi$ fermionic creation and annihilation operators, $n = \psi^\dagger\psi$ the density operator, and $\int_x = \int_{-L/2}^{L/2} \mathrm{d}x$. The dynamics of the full model is then described by the quantum master equation (3.2), whose dissipator incorporates localized losses, with the use of the interacting Hamiltonian (4.1). Moreover, the dynamics of the corresponding lattice model for the wire is generated by the interacting Hamiltonian

$$H = -J\sum_j \left(\psi_{j+1}^\dagger\psi_j + \text{h.c.}\right) + U\sum_j n_j n_{j+1}, \tag{4.2}$$

with $\psi_j, \psi_j^\dagger$ the fermionic annihilation and creation operators on site j, and $\sum_j = \sum_{j=j_{\min}}^{j_{\max}}$. We recall, the summation index runs from $j_{\min} = \lfloor -(L-1)/2 \rfloor$ to $j_{\max} = \lfloor (L-1)/2 \rfloor$, with $\lfloor x \rfloor$ the floor function, and periodic boundary conditions are assumed, i.e., $\psi_{j_{\max}+1} = \psi_{j_{\min}}$ and $\psi^\dagger{}_{j_{\max}+1} = \psi^\dagger{}_{j_{\min}}$. Accordingly, the time-evolution of the lattice model in presence of a localized loss is characterized by the quantum master equation (3.4) using the interacting Hamiltonian (4.2).

4.2. Formulation of the RG scheme

The formulation of the non-Hermitian scattering problem associated with the localized loss (see Sec. 3.3.3) proved to be valuable in characterizing the dynamics and depletion properties of the system. It also provides a convenient starting point for studying interaction effects as discussed in the following. To this end, we first derive the perturbative corrections to the scattering amplitudes t_k, r_k due to the interaction strength V for the continuum model (4.1), in analogy to the analysis of the potential barrier problem [85, 86]. These corrections will then be effectively resummed yielding RG flow equations for the scattering probabilities defined in Sec. 3.3.3.

The microscopic character of the approach allows for a transparent physical picture of these renormalization effects, which can be understood in terms of repeated virtual scattering processes between the bare loss barrier and an effective one created by the Friedel oscillations in the presence of interactions [85, 86]. Hereby, the scattering at the effective potential created by the

[1] Several sections contain paragraphs and sentences that appear verbatim in publication [134].

Friedel oscillations depends sensitively on the momentum k of the incoming particle. For k close to the initial Fermi momentum k_F, the perturbative corrections to the scattering amplitudes are found to diverge logarithmically. The momentum dependence $k \sim k_F$ is a consequence of the periodicity of the Friedel oscillations, determined by the initial Fermi momentum k_F. In turn, the logarithmic divergence originates from the slow spatial decay $\sim 1/x$ of the oscillation amplitude. The divergent corrections can then be resummed using a real-space RG scheme where the individual RG steps correspond to a gradual increase of the effective scattering region. This procedure yields a description of the effective scattering amplitudes in terms of RG flow equations, where we focus particularly on the loss probability η_k.

4.2.1. Perturbative corrections

The scattering problem constituted by the loss barrier can be conveniently formulated in terms of the retarded Green's function (cf. Sec. 3.3.2). We consider a plane wave with momentum $k > 0$ incoming from the left and $k \sim k_F$ close to the Fermi momentum. We recall that the scattering amplitudes can be defined (cf. Sec. 3.3.3) by the asymptotic form of $G(x, k, \omega)$ (3.24):

$$G(x, k, \omega \simeq \epsilon_k) = G_0(\epsilon_k, k) \times \begin{cases} \mathrm{e}^{ikx} + r_k \mathrm{e}^{-ikx}, & x < 0, \\ t_k \mathrm{e}^{ikx}, & x > 0. \end{cases} \tag{4.3}$$

To this end, we consider corrections δG to the retarded Green's function, $G + \delta G$, where G denotes the Green's function (3.24) in the presence of the localized loss but without interactions, i.e., $V = 0$. The perturbative corrections can then be obtained within a first-order Born approximation according to [85, 86]

$$\delta G(x, k, \omega) = \int_{x', y'} G(x, x', \omega) \left[V_H(x', y') + V_{\mathrm{ex}}(x', y') \right] G(y', k, \omega), \tag{4.4}$$

with the Hartree and exchange potentials V_H and V_{ex} given by

$$V_H(x, y) = \delta(x - y) \int_{x'} V(x - x') C(x', x', t, t), \tag{4.5a}$$

$$V_{\mathrm{ex}}(x, y) = -V(x - y)\, C(y, x, t, t). \tag{4.5b}$$

Here, the correlation function $C(x, y, t, t)$ is evaluated in the stationary limit and reported in Eq. (3.32). We will consider the case in which the system is prepared at $T = 0$, so that the single-particle correlations and density contain Friedel oscillations with the asymptotic behavior reported in Eq. (3.59). For the evaluation of Eq. (4.4), the asymptotic form of $G(x, y, \omega \simeq \epsilon_k)$ is also required, which we obtain from Eq. (3.22) in the limit $x \gg y$ as

$$G(x, y, \omega \simeq \epsilon_k) = \frac{1}{i v_k} \times \begin{cases} t_k \mathrm{e}^{ik(x-y)}, & y > 0, \\ \mathrm{e}^{ik(x-y)} + r_k \mathrm{e}^{ik(x+y)}, & y < 0, \end{cases} \tag{4.6}$$

and in the limit $x \ll y$ as

$$G(x, y, \omega \simeq \epsilon_k) = \frac{1}{i v_k} \times \begin{cases} \mathrm{e}^{ik(y-x)} + r_k \mathrm{e}^{-ik(x+y)}, & y < 0, \\ t_k \mathrm{e}^{ik(y-x)}, & y > 0. \end{cases} \tag{4.7}$$

In order to extract the corrections to the scattering amplitudes r_k and t_k, we can then evaluate the corrections δG (4.4) in the two asymptotic limits $x \to \pm\infty$, respectively. For $x \to \infty$, we find perturbative corrections of the form $\delta G(x, k, \omega \simeq \epsilon_k) \sim \delta t_k \, \mathrm{e}^{ikx}$ which by comparison with Eq. (4.3) allows us to identify δt_k as the corrections to the transmission amplitude t_k. Analogously, for $x \to -\infty$, we obtain $\delta G(x, k, \omega \simeq \epsilon_k) \sim \delta r_k \mathrm{e}^{-ikx}$ yielding the corrections δr_k to the reflection amplitude.

The perturbative corrections in Eq. (4.4) to the Green's function consist of two contributions, i.e., $\delta G \equiv \delta G_H + \delta G_{\mathrm{ex}}$, originating form the Hartree and the exchange interaction potentials (4.5), respectively. With the use of Eqs. (4.5)-(4.7) we can now evaluate $\delta G(x, k, \omega)$. Considering first the asymptotic form for $x \to \infty$, we obtain the corrections to the transmission amplitude, $\delta t_k = \delta t_k^{\mathrm{H}} + \delta t_k^{\mathrm{ex}}$, with

$$\delta t_k^{\mathrm{H,ex}} = \frac{1}{iv_k} \int_{x',y'} \left[\mathrm{e}^{-ikx'} + r_k \mathrm{e}^{ik|x'|}\right] V_{\mathrm{H,ex}}(x', y') \left[\mathrm{e}^{iky'} + r_k \mathrm{e}^{ik|y'|}\right]. \tag{4.8}$$

Analogously, in the limit $x \to -\infty$ we obtain the corrections to the reflection amplitude, $\delta r_k = \delta r_k^{\mathrm{H}} + \delta r_k^{\mathrm{ex}}$, with

$$\delta r_k^{\mathrm{H,ex}} = \frac{1}{iv_k} \int_{x',y'} \left[\mathrm{e}^{ikx'} + r_k \mathrm{e}^{ik|x'|}\right] V_{\mathrm{H,ex}}(x', y') \left[\mathrm{e}^{iky'} + r_k \mathrm{e}^{ik|y'|}\right]. \tag{4.9}$$

In the following, we evaluate explicitly the individual contributions. The derivation is instructive as is highlights the physical mechanism underlying the corrections of the scattering amplitudes.

Evaluation of the Hartree term

As a starting point, we focus on the corrections originating from the Hartree term, given by δt_k^{H} (4.8) and δr_k^{H} (4.9). In order to evaluate the Hartree potential (4.5a), we consider the density $C(x, x, t, t) = n(x) = n_{\mathrm{bg}} + \delta n(x)$ in the NESS reported in Eq. (3.56). Hence, we obtain using Eq. (4.5a)

$$\begin{aligned}\delta t_k^H =& \frac{1}{iv_k} \int_{x'<0} \int_{x''} t_k \mathrm{e}^{-ikx'} V(x' - x'') n(x'') \left[\mathrm{e}^{ikx'} + r_k \mathrm{e}^{-ikx'}\right] \\ &+ \frac{1}{iv_k} \int_{x'>0} \int_{x''} \left[\mathrm{e}^{-ikx'} + r_k \mathrm{e}^{ikx'} V(x' - x'') n(x'')\right] t_k \mathrm{e}^{ikx'}.\end{aligned} \tag{4.10}$$

Analogously, we obtain with Eq. (4.5b)

$$\begin{aligned}\delta r_k^H =& \frac{1}{iv_k} \int_{x'<0} \int_{x''} \left[\mathrm{e}^{ikx'} + r_k \mathrm{e}^{-ikx'}\right] V(x' - x'') n(x'') \left[\mathrm{e}^{ikx'} + r_k \mathrm{e}^{-ikx'}\right] \\ &+ \frac{1}{iv_k} \int_{x'>0} \int_{x''} t_k \mathrm{e}^{ikx'} V(x' - x'') n(x'') \, t_k \mathrm{e}^{ikx'}.\end{aligned} \tag{4.11}$$

While these expressions are valid for a generally shaped barrier, we focus in the following on a symmetric barrier for which the density profile fulfills $n(x) = n(-x)$. Further, we can use that

the interaction potential is symmetric, $V(x) = V(-x)$, to obtain the more concise expressions

$$\delta t_k^H = \frac{1}{iv_k} \int_{x'>0} \int_{x''} n(x'') V(x' - x'')\, 2t_k \left[1 + r_k e^{i2kx'}\right], \tag{4.12a}$$

$$\delta r_k^H = \frac{1}{iv_k} \int_{x'>0} \int_{x''} n(x'') V(x' - x'') \left[2r_k + e^{-i2kx'} + (t_k^2 + r_k^2) e^{i2kx'}\right]. \tag{4.12b}$$

For the sake of simplicity, we consider directly the asymptotic form of the density, anticipating that the dominant contributions originate from the asymptotic regions of the integration domain in Eqs. (4.8) and (4.9). To this end, we recall that the asymptotic density oscillations (3.59) for $|x| \gg 1$ are described by

$$\delta n(x) \simeq r_{k_F} \frac{\sin(2k_F x)}{2\pi x} \simeq r_{k_F} \int_0^{k_F} \frac{\mathrm{d}q}{2\pi} \left(e^{i2qx} + e^{-i2qx}\right). \tag{4.13}$$

We now identify the dominating contributions to the perturbative corrections by noting that certain terms in Eq. (4.12) yield a non-oscillating integrand. These terms are found to originate from the oscillating part of the density profile $\delta n(x)$. In order to evaluate Eq. (4.12), we include the two following considerations. First, we introduce a short-ranged spatial cutoff $d > 0$ [81, 85, 86]. Here, the scale d corresponds to the characteristic scale of the interaction potential and has to be chosen the largest of the range of $V(x)$ and the Fermi-wavelength [81]. In turn, d determines the typical scale of the momentum transfer due to scattering events. Therefore, this scale defines an energy interval $\epsilon_F \pm v_F/d$ around the Fermi level such that modes with an energy inside this interval are strongly affected by the scattering with the Friedel oscillations [85]. Second, the double real-space integral in Eqs. (4.12) can be decomposed into contributions from each half-space only, i.e., $\int_{x',y'} \simeq \int_{x'>d,y'>d} + \int_{x'<d,y'<d}$, since the interaction potential $V(x)$ is short-ranged. Here, and we made use of the scale d to exclude the non-universal impurity region near $x = 0$. The comparison with Fig. 3.2 (lower panel) reveals that beyond a distance of $\lambda_F = 8$ sites from the impurity the density is indeed well described by a constant background with superimposed oscillations, while in contrast closer to the impurity the density is further depleted.

We can now identify in Eq. (4.12) two types of contributions. First, terms which include oscillating factors also for $q = k$ and thus can be neglected, and terms that do not oscillate for $k = q$ which give rise to divergences. The latter terms originate from the non-translational-invariant part of the Hartree potential which contains Friedel oscillations (4.13). Thus, we obtain the leading contributions for $k \sim k_F$:

$$\delta t_k^H \simeq 2r_k^2 t_k I_k^H, \tag{4.14a}$$

$$\delta r_k^H \simeq r_k (t_k^2 + r_k^2) I_k^H + r_k I_{-k}^H, \tag{4.14b}$$

where we defined the integral

$$I_{\pm k}^H = \frac{1}{iv_k} \int_{x'>d} \int_{x''>d} \int_0^{k_F} \frac{\mathrm{d}q}{2\pi} V(x' - x'') e^{\pm i(2kx' - 2qx'')}. \tag{4.15}$$

Equation (4.14) contains the leading contribution for $k \sim k_F$ since the integral (4.15) is logarithmically divergent for $k = k_F$, which will be substantiated below. Further, we assumed that the bare scattering amplitudes t_k, r_k as a function of k change only slowly in the vicinity of the Fermi

momentum and thus we can identify $r_{k_F} \simeq r_k$. This assumption is reasonable in the absence of resonant tunneling for the bare barrier [80, 81, 137], and therefore valid for the presently discussed delta-shaped barrier. In Eq. (4.14), we further omitted terms independent of k which diverge as the volume L, see App. B.1. The latter terms are not sensitive to the limit $k \to k_F$ and correspond to a uniform energy shift due to the switching on of the interactions in accordance with a shift of the chemical potential.

We now work out the asymptotic behavior of the integral $I^H_{\pm k}$ for k close to the Fermi momentum $k \sim k_F$, where we find a logarithmic divergence at $k = k_F$. In order to evaluate the integral (4.15), we introduce the center and relative coordinates $X = x' + x''$ and $\chi = x' - x''$ and obtain

$$I^H_{\pm k} = \frac{1}{2iv_F} \int_{X>d} \mathrm{d}X \int_{-X}^{X} \mathrm{d}\chi \int_0^{k_F} \frac{\mathrm{d}q}{2\pi} V(\chi) \mathrm{e}^{\pm i\chi(k+q) \pm iX(k-q)}. \tag{4.16}$$

Since $V(x)$ is assumed to be short-ranged, we can extend the boundaries of the χ-integration to infinity. This allows us to identify the Fourier transform of $V(x)$, which we denote by $\widetilde{V}(k)$, and arrive at

$$I^H_{\pm k} \simeq \frac{\widetilde{V}(2k_F)}{2iv_F} \int_{X>d} \int_0^{k_F} \frac{\mathrm{d}q}{2\pi} \mathrm{e}^{\pm iX(k-q)} = \mp \frac{\widetilde{V}(2k_F)}{2iv_F} \int_d^\infty \mathrm{d}X \, \frac{\mathrm{e}^{\pm iX(k-k_F)}}{2\pi iX}, \tag{4.17}$$

where we identified $\widetilde{V}(2k_F)$ using $k + q \sim 2k_F$ and $\widetilde{V}(k) = \widetilde{V}(-k)$. The remaining integration in Eq. (4.17) yields

$$\int_d^\infty \mathrm{d}X \, \frac{\mathrm{e}^{\pm iX(k-k_F)}}{X} = \int_{\mp i(k-k_F)d}^\infty \mathrm{d}t \, \frac{\mathrm{e}^{-t}}{t} \equiv \mathrm{Ei}(\mp i(k-k_F)d), \tag{4.18}$$

with $\mathrm{Ei}(z)$ the exponential integral. By making use of the series expansion $\mathrm{Ei}(z) \simeq -\ln(|z|)$ for $|z| \ll 1$ [140] we obtain

$$I^H_{\pm k} \simeq \mp \frac{\alpha_1}{2} \log(d\,|k - k_F|), \tag{4.19}$$

where the dimensionless parameter $\alpha_1 = \widetilde{V}(2k_F)/2\pi v_F$ was introduced. We can infer from this expression that d^{-1} indeed acts as a typical momentum scale determining the interval $|k - k_F| < d^{-1}$ in which the perturbative corrections to the scattering properties are large.

Evaluation of the exchange term

The perturbative corrections to the scattering amplitudes originating from the exchange terms given by δt^{ex}_k (4.8) and δr^{ex}_k (4.9) are evaluated analogously to their Hartree counterparts. Readers who are primarily interested in the result of the perturbative computation may want to skip ahead to Eqs. (4.31). The exchange potential (4.5b) is determined from the two-point correlation function $C(x, x', t, t) \equiv C(x_1, x_2)$ evaluated in the NESS which is reported in Eq. (3.32). After splitting the double real-space integral in Eqs. (4.8) according to $\int_{x',y'} \simeq \int_{x'>d,y'>d} + \int_{x'<d,y'<d}$, we can focus on the two-point correlation function with the same sign of its arguments, which we denote as

$$C(x, x') = \begin{cases} C^-_>(x, x') + C^+_>(x, x') & \text{for } x > 0, x' > 0, \\ C^-_<(x, x') + C^+_<(x, x') & \text{for } x < 0, x' < 0. \end{cases} \tag{4.20}$$

Here, we labeled the different contributions according to the relative sign in the arguments of the oscillating factors:

$$C^+_>(x,x') = C^+_<(x,x') = \int_0^{k_F} \frac{\mathrm{d}q}{2\pi} \left[r_q \mathrm{e}^{iq(x+x')} + r_q \mathrm{e}^{-iq(x+x')} \right],$$
$$C^-_>(x,x') = C^-_<(-x,-x') = \int_0^{k_F} \frac{\mathrm{d}q}{2\pi} \left[\mathrm{e}^{iq(x-x')} + (1+2r_q+2r_q^2)\mathrm{e}^{-iq(x-x')} \right]. \tag{4.21}$$

First, we focus on the evaluation of the correction to the reflection amplitude δr^{ex} (4.9) and obtain with the exchange potential (4.5b)

$$\delta r_k^{\mathrm{ex}} = -\frac{1}{iv_k} \int_{x'>0} \int_{x''>0} V(x'-x'') \Big(\left[\mathrm{e}^{-ikx'} + r_k \mathrm{e}^{ikx'} \right] \times \left[\mathrm{e}^{-ikx''} + r_k \mathrm{e}^{ikx''} \right] + t_k^2 \mathrm{e}^{ik(x'+x'')} \Big) \Big(C^+_>(x'',x') + C^-_<(x'',x') \Big), \tag{4.22}$$

where we used the properties $C^+_<(-x,-x') = C^+_>(x,x')$ and $C^-_<(-x,-x') = C^-_>(x,x')$. The contribution originating from $C^+_>(x,x')$ contains logarithmic divergences for $k = k_F$, while in contrast the term $\sim C^-_>(x,x')$ does not contain such divergences (see App. B.1). Therefore, we can neglect the latter terms and obtain

$$\delta r_k^{\mathrm{ex}} \simeq -\frac{1}{iv_k} \int_{x'>0} \int_{x''>0} \int_0^{k_F} \frac{\mathrm{d}q}{2\pi} V(x'-x'') \left[r_k \mathrm{e}^{ik(x'-x'')} + r_k \mathrm{e}^{-ik(x'-x'')} + \mathrm{e}^{-ik(x'+x'')} + (r_k^2+t_k^2)\mathrm{e}^{ik(x'+x'')} \right] \times \left[r_q \mathrm{e}^{iq(x'+x'')} + r_q \mathrm{e}^{-iq(x'+x'')} \right], \tag{4.23}$$

where we identified $t_k = 1 + r_k$. Retaining only the divergent contributions, we arrive at

$$\delta r_k^{\mathrm{ex}} \simeq (r_k^2 + t_k^2) I_k^{\mathrm{ex}} + I_{-k}^{\mathrm{ex}}, \tag{4.24}$$

where we could omit terms with oscillating integrand. The integrals $I^{\mathrm{ex}}_{\pm k}$ are defined as

$$I^{\mathrm{ex}}_{\pm k} = -\frac{1}{iv_k} \int_{x'>0} \int_{x''>0} \int_0^{k_F} \frac{dq}{2\pi} r_q V(x'-x'') \mathrm{e}^{\pm i(k-q)(x'+x'')}. \tag{4.25}$$

Analogously, we obtain for the corrections to the transmission amplitude (4.8)

$$\delta t_k^{\mathrm{ex}} = -\frac{1}{iv_k} \int_{x'>0} \int_{x''>0} V(x'-x'') \Big(t_k \mathrm{e}^{ikx'} \left[\mathrm{e}^{-ikx''} + r_k \mathrm{e}^{ikx''} \right] + \left[\mathrm{e}^{-ikx'} + r_k \mathrm{e}^{ikx'} \right] t_k \mathrm{e}^{ikx''} \Big) \Big(C^+_>(x'',x') + C^-_<(x'',x') \Big), \tag{4.26}$$

from which we extract the leading contribution (cf. App. B.1)

$$\delta t_k^{\mathrm{ex}} = 2 t_k r_k I_k^{\mathrm{ex}}. \tag{4.27}$$

Finally, we derive the asymptotic behavior of the integrals $I^{\mathrm{ex}}_{\pm k}$ for $k \sim k_F$, revealing logarithmic divergences for $k = k_F$. This fact is seen analogously to the derivation of the Hartree contribution

by first rewriting the integrals as

$$I^{\mathrm{ex}}_{\pm k} = -\frac{1}{i2v_k}\int_{X>d} \mathrm{d}X \int_{-X}^{X} \mathrm{d}\chi \int_0^{k_F} \frac{\mathrm{d}q}{2\pi} r_q V(\chi) \mathrm{e}^{\pm i(k-q)X}. \tag{4.28}$$

Here, we identify the Fourier transform $\widetilde{V}(k)$ of the interaction potential evaluated at $k = 0$ and obtain

$$I^{\mathrm{ex}}_{\pm k} = \pm\frac{1}{i4\pi v_k} r_k \widetilde{V}(0) \int_d^{\infty} \mathrm{d}X \, \frac{\mathrm{e}^{\pm i(k-q)X}}{iX}, \tag{4.29}$$

where we used that the integral is dominated by $q \sim k$ and thus replaced $r_q = r_k$, assuming the microscopic amplitudes change slowly as a function of k. Hence, we encounter the same integral (4.17) appearing in the Hartree contribution, and obtain the logarithmically divergent expression

$$I^{\mathrm{ex}}_{\pm k} \simeq \pm r_k \frac{\alpha_2}{2} \log(d|k - k_F|), \tag{4.30}$$

where we introduced the dimensionless parameter $\alpha_2 = \widetilde{V}(0)/2\pi v_F$.

Result for the perturbative corrections

Collecting all results from Eqs. (4.14), (4.19), (4.27) and (4.30), the perturbative corrections to the scattering amplitudes for an incoming plane wave with momentum $k \sim k_F$ are obtained as

$$\delta t_k = \alpha \, t_k r_k^2 \, \log|d(k - k_F)|, \tag{4.31a}$$

$$\delta r_k = \frac{\alpha}{2} r_k \left(r_k^2 + t_k^2 - 1\right) \, \log|d(k - k_F)|. \tag{4.31b}$$

Here, d the is characteristic length scale which has to be chosen as the largest between the spatial range of the interaction $V(x)$ and the Fermi wavelength. Further, we defined the dimensionless parameter

$$\alpha \equiv \alpha_2 - \alpha_1 \equiv [\widetilde{V}(0) - \widetilde{V}(2k_F)]/(2\pi v_F), \tag{4.32}$$

which thus encodes the interaction strength. Moreover, $\alpha > 0$ corresponds to repulsive interactions, and $\alpha < 0$ to attractive ones [85, 86]. Indeed, for a generic interaction potential, $\widetilde{V}(k)$ decreases as a function of $|k|$ and hence the sign of α is directly determined by the sign of $V(x)$.

The perturbative corrections (4.31) posses a clear interpretation as repeated virtual scattering processes between the bare barrier and the effective one established by the Friedel oscillations in the presence of interactions [85], as illustrated in Fig. 4.1. The contribution $\sim t_k r_k^2$ to δt_k, for example, corresponds to a sequence of virtual scattering events (see upper right panel of Fig. 4.1) in which a particle is first scattered back at the microscopic loss barrier, then scattered again by the Friedel oscillations towards the loss site and finally transmitted through the microscopic barrier. All similar sequences with at most three scattering events contribute to the first-order corrections to the scattering amplitudes. Therefore, we can interpret the renormalization of the scattering amplitudes as the result of the interference of these virtual scattering processes dressing the bare barrier.

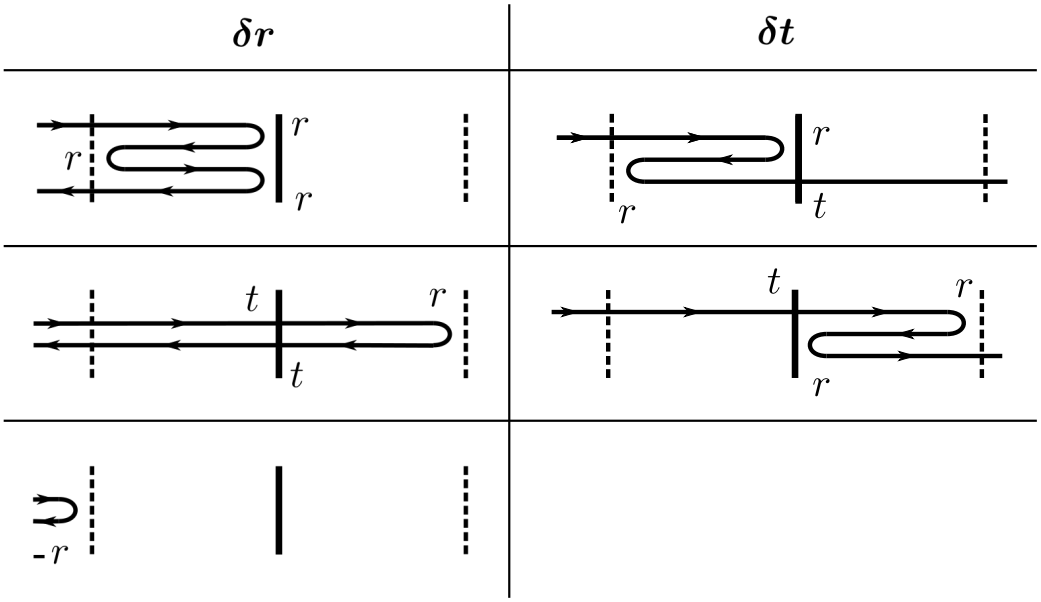

Fig. 4.1. Sequences of virtual scattering events contributing to the perturbative corrections δr_k (left column) and δt_k (right column). Solid vertical lines depict the bare loss barrier, dashed vertical lines the effective barrier constituted by the Friedel oscillations.

4.2.2. Resummation

Equations (4.31) exhibit logarithmic divergences for momenta $k \sim k_F$, originating from the interference between Friedel oscillations (see Eq. (3.59)) and particles with comparable wavenumber. While in principle the perturbative expansion in the interaction strength is controlled by the parameter $\alpha \ll 1$, the perturbation theory breaks down at $k \sim k_F$, as a consequence of these unphysical divergences. This breakdown reflects that the renormalization of the effective barrier is not adequately captured by the simple perturbative calculation. Indeed, the Hartree and exchange potentials (4.5) depend themselves on the reflection amplitudes and the feedback of the corrections on them should be taken into account. A suitable treatment can be formulated by an RG scheme in real or frequency space [85, 86] effectively resumming the logarithmic divergences, and resembling the poor man's renormalization by Anderson [141]. We focus on the real-space variant of the RG scheme [86] as it provides an intuitive picture of the underlying physical mechanism. The RG scheme can be understood as a gradual enlarging of the considered effective barrier, whereby in each step the corrections are evaluated for the effective barrier of the previous step, thus taking into account adequately the effective scattering properties at the respective scale. The procedure is sketched in Fig. 4.2 and the individual steps are demonstrated in the following.

To begin with, we consider a spatial region $(-l, l)$ with $l \gg d$ and centered around the loss site, which acts as the effective barrier for particles outside (with d the characteristic length scale of the interactions, see discussion below Eq. (4.31)). If the size of the region l is chosen small enough such that $\alpha \ln(l/d) \ll 1$, the perturbative evaluation of Eqs. (4.31) is valid, leading to the effective scattering amplitudes t_1, r_1 of this region

$$t_1 = t_0 - \alpha t_0 r_0^2 \ln \Lambda, \qquad r_1 = r_0 - \frac{\alpha}{2} r_0 \left(r_0^2 + t_0^2 - 1\right) \ln \Lambda, \tag{4.33}$$

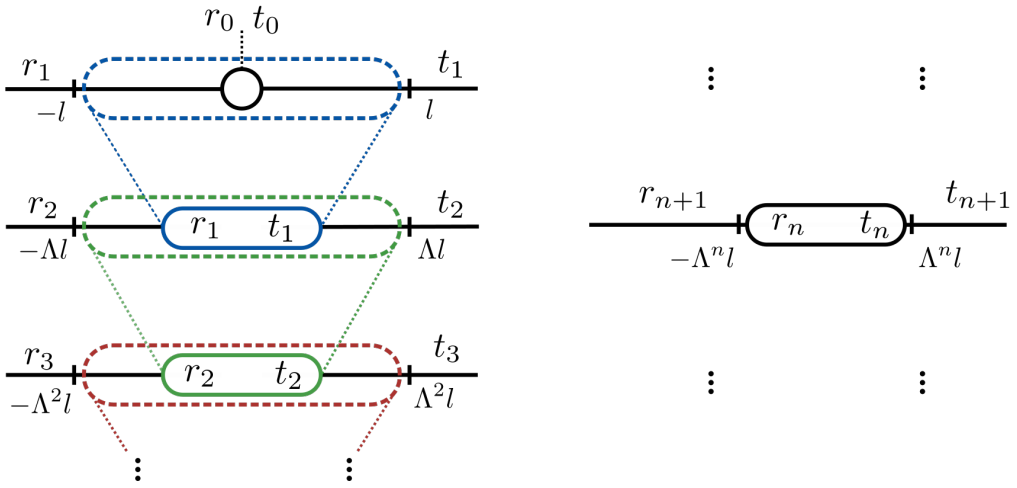

Fig. 4.2. Illustration of the RG procedure described in the main text. Left panel: Starting from the bare barrier (t_0, r_0) (white circle) an effective barrier (t_1, r_1) (blue lines) is constructed in a region $(-l, l)$. At the next step, a new effective barrier (t_2, r_2) (green lines) is formed in a region $(-\Lambda l, \Lambda l)$ around the effective barrier of the previous step. Right panel: The procedure is iterated, such that at the $(n+1)$-th step the effective barrier (t_{n+1}, r_{n+1}) in the region $(-\Lambda^n l, \Lambda^n l)$ is constructed from the effective barrier (t_n, r_n) at the previous step.

with $\Lambda = l/d \gg 1$ and t_0, r_0 the scattering amplitudes of the microscopic loss barrier. Here, we suppress in the notation the momentum index k in favor of readability and denote with $t_n \equiv t_{k,n}$ the transmission amplitude for a given momentum k at the n-th step (accordingly for the reflection amplitude). At the next step, the considered scattering region is increased by a factor Λ and we compute perturbatively the corrections due to Friedel oscillations in the extended region induced by the effective barrier from the last step, as depicted in Fig. 4.2. At the n-th step on the scale $L_s = \Lambda^n l$ this method yields

$$t_{n+1} = t_n - \alpha t_n r_n^2 \ln \Lambda, \qquad r_{n+1} = r_n - \frac{\alpha}{2} r_n \left(r_n^2 + t_n^2 - 1\right) \ln \Lambda. \tag{4.34}$$

The procedure has to be iterated until the scale $l_k = |k - k_F|^{-1}$ is reached, on which a particle with momentum k loses phase coherence with the Friedel oscillations [86]. Indeed, the integrand in Eqs. (4.17) and (4.29) becomes oscillating at a scale $X \sim l_k$.

By taking the continuity limit of the RG steps (4.34) and parameterizing the flow with a continuous parameter $\ell = \ln(L_s/d)$, we arrive at the flow equations reported in Eqs. (4.35) below.

4.3. Renormalization group flow of the scattering probabilities

The resummation of the corrections perturbative in the interaction strength within the real-space RG scheme produces the flow equations:

$$\frac{\mathrm{d}t(\ell)}{\mathrm{d}\ell} = -\alpha\, t(\ell) r^2(\ell), \tag{4.35a}$$

$$\frac{\mathrm{d}r(\ell)}{\mathrm{d}\ell} = -\frac{\alpha}{2}\, r(\ell)\left(t^2(\ell) + r^2(\ell) - 1\right). \tag{4.35b}$$

The RG flow equations have to be solved with the initial conditions $t(\ell = 0) = t_0, r(\ell = 0) = r_0$, with t_0, r_0 the bare values, and with the flow to be stopped at $\ell_k = -\ln|d(k - k_F)|$. The latter relation can be used to restore the momentum dependence of the renormalized scattering parameters, i.e., the renormalized values are given by $t(\ell_k), r(\ell_k)$. Consequently, the renormalization exactly at the Fermi level is described by $\ell \to \infty$. One can readily check that, under the RG flow, the continuity relation $t_k = 1 + r_k$ is preserved and $t(\ell), r(\ell)$ remain real-valued (cf. Sec. 3.3.3), so that one can effectively consider just one of the two equations (4.35).

As our main interest is the characterization of the loss probability η_k, we infer from Eqs. (4.35) the RG equations for the scattering probabilities (3.38):

$$\frac{\mathrm{d}\mathcal{T}}{\mathrm{d}\ell} = -2\alpha\, \mathcal{T}\mathcal{R}, \tag{4.36a}$$

$$\frac{\mathrm{d}\mathcal{R}}{\mathrm{d}\ell} = -\alpha\, \mathcal{R}\left(\mathcal{R} + \mathcal{T} - 1\right), \tag{4.36b}$$

with $\mathcal{T}, \mathcal{R} \equiv \mathcal{T}_k, \mathcal{R}_k$ for $k \sim k_F$. The renormalization of $\eta \equiv \eta_k$, for $k \sim k_F$, can then be obtained from these flow equations with the use of Eq. (3.36).

The flow equations admit the followings stable fixed points:

$$\mathcal{T}^* = 0, \quad \mathcal{R}^* = 1, \quad \eta^* = 0, \qquad \alpha > 0, \tag{4.37a}$$

$$\mathcal{T}^* = 1, \quad \mathcal{R}^* = 0, \quad \eta^* = 0, \qquad \alpha < 0. \tag{4.37b}$$

Physically, this entails that at the fixed points tunneling through the dissipative impurity is suppressed for modes near k_F for repulsive interactions; in contrast, for attractive interactions, perfect transmission is restored despite the presence of a barrier. The transport properties at the fixed points characterized in this way are thus analogous to the case of a coherent potential impurity [85, 86]. However, two novel remarkable features emerge from the solutions of Eqs. (4.36), compared to the potential barrier problem. First, as a central result, the loss probability η vanishes for $\ell \to \infty$ for both repulsive and attractive interactions, i.e., $\eta^* = 0$. This entails that the loss of modes with momenta $k \sim k_F$ is suppressed, and particles are actually "trapped" inside the wire, effectively restoring unitarity at the Fermi level. Second, $\eta(k)$ approaches its fixed-point value in qualitatively different ways, depending on the sign of α, as discussed in the following. This asymptotic approach to the fixed points is qualitatively different from the equilibrium counterpart of a coherent potential barrier [85, 86].

In order to derive the asymptotic behavior, i.e., $\ell \gg 1$, of the flow equations near the stable fixed points, it is sufficient to consider the flow equation for the transmission amplitude (4.35) (see

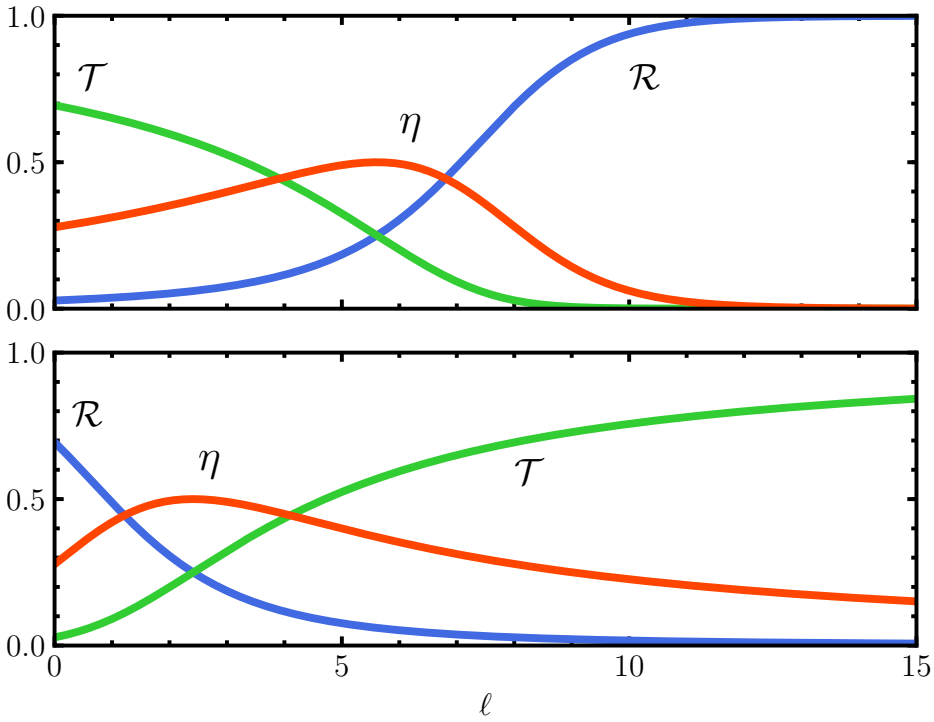

Fig. 4.3. RG flow of $\mathcal{T}$, $\mathcal{R}$, and η. For $\alpha > 0$ (upper panel, $\gamma = 0.2$) a fully reflective fixed point is approached, while for $\alpha < 0$ (lower panel, $\gamma = 5$) the system is perfectly transmissive at the fixed point. In both cases the loss probability η vanishes asymptotically.

discussion below Eq. (4.35)). We linearize the flow equation by considering small deviations from the fixed point value t^*, i.e., $t(\ell) = t^* + \delta t(\ell)$, where $t^* = 0$ for repulsive and $t^* = 1$ for attractive interactions, respectively. The linearized equation reads using $t(\ell) = 1 + r(\ell)$:

$$\frac{\mathrm{d}\delta t}{\mathrm{d}\ell} = \begin{cases} -\alpha\delta t + \mathcal{O}(\delta t^2) & \text{for } \alpha > 0, \\ -\alpha(\delta t)^2 & \text{for } \alpha < 0. \end{cases} \tag{4.38}$$

Remarkably, for attractive interactions, $\alpha < 0$, the flow equations can not be linearized, resulting in a logarithmically slow approach of the fixed point.

Focusing on the loss probability η, we obtain in the vicinity of the fixed point the asymptotic behavior

$$\eta \sim \begin{cases} |k - k_F|^\alpha & \text{for} \quad \alpha > 0, \\ -1/\log|d(k - k_F)| & \text{for} \quad \alpha < 0. \end{cases} \tag{4.39}$$

The logarithmic approach for attractive interactions has no analog in the case of a coherent potential barrier, where the fixed points are approached algebraically in $|k - k_F|$ in both cases [85, 86]. Equation (4.39) is the key result of the present chapter. The loss probability of modes near the Fermi level is strongly renormalized by fluctuations resulting in its suppression. For $\alpha > 0$, a particle is rather reflected back than lost from the wire, as if $\gamma \to \infty$, thus establishing a *fluctuation-induced* quantum Zeno effect. For $\alpha < 0$, instead, the renormalized barrier becomes fully transparent, as if $\gamma \to 0$, constituting a *fluctuation-induced* transparency.

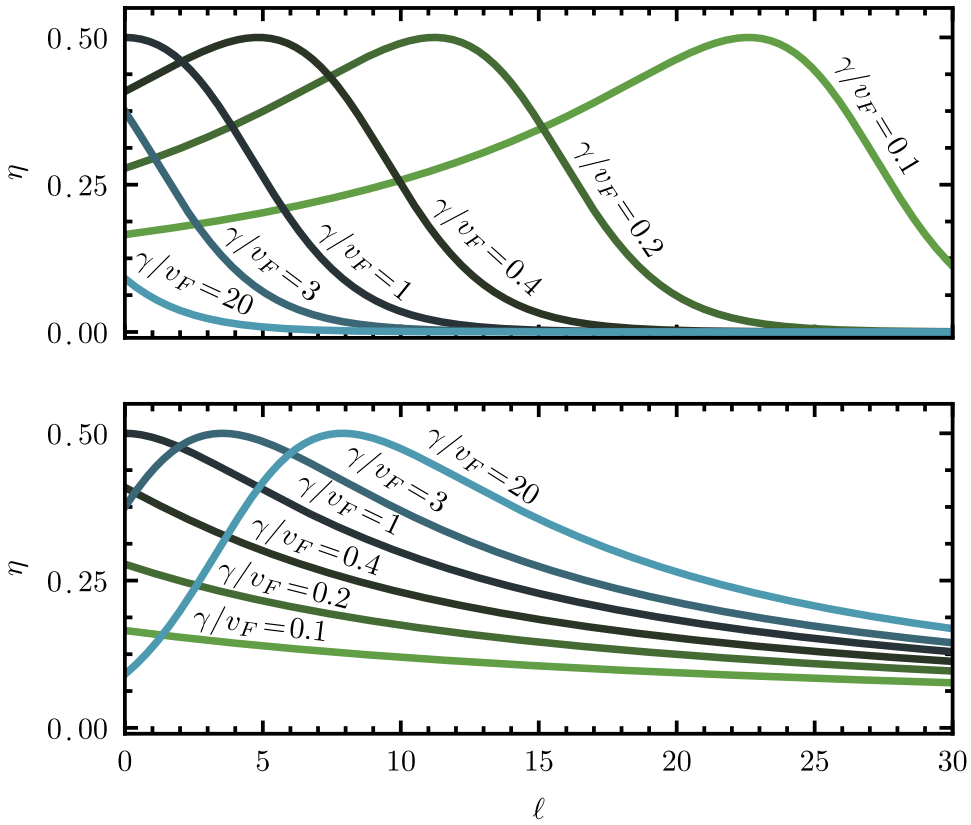

Fig. 4.4. RG flow of the loss probability η near the Fermi level for different bare values of γ. In the upper panel interactions act repulsively, i.e., $\alpha > 0$, in the lower panel attractively, i.e., $\alpha < 0$.

In Figure 4.3 the RG flow of $\mathcal{T}$, $\mathcal{R}$, and η is shown, for both repulsive and attractive interactions. The different approach of η to the fixed points for repulsive and attractive interactions, respectively, is also reflected in the behavior of $\mathcal{T}(\ell)$ and $\mathcal{R}(\ell)$. Moreover, the flow of η may be non-monotonic, as the one shown in Fig. 4.3, depending on the sign of α and the bare value of γ determining the initial conditions of the flow. In contrast, the RG flow of $\mathcal{T}$, $\mathcal{R}$ is always monotonic. In Fig. 4.4, the RG flow of the loss probability η is depicted for various dissipation strengths γ for both repulsive and attractive interactions, leading to a non-monotonic or monotonic RG flow depending on the bare parameters.

With the use of the relation $\ell = -\log|d(k - k_F)|$ one can reconstruct the renormalized value of η for a given momentum in the vicinity of k_F by stopping the RG flow at the corresponding scale. Consequently, the way the fixed point is approached (cf. Fig. 4.4) reflects onto the shape of η_k for $k \sim k_F$. In Fig. 4.5 we show the value of η_k as a function of k reconstructed from the RG flow. For momenta close to k_F, η always decreases, *vanishing* exactly at k_F, for both repulsive and attractive interactions. However, depending on the bare value of γ, the RG flow can be non-monotonic and thus the loss probability of modes on intermediate scales near k_F can be enhanced before eventually dropping to zero at k_F: these modes thus experience a renormalized loss barrier resulting in an effectively enhanced loss probability.

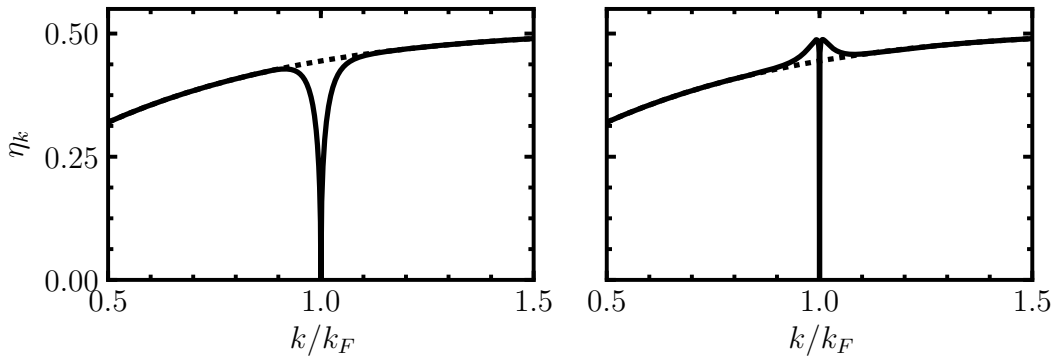

Fig. 4.5. Renormalized η (solid) as a function of momentum in comparison to the non-interacting value η_0 (dashed), for $\alpha > 0$ (left panel) and $\alpha < 0$ (right panel). For all curves $\gamma/v_F = 4$.

4.4. Observability of the renormalized loss probability

The loss probability η_k has been identified in Chapter 3 as the key quantity to describe depletion effects in several observables. Therefore, its suppression at the Fermi level, found in the previous section, is expected to have a clear impact on the dynamics in the presence of a localized loss. The open nature of the system under consideration allows for the identification of observables without equilibrium counterparts. To this end, the flow of particles emitted from the wire can be leveraged to a non-destructive measurement to probe the renormalization effects on the loss probability. In turn, a measurement of the particles remaining in the wire allows one to draw conclusions on the preceding depletion processes, as discussed in the analysis of the momentum distribution dynamics in Sec. 3.6. Moreover, a finite size or temperature of the wire in realistic experimental platforms provides a cutoff scale of the RG flow. A variation of these scales is reflected by a scaling of η.

In the following, we consider explicitly the renormalization of the particle loss rate in a momentum-resolved picture and find a direct correspondence with the RG flow of the loss probability. Moreover, we consider the signature of a suppressed loss probability on the depletion dynamics of the momentum distribution, leading to an increased occupation near k_F. Finally, we work out the impact of cutoff scales due to finite size and temperature on the RG flow and estimate the experimentally accessible scaling of η obtained by varying these scales.

4.4.1. Momentum-resolved loss rate

The particle loss rate is a natural quantity to probe the renormalization effects of the loss probability. Since the suppression of the loss probability takes place only in the vicinity of the Fermi level, it is desirable to consider the particle loss rate in a momentum-resolved way. The study of the non-interacting system in Chapter 3 revealed that to the total particle loss rate each mode k contributes indeed with an amount proportional to η_k, see Eq. (3.64). In this section, we define a momentum-resolved loss rate which is shown to exhibit two important properties. First, it is proportional to the loss probability η_k on the microscopic level. Second, its RG flow, incorporating the presence of interactions, coincides with the one of η. Hence, it is suitable for probing the renormalization effects of the loss probability elaborated in Sec. 4.3.

In order to define a definite momentum-resolved loss rate, we consider the following model of a localized loss inspired by the input-output formalism of quantum optics [5]. To this end, we assume the wire, described by the Hamiltonian (4.1), to be coupled locally to a continuum of untrapped fermionic modes such that particles can exit the wire by expanding isotropically in the surrounding vacuum. Experimentally, this could be realized, e.g., by a local transfer to an untrapped internal state [142]. The untrapped modes are described by annihilation and creation operators $c_{\mathbf{q}}, c_{\mathbf{q}}^\dagger$, and energy $\epsilon_{\mathbf{q}}$ with $\mathbf{q}$ a three-dimensional momentum. The coupling at position $x = 0$ is specified by the Hamiltonian

$$H_{\mathrm{c}} = \sum_{\mathbf{q}} (g_{\mathbf{q}} c_{\mathbf{q}}^\dagger \psi(x=0) + \mathrm{h.c.}), \tag{4.40}$$

with $g_{\mathbf{q}}$ the coupling of the $\mathbf{q}$-mode to the wire. The spectral function $J(\omega)$ of the bath satisfies $J(\omega) = 2\pi \sum_{\mathbf{q}} |g_{\mathbf{q}}|^2 \delta(\omega - \epsilon_{\mathbf{q}}) = 2\gamma$.

In the NESS, the constant rate of particles with momentum $\mathbf{q}$ arriving in the bath after being emitted from the wire can be straightforwardly expressed in terms of system operators only:

$$\begin{aligned} \frac{\mathrm{d}\langle c_{\mathbf{q}}^\dagger c_{\mathbf{q}} \rangle}{\mathrm{d}t} &= |g_{\mathbf{q}}|^2 \int_t \mathrm{e}^{-i\omega_{\mathbf{q}} t} \langle \psi^\dagger(x=0,t)\psi(x=0,0)\rangle \\ &= |g_{\mathbf{q}}|^2 C(x=0, x=0, \omega=\epsilon_{\mathbf{q}}). \end{aligned} \tag{4.41}$$

Here, $C(x=0, x=0, \omega)$ is the Fourier transform of the correlation function $C(x=0, x=0, t-t') \equiv C(x=0, x=0, t, t')$ which is obtained from Eq. (3.28) as

$$C(x=0, x=0, t-t') = \int_k G^*(x=0, -k, t) G(x=0, -k, t') n_{0,k}. \tag{4.42}$$

This explicit form is the starting point of the RG study below. As a consistency check, one can recover from Eq. (4.41) the identity (3.64) by summing all modes $\mathbf{q}$, connecting the loss rate to the density at the loss site. The two-time correlation function $C(0,0,\omega)$ in Eq. (4.41) is evaluated in the NESS and obtained from the solution of the single-particle problem in Eq. (3.32).

The momentum-resolved loss rate is thus found in terms of $G(x=0, p, \omega)$ which we can interpret as the response to a plane wave perturbation at the loss site $x = 0$ (cf. discussion in Sec. 3.3.3). To this end, we introduced the amplitude $t_\eta(\omega)$ of the propagator (3.24)

$$G(x=0, p, \omega) = t_\eta(\omega) G_0(p, \omega), \tag{4.43}$$

whose renormalization due to interactions is studied in the following, analogous to the real-space RG analysis of the scattering amplitudes t_k, r_k in Sec. 4.2. Following these considerations, we evaluate Eq. (4.41) and obtain the momentum resolved loss rate as

$$\frac{\mathrm{d}\langle c_{\mathbf{q}}^\dagger c_{\mathbf{q}} \rangle}{\mathrm{d}t} = |g_{\mathbf{q}}|^2 \frac{\theta(\epsilon_F - \epsilon_{\mathbf{q}})}{\sqrt{\epsilon_{\mathbf{q}}}} |t_\eta(\omega = \epsilon_{\mathbf{q}})|^2, \tag{4.44}$$

with $\epsilon_F = k_F^2/2m$ the Fermi energy. One can readily verify that $t_\eta(\omega)$ is related to the loss probability η_k on the microscopic level as

$$\frac{2\gamma}{|v_k|} t_{\eta,k}^2 = \eta_k, \tag{4.45}$$

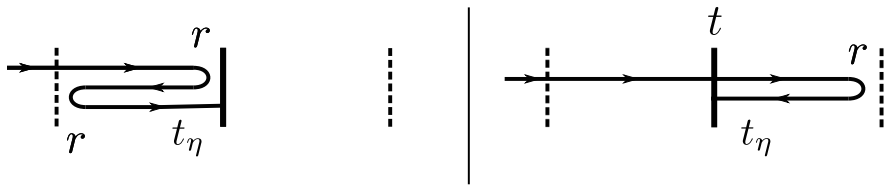

Fig. 4.6. Sequences of virtual scattering events contributing to the renormalization of the amplitude t_η. The vertical solid line represents the bare barrier and vertical dashed lines the effective one created by the Friedel oscillations.

with $t_{\eta,k} \equiv t_\eta(\epsilon_k)$.

We now study the interaction effects on the momentum-resolved loss rate in analogy to the renormalization of the scattering amplitudes in the previous sections. Having already identified the relevant amplitude t_η, we can consider the perturbative corrections $\delta G(x=0,p,\omega)$ described by Eq. (4.4). As before, logarithmic divergences are encountered and we can straightforwardly adapt the renormalization scheme developed in Sections 4.2.1 and 4.2.2 to obtain RG flow equations of t_η.

The corrections to the Green's function $G(x=0,p,\omega)$ within the first-order Born approximation [85, 86] read explicitly (4.4)

$$\delta G(x=0,p,\omega) = \int_{x',y'} G(x=0,x',\omega)\left[V_H(x',y') + V_{\text{ex}}(x',y')\right] G(y',p,\omega). \tag{4.46}$$

Crucially, $t_{\eta,k}$ enters this expression via $G(x=0,x',\omega)$, see Eq. 4.43. In contrast, the logarithmic divergences in the perturbative corrections originate from the asymptotic forms of $G(y',p,\omega)$, $V_H(x',y')$, and $V_{\text{ex}}(x',y')$, respectively, which are consequently functions of the scattering amplitudes t_k, r_k. In close analogy to the case of the scattering amplitudes in Sec. 4.2.1, one can then evaluate and resum the perturbative corrections, resulting in the RG flow equation

$$\frac{\mathrm{d}t_\eta}{\mathrm{d}\ell} = -\frac{\alpha}{2} t_\eta \left(r^2 + tr\right), \tag{4.47}$$

with $t_\eta \equiv t_{\eta,k}$, for $k \sim k_F$.

Similar to the corrections of the scattering amplitudes t, r (4.31), the RG equation can be interpreted in terms of virtual scattering events between the bare impurity and the effective one created by the Friedel oscillations, as illustrated in Fig. 4.6. A particle initially reflected from (or transmitted across) the impurity scatters back from the Friedel oscillations and finally reaches the loss site. Hence, we can interpret the suppression of loss at the Fermi level as a destructive interference of such processes.

From both the RG flow equation (4.47) for t_η and the ones (4.36) for the scattering probabilities, we readily find that the identity (4.45), relating η and t_η^2, is preserved during the RG flow. Therefore, we obtain from Eq. (4.44) the central result

$$\frac{\mathrm{d}\langle c_{\mathbf{q}}^\dagger c_{\mathbf{q}}\rangle}{\mathrm{d}t} = \theta(\epsilon_F - \epsilon_{\mathbf{q}}) \frac{|g_{\mathbf{q}}|^2}{\gamma} \eta(\epsilon_{\mathbf{q}}), \tag{4.48}$$

relating the constant rate of particles with momentum $\mathbf{q}$ arriving at the bath and the renormalized loss probability η, thus providing a direct connection between η and an experimentally accessible quantity. We remark that in Eq. (4.48), the bare Fermi distribution enters as the approach is perturbative in the interactions. It is expected to be smeared out by stronger interactions [84].

4.4.2. Momentum distribution dynamics

As discussed in Sec. 3.6 for the non-interacting system, the momentum distribution $n_{\text{ness}}(k)$ of particles remaining in the wire bears a characteristic signature of the losses via a simple dependence on the loss probability η, according to (3.82)

$$n_{\text{ness}}(k) = n_{0,k}\left[1 - \frac{\eta_k}{2}\right]. \tag{4.49}$$

Moreover, we substantiated in Sec. 4.4.1 that the renormalized loss rate in a momentum-resolved picture is indeed characterized by the renormalized value of η. Therefore, the momentum distribution is expected to remain a good measure of the loss processes in the presence of interactions, as long as redistribution processes among the modes are small, i.e., for weak interactions, as described by the present approximation. In Fig. 4.7 we display the momentum distribution $n_{\text{ness}}(k)$ (4.49) as reconstructed from the RG flow of η, i.e., by replacing the bare η_k by its RG improved counterpart (cf. Fig. 4.5). The depletion is suppressed near k_F, resulting in a peak in the distribution of remaining particles. In the vicinity of k_F, either a domain of suppressed or increased depletion exists, depending on the bare parameters, as a consequence of the monotonic or non-monotonic RG flow of η.

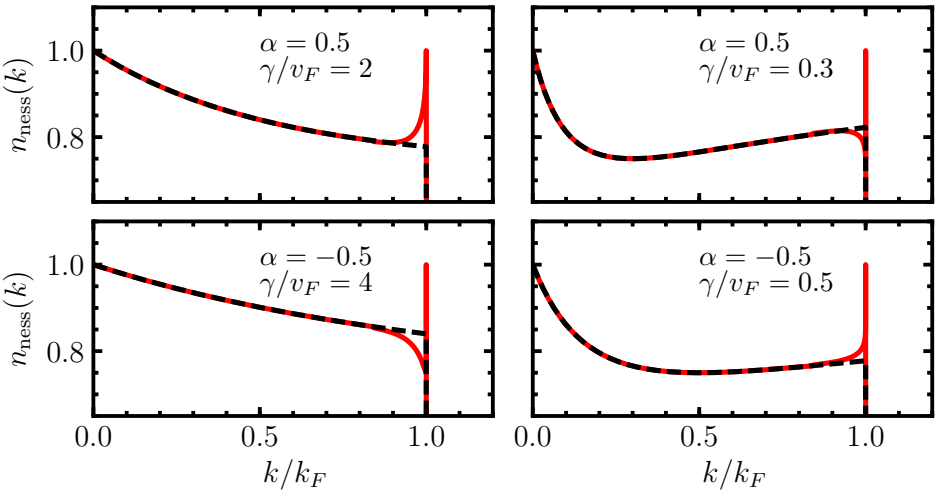

Fig. 4.7. Momentum distributions $n_{\text{ness}}(k)$ (solid red line) in the NESS, reconstructed from the RG flow of η, for different values of the microscopic parameters γ and α, respectively. The momentum distribution of the non-interacting system (dashed black line) is shown for comparison.

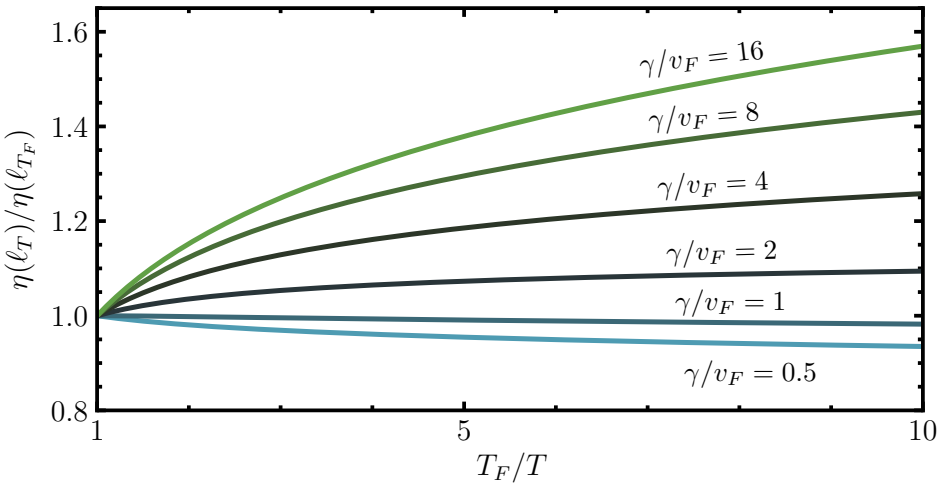

Fig. 4.8. Loss probability $\eta(\ell_T)$ as a function of temperature T for attractive interactions $\alpha = -0.5$ and different values of γ/v_F.

4.4.3. Cutoff scales: Scaling of the loss probability

The presence of a finite global temperature and system size both introduce a scale at which the RG flow is cut off. In this section, we provide estimates on the observability of the fluctuation-induced quantum Zeno effect when taking into account these scales. Moreover, in Sec. 6.4.2 of Chapter 6 we discuss the generation of a local effective temperature emerging at the impurity site which likewise can cut off the RG flow.

A finite system size L imposes a cutoff scale

$$\ell_L \simeq \log(L/d), \tag{4.50}$$

at which the RG scheme in Sec. 4.2.2 is stopped, since the size of the effective barrier cannot be further increased. Analogously, a finite temperature T cuts off the RG flow at a scale

$$\ell_T \simeq -\log(\sqrt{T/T_F}), \tag{4.51}$$

with T_F the Fermi temperature, corresponding to a scale in Sec. 4.2.2 where a particle loses phase coherence with the Friedel oscillations due to thermal fluctuations, set by the thermal wavelength. Consequently, the variation of the temperature or system size allows one to probe the RG flow of $\eta(\ell)$ (cf. Fig. 4.4), mapping out, for instance, the non-monotonic behavior of the RG flow of η as a function of T or L. In recent experiments [43, 44, 142, 143] systems were realized that were typically characterized by sizes up to $L \sim 12\mu m$ and temperatures down to $T \sim 0.1T_F$, with T_F the Fermi temperature, and Luttinger interaction parameters g ranging between 1 and 1.6. The temperature scaling of η using these exemplary parameters is shown in Fig. 4.8: an enhancement of η up to 60% from its microscopic value is expected in the range of temperatures considered, corresponding to the RG flow stopping at a scale $\ell_T \simeq 1.15$.

The presence of a cutoff scale also affects the momentum distribution in the NESS discussed in Sec. 4.4.2. In Fig. 4.9 the momentum distribution $n_{\text{ness}}(k)$ is shown obtained from the renormalized value of η_k in the presence of a cutoff scale $\ell_{T/L}$. The effect of $\ell_{T/L}$ is to stop the RG flow for momenta with $\ell_k > \ell_{T/L}$, corresponding to a narrow region in the vicinity of k_F.

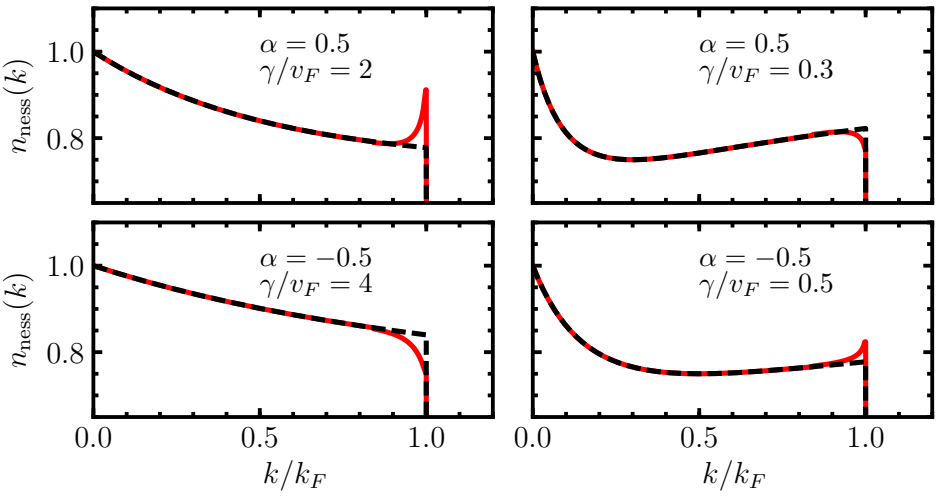

Fig. 4.9. Momentum distributions $n_{\mathrm{ness}}(k)$ for the same parameters as in Fig. 4.7 but with a cutoff scale $\ell_{T/L} = 4$ (cf. Sec. 4.4.3).

The distribution exactly at k_F is no longer fixed to unity, but depleted to a value specified by the microscopic parameters and the cutoff scale.

4.5. Renormalization group flow equations for generalized loss profiles

As a forward direction, we discuss the adaptation of the real-space RG analysis to generally shaped barriers (cf. the discussion of the variation of the loss profile in Sec. 3.9). The derivation of the perturbative corrections in Sec. 4.2.1, is based on the assumption of, first, the symmetry of the barrier leading to identical scattering properties for particles incoming from the left or right, and second, real-valued scattering amplitudes, which is a specific property of the dissipative delta barrier. Both assumptions can be easily relaxed by effectively keeping track of the position and orientation of the virtual scattering events (cf. Fig. 4.1).

To this end, we consider a generic, asymmetric barrier characterized by complex-valued scattering amplitudes r, r', t, t' different from both sides, where the primed quantities correspond to the scattering of modes incoming from the right, and the unprimed ones to modes incoming from the left. The RG analysis then proceeds as before based on the perturbative corrections (4.4). A finite width of the bare barrier is not taken into account explicitly since the leading contributions of the perturbative corrections originate from the asymptotic regions far away from the loss region. However, a finite width affects the microscopic scattering amplitudes constituting the initial conditions of the RG flow. Further, the microscopic scattering amplitudes are still assumed to vary slowly as a function of the momentum, hence excluding the study of resonant tunneling effects.

The asymptotic forms of the Green's functions (4.6) and (4.7) are readily adapted for the asymmetric scattering problem, and determine the correct choice of either the "left" or "right" scattering amplitude in the individual contributions. In addition, the Friedel oscillations acquire

an additional phase for complex-valued scattering coefficients and their asymptotic form is given by [86]:

$$\delta n(x) \simeq \frac{\sin(2k_F|x| + \arg r_{k_F})}{2\pi|x|} \times \begin{cases} |r_{k_F}| & \text{for } x < 0, \\ |r'_{k_F}| & \text{for } x > 0. \end{cases} \tag{4.52}$$

In the evaluation of the perturbative corrections (4.12), the leading terms are determined by factors of the form (focusing on the Hartree term and using $V(x)$ is short-ranged)

$$\int_{y>0} \frac{\sin(2k_F y + \zeta_1 \arg r_0) e^{\zeta_2 i 2k_F y}}{y} \sim \int_{y>0} \frac{e^{i2(k_F y + \zeta_2 k)} e^{i\zeta_1 \arg r_0} - e^{-i2(k_F y - \zeta_2 k)} e^{-i\zeta_1 \arg r_0}}{y}, \tag{4.53}$$

with $\zeta_{1,2} = \pm 1$, leading to logarithmically divergent contributions if the integrand is non-oscillating for $k \sim k_F$. Here, the parameter ζ_1 is determined by the position of the virtual scattering event, $\zeta_1 = 1$ for $x > 0$ and $\zeta_1 = -1$ for $x < 0$, and ζ_2 is fixed by the incoming direction, $\zeta_2 = 1$ for a right-traveling and $\zeta_2 = -1$ for a left-traveling mode. The divergent contributions are then identified depending on ζ_1 and ζ_2, which in turn determine the additional phase factor $\sim \exp(\pm i \arg r_0)$. The generalization of the flow equations then reduces to a bookkeeping of the position and direction of the virtual scattering events with logarithmically divergent amplitudes and the resummation produces the flow equations:

$$\frac{dt}{d\ell} = -\frac{\alpha}{2} t(|r|^2 + |r'|^2), \tag{4.54a}$$

$$\frac{dr}{d\ell} = -\frac{\alpha}{2}(tt' r'^* + |r|^2 r - r), \tag{4.54b}$$

$$\frac{dt'}{d\ell} = -\frac{\alpha}{2} t'(|r|^2 + |r'|^2), \tag{4.54c}$$

$$\frac{dr'}{d\ell} = -\frac{\alpha}{2}(tt' r^* + |r'|^2 r' - r'). \tag{4.54d}$$

Clearly, the flow equations of t, t' coincide and thus the identity $t = t'$ (cf. Sec. 3.9) is preserved during the RG flow.

In addition to the fixed points discussed in Sec. 4.3, the RG flow equations (4.54) admit fixed points characterized by

$$r = 0,\ r' = 0, \qquad t = t' \neq 0, \qquad \eta = \eta' \neq 0. \tag{4.55}$$

In the case of attractive interactions, this establishes a stable line of reflectionless fixed points with a finite loss probability. These fixed points are in principle also admitted by Eqs. (4.35). However, the fixed points (4.55) are not accessible by the RG flow of a delta barrier due to the constraint $t = 1 + r$. In contrast, for generalized barriers with a finite width, the RG flow can reach the line of fixed points (4.55), which can be easily seen by solving numerically the flow equations using the generalized initial conditions provided in Ref. [138]. A closer inspection of the in this way generalized RG flow is performed in a separate work in Ref. [137].

The necessity of a finite width in order to reach the fixed points (4.55) allows the following physical interpretation. In the case of a delta-shaped loss, the constructive interference of the virtual scattering processes entailed in the RG flow for attractive interactions can completely mask the point-like dissipation in the system. In contrast, for a barrier of finite width, the masking is incomplete and a particle transmitted through the loss region still experiences a

finite amount of dissipation. However, the loss probability of the resulting effective barrier may still be strongly modified by interactions, depending on the microscopic parameters. Contrary, for repulsive interactions, the efficient backscattering can completely screen even a finite-width loss region, and no stable fixed points with a finite dissipation are available.

4.6. Functional renormalization group approach

As an additional forward direction, we outline the application of the functional renormalization group (FRG) [6, 144] to coherent impurity problems and possible generalizations of the method to dissipative impurities. The FRG has been utilized to study coherent potential barriers in one-dimensional systems of spinless interacting fermions [118–121]. The approach is able to capture, e.g., modifications of the asymptotic behavior of Friedel oscillations by interactions [89] (cf. Sec. 2.3.4) and the power-law suppression of the local density of states at the Fermi level due to the presence of an impurity [118–121].

First, we briefly discuss the formulation of the FRG within the Matsubara formalism [1], applicable to coherent impurities in equilibrium states. The FRG is based on an infrared regulator term ΔS^Λ depending on a scale Λ, which is artificially added to the action: $S^\Lambda[\psi] = S[\psi] + \Delta S^\Lambda[\psi]$. The purpose of the regulator term is to suppress fluctuations below the scale Λ, where the implementation can be chosen problem-specific. As a result, Λ smoothly interpolates between an action where fluctuations are completely suppressed ($\Lambda = \infty$) and the desired full action ($\Lambda = 0$) including all fluctuations. A typical regularization scheme in momentum space is given by

$$\Delta S^\Lambda[\psi] = \int_q \psi(q)^* R^\Lambda(q) \psi(q), \tag{4.56}$$

where the regulator term R^Λ provides the intended regularization according to

$$\lim_{q^2/\Lambda^2 \to 0} R^\Lambda(q) = \Lambda^2, \qquad \lim_{q^2/\Lambda^2 \to \infty} R^\Lambda(q) = 0, \tag{4.57}$$

i.e., Λ corresponds to a mass scale. The interpolation to the full action then requires the gradual removal of the artificial cutoff Λ, leading to an FRG flow described by the Wetterich equation [144]

$$\partial_\Lambda \Gamma^\Lambda[\psi] = \frac{1}{2} \mathrm{tr} \left(\Gamma^{\Lambda(2)}[\psi] + R^\Lambda \right)^{-1} \partial_\Lambda R^\Lambda. \tag{4.58}$$

Here, Γ denotes the effective action which is derived from the action S [6], and $\Gamma^{(n)}$ the n-th variation of Γ. The functional differential equation (4.58) corresponds to an exact reformulation of the functional integral and can be understood as a stepwise inclusion of fluctuations [6].

The FRG was applied [118–121] to coherent impurity problems for the interacting lattice model (4.2) with an impurity term $H_\mathrm{imp} = u \psi^\dagger_{j=0} \psi_{j=0}$. The approach yields an effective description in terms of a renormalized frequency-independent self-energy Σ^Λ, which provides an effective potential via the Dyson equation $G^\Lambda = \left[(G_0^\Lambda)^{-1} - \Sigma^\Lambda \right]^{-1}$. The method is based on a regularization scheme in frequency space. To this end, a sharp frequency cutoff is introduced in the bare retarded Green's function $G_0^\Lambda(i\omega)$ (i.e., no interactions or impurity):

$$G_0^\Lambda(i\omega) = \theta(|\omega| - \Lambda) G_0(i\omega), \tag{4.59}$$

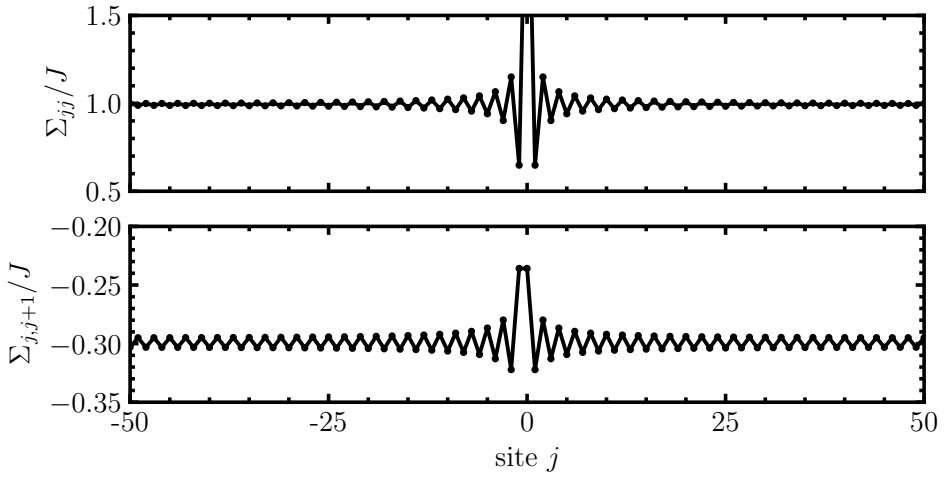

Fig. 4.10. Diagonal (upper panel) and off-diagonal parts (lower panel) of the effective potential provided by the renormalized self energy $\Sigma \equiv \Sigma^{\Lambda\to 0}$, in the vicinity of a coherent impurity. For all curves $L = 1025, U = J, u = 1.5J, \nu = 0.5$.

leading to a simple form of the flow equations. The in this way obtained exact FRG flow is described by an infinite hierarchy of flow equations for higher-order vertex functions $\Gamma^{(n)}$. In order to obtain solutions, the hierarchy of flow equations is then truncated by replacing the renormalized two-particle vertex $\Gamma^{\Lambda(4)}$ with the bare interaction potential, which for spinless fermions corresponds to an approximation to leading order in the interactions and results in a frequency-independent self energy [119]. This procedure yields flow equations for the self-energy given by

$$\partial_\Lambda \Sigma^\Lambda_{j,j} = -\frac{U}{2\pi} \sum_{s=\pm 1} \sum_{\omega=\pm\Lambda} G^\Lambda_{j+s,j+s}(i\omega), \qquad \partial_\Lambda \Sigma^\Lambda_{j,j\pm 1} = \frac{U}{2\pi} \sum_{\omega=\pm\Lambda} G^\Lambda_{j,j\pm 1}(i\omega), \tag{4.60}$$

i.e, the self energy remains tridiagonal. Accordingly, the diagonal part of the self energy provides an effective on-site potential while the off-diagonal part modifies the hopping terms.

Figure 4.10 shows the self energy obtained by solving the FRG flow ($\Lambda \to 0$) for a coherent impurity by implementing the method of Refs. [119, 120]. The self energy exhibits oscillations in its diagonal (upper panel) and minor diagonal part (lower panel), similar to the Hartree and exchange potentials (4.5) considered in the analysis of the present chapter. In contrast to the latter, within the FRG approach, the effective self energy is modified by the interactions. From these effective potentials, e.g., the single-particle density of states $\mathrm{LDoS}_j(\omega) = -\mathrm{Im}G_{jj}(\omega + i0^+)$ [120] can be reconstructed, which near the impurity is found to be suppressed at the Fermi level, as shown in Fig. (4.11), signaling an obstruction of transport.

The generalization of the so far discussed FRG approach to dissipative impurities appears promising. However, a straightforward adaptation leads to significant problems, as laid out in the following. First, the Wetterich equation can be straightforwardly generalized to non-equilibrium problems formulated within a Keldysh framework [6]. Formally, a sharp-frequency cutoff (4.59) in the retarded Green's function is compliant with the Keldysh structure and FRG flow equations for the self-energy can be derived in analogy to the Matsubara formalism. However, the adaptation of the simple frequency regularization scheme (4.59) to the Keldysh FRG fails because the obtained flow equations violate causality [145]. The violation of causality

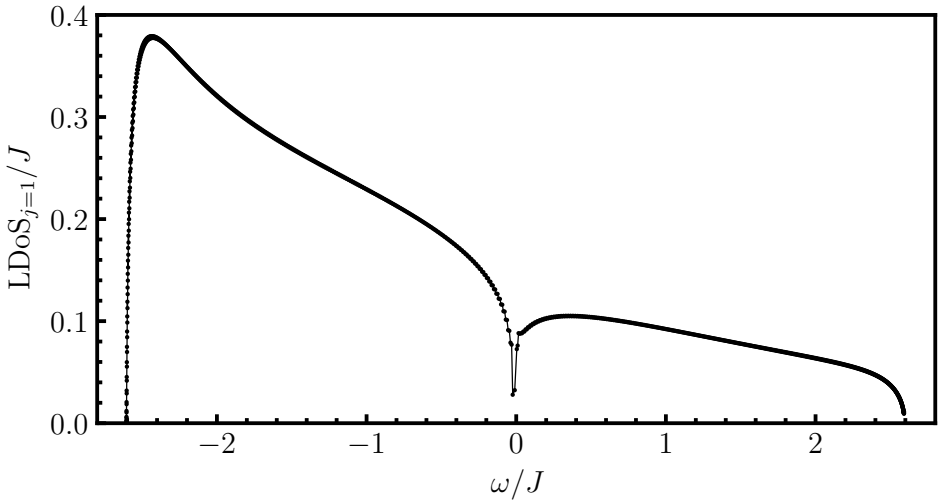

Fig. 4.11. Local density of states at site $j = 1$ next to the impurity as a function of frequency ($\omega = 0$ corresponds to the Fermi level), for $L = 1025, U = J, u = 1.5J, \nu = 0.5$.

can be rationalized by the following simple argument. In the imaginary-time Matsubara formalism, a real positive regulator term cannot shift the poles of the retarded Green's function, $G_0^\Lambda \sim (i\omega + R_\Lambda)^{-1}$. In contrast, in the real-time Keldysh approach such a regulator can lead to a shift the poles, $G_0^\Lambda \sim (\omega + R_\Lambda)^{-1}$. As a consequence, the sharp frequency cutoff scheme can result in a violation of causality in the Keldysh framework and the in this way obtained FRG flow is unphysical, which is signaled by a numerically unstable flow. Consequently, improvements of the regularization scheme are required for the application of the FRG method to dissipative impurity problems. The comparison of the Matsubara and Keldysh pole structures suggests a possible regularization via an imaginary regulator term, $G_0^\Lambda \sim (\omega + iR_\Lambda)^{-1}$. Moreover, real-time approaches as conducted in Ref. [10] seem promising candidates for the generalization to dissipative impurities.

4.7. Conclusion and outlook

In conclusion, we extended the microscopic model of a fermionic wire subject to a localized loss by including interparticle interactions. A study of interaction effects was performed perturbative in the interaction strength V, and for arbitrary dissipation strengths γ. Within a real-space RG scheme, we obtained the effective scattering probabilities of modes near the Fermi energy. Due to the effective barrier constituted by Friedel oscillations in the vicinity of the loss site, the scattering probabilities are strongly renormalized. As a central result, the loss probability near k_F is suppressed for both repulsive and attractive interactions, vanishing exactly at k_F. In the vicinity of this domain of suppressed loss, modes can experience either increased or decreased dissipation, depending on the microscopic parameters. Moreover, the transport properties are strongly modified near the Fermi level, leading to perfect reflection for repulsive, and perfect transmission for attractive interactions. The RG flow near the fixed points exhibits a universal behavior. For repulsive interactions, the stable fixed point is approached algebraically with an exponent depending only on the microscopic interaction strength, typical for interacting fermions in one dimension. For attractive interactions, a new type of scaling behavior is shown

where the fixed point is approached logarithmically. Moreover, the renormalization of the loss probability is reflected in observables characterizing the depletion of the system in the presence of a localized loss. A momentum-resolved particle loss rate was defined whose renormalization due to interactions directly reflects the renormalization of the loss probability. In turn, the distribution of particles remaining in the wire is expected to signal the suppressed loss probability by an increased occupation of modes near the Fermi level. An estimate of the scaling of the renormalized loss probability in experimental setups with finite size and finite temperature suggests the principle accessibility of the renormalization effects.

A probe of the renormalization effects by measuring the momentum distribution inside the wire is feasible with time-of-flight measurements. However, the author is not aware of an experimental setup in which up to now a momentum-resolved measurement of the stream of emitted particles was performed.

In Chapter 5 the modified depletion of the momentum distribution due to interaction effects is probed numerically within a Hartree-Fock approximation. Moreover, non-perturbative methods such as bosonization provide a well-established toolbox to include interaction effects in systems of one-dimensional interacting fermions (cf. Sec. 2.3). Hence, in Chapter 6, we perform a study of a localized loss in a Luttinger liquid theory, establishing an approach complementary to the perturbative analysis of the present chapter.

The approach within the first-order Born approximation in this chapter neglects higher-order processes which can lead to a redistribution of the increased occupation of modes near the Fermi level. However, since the depletion proceeds in time, an increased occupation is still expected to be observable as long as the depletion takes place on a time scale shorter than the one of redistribution processes. Nevertheless, a closer inspection of the distribution dynamics including self-thermalization effects is desirable. Moreover, the adaptation of different microscopic approaches such as the FRG to dissipative impurity problem can be expected to yield additional insights. The extension to generalized barrier shapes introduces an enriched structure of the RG flow, as discussed in Sec. 4.5, calling for an extensive study of the fixed points and associated scaling behavior, which is performed in a separate work in Ref. [137]. As the RG flow suggests a strong modification of the transport properties across a loss barrier, a more extensive study of transport is also desirable, calling for a generalization of Landauer transport in the presence of both a localized loss and a voltage bias as sources of currents. To this end, a closer inspection of the transport properties of an interacting wire with a localized loss connected to reservoirs at its far ends has been studied in a separate work in Ref. [146]. Moreover, the real-space RG scheme developed for a coherent barrier was adapted to settings exhibiting resonant tunneling [147]. The discussion of resonant tunneling effects for lossy barriers is discussed in Ref. [137]. In addition, the real-space RG scheme for coherent impurities was also adapted to spinful fermions [85, 86] leading to novel effects in the presence of a magnetic field due to scattering processes between the two species, thus suggesting a study of localized dissipation in these systems.

CHAPTER 5

DYNAMICAL HARTREE-FOCK APPROACH

Coherent impurities in one-dimensional fermionic systems have been investigated within Hartree-Fock approximation schemes revealing several aspects predicted from the Luttinger liquid theory [118, 119, 148–155]. In Chapter 3, we investigated the dynamics of the non-interacting system in the presence of localized loss by making use of the correlation matrix $C_{ij}(t)$. The method can be straightforwardly adapted to include interactions within a Hartree-Fock approximation. This allows us to study the effect of interactions on the results discussed in Chapter 3, such as the dynamical regimes, the particle loss rate, and the density profile after the quench. In addition, we study the modification of the momentum distribution due to interactions and compare the result with the predictions discussed in Chapter 4. We find an increased occupation of particles remaining in the wire with momentum $k \sim k_F$ (cf. Sec. 3.6), reflecting the suppression of losses near the Fermi momentum.

The main results of this chapter have been published in publication [134]. We present here a more detailed discussion complemented by additional results.[1]

5.1. Hartree-Fock approximation scheme

We consider a lattice model of localized loss described by the quantum master equation (3.4), whose coherent part of the dynamics is generated by the interacting Hamiltonian (4.2)

$$H = -J \sum_j \left(\psi_{j+1}^\dagger \psi_j + \text{h.c.} \right) + U \sum_j n_j n_{j+1}, \tag{5.1}$$

with $n_j \equiv \psi_j^\dagger \psi_j$ the density operator, and U the microscopic interaction strength. The dynamical Hartree-Fock approximation [156] is then implemented as follows. Starting from the adjoint quantum master equation (3.6), we derive the equation of motion for the correlation matrix $C_{ij}(t) = \langle \psi_i^\dagger(t) \psi_j(t) \rangle$ (3.5). As a consequence of the interacting Hamiltonian (5.1), the resulting equation of motion is not closed but depends on quartic correlators, which in turn depend on

[1] Sections 5.2.2, 5.2.4, and 5.3 contain large parts which can be found with minor adaptions in publication [134]. Other sections may contain paragraphs and sentences that appear verbatim in publication [134].

sextic correlators and so on. Therefore, in contrast to the non-interacting model (cf. Sec. 3.2.1), a hierarchy of coupled equations of motions for higher order correlation functions is obtained. The Hartree-Fock approximation then consists in closing the equations of motion for the correlation matrix by reducing the quartic correlators into a product of quadratic correlators by the means of Wick's theorem, i.e., by replacing $\psi_j^\dagger\psi_j\psi_{j+1}^\dagger\psi_{j+1} \to C_{j,j}\psi_{j+1}^\dagger\psi_{j+1} + C_{j+1,j+1}\psi_j^\dagger\psi_j - C_{j+1,j}\psi_j^\dagger\psi_{j+1} - C_{j,j+1}\psi_{j+1}^\dagger\psi_j$. As a result, the time-evolution of the correlation matrix is determined by the equation of motion

$$\frac{\mathrm{d}}{\mathrm{d}t}C_{ij}(t) = i\sum_l \left(\widetilde{H}_{HF,il}^\dagger(t)C_{lj}(t) - C_{il}(t)\widetilde{H}_{HF,lj}(t)\right), \tag{5.2}$$

with the following time-dependent non-Hermitian Hamiltonian:

$$\widetilde{H}_{\mathrm{HF}}(t) = \sum_j \left[\left(-J_j(t)\,\psi_{j+1}^\dagger\psi_j + \mathrm{h.c.}\right) - \mu_j(t)\,\psi_j^\dagger\psi_j - i\gamma\delta_{j,0}\psi_j^\dagger\psi_j\right]. \tag{5.3}$$

Here, J_j and μ_j are the effective hopping strength and on-site potential, respectively,

$$\mu_j(t) = -U\left[C_{j-1,j-1}(t) + C_{j+1,j+1}(t)\right], \tag{5.4a}$$
$$J_j(t) = J + UC_{j,j+1}(t). \tag{5.4b}$$

As before, we consider the system to be prepared in its thermal ground state before switching on the localized loss. Since the initial state is translational invariant, it is characterized by homogeneous values of J_j and μ_j, and described by Eqs. (3.10) and (3.11) with a redefined hopping strength and chemical potential. Observables are computed by numerically solving Eq. (5.2) with the Hamiltonian (5.3) and initial state (3.10). The numerical solution is performed by integrating the coupled equations of motion (5.2) for the $L(L+1)/2$ independent complex components of the correlation matrix (3.5). Hence, the computational effort is significantly increased compared to the non-interacting model where an explicit solution (3.9) at time t was available for numerical evaluation.

5.2. Real-space dynamics

Based on the dynamical Hartree-Fock description developed in the previous section, we discuss the dynamics of observables such as the particle loss rate and density profile in the presence of a localized loss. This enables us to investigate interaction effects on the properties of the dynamical regimes which were elaborated in Chapter 3. While the validity of the qualitative description is confirmed, modifications of the dynamics are encountered depending on the interaction strength.

5.2.1. Particle loss rate: Temporal regimes

The description of the dynamics in terms of the three temporal regimes identified for the interaction-free model in Sec. 3.2.2 remains valid in the presence of interactions. In order to clarify this aspect, in Fig. 5.1 the total particle loss rate is shown for different interaction strengths U as a function of time elapsed from the quench. Both, repulsive and attractive

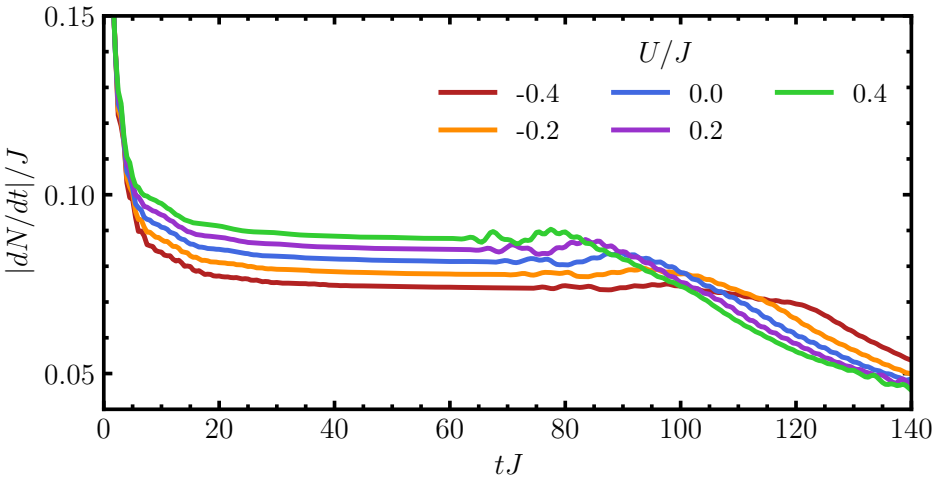

Fig. 5.1. Particle loss rate from the Hartree-Fock approximation as a function of time elapsed from the quench for different interaction strengths U. For all curves $\gamma = 0.5, \nu = 0.25, L = 141$.

interactions are considered as well as the non-interacting case for comparison. The initial drop of the loss rate characterizing the first temporal regime proceeds independently of the interaction strength. This behavior is a consequence of the locality of the depletion in the first regime, cf. the discussion in Sec. 3.2.2. In contrast, the constant loss rate in the second temporal regime depends on the interaction strength. The loss rate is enhanced for repulsive interactions while it is suppressed for attractive ones, with the amount of enhancement and suppression increasing with the strength of the interactions, respectively. We elaborate more on this effect in Sec. 5.2.4. Furthermore, the end of the second temporal regime occurs earlier in time for repulsive interactions, while, in turn, it occurs later for attractive ones, as compared to the non-interacting case. This observation suggests a modification of the light-cone speed (cf. Secs. 3.2.2 and 3.2.4) due to interactions, which is examined in more detail in Sec. 5.2.3.

5.2.2. Density profile

In Fig. 5.2 the density profile is shown for repulsive ($U > 0$, red curve) and attractive ($U < 0$, blue curve) interactions, in comparison to the density profile of the non-interacting system (yellow curve). The density profiles are evaluated after the same time elapsed from the quench for different interactions. The density profile exhibits density oscillations which decay in space with increasing distance from the loss site. The period of the oscillations is identical in all cases, determined solely by k_F (cf. Eq. (3.59)) as expected for Friedel oscillations also in the presence of interactions [89]. On the other hand, the amplitude of the envelope of the oscillations is increased (decreased) for repulsive (attractive) interactions. The extent of the depleted region and consequently the propagation velocity of the light cone (cf. Secs. 3.2 and 3.2.4) is visibly dependent on the interaction strength. This can be understood by noticing that the group velocity v_k (cf. discussion in Sec. 3.2) of the non-interacting problem is modified due to interactions, which is quantified in the following section.

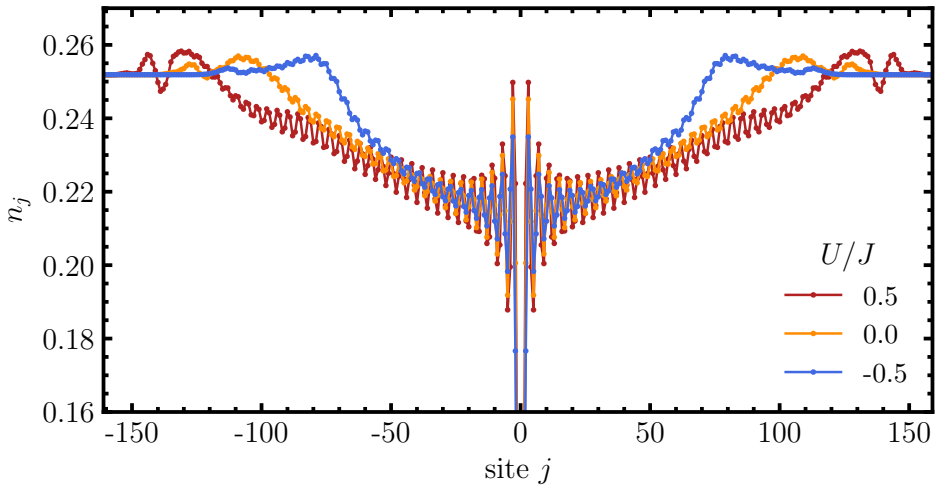

Fig. 5.2. Density profile from the Hartree-Fock approximation for different interaction strengths at time $tJ = 65$ elapsed from the quench. For all curves $\gamma = 3J, L = 401, \nu = 0.25$.

5.2.3. Modified group velocity

We now compute the modification of the group velocity v_k due to interactions within the present approximation. A modified group velocity rationalizes the interaction dependence of the light-cone speed v observed in Figs. 5.1 and 5.2, due to the simple relationship between v and v_k found in Sec. 3.4. Moreover, in Sec. 5.2.4 below, the modified group velocity is utilized in order to quantify the dependence of the total particle loss rate on the interaction strength.

To this end, we compute the corrections to the hopping strength in the initial state by evaluating Eq. (5.4b) using the correlations (3.10), yielding [157]

$$C_{j,j+1} = \int_{k,k'} \mathrm{e}^{-ijk+ijk'+ik'} C_{k,k'} = \int_k \mathrm{e}^{ik}\theta(\epsilon_F - \epsilon_k) = \int_{-k_F}^{k_F} \frac{dk}{2\pi}\mathrm{e}^{ik} = \frac{\sin k_F}{\pi}, \tag{5.5}$$

where we used $C_{k,k'} = \delta_{k,k'}\theta(\epsilon_F - \epsilon_k)$ for the homogeneous initial state. Hence, we obtain from Eq. (5.4b) a renormalized hopping strength according to $J \to J + U\sin(k_F)/\pi$, with J the hopping strength in the absence of interactions. By taking the Fourier transform of the effective Hamiltonian (5.3) we infer the group velocity

$$v_{\mathrm{HF},k} = \left(1 + \frac{U}{\pi J}\sin k_F\right) v_k, \tag{5.6}$$

i.e., the group velocity is modified by a factor depending only on the filling and interaction strength. Hence, the propagation of the light cone (cf. Sec. 3.4) is faster (slower) for repulsive (attractive) interactions as compared to the non-interacting system, in agreement with Figs. 5.1 and 5.2.

5.2.4. Particle loss rate: Interaction effects

The total particle loss rate in the second regime (cf. Sec. 3.2) is shown in Fig. 5.3 as a function of γ for different interaction strengths (dots). The non-monotonic behavior due to the microscopic

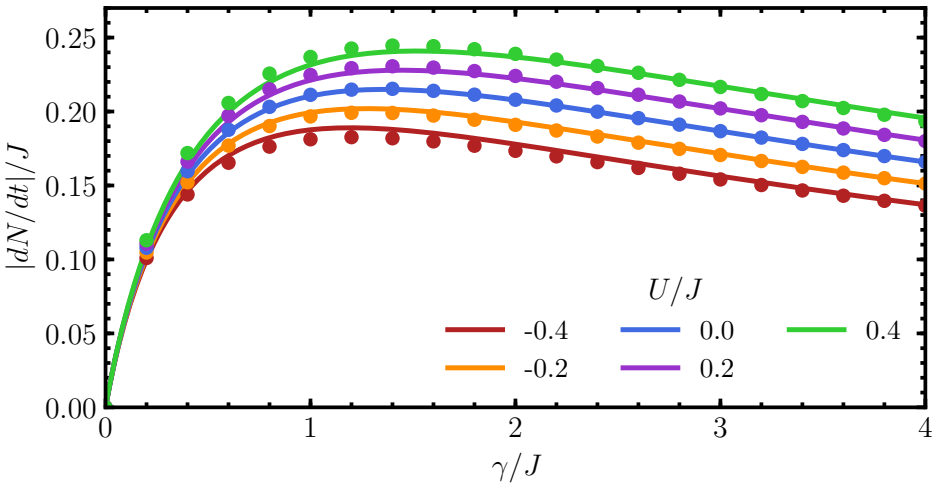

Fig. 5.3. Total particle loss rate in the second regime as a function of γ for different interaction strengths U, for $L = 151, \nu = 0.4$ from the Hartree-Fock approximation (dots), in comparison to the analytical prediction (lines).

quantum Zeno effect is clearly visible for all values of U. For all γ, the loss rate is increased for repulsive interactions while it is decreased for attractive ones, respectively. The dependence of the particle loss rate on the interaction strength can be described analytically (solid lines) by using the modified group velocity (5.6), resulting in good agreement with the numerical results. More precisely, the solid lines represent analytical results obtained from Eq. (3.80) with the interaction-dependent group velocity given by Eq. (5.6), yielding

$$\frac{\mathrm{d}N}{\mathrm{d}t} = -\int_k |v_{\mathrm{HF},k}|\, \eta_k(\gamma/v_{\mathrm{HF},k})\, n_{0,k}, \tag{5.7}$$

where the modified group velocity enters also in the expression for the loss probability (3.37) according to

$$\eta_k(\gamma/v_{\mathrm{HF},k}) \equiv \frac{2\gamma|v_{\mathrm{HF},k}|}{(\gamma+|v_{\mathrm{HF},k}|)^2}. \tag{5.8}$$

5.3. Momentum distribution: Fluctuation-induced quantum Zeno effect

According to the discussion in Chapter 4, we expect strong interaction effects on the loss probability near the Fermi momentum, suppressing the depletion of modes near k_F for repulsive interactions. Since the total particle loss rate, considered in the previous section, contains contributions of all momenta, it is not a well-suited observable to study this effect. Instead, we consider the momentum distribution n_k, which can be regarded as a measure of the particles remaining in the system (cf. Secs. 3.6 and 4.4.2). A suppression of loss at the Fermi edge reveals itself as an increased occupation in n_k at these modes. In the presence of interactions n_k remains a good measure of the loss processes as long as redistribution processes of the modes take place on time scales larger than the one of depletion processes. Within the present approximation, such redistribution processes are neglected.

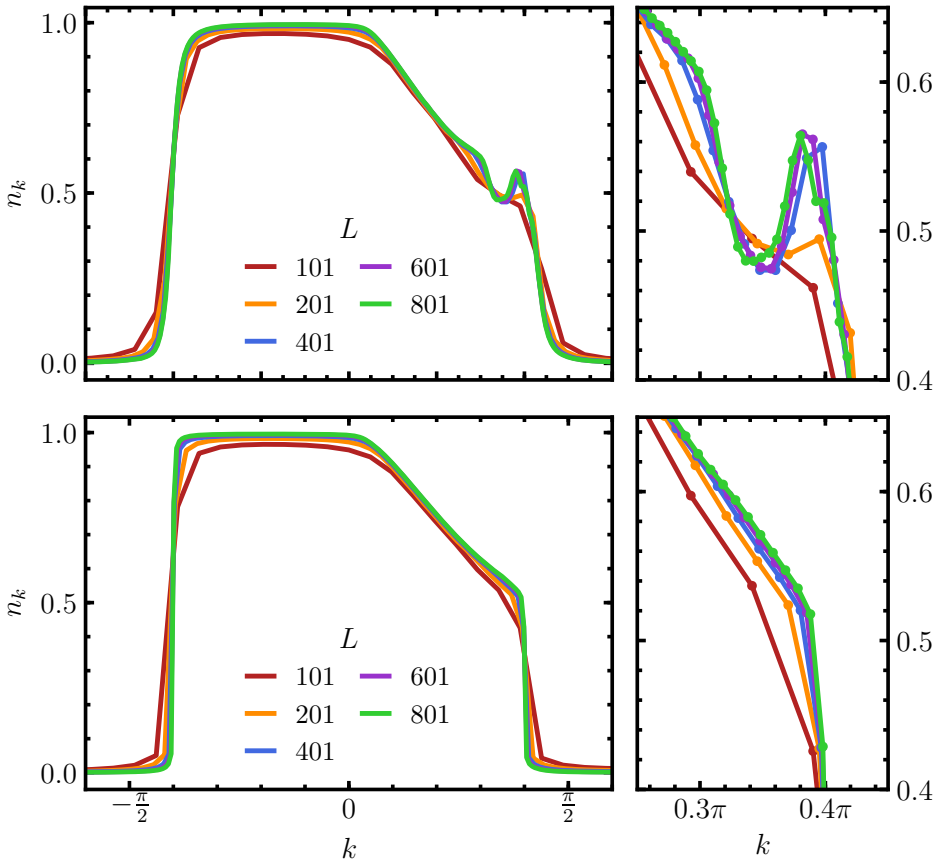

Fig. 5.4. Momentum distribution n_k for repulsive interactions $\nu U = 3/5J$ (upper panels) and the non-interacting system $\nu U = 0J$ (lower panels) for increasing system sizes L. The distribution is obtained at $tJ = L/7$ close to the end of second regime, in a segment with sites $j \in [0, 2L/5]$ right to the impurity corresponding to the depleted region at that time. The smaller panels show a magnified view of the distribution in the respective panel to the left around $k_F = \nu\pi$. For all curves $\gamma = 3J, \nu = 0.4$.

In Fig. 5.4 (upper panels) we report the momentum distribution in a segment of the wire right to the loss site within the light cone (see discussion below; cf. Sec. 3.6.3) at a time near the end of the second regime. The momentum distribution reveals a pronounced peak in the occupation of modes at the Fermi momentum. As a comparison, in the non-interacting system such a peak is absent, as shown in the lower panels in Fig. 5.4. The presence of a peak at k_F in the momentum distribution is consistent with the results of Chapter 4 stating that the loss of particles with a momentum close to k_F is reduced in the presence of interactions, resulting in an enhanced occupation at this scale. Thus, we interpret the increased occupation near k_F as a signature of the fluctuation-induced quantum Zeno effect. The peak builds up with increasing system size, with which also the absolute size of the region exhibiting Friedel oscillations grows, providing the physical mechanism of the suppression of loss near k_F. The evaluation time is scaled with the system size such that the considered segment represents a constant fraction of the system.

The asymmetric shape of the momentum distribution in Fig. 5.4 results from the choice of a segment of the wire situated to the right of the loss site (but within the light cone). With this choice, all particles with $k > 0$ have scattered off the impurity and thus bear the signature of depletion effects. Particles with $k < 0$, instead, arrive from the right and have not encountered

the loss site yet (cf. Eq. (3.83)). This specific segment is chosen in order to maximize the visibility of the peak, which is reduced by the smearing of the momentum distribution near the Fermi edge (see Fig. 5.4 and Figs. 3.8–3.10). Instead, if a segment centered at the loss site is considered, the population of each momentum k takes two contributions: from particles that do not encounter the loss (whose distribution resembles the left-hand side of the distribution in Fig. 5.4, upper-left panel), and from particles that do (whose distribution resembles the right-hand side of the distribution in Fig. 5.4, upper-left panel). One can check that the distribution for a segment centered symmetrically at the loss site, $n_{\mathrm{symm}}(k)$, can indeed be reconstructed from the distribution obtained only from the right-hand side of this segment, $n_{\mathrm{rhs}}(k)$, as $n_{\mathrm{symm}}(k) = 1/2(n_{\mathrm{rhs}}(k) + n_{\mathrm{rhs}}(-k))$. As a consequence, the peak would be averaged with the smeared, undepleted part of the distribution, thus lowering the visibility of the peak. We consequently can eliminate this contribution by choosing the segment only at one side of the impurity. Further, we note that the peak appears slightly to the left of k_F, which we similarly interpret as a smearing effect.

The height of the peak present in Fig. 5.4 can be compared to the expectations for the renormalized value of η based on the results of Chapter 4. To this end, we estimate the interaction parameter α (4.32) and the cutoff scale ℓ_L (4.50) due to the finite size of the system (cf. Sec. 4.4.3). For the size of the largest segment considered (320 sites), we obtain a cutoff scale $\ell_L = \ln L/\lambda_F \simeq 4$. In order to estimate the interaction parameter α, we rewrite the interacting part of the Hamiltonian (5.1) in a symmetrized way

$$H_{\mathrm{int}} = \sum_{i,j} U_{i,j} n_i n_j, \qquad U_{i,j} = \frac{U}{2}(\delta_{i,j+1}, +\delta_{j+1,i}), \tag{5.9}$$

and obtain as the Fourier transform of the interaction vertex $U_{i,j}$

$$\widetilde{U}_{k,k'} = \delta_{k,k'} U_k, \qquad \widetilde{U}_k = U \cos k. \tag{5.10}$$

With the identification of $\widetilde{U}_k$ and $\widetilde{V}(k)$ in Eq. (4.32), we obtain an estimate of the interaction parameter as

$$\alpha = \frac{2U(1 - \cos 2k_F)}{2\pi v_F}, \tag{5.11}$$

yielding $\alpha \approx 0.5$ for the microscopic parameters considered in Fig. 5.4. With this at hand, we can compute the renormalized value of η by solving the RG flow equations (4.36) and, in turn, reconstruct the momentum distribution at k_F, i.e., n_{k_F} (cf. Sec. 4.4.2). This procedure predicts an increase of the occupation by a factor $n_{k_F}(\ell = 4)/n_{k_F}(\ell = 0) \simeq 1.08$. On the other hand, we quantify the increase of the occupation at k_F seen in Fig. 5.4 by comparing the occupation at the peak $n_k \sim 0.56$ for the interacting system (upper right panel), to the occupation at the Fermi level $n_k \sim 0.52$ for the non-interacting system (lower right panel). These values correspond to an increase of the occupation in the interacting system by a factor $\simeq 1.08$, in good agreement with the estimate based on the RG flow. Finally, also the expected width of the feature near the Fermi level given by $2d^{-1} = 2\lambda_F^{-1} \simeq 0.4$ agrees with the width of peak observed in Fig. 5.4 ($\sim 0.1\pi$).

5.4. Conclusion and outlook

The inclusion of interactions within a dynamical Hartree-Fock approximation scheme complements the analysis of the dynamics in presence of a localized loss provided in Chapter 3 for the non-interacting system. The notion of three temporal regimes is found to remain well-defined, where most importantly a NESS is revealed, characterized by a constant loss rate and Friedel oscillations in the vicinity of the loss site. Observables such as the total particle loss rate and light-cone speed are modified as a result of an interaction-dependent group velocity. Here, repulsive interactions lead to an increase of the group velocity, whereas attractive interactions lead to a decrease. This behavior, in turn, corresponds directly to an increase or decrease, respectively, of the total particle loss rate and light-cone speed. While the group velocity is modified in a momentum-independent way, the momentum distribution of remaining particles exhibits an increased occupation of modes near the Fermi level. This feature is characteristic for the suppression of losses for modes near k_F in accordance with the analysis of Chapter 4.

In a recent numerical study [25], the interacting lattice model (3.4) with a localized loss was investigated within a DMRG approach, incorporating interactions exactly. The therein found results are consistent with the in the present chapter developed description of temporal regimes, Friedel oscillations, and momentum distribution dynamics.

We conclude with a brief discussion on the validity of the Hartree-Fock approach applied in the present section. Static Hartree-Fock approximation schemes have been applied to impurity and boundary problems in one-dimensional quantum systems [119, 150–152]. Applications of self-consistent Hartree-Fock schemes have been discussed as leading in some cases to Friedel oscillations being non-decaying at large distances from an impurity [149, 150]. This can be interpreted [152] as an onset of charge-density-wave order different from the expected Luttinger liquid behavior. In other studies, however, no charge-density-wave order was found [153–155, 158]. We expect the here applied dynamical Hartree-Fock approach to capture qualitatively the local physics around the localized loss in the second temporal regime. An instability towards charge-density order would be signaled by a non-decaying amplitude of Friedel oscillations building up within the light cone. The study of charge-density ordered systems is itself an interesting problem where a fluctuation-induced quantum Zeno effect could emerge due to the formation of a gap at k_F [150].

CHAPTER 6

LUTTINGER LIQUIDS WITH LOCALIZED LOSSES

The Luttinger liquid is an effective theory able to capture the low-energy, collective behavior of gapless one-dimensional quantum systems with arbitrary interaction strengths [84, 159] (see Sec. 2.3). Among its many applications, it has been widely used in the study of impurities in fermionic systems [159], notably the paradigmatic Kane-Fisher problem [79, 80]. In these approaches, the effect of an impurity on the low-energy properties of the system is formulated in terms of an effective impurity strength renormalized by interactions [79–81]. As a result, for repulsive interactions, even a small microscopic impurity is found to effectively disjoint the wire at zero temperature, while contrary, for attractive interactions, perfect conductance is restored even in presence of a strong microscopic barrier.

We utilize the toolbox of Luttinger liquid theory to study the effects of a localized loss on the low-energy properties of an interacting quantum wire. To this end, we apply the bosonization technique [84] to obtain a Luttinger liquid description (cf. Sec. 2.3) of the microscopic interacting model with a localized loss defined in Sec. 4.1. As the system under consideration is driven out of equilibrium by the localized loss, a convenient functional description is then provided by the Keldysh field theory [4, 6]. In this formulation of the problem, the effect of the dissipative impurity on low-energy modes can be revealed by studying its RG flow. A first approach, perturbative at first order in the impurity strength, captures the effects of the renormalization of the loss impurity consistently with the microscopic approach presented in Chapter 4. This entails that for both attractive and repulsive interactions the loss of modes near the Fermi level is suppressed. In the case of attractive interactions, the dissipation strength γ is found to renormalize to zero, thus describing a fully transmissive barrier and the absence of losses, establishing a fluctuation-induced transparency. For repulsive interactions, the dissipation strength γ is instead enhanced infinitely leading to a fully reflective barrier. However, also in this case losses are expected to be suppressed via the quantum Zeno effect. Hence, the effective barrier for repulsive interactions constitutes a fluctuation-induced quantum Zeno effect. The Luttinger liquid approach in this chapter is valid for arbitrary interactions but perturbative in the impurity strength. Thus, it establishes a complementary method to the microscopic study in Chapter 4, as the latter is perturbative in the interaction strength but valid for arbitrary dissipation strengths.

Moreover, in Luttinger liquids out of equilibrium, an effective local temperature can be generated by self-thermalization effects due to the nonlinear terms of the impurity action [9, 11, 122, 123]. These effects are not captured within a treatment at first order in the impurity strength but require an extension of the RG description to second order [9, 11, 122, 123]. The main effect of an effective local temperature is to effectively cut off the RG flow. By performing a second-order analysis, we are able to identify different regimes depending on the microscopic parameters in which either the first-order results qualitatively persist or the effective temperature dominates the RG flow.

This chapter is structured as follows. As a starting point, we formulate a description of the Luttinger liquid theory with localized losses in terms of a Keldysh functional integral. We then perform an RG analysis perturbative to first order in the dissipation strength γ and study its RG flow. As a benchmark, we apply the Keldysh formalism also to a coherent impurity, recovering the results of Refs. [79, 80]. A complementary perturbative study is performed for large dissipation strength by mapping the problem to two disjoint wires with the loss site providing a weak link $\sim \gamma^{-1}$. With the RG analysis for the weak and strong dissipation limits at hand, we can study the RG flow of γ and the scaling behavior near the fixed points, allowing a comparison to the results of the microscopic approach performed in Chapter 4. The RG analysis is then extended to second order in the dissipation strength in order to investigate the generation of an effective local temperature and its consequences.

The main results of this chapter have been published in publications [133] and [134].[1] We present here a more in-depth derivation and discussion of the results.

6.1. Luttinger liquid description

Bosonization is a powerful technique providing exact results for the low-energy properties of one-dimensional quantum systems even in the presence of interactions by exploiting the collective nature of low-energy excitations in these systems (see Sec. 2.3). We first formulate the Keldysh field theory in the language of bosonization for an unperturbed Luttinger Liquid, i.e., in the absence of any impurity.

The low-energy properties of the microscopic interacting Hamiltonian (4.1) are then described by the Luttinger liquid Hamiltonian (2.77) [84, 159]

$$H = \frac{v}{2\pi} \int_x \left[g \left(\partial_x \phi\right)^2 + g^{-1} \left(\partial_x \theta\right)^2 \right], \tag{6.1}$$

with θ and ϕ real bosonic fields related to density and phase fluctuations, respectively, $v > 0$ the sound velocity and g the Luttinger parameter, both encoding the effect of interactions. In particular, $g < 1$ corresponds to microscopic repulsive interactions and $g > 1$ to attractive ones, with $g = 1$ for a non-interacting system. The fields θ and ϕ are canonically conjugate (on an operatorial level) and thus their fluctuations compete according to the Heisenberg uncertainty principle. The Hamiltonian can readily be interpreted in terms of this competition: for repulsive interactions, $g < 1$, density fluctuations are suppressed whereas for attractive interaction, $g > 1$, phase fluctuations are suppressed.

[1] Several paragraphs and sentences in this chapter can be found almost identically in publication [134].

The low-energy physics of the interacting models defined in Sec. (4.1) is captured for arbitrary interaction strength by the Luttinger Hamiltonian (6.1), with the only exception being the lattice model at half filling which requires additionally $|U| < 2$ [84]. In the latter case, the Luttinger parameter g can be expressed in a simple way as a function of the microscopic parameters, $g^{-1} = 2\arccos(-U/2J)/\pi$ [119].

The Keldysh partition function Z describing the thermal state $\sim \exp(-H/T)$ can be formulated in terms of the functional integral [12, 160, 161] (cf. Sec. 2.1.2)

$$Z = \int \mathcal{D}\left[\phi_+, \phi_-, \theta_+, \theta_-\right] e^{iS_0[\phi_+,\phi_-,\theta_+,\theta_-]}. \tag{6.2}$$

Here, S_0 is the Keldysh action of the unperturbed system which consists of four real fields $\phi_+, \phi_-, \theta_+, \theta_-$, with $+, -$ the Keldysh contour indices, and reads [162]

$$S_0\left[\phi_+, \phi_-, \theta_+, \theta_-\right] = \int_{t,x} \left[\left(\frac{1}{\pi}\partial_t\phi_+\partial_x\theta_+ - H(\phi_+, \theta_+)\right) - \left(\frac{1}{\pi}\partial_t\phi_-\partial_x\theta_- - H(\phi_-, \theta_-)\right)\right]. \tag{6.3}$$

The structure of S_0 reflects that the fields $\partial_x\theta$ and ϕ are conjugate variables [84]. Since it is more convenient to work in the RAK basis (see Sec. 2.1.2), we perform the Keldysh rotation $\phi_\pm = (\phi_c \pm \phi_q)/\sqrt{2}$ (and analogously for $\theta_\pm$), where c, q denote the classical and quantum fields [4]. Moreover, by taking the Fourier transform (3.17) we arrive at

$$S_0 = \frac{1}{2}\int_{k,\omega} \chi^\dagger(k,\omega) \begin{pmatrix} 0 & P_R^\dagger(k,\omega) \\ P_R(k,\omega) & P_K(k,\omega) \end{pmatrix} \chi(k,\omega), \tag{6.4}$$

with $\chi \equiv (\phi_c, \theta_c, \phi_q, \theta_q)^T$, where χ is subject to the condition $\chi^\dagger(k,\omega) = \chi^T(-k,-\omega)$ since the fields are real-valued. Here, the Keldysh inverse propagators P_K and retarded P_R are given by

$$P_R = \frac{1}{\pi}\begin{pmatrix} -k^2vg & k(\omega + i\epsilon) \\ k(\omega + i\epsilon) & -k^2vg^{-1} \end{pmatrix}, \qquad P_K = \frac{2}{\pi}\begin{pmatrix} 0 & ik\epsilon\coth\frac{\omega}{2T} \\ ik\epsilon\coth\frac{\omega}{2T} & 0 \end{pmatrix}. \tag{6.5}$$

The infinitesimal dissipation ϵ acts as a regularization ensuring causality [4], while the form of P_K has been chosen to enforce the fluctuation-dissipation relation (cf. Sec. 2.1.2), and, consequently, thermal equilibrium [6]. The retarded, advanced, and Keldysh Green's functions G_R, G_A, and G_K, respectively, are obtained according to Eq. (2.40) by

$$\begin{pmatrix} G_K & G_R \\ G_A & 0 \end{pmatrix} = \begin{pmatrix} -P_R^{-1}P_KP_A^{-1} & P_R^{-1} \\ P_R^{\dagger -1} & 0 \end{pmatrix}, \tag{6.6}$$

from which the correlation functions are derived via Eq. (2.41). One can straightforwardly verify that the Green's functions (6.6) indeed fulfill the fluctuation-dissipation theorem (cf. Eq. (2.47))

$$G^K = \coth\frac{\omega}{2T}(G^R - G^A), \tag{6.7}$$

for bosonic degrees of freedom in an equilibrium state with temperature T.

It is instructive to integrate out one of the two fields θ, ϕ in the action (6.4) to obtain a reduced representation in terms of the remaining field. The effective action after the integration [6] of

the ϕ-fields is given by

$$S\left[\theta_q, \theta_c\right] = \frac{1}{2}\int_{k,\omega} \begin{pmatrix} \theta_c(-k,-\omega) & \theta_q(-k,-\omega) \end{pmatrix} P_\theta(\omega,k) \begin{pmatrix} \theta_c(k,\omega) \\ \theta_q(k,\omega) \end{pmatrix}, \tag{6.8}$$

with the inverse propagator

$$P_\theta(\omega,k) = \frac{1}{\pi}\begin{pmatrix} 0 & g^{-1}v^{-1}\left[v^2k^2-(\omega-i\epsilon)^2\right] \\ g^{-1}v^{-1}\left[v^2k^2-(\omega+i\epsilon)^2\right] & 2i\epsilon k\coth\frac{\omega}{2T} \end{pmatrix}. \tag{6.9}$$

Alternatively, one can integrate out the field θ instead, resulting in a dual version of the action (6.8) with the replacement $g \to g^{-1}$. The reduced action thus highlights a duality structure present in S_0 (6.4): the action remains invariant when the fields θ and ϕ are exchanged and the replacement $g \to g^{-1}$ is made. Consequently, the correlation functions of ϕ and θ are connected by a simple transformation where g is replaced by its inverse. However, in the following we encounter that the action for a localized loss necessarily contains both fields θ and ϕ, as opposed to the action of a coherent impurity where only θ appears. Therefore, only in the latter case can a field be eliminated in the description.

6.2. Localized loss: Bosonization

By applying the bosonization transformations on the Hamiltonian and Lindblad operators, the quantum master equation (3.2) can be mapped onto a Keldysh action [12, 160, 161]. The localized loss is included in the Keldysh action by mapping the dissipator term of the Lindblad superoperator in Eq. (3.2) onto the action as [6] (cf. Eq. (2.33))

$$S_{\text{loss}} = -i\gamma\int_{x,t}\delta(x)\left[\mathrm{L}_-^*\mathrm{L}_+ - \frac{1}{2}\left(\mathrm{L}_+^*\mathrm{L}_+ + \mathrm{L}_-^*\mathrm{L}_-\right)\right]. \tag{6.10}$$

Here, the fermionic Lindblad operators in Eq. (3.2) are mapped onto the bosonic degrees of freedom by the nonlinear transformation (2.82) [81]

$$\psi \simeq e^{ik_Fx}e^{i(\phi+\theta)} + e^{-ik_Fx}e^{i(\phi-\theta)}, \tag{6.11}$$

where only the two most relevant harmonics are retained [80, 84] (cf. Sec. 2.3.2). The inclusion of higher harmonics (2.84) produces terms less relevant in the RG sense in analogy to the coherent barrier problem [80] (see App. C.2 for a discussion of irrelevant terms in Eq. (2.84)). The contributions to the impurity action (6.10) expressed by the Luttinger fields ϕ and θ read

$$L_\pm^*L_\pm = e^{i2k_Fx}\mathrm{e}^{i2\theta_\pm} + e^{-i2k_Fx}\mathrm{e}^{-i2\theta_\pm} + 2, \tag{6.12a}$$

$$\begin{aligned} L_-^*L_+ = {} & e^{i2k_Fx}e^{i(\phi_+-\phi_-)}e^{i(\theta_++\theta_-)} + e^{-i2k_Fx}e^{i(\phi_+-\phi_-)}e^{-i(\theta_++\theta_-)} \\ & + e^{i(\phi_+-\phi_-)}e^{i(\theta_+-\theta_-)} + e^{i(\phi_+-\phi_-)}e^{-i(\theta_+-\theta_-)}. \end{aligned} \tag{6.12b}$$

Thus, by means of the mapping (6.11) the impurity term (6.10) produces a backscattering contribution (S_{b}) to the Keldysh action, originating from the $2k_F$ terms in Eq. (6.12), and a

noise-like (S_n) contribution, containing only Keldysh quantum fields:

$$S_\mathrm{b} = -i\gamma \int_{x,t} \delta(x) \big[e^{i\sqrt{2}(\phi_q+\theta_c)} + e^{i\sqrt{2}(\phi_q-\theta_c)} - \frac{1}{2}\left(\mathrm{e}^{i\sqrt{2}(\theta_c+\theta_q)} + \mathrm{e}^{-i\sqrt{2}(\theta_c+\theta_q)} + \mathrm{e}^{i\sqrt{2}(\theta_c-\theta_q)} + \mathrm{e}^{-i\sqrt{2}(\theta_c-\theta_q)} \right) \big], \tag{6.13a}$$

$$S_\mathrm{n} = -i\gamma \int_{x,t} \delta(x) \big[e^{i\sqrt{2}(\phi_q+\theta_q)} + e^{i\sqrt{2}(\phi_q-\theta_q)} - 2 \big]. \tag{6.13b}$$

The two contributions S_b and S_n individually preserve the Keldysh causality structure, i.e., $S_{\mathrm{b/n}}[\phi_q = 0 = \theta_q] \equiv 0$ (cf. Sec. 2.1.2). The formulation of the impurity action in terms of exponential functions of the fields is particularly convenient in order to infer the RG scaling below. Moreover, the Keldysh action of a localized loss can be written in a more compact form as

$$S_\mathrm{b} = -2i\gamma \int_{x,t} \delta(x) \left(\mathrm{e}^{i\sqrt{2}\phi_q} - \cos\sqrt{2}\theta_q \right) \cos\sqrt{2}\theta_c, \tag{6.14a}$$

$$S_\mathrm{n} = -2i\gamma \int_{x,t} \delta(x) \left(\mathrm{e}^{i\sqrt{2}\phi_q} \cos\sqrt{2}\theta_q - 1 \right). \tag{6.14b}$$

The action thus acquires cosine terms, typical for impurity problems in a Luttinger liquid description [11, 79, 80, 123]. However, Eqs. (6.14) exhibit several differences compared to the case of a coherent barrier [79, 80].

First, the dependence on ϕ_q, absent for a coherent barrier, signals the breakdown of particle-number conservation due to the loss: this term, in fact, explicitly breaks the global $U(1)$ symmetry of the system, which in the Keldysh bosonized action reads $\phi_c \to \phi_c + \alpha_c$, $\phi_q \to \phi_q + \alpha_q$, with $\alpha_{c,q}$ arbitrary real numbers [6]. Moreover, the presence of odd powers of ϕ_q in the action entails that the average of the particle current is not zero, as expected. Second, the backscattering term (6.14a) differs from the one obtained for a coherent barrier. In particular, besides the prefactor being imaginary instead of real, the functional form varies from the one for a coherent barrier, i.e., $\sin\sqrt{2}\theta_q \sin\sqrt{2}\theta_c$ [11, 123] (cf. Sec. 6.3.2). This leads to qualitatively different RG equations at second order, as shown in Sec. 6.4. Third, the noise term S_n in Eq. (6.14b) does not have a counterpart in the coherent case. As it directly descends from the quantum jump term in Eq. (3.2) (i.e., the term containing $\mathrm{L}_-^* \mathrm{L}_+$ in Eq. (6.10)) and contains only Keldysh quantum fields, we conclude that it accounts for the quantum noise induced by the losses, and therefore it does not directly take part in the scattering induced by the impurity. Moreover, as discussed further below in Secs. 6.3 and 6.4, it is neither renormalized nor does it contribute to the renormalization of other terms on the action, at least up to second order in the impurity strength. For these reasons, we will not focus on it in the following.

6.3. Renormalization group analysis to first order

We now turn to the analysis of the effective low-energy properties of localized losses in a Luttinger liquid. In order to gain first insights, we perform an RG analysis perturbative to first order in the dissipation strength γ. In addition to the weak coupling limit (small microscopic γ), we also consider the case of strong dissipation (large microscopic γ). A strong dissipative potential results via the quantum Zeno effect in a decoupling of the two parts of the wire

separated by the loss site (cf. Sec. 3.3.3). Hence, this limit can be described in terms of two separate wires coupled by a weak dissipative link whose strength is quantified by a parameter $D \sim \gamma^{-1}$, in analogy to a strong coherent potential barrier [80, 81]. This allows us to extend the analysis by an RG study perturbative to first order in the weak dissipative link, i.e., to order $\mathcal{O}(D)$.

The obtained results are valid for the low-energy sector of the theory by the construction of the Luttinger liquid description, i.e., for modes near the Fermi energy. For repulsive interactions, the effective loss impurity is indefinitely enhanced, while for attractive interactions the opposite behavior of a vanishing loss barrier is obtained. Since γ controls the strengths of a backscattering term in the action, the transport properties at the fixed points are accordingly modified, similarly to the case of a coherent barrier [79–81]. Moreover, in the present non-equilibrium setup the renormalized dissipation strength bears information about the depletion processes in the system, which are in fact expected to be suppressed in both cases of repulsive and attractive interactions. For attractive interactions, the suppression of loss at the Fermi level is a manifestation of the effectively vanishing dissipation strength, which realizes a fluctuation-induced transparency. Instead, in the case of repulsive interactions, the effective loss barrier becomes fully opaque at the Fermi level and thus the suppression of loss is a consequence of the quantum Zeno effect, hence establishing a fluctuation-induced quantum Zeno effect. Thus, the RG flow of the effective dissipation strength captures the strong renormalization effects of the loss probability near the Fermi level encountered in Chapter 4. Finally, we can draw a comparison to the microscopic real-space RG approach performed in Chapter 4, in particular of the fixed point structure and scaling nearby.

6.3.1. Weak coupling limit

We perform a renormalization group analysis by integrating out fast modes lying in the momentum-shell $|k| \in [\Lambda/b, \Lambda]$, with $b > 1$, and subsequently rescaling space and time according to $(x, t) \to (bx, bt)$, which restores Λ as the original ultraviolet cutoff of the theory. While the quadratic part of the action remains scale invariant under this protocol, the nonlinear term S_{loss} is rescaled to account for the effect of the high-frequency modes eliminated from the description. We decompose the bosonic fields into contributions of slow and fast momenta according to $\chi = \chi_{\text{s}} + \chi_{\text{f}}$ (with χ defined below Eq. (6.4)), where χ_{s} is defined for momenta $|k| \in [0, \Lambda/b]$, while χ_{f} is defined on the momentum shell $|k| \in [\Lambda/b, \Lambda]$. In the weak coupling limit ($\gamma \ll 1$), we consider the leading term in the expansion in γ, and perform the RG step as:

$$\langle \mathrm{e}^{iS_{\text{loss}}} \rangle_{\text{f}} \simeq \langle 1 + iS_{\text{loss}} \rangle_{\text{f}} \simeq \mathrm{e}^{\langle iS_{\text{loss}} \rangle_{\text{f}}}, \tag{6.15}$$

with the fast-modes average defined by

$$\langle \dots \rangle_{\text{f}} = \int \mathcal{D}\chi_{\text{f}} \ \dots \ \mathrm{e}^{iS_0[\chi_{\text{f}}]}. \tag{6.16}$$

As a result of the exponential dependence of the impurity action (6.13) on the bosonic fields, this decomposition results in a multiplicative structure for each term of the form: $\exp(X_{\text{s}} + X_{\text{f}}) = \exp(X_{\text{s}}) \exp(X_{\text{f}})$, with $X = \theta_{c/q}, \phi_{c/q}$. The fast mode average can then be further simplified

with the use of the cumulant identity

$$\langle \exp(\pm x) \rangle_{\mathrm{f}} = \exp\left(\langle x^2 \rangle_{\mathrm{f}} / 2 \right), \tag{6.17}$$

which holds since the average involves only the unperturbed Gaussian action for the fast modes. Therefore, in order to perform the fast mode average $\langle S_{\mathrm{loss}} \rangle_{\mathrm{f}}$ in Eq. (6.15), we are left to evaluate the following correlation functions (6.13):

$$\langle (\phi_q \pm \theta_c)^2 \rangle_{\mathrm{f}} = \langle \phi_q^2 \rangle_{\mathrm{f}} + \langle \theta_c^2 \rangle_{\mathrm{f}} \pm \left(\langle \phi_q \theta_c \rangle_{\mathrm{f}} + \langle \theta_c \phi_q \rangle_{\mathrm{f}} \right), \tag{6.18a}$$

$$\langle (\phi_q \pm \theta_q)^2 \rangle_{\mathrm{f}} = \langle \phi_q^2 \rangle_{\mathrm{f}} + \langle \theta_q^2 \rangle_{\mathrm{f}} \pm \left(\langle \phi_q \theta_q \rangle_{\mathrm{f}} + \langle \theta_q \phi_q \rangle_{\mathrm{f}} \right). \tag{6.18b}$$

Outright, we can eliminate several contributions as a consequence of the Keldysh causality structure, see Sec 2.1.2. First, Keldysh quantum fields cannot acquire a finite expectation value, hence $\langle \phi_q^2 \rangle = \langle \theta_q^2 \rangle = \langle \phi_q \theta_q \rangle = \langle \theta_q \phi_q \rangle = 0$. Second, the sum of advanced and retarded Green functions at equal times vanishes and hence $\langle \phi_q \theta_c \rangle + \langle \theta_c \phi_q \rangle = 0$. As a consistency check, the latter is shown explicitly in App. C.1. By incorporating these considerations we obtain for the fast mode average of the backscattering term

$$\langle S_{\mathrm{b}}[\phi_{\mathrm{f}} + \phi_{\mathrm{s}}, \theta_{\mathrm{f}} + \theta_{\mathrm{s}}] \rangle_{\mathrm{f}} = S_{\mathrm{b}}[\phi_{\mathrm{s}}, \theta_{\mathrm{s}}] \mathrm{e}^{-\left\langle \theta_c^2(x,t) \right\rangle_{\mathrm{f}}}. \tag{6.19}$$

The noise term S_{n} (6.14b) is not renormalized at first order (nor at second order) and not considered in the following for the reasons discussed in Sec. 6.2.

Consequently, only density fluctuations $\left\langle \theta_c^2 \right\rangle_{\mathrm{f}}$ contribute to the renormalization of S_{b}, in analogy to the case of a coherent barrier [11, 79, 80] (cf. Sec. 6.3.2). The task therefore remains to evaluate the correlation function

$$\left\langle \theta_c^2(x,t) \right\rangle_{\mathrm{f}} = \int_{\mathrm{f}} \int_{\omega} \langle \theta_c(-k,-\omega) \theta_c(k,\omega) \rangle, \tag{6.20}$$

where $\int_{\mathrm{f}} \equiv \int_{|k| \in [\Lambda/b, \Lambda]} \mathrm{d}k/(2\pi)$, which is in turn obtained from the action (6.4) via

$$\langle \theta_c(-k,-\omega) \theta_c(k,\omega) \rangle = -i G_{K\theta\theta}. \tag{6.21}$$

To this end, the Keldysh Green's function $G_K = -P_R^{-1} P_K P_A^{-1}$ is derived from the inverse propagators given in Eq. (6.5), and we obtain in the θ sector:

$$G_{K\theta\theta}(k,\omega) = \frac{-4\pi i \epsilon g v \omega \coth \frac{\omega}{2T}}{(\omega^2 - k^2 v^2)^2 + \epsilon^2 (2\omega^2 + 2k^2 v^2)}. \tag{6.22}$$

In this expression, we identify the Lorentzian representation of the delta function,

$$\delta(x) = \lim_{\epsilon \to 0} \frac{1}{\pi} \frac{\epsilon}{x^2 + \epsilon^2}, \tag{6.23}$$

and obtain in the respective limit

$$G_{K\theta\theta}(k,\omega) = \frac{-\pi^2 i g v \omega \coth \frac{\omega}{2T}}{k^2 v^2} \delta\left(\frac{\omega^2 - k^2 v^2}{2|k|v} \right). \tag{6.24}$$

As the next step, we carry out the frequency integration in Eq. (6.20). Here, we take the zero temperature limit, $T \to 0$, by which the distribution function simplifies according to

$\omega \coth \frac{\omega}{2T} \to |\omega|$. Further, we make use of the identity $\int f(x)\delta(g(x)) = \sum_{x_i} f(x_i)/|g'(x_i)|$, with x_i a zero of $g(x)$, i.e., $g(x_i) = 0$. Therefore, we obtain

$$\int_\omega G_{K\theta\theta}(k,\omega) = -i2\pi\frac{g}{2|k|}. \tag{6.25}$$

Finally, the remaining integration over the momentum shell in Eq. (6.20) yields

$$\langle\theta_c^2(x,t)\rangle_\mathrm{f} = g\int_{\Lambda \mathrm{e}^{-\ell}}^{\Lambda}\frac{\mathrm{d}k}{k} = g\ell, \tag{6.26}$$

where we introduced $\ell = \ln b$. Note that the integral in Eq. (6.26) diverges logarithmically if the integration was performed in a single step including all scales. As a further remark, we note that the limit $\omega \coth \frac{\omega}{2T} \to |\omega|$ is valid for $\omega \gg T$. Therefore, for a finite temperature of the wire the zero-temperature scaling breaks down at the scale $\omega \sim T$ and the flow is cut off, as in the regime $\omega < T$ the scaling behavior is qualitatively changed according to $\coth \omega/2T \to 2T/\omega$.

From the result (6.26) we obtain the fluctuation contribution in Eq. (6.19) as

$$\langle S_\mathrm{b}[\phi_\mathrm{f}+\phi_\mathrm{s}, \theta_\mathrm{f}+\theta_\mathrm{s}]\rangle_\mathrm{f} = S_\mathrm{b}[\phi_\mathrm{s},\theta_\mathrm{s}]e^{-g\ell}. \tag{6.27}$$

Hence, the structure of the partition function is preserved and no additional contributions are generated at first order. The original ultraviolet cutoff Λ of the theory is then restored by a rescaling

$$k \to bk, \qquad \omega \to b\omega, \qquad \gamma \to be^{-g\ell}\gamma, \tag{6.28}$$

fixed by requiring a vanishing scaling dimension of the quadratic part of the action. We emphasize that the Luttinger parameters v, g are not renormalized due to the local perturbation [84]. By noticing that the canonical scaling dimension of the dissipation strength is $[\gamma] = 1$, we finally obtain the flow equation

$$\frac{\mathrm{d}\gamma}{\mathrm{d}\ell} = (1-g)\gamma. \tag{6.29}$$

The RG flow equation (6.29) constitutes a central result of this Chapter. Remarkably, this RG equation is analogous to the flow equation obtained for the case of a weak potential barrier [79, 80] despite the non-equilibrium nature of the present model. The flow equation (6.29) entails that for attractive interactions ($g > 1$) the dissipation strength γ is renormalized to zero by quantum fluctuations, being irrelevant in the RG sense. The loss barrier thus becomes fully transparent and losses of low-energy modes, i.e., near the Fermi energy, are suppressed. On the converse, for repulsive interactions ($g < 1$) the dissipation strength γ is infinitely enhanced by quantum fluctuations, and therefore it is a relevant perturbation in the RG sense. Formally, in the latter case the perturbative analysis breaks down, motivating the study of the strong dissipation limit performed in Sec. 6.3.3. We elaborate more on the interpretation of the RG flow in Sec. 6.3.4.

As a final remark, we note that higher harmonics of order m in Eq. (2.84), which were omitted in the bosonization mapping in Eq. (6.11), are found to contribute to the flow equation (6.29) with a term $\sim -m^2 g\gamma$ and are therefore less relevant in the RG sense, analogous to the bosonization of a coherent barrier [80, 81].

6.3.2. Benchmark: Coherent impurity

Before we continue with the study of localized dissipation, we adapt the RG analysis within the present Keldysh framework to the case of a coherent potential barrier. This study provides both a comparison of the localized loss with a coherent impurity and a benchmark of the formalism by reproducing the results of Refs. [79, 80]. The bosonized description of a weak coherent potential is obtained as follows. A coherent impurity is incorporated in the microscopic Hamiltonian by a term

$$H_{\text{imp}} = \int_x u\delta(x)\psi^\dagger(x)\psi(x), \tag{6.30}$$

where $u \in \mathbb{R}$ describes the amplitude of the localized perturbation. By using the bosonization identity for the fermionic operators (6.11) the impurity Hamiltonian (6.30) is mapped to [79–81]

$$H_{\text{imp}} = u\int_x \delta(x)e^{2i\theta} + \text{h.c.} = 2u\int_x \delta(x)\cos(2\theta), \tag{6.31}$$

where irrelevant constants have been dropped. The term H_{imp} is then simply included in the Keldysh action (6.3) on each time contour in the Hamiltonian. As a result, we obtain the Keldysh impurity action [11, 123]

$$S_{\text{imp}} = 4u\int_{t,x} \delta(x)\sin(\sqrt{2}\theta_c)\sin(\sqrt{2}\theta_q), \tag{6.32}$$

in which only the bosonic field θ enters. One can then integrate out the field ϕ also in the quadratic action S_0 as reported in Eq. (6.8), yielding a consistent description solely in terms of the field θ.

In the impurity action for a localized loss (6.10) terms occur (6.12a) which contain only fields situated on the same Keldysh contour, originating from $\{L_\pm^\dagger L_\pm, \rho\}$. These terms are indeed analogous to the terms in the impurity action of a coherent impurity (6.31). However, the contribution $L_+L_-^*$ (6.12b) to the localized loss action, emerging from the jump term $L\rho L^\dagger$ in the quantum master equation, has no analog in the coherent case. We note that via these terms the phase field ϕ enters the action, resulting in the violation of the $U(1)$ symmetry, as discussed in Sec. 6.2, thus revealing the non-equilibrium character of the action.

The perturbative RG analysis for the coherent impurity action follows closely the lines presented in the previous section for the case of a localized loss. The integration of fast modes in the momentum shell $|k| \in [\Lambda/b, \Lambda]$ produces for a single RG step the analog of Eq. (6.19). Hence, the fast fluctuation contribution involves only the correlation function $\langle\theta_c^2\rangle_{\text{f}}$ which we evaluated in Eq. (6.26). Consequently, by noticing the canonical scaling dimension $[u] = 1$, we acquire the RG flow equation

$$\frac{\mathrm{d}u}{\mathrm{d}\ell} = (1-g)u. \tag{6.33}$$

Equation (6.33) is analogous the RG flow equation for γ (6.29) and in agreement with the results obtained in Refs. [79–81]. It entails that for repulsive interactions ($g < 1$) even a small impurity acts effectively as a large barrier near the Fermi level. In contrast, for attractive interactions ($g > 1$), the impurity is completely masked by fluctuations. The RG analysis can be adapted for the complementary case of a strong barrier. We consider the dissipative counterpart to the strong barrier, i.e., a strong localized loss, in the following section.

With the results for weak and strong coupling at hand, in Refs. [79–81] the effect of the renormalized barrier strength on the conductance of the wire was studied (see Sec. 2.3.4), where the behavior of the conductance directly reflects the expectations based on the effective impurity strength.

6.3.3. Strong coupling limit

Given the non-linearity of the impurity action (6.14a), its effect can only be included perturbatively, which is possible for $\gamma \to 0$. However, in the limit $\gamma \to \infty$, the effect of the impurity is indistinguishable from the one of an infinitely strong barrier (cf. Eq. (3.23)). More precisely, it separates the wire in two semi-infinite, disconnected parts, due to the microscopic quantum Zeno effect. The density field is then pinned to zero at the impurity site [84]. Accordingly, the effect of a very large but finite γ can be treated as a perturbation around this disconnected-wire configuration. The perturbation is then implemented by a weak dissipative tunneling between the two parts of the wire, in analogy to the coherent tunneling for the case of a large but finite potential barrier [79–81]. The exact form of this dissipative tunneling is obtained by integrating out the dissipative site in leading order in γ^{-1}. The resulting impurity action can then be analyzed within the previously developed perturbative RG scheme, yielding RG flow equations for the effective strength of the dissipative tunneling $D \sim \gamma^{-1}$.

First, we derive the explicit form of the dissipative tunneling between two semi-infinite wires which are separated by a strong loss barrier. To this end, we study a three-site system with a localized loss at its central site. By integrating out the central site, we obtain an effective dissipative coupling between the remaining two sites. The generalization to semi-infinite wires is then straightforward. We consider three sites labeled as $j = A, X, B$ and described by the Hamiltonian

$$H = -J(\psi_X^\dagger \psi_A + \psi_B^\dagger \psi_X + \text{h.c.}), \tag{6.34}$$

and Lindblad operators $\mathrm{L}_j = \psi_j \delta_{j,X}$, implementing a localized loss at the central site X via a quantum Master equation (3.4). Here, ψ_j, $\psi_j^\dagger$ denote fermionic operators. The total action is then given by

$$S[\psi_A, \psi_X, \psi_B] = S_0[\psi_A, \psi_B] + S_0[\psi_X] + S_{\text{int}}[\psi_A, \psi_X, \psi_B], \tag{6.35}$$

with S_0 the actions for the decoupled sites and S_{int} the action describing the tunneling produced by H. The effective action $S_{\text{eff}}[\psi_A, \psi_B]$, coupling the sites A and B, is obtained by integrating out the central site X according to [6]

$$\int \mathcal{D}\psi_X \, \mathrm{e}^{iS_0[\psi_X] + iS_{\text{int}}[\psi_A, \psi_X, \psi_B]} = \mathrm{e}^{iS_{\text{eff}}[\psi_A, \psi_B]}, \tag{6.36}$$

which yields

$$S_{\text{eff}} = \int_\omega \left[i \frac{2J^2\gamma}{\omega^2 + \gamma^2} T_q^* T_q - \left(\frac{J^2}{\omega + i\gamma} T_q^* T_c + \text{h.c.} \right) \right], \tag{6.37}$$

with $T_{c/q} = \psi_{c/q,A} + \psi_{c/q,B}$. We now expand in orders of γ^{-1}

$$\frac{2\gamma}{\omega^2 + \gamma^2} = 2\gamma^{-1} + \mathcal{O}(\gamma^{-3}), \qquad (\omega \pm i\gamma)^{-1} = \mp i\gamma^{-1} + \mathcal{O}(\gamma^{-2}), \tag{6.38}$$

and obtain to leading order in γ^{-1}

$$S_D = -iD \int_\omega \left[-2T_q^* T_q + \left(T_c^* T_q - T_q^* T_c \right) \right], \tag{6.39}$$

with $D = \gamma^{-1} J^2$. The action S_D corresponds exactly to the one obtained from the dissipator of a quantum master equation (3.2) for Lindblad operators of the form $\mathrm{L} = \psi_A + \psi_B$. We therefore infer that the effect of a large but finite localized loss can be modeled as two disconnected leads coupled by a dissipative tunneling implemented by the Lindblad operator

$$\mathrm{L} = \psi_A(x=0) + \psi_B(x=0), \tag{6.40}$$

with $\psi_{A,B}(x=0)$ corresponding to the fermionic annihilation operators on the edges of the two semi-infinite wires A and B. The dissipative tunneling strength is then quantified by a coupling $D \simeq \gamma^{-1}$.

The bosonized representation of the electron annihilation operator of the weak link is given by [84]

$$\psi_{A/B}(0) = \mathrm{e}^{i\phi_{A/B}(0)}, \tag{6.41}$$

as the density fluctuations θ are frozen by the boundary constraint, which is realized in the case of a dissipative barrier via the quantum Zeno effect. We obtain for the terms appearing in the quantum master equation (3.2) with the Lindblad operators (6.40) the bosonic representations

$$T_\pm^* T_\pm = \mathrm{e}^{i(\phi_{B,\pm} - \phi_{A,\pm})} + \mathrm{e}^{i(\phi_{A,\pm} - \phi_{B,\pm})} + 2, \tag{6.42a}$$

$$T_-^* T_+ = \mathrm{e}^{i(\phi_{A,+} - \phi_{A,-})} + \mathrm{e}^{i(\phi_{B,+} - \phi_{B,-})} + \mathrm{e}^{i(\phi_{B,+} - \phi_{A,-})} + \mathrm{e}^{i(\phi_{A,+} - \phi_{B,-})}. \tag{6.42b}$$

It is then convenient to work with new fields

$$\varphi = (\phi_A - \phi_B)/2, \qquad \widetilde{\varphi} = (\phi_A + \phi_B)/2, \tag{6.43}$$

corresponding to symmetric and antisymmetric linear combinations of the fields in the two semi-infinite wires, respectively [84, 159]. In the quadratic part of the action $\varphi, \widetilde{\varphi}$ remain decoupled under this mapping, i.e., $S_0[\phi_A] + S_0[\phi_B] \sim S_0[\varphi] + S_0[\widetilde{\varphi}]$. The implementation of these considerations produces, analogous to the weak coupling limit, a backscattering ($S_{D\mathrm{b}}$) and a noise-like ($S_{D\mathrm{n}}$) contribution to the Keldysh action of a weak dissipative tunneling:

$$S_{D\mathrm{b}} = -2iD \int_{x,t} \delta(x) \cos\sqrt{2}\varphi_c \left(\mathrm{e}^{i\sqrt{2}\widetilde{\varphi}_q} - \cos\sqrt{2}\varphi_q \right), \tag{6.44a}$$

$$S_{D\mathrm{n}} = -2iD \int_{x,t} \delta(x) \left(\mathrm{e}^{i\sqrt{2}\widetilde{\varphi}_q} \cos\sqrt{2}\varphi_q - 1 \right). \tag{6.44b}$$

We focus in the following on the backscattering contribution $S_{D\mathrm{b}}$ since regarding the noise contribution the same reasoning applies as discussed in Sec. 6.2 for S_n. Remarkably, the construction produces an impurity action formally identical to S_loss in Eq. (6.14) upon the following duality transformation:

$$\theta \to \varphi, \qquad \phi \to \widetilde{\varphi}, \qquad \gamma \to D. \tag{6.45}$$

In addition to the duality of the impurity actions for both cases, the bare action (6.4) exhibits a duality upon interchanging θ and ϕ, and replacing g with g^{-1}, which results in the correlation

functions of phase and density fields to be connected by a transformation $g \rightarrow g^{-1}$ (see discussion below Eq. (6.9)). For this reason, the full action in the strong coupling regime exhibits a duality with the action in the weak coupling regime, resulting in the RG flow of D being identical to the RG flow of γ upon replacing g with g^{-1}. As a consequence of the duality, we obtain the RG flow equation

$$\frac{\mathrm{d}D}{\mathrm{d}\ell} = (1 - g^{-1})D. \tag{6.46}$$

This result entails the analogous behavior to the one obtained in the weak coupling limit, formulated in terms of a link instead of a barrier: for repulsive interactions, the weak link is cut, while for attractive interactions it is enhanced, reconnecting the two semi-infinite wires. The same duality between the weak and strong coupling limit is encountered the equilibrium counterpart of a coherent potential impurity [79–81]. However, in this case the field $\widetilde{\varphi}$ does not appear in the impurity action.

We briefly comment on a subtlety regarding the proper treatment the correlation functions close to a boundary of a Luttinger liquid. As a consequence of the constraint imposed on the density field θ at the boundary, also the fluctuations of the conjugate field ϕ are modified [84]. As a rule of thumb [84], this results in a replacement $g \rightarrow g/2$ in the correlation functions. In fact, we implicitly accounted for this factor with the mapping (6.43) which introduces a factor of two in the bare action and hence we can directly calculate the correlation functions with the use of S_0 given in Eq. (6.4).

6.3.4. First-order results and relation to real-space renormalization group approach

The RG flow of the dissipation strength obtained in both limits of weak and strong bare coupling entailed in the RG flow Eqs. (6.29) and (6.46) can be depicted as shown in Fig. 6.1. Notice that the directions of the RG flows for γ and D are compatible. It is then reasonable to assume that the fully reflective and transmissive fixed points obtained in the perturbative regimes constitute an exhaustive description of the fixed-point structure, allowing one to connect the RG flow on intermediate scales [79–81, 119]. This leads to the conclusion that losses are always suppressed in the vicinity of the Fermi energy by gapless fluctuations, restoring unitarity at this scale, for both repulsive and attractive interactions. For attractive interactions ($g > 1$), the perturbation is irrelevant in the RG sense as $\gamma \rightarrow 0$ and the dissipation strength is suppressed, describing a transparent barrier and the absence of losses. This establishes a fluctuation-induced transparency as encountered in Chapter 4 for attractive interactions. In contrast, for repulsive interactions ($g < 1$) the perturbation by the localized loss is relevant in the RG sense and γ flows to infinity. The effective barrier is fully reflective so that losses are suppressed as a fluctuation-induced quantum Zeno effect, in analogy to the results of Chapter 4.

The relation between the real-space RG developed in Chapter 4 and the RG developed in this chapter in the context of Luttinger liquid theory is further investigated in the following. While the two approaches are developed to encompass different regimes (arbitrary impurity strength and weak interaction in the former case, weak and strong impurity strength and arbitrary interaction for the latter case), a regime where both approaches are applicable exists (i.e., weak and strong impurity strength and weak interactions). Here, both approaches lead to

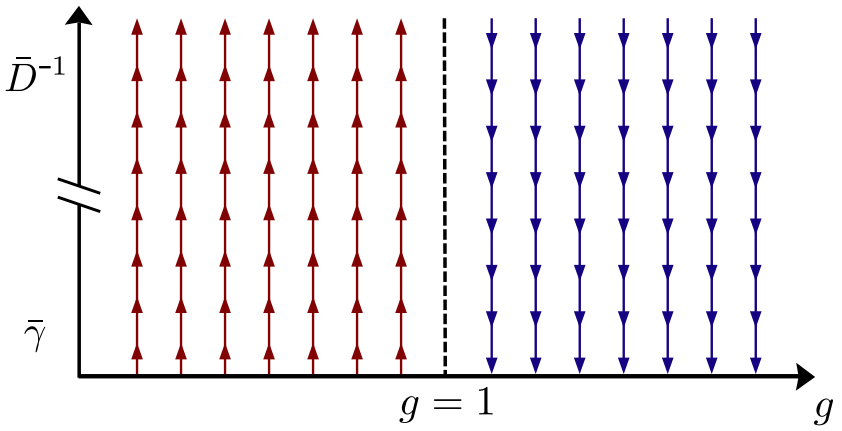

Fig. 6.1. Schematic RG flow of the dissipation strength γ, respectively D, in dependence on the Luttinger parameter g at first order.

the same result for the case of a coherent impurity [81]. A natural question concerns whether this connection persists for dissipative impurities.

In Chapter 4 we obtained within a microscopic approach a description in terms of RG flow equations for the scattering probabilities near the Fermi level, reported in Eqs. (4.36). Here, the RG flow of the probabilities for transmission $\mathcal{T}(k)$, reflection $\mathcal{R}(k)$, and loss $\eta(k)$ can be reparametrized with the use of a single dimensionless function $\widetilde{\gamma}(k)$. The RG flow is then recast in terms of an RG flow of $\widetilde{\gamma}(k)$. This reparametrization is practicable as under the RG flow the continuity relation $t_k = 1 + r_k$ is preserved as well as $t(\ell), r(\ell)$ remain real-valued thus reducing the independent variables. We choose to parametrize the scattering coefficients by replacing $\gamma/|v_k| \to \widetilde{\gamma}$ in Eqs. (3.35) and (3.37), according to which $\widetilde{\gamma}$ takes the role of an effective dissipation strength, which allows one to compare the RG flow of $\widetilde{\gamma}$ and the RG flow of γ discussed in the present chapter.

The RG flow of $\widetilde{\gamma}$ can be determined from the flow equations of the scattering amplitudes in Eqs. (4.35) and reads

$$\frac{\mathrm{d}\widetilde{\gamma}}{\mathrm{d}\ell} = \alpha \frac{\widetilde{\gamma}^2}{1+\widetilde{\gamma}}. \tag{6.47}$$

This equation admits respectively one stable fixed point $\widetilde{\gamma}^* = \infty$ for $\alpha > 0$ and $\widetilde{\gamma}^* = 0$ for $\alpha < 0$, corresponding to the fixed points of $\mathcal{T}, \mathcal{R}$, η in Eqs. (4.37). For what concerns the Luttinger impurity strengths γ and D, we will consider for the comparison the first-order equations discussed so far, because the second-order equations account for coupling between different momenta (cf. Sec. 6.4.2), an effect not included in the real-space RG.

Based on these considerations, the following unified picture emerges connecting the results of Chapters 4 and 6. The behavior of the loss probability η under RG can be rationalized in terms of the flow of an effective dissipation strength γ as shown in Fig. 1.3: η reaches its fixed point $\eta^* = 0$ either for $\gamma \to \infty$ or for $\gamma \to 0$, in the former case thus resulting in a fluctuation-induced quantum Zeno effect, and in the latter case in a fluctuation-induced transparency.

Moreover, we study the scaling behavior of $\widetilde{\gamma}$ (6.47) in the limiting cases of weak and strong dissipation strength and compare it to the one of γ. In the limit $\widetilde{D} \equiv \widetilde{\gamma}^{-1} \ll 1$, i.e., the strong

dissipation limit, we obtain

$$\frac{\mathrm{d}\widetilde{D}}{\mathrm{d}\ell} = -\alpha\widetilde{D}. \tag{6.48}$$

This flow equation corresponds exactly to the one obtained in the Luttinger liquid RG in the strong dissipation regime (6.46) upon the identification $\widetilde{D} \equiv D$, and by realizing that α relates to the Luttinger parameter g as $\alpha \approx 1 - g \approx g^{-1} - 1$ for weak interactions ($\alpha \ll 1$, respectively $g \simeq 1$) [81]. In the opposite limit of $\widetilde{\gamma} \ll 1$, we obtain the flow equation

$$\frac{\mathrm{d}\widetilde{\gamma}}{\mathrm{d}\ell} = \alpha\widetilde{\gamma}^2. \tag{6.49}$$

The comparison to the flow equation in the Luttinger liquid description (6.29) reveals that both equations indeed admit the same stable fixed points, however, the approach to them differs. With the microscopic analysis at hand, we can understand this discrepancy as follows. In the limit of large γ, the presence of the loss site is already taken into account in the unperturbed state (in the interactions) by the assumption of two decoupled systems. We thus perturb around a state in the second temporal regime, in agreement with the microscopic RG approach. Compared to this, in the weak coupling limit, the unperturbed state is homogeneous and we operate rather in the first temporal regime. Nevertheless, the strong renormalization effects obtained are consistent with the microscopic analysis, as density oscillations can build up also in the first temporal regime since the light-cone speed is independent of the relaxation at the loss site.

6.4. Renormalization group analysis to second order

In Luttinger liquids out of equilibrium typically an effective temperature is generated during the RG flow when nonlinear terms are included at second order in the RG equations [9, 11, 122, 123]. While within the first-order scaling a back action on the quadratic part of the action is absent, the latter can acquire corrections at second order due to the coupling between high- and low-energy modes established by the nonlinear terms. Upon integrating out the high-energy modes, the effective description for the low-energy modes then must account for this coupling leading to the generation of an effective temperature. Hereby, a localized perturbation, as in the model under consideration, results in a renormalization of the local properties at $x = 0$ only. Therefore, the main effect of the extension of the RG scheme to second order is the generation of a *local* effective temperature which effectively cuts off the RG flow. While, in principle, such a cutoff scale could be even more severe than the one provided by the global temperature and system size, upon choosing proper microscopic values of the impurity strength γ and of the interaction strength g, a regime can be achieved where the cutoff scale is sufficiently large to obtain a sizable renormalization.

Due to the locality of the generated corrections, it is convenient to formulate a description reduced to the local action at $x = 0$. We then outline the derivation of the flow equations at second order and subsequently focus on the analysis and interpretation of the RG flow. Here, a phase diagram is described entailing the qualitatively different behaviors of the RG flow depending on the microscopic parameters. Finally, the exact flow equations can be solved numerically to benchmark the obtained phase diagram.

6.4.1. Flow equations at second order

We extend the RG scheme formulated in Sec. 6.3.1 in the following way. The nonlinear term $S_{\rm loss}$ is taken into account perturbatively in γ so that the integration over fast momenta can be performed, but this time we truncate the cumulant expansion at second order in γ:

$$\left\langle \mathrm{e}^{iS_{\rm loss}} \right\rangle_{\rm f} \simeq \mathrm{e}^{i\langle S_{\rm loss}\rangle_{\rm f} - \left(\langle S_{\rm loss}^2\rangle_{\rm f} - \langle S_{\rm loss}\rangle_{\rm f}^2\right)/2}. \tag{6.50}$$

We will also consider the dual case perturbative in γ^{-1} (see Sec. 6.3.3). Since we already evaluated $\langle S_{\rm loss}\rangle_{\rm f}$ during the first-order analysis (cf. Eq. (6.27)), we can focus on the evaluation of $\langle S_{\rm loss}^2\rangle_{\rm f}$. Moreover, two important structural aspects encountered at first-order (see Sec. 6.3.1) carry over to the second-order computation. First, the noise contribution $S_{\rm n}$ (6.13b) drops out of the RG equations since it neither acquires any renormalization, nor does it contribute to the renormalization of other couplings. Second, if $S_{\rm b}$ (6.13a) contains both fields ϕ and θ, only correlations of θ enter the evaluation of the renormalization integrals.

As a starting point, we consider which couplings are expected to be renormalized at second order additionally to the impurity strength γ, which was already renormalized at first order. As before, the local perturbation due to the localized loss cannot globally renormalize the parameters g and v in the quadratic action (6.4), however, their local values at $x = 0$ can acquire corrections. For this reason, it is natural to reduce the description to an effective one for the density field at the loss site $\Theta \equiv \theta(x = 0)$ (ϕ does not enter the renormalization). This can be achieved by integrating out the unperturbed wires outside the loss region yielding the effective quadratic action at $x = 0$ [159]

$$S_0^\Theta = \frac{i}{\pi g}\int_\omega \begin{pmatrix}\Theta_c^* & \Theta_q^*\end{pmatrix}\begin{pmatrix}0 & -\omega \\ \omega & 2\omega\coth\frac{\omega}{2T}\end{pmatrix}\begin{pmatrix}\Theta_c \\ \Theta_q\end{pmatrix}. \tag{6.51}$$

Equation (6.51) can be interpreted as the action of a quantum particle coupled to an Ohmic quantum bath imposing a temperature T and friction $1/g$ [123].

The adaption to the strong coupling case is straightforward as a consequence of the duality (6.45). Here, the fluctuations of the field $\widetilde{\varphi}$ do not contribute to the renormalization, and one obtains a local effective action for the field $\Phi = \varphi(x = 0)$, dual to the action in Eq. (6.51) by the transformation $\Theta \to \Phi$ and $g \to g^{-1}$.

The Keldysh component $\omega\coth[\omega/(2T)]$ in the action (6.51) is not suitable for being renormalized due to the infinite series of powers entering the hyperbolic cotangent function, making it intractable to keep track of the entire RG flow. Therefore, we approximate it with a simpler function of ω interpolating between quantum ($T \to 0$) and classical scaling [123]. To this end, we consider the limit $T \to 0$ and obtain the scaling near the quantum fixed point $\sim |\omega|$. The most relevant correction in the RG sense can then be obtained by expanding in powers of ω for finite T yielding a scaling $\sim 2T + \mathcal{O}(\omega^2)$. The action (6.51) can thus be recast as

$$S_0^\Theta = \frac{i}{\pi}\int_\omega \begin{pmatrix}\Theta_c^* & \Theta_q^*\end{pmatrix}\begin{pmatrix}0 & -\kappa\omega \\ \kappa\omega & 2\kappa_0|\omega| + 4\kappa T\end{pmatrix}\begin{pmatrix}\Theta_c \\ \Theta_q\end{pmatrix}, \tag{6.52}$$

where we anticipated that the prefactors of the terms $\omega\Theta_q^*\Theta_c$ (and c.c.) and $|\Theta_q|^2$ obtain a fluctuation contribution under renormalization and therefore are denoted as κ and T, where

the microscopic value of κ is given by $\kappa_0 = 1/g$. In contrast, the prefactor of $|\omega|$ is not expected to be renormalized and remains at its initial value κ_0 since the perturbative corrections cannot generate a non-analytic function of the frequency. Hence, the zero-frequency Keldysh component is associated with an effective temperature generated during the RG flow. As a consequence of the duality connecting weak and strong coupling limit (cf. Sec. 6.3.3), the effective action for Φ is simply given by Eq. (6.52) upon replacing $\kappa_0 = 1/g \to g$.

The canonical scaling dimensions of the flowing couplings are obtained from Eqs. (6.14) and (6.52) as $\kappa \sim \Lambda^0$, $\gamma \sim \Lambda$, and $T \sim \Lambda$. It is then convenient to introduce the rescaled dimensionless quantities $\bar{\gamma} \equiv \gamma/\Lambda$ and $\bar{T} \equiv T/\Lambda$. Having achieved a convenient description in terms of the local effective action (6.52), we now outline[2] the derivation of the RG equations for $\bar{\gamma}$, κ and $\bar{T}$ by evaluating $\langle S^2_{\mathrm{loss}}\rangle_{\mathrm{f}}$. First, from the action (6.52) one obtains

$$\langle \theta_c^2(x,t)\rangle_f = \ell\left(\frac{\kappa_0}{\kappa^2} + \frac{2\bar{T}}{\kappa}\right), \tag{6.53}$$

in analogy to the first-order computation. Moreover, in the second order cumulant for $S_{\mathrm{loss}} = S_{\mathrm{b}} + S_{\mathrm{n}}$ in Eq. (6.50) only the term $\langle S^2_{\mathrm{b}}\rangle_f - \langle S_{\mathrm{b}}\rangle^2_f$ contributes to the renormalization of S_0^{Θ}. Its most relevant contribution in the RG sense consists of terms

$$\int_{t,t'} \langle \cos\alpha(\Theta_c \pm \Theta_c' \pm \Theta_q \pm \Theta_q')\rangle_f = \int_{t,t'} \cos\alpha(\Theta_c^s \pm \Theta_c'^s \pm \Theta_q^s \pm \Theta_q'^s) \mathrm{e}^{-\frac{\alpha^2}{2}\langle(\Theta_c^f \pm \Theta_c'^f \pm \Theta_q^f \pm \Theta_q'^f)^2\rangle_f}. \tag{6.54}$$

Further progress can be made by an expansion in the central and relative time coordinates, $t_c = t + t'$ and $t_r = (t - t')/2$, according to

$$\Theta_{c/q}(t) + \Theta_{c/q}(t') = 2\Theta_{c/q}(t_c) + \mathcal{O}(t_r^2), \qquad \Theta_{c/q}(t) - \Theta_{c/q}(t') = t_r \frac{\mathrm{d}\Theta_{c/q}}{\mathrm{d}t_c}(t_c) + \mathcal{O}(t_r^2).$$

Finally, by comparing the obtained leading contributions with the quadratic action (6.52), we obtain the RG equations

$$\frac{\mathrm{d}\bar{\gamma}}{\mathrm{d}\ell} = \bar{\gamma}\left(1 - \frac{\kappa_0}{\kappa^2} - 2\frac{\bar{T}}{\kappa}\right), \tag{6.55a}$$

$$\frac{\mathrm{d}\bar{T}}{\mathrm{d}\ell} = \bar{T} + \frac{\bar{\gamma}^2}{\kappa} I_T - \frac{\bar{\gamma}^2\bar{T}}{\kappa} I_\kappa, \tag{6.55b}$$

$$\frac{\mathrm{d}\kappa}{\mathrm{d}\ell} = \bar{\gamma}^2 I_\kappa. \tag{6.55c}$$

Here, we defined the integrals $I_{T,\kappa} \equiv I_{T,\kappa}(\kappa_0, \kappa, T)$ whose explicit form is given by

$$I_T(\kappa_0,\kappa,T) = \pi\,\mathrm{Re}\left[\int_0^\infty \mathrm{d}t\, \mathrm{e}^{f(t)}\, h(t)\right], \tag{6.56a}$$

$$I_\kappa(\kappa_0,\kappa,T) = -2\pi\,\mathrm{Im}\left[\int_0^\infty \mathrm{d}t\, t\, \mathrm{e}^{f(t)}\, h(t)\right]. \tag{6.56b}$$

[2] Further details of the second order cumulant expansion can be found in the appendix of publication [134] and reflect contributions of the coauthors of this publication.

The functions $h(t)$ and $f(t)$, respectively, are given by

$$h(t) = \left[2\left(\frac{\kappa_0}{\kappa^2} + \frac{2\bar{T}}{\kappa}\right)(1+\cos t) - \frac{i}{\kappa}\sin t\right], \tag{6.57a}$$

$$f(t) = \frac{2\kappa_0}{\kappa^2}\left[-\gamma_{EM} + \mathrm{Ci}(t) - \log t\right] + \frac{4\bar{T}}{\kappa}\left[1 - \cos t - t\,\mathrm{Si}(t)\right] - \frac{2i}{\kappa}\mathrm{Si}(t), \tag{6.57b}$$

where γ_{EM} is the Euler-Mascheroni constant, and $\mathrm{Ci}(t), \mathrm{Si}(t)$ are the cosine integral and sine integral functions, respectively. The same form of the equations (6.55) is obtained in the dual case with the replacement $\gamma \to D$ and $\kappa_0 = 1/g \to g$.

The connection to the first-order result is established by omitting terms $\bar{\gamma}^2$ and by noting that the resulting flow of T is trivial and admits an unstable fixed point at $T = 0$, which is left for any finite initial temperature $T > 0$, while κ does not flow but remains at its initial value κ_0. Hence, if the initial temperature is tuned to $T = 0$, γ acquires the renormalization described in Sec. (6.29).

In the following, we study the flow of κ and $\bar{T}$ for the initial conditions $\kappa = \kappa_0$ and $\bar{T} = 0$, which represent the microscopic model in a pre-quench state at zero temperature. The solutions of Eqs. (6.55) will enable us to understand the emergence of an effective temperature $\bar{T}$ and its consequences for the flow of $\bar{\gamma}$.

6.4.2. Second-order result

The exact solution of Eq. (6.55) can only be accessed numerically, as the integrals $I_{\kappa,T}$ can not be solved in a closed form. Before considering the exact solutions, we discuss several important properties of the RG equations and, based on this discussion, study the qualitative behavior of the RG flow.

The integrals I_T, I_κ (6.56) are found to diverge for $g < 1$ (respectively for $g > 1$ in the dual case), implying that the perturbative analysis breaks down at $g = 1$. A similar breakdown of the perturbative analysis was pointed out for different non-equilibrium impurity problems in Refs. [11, 123], where the breakdown was shown to happen at $g = 1/2$. Moreover, in the convergence region, the integrals I_T, I_κ are positive quantities, implying that $\bar{T}$ and κ can only increase, as seen in Fig. 6.2 where the values of the integrals are shown in the convergent regions, for $T = 0$. The positivity of $I_{T,\kappa}$ is consistent with the expectation that a localized dissipative impurity increases the local effective temperature and the amount of friction (quantified by κ). Moreover, even if the microscopic value of the temperature is fixed to $T = 0$, Eq. (6.55b) entails that a finite temperature is always generated at $\mathcal{O}\left(\bar{\gamma}^2\right)$. We emphasize that this temperature corresponds to a local effective temperature at the dissipative site and not to a global temperature in the wire.

The generation of a finite local effective temperature has the main effect of cutting off the RG flow of $\bar{\gamma}$, similarly to a finite global temperature in the pre-quench state or a finite system size (see Sec. 4.4.3). In order to quantify this effect, we define the RG scale ℓ_T at which the effective temperature T becomes of the order of the UV cutoff Λ or, equivalently, when the dimensionless temperature $\bar{T}$ becomes $\bar{T} \sim 1$. The regime of validity of the description is then exited upon reaching this scale and, consequently, the RG flow has to be stopped. Moreover, by focusing on the case $g > 1$, when $\bar{\gamma}$ is irrelevant according to the first-order RG analysis (see Eq. (6.29)), we

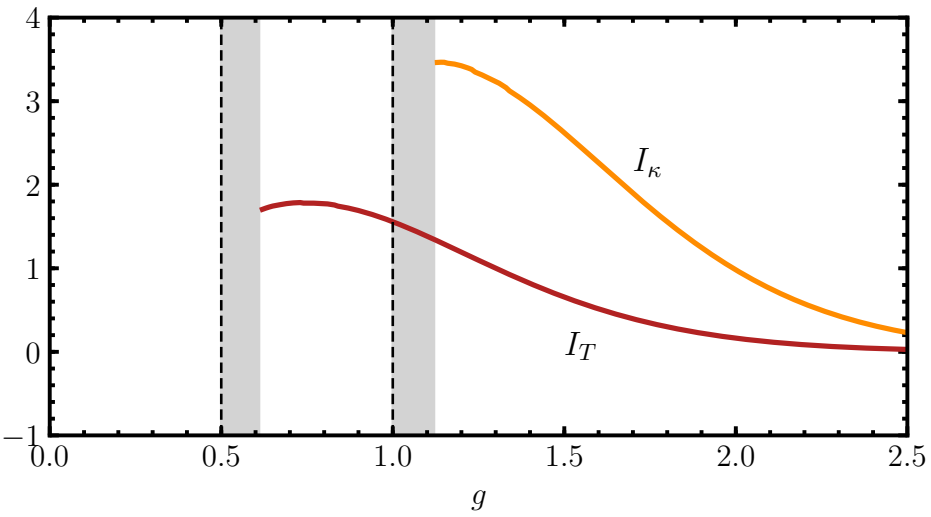

Fig. 6.2. Integrals I_T and I_κ as a function of the Luttinger parameter g for $T = 0$. The vertical dashed lines mark the boundaries of the convergence region. The gray-shaded areas indicate insufficient numerical convergence.

define a scale ℓ_c at which $\bar{\gamma}$ is decreased by a factor of e^{-c} from its microscopic value. Hence, the competition between the two scales ℓ_T and ℓ_c reveals whether the generation of an effective temperature can significantly affect the qualitative behavior of the first-order RG flow. For $\ell_c < \ell_T$, quantum fluctuations renormalize the value of $\bar{\gamma}$ by a factor of at least e^{-c} before the RG stops, thus unveiling the flow described in Sec. 6.3. Contrary, if $\ell_c > \ell_T$, the RG flow stops before the quantum fluctuations renormalize $\bar{\gamma}$ by a factor of e^{-c}.

We can estimate the scales ℓ_T and ℓ_c based on the following approximate solutions of the RG equations (6.55). First, the value of ℓ_c can be estimated from the solution of Eq. (6.29) and reads

$$\ell_c = \frac{c}{g-1}. \tag{6.58}$$

Second, the scale ℓ_T can be estimated as follows. To begin with, we simplify Eq. (6.55b) by keeping only contributions in leading order of $\bar{\gamma}_0$, where $\bar{\gamma}_0 \equiv \bar{\gamma}(\ell = 0)$. Since the corrections generated for T are of order $T = 0 + \mathcal{O}(\gamma_0^2)$, we can neglect terms $\mathcal{O}(T\gamma_0^2)$. Further, this enables us to replace $I_T = I_{0T} + T\frac{\mathrm{d}I_T}{\mathrm{d}T} + \ldots$ by $I_{0T} \equiv I_T(\kappa_0, \kappa_0, 0)$. Eventually, by plugging in the solution of Eq. (6.29) into Eq. (6.55b) we obtain

$$\frac{\mathrm{d}\bar{T}}{\mathrm{d}\ell} = \bar{T}(\ell) + g\bar{\gamma}_0^2 I_{0T}\mathrm{e}^{2(1-g)\ell}. \tag{6.59}$$

The solution of this differential equation yields for the initial condition $\bar{T}(\ell = 0) = 0$:

$$\bar{T}(\ell) = \bar{\gamma}_0^2 \frac{g I_{0T}}{1-2g}\left(\mathrm{e}^{2(1-g)\ell} - \mathrm{e}^{\ell}\right) \approx \bar{\gamma}_0^2 \frac{g I_{0T}}{2g-1}\mathrm{e}^{\ell}, \tag{6.60}$$

where in the last equality we retained the growing exponential. Finally, we find from this equation the scale

$$\ell_T = \log\left(\frac{2g-1}{\bar{\gamma}_0^2 g I_{0T}}\right). \tag{6.61}$$

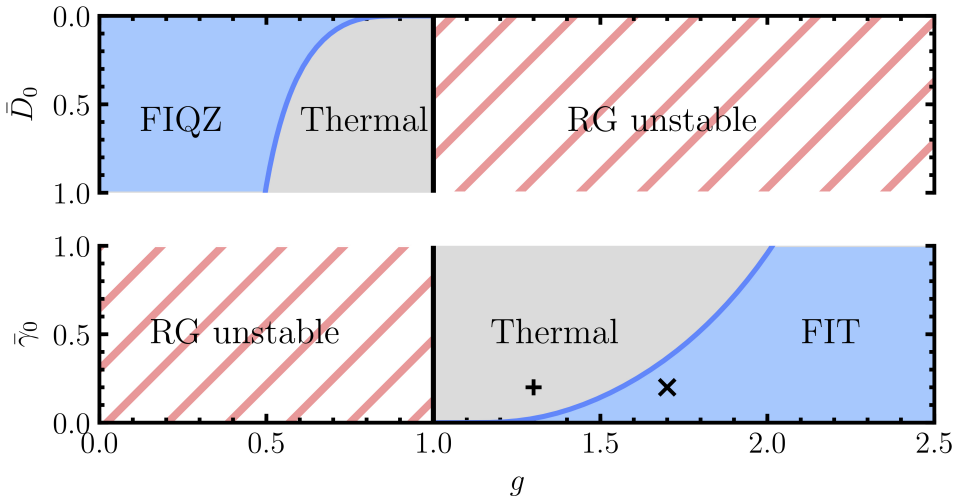

Fig. 6.3. Phase diagram for the dissipative impurity from the second-order RG equations, for different values of the microscopic dissipation strength $\bar{\gamma}_0$ ($\bar{D}_0$ in the dual regime) and of the Luttinger parameter g. The blue-shaded area in the lower-right corner corresponds to values where the fluctuation-induced transparency (FIT) is visible, while the upper-left one corresponds to values where the fluctuation-induced quantum Zeno effect (FIQZE) is visible. The gray-shaded areas correspond to values where the effective temperature hinders these effects. The solid lines are obtained using Eqs. (6.58) and (6.61) with $c = \log 10$. The striped regions correspond to values where the perturbative RG breaks down.

The corresponding results in the dual regime can be obtained simply by replacing $\bar{\gamma} \to \bar{D}$ and $g \to 1/g$ in Eq. (6.61).

The comparison of ℓ_c with ℓ_T then yields the phase diagram shown in Fig. 6.3 (for $c = \log 10$). Here, the blue-shaded area corresponds to values of $\bar{\gamma}_0$ and g for which the scaling of Eq. (6.29) is visible ($\ell_c < \ell_T$), while the gray-shaded area corresponds to values of $\bar{\gamma}_0$ and g for which the effective temperature dominates over the scaling ($\ell_c > \ell_T$). The solid blue lines indicate the crossover between the two regions and are analytically determined from the condition $\ell_c = \ell_T$. Further, the dashed areas correspond to regions where the perturbative analysis breaks down. We conclude that for weak interactions ($g \approx 1$), the effect of the effective temperature washes out the renormalization due to quantum fluctuations. However, for stronger interactions the renormalization remains visible and strongly modifies the value of the effective barrier.

In order to benchmark the previous estimates, we numerically solve the full RG equations (6.55) and compare the results with the picture provided in Fig. 6.3. In Fig. 6.4 (upper panel), the flow of $\bar{\gamma}$ and $\bar{T}$ is shown for values corresponding to the $+$ symbol in Fig. 6.3, within the thermal regime of the phase diagram. In this case, the flow of $\bar{\gamma}$ is rather distorted compared to the scaling (6.29) and decays only for $\ell > \ell_T$. The effect of quantum fluctuations is washed out by the effective temperature, in agreement with the prediction in Fig. 6.3. In contrast, in Fig. 6.4 (lower panel) we report the flow of $\bar{\gamma}$ and $\bar{T}$ for values corresponding to the $\times$ symbol in Fig. 6.3, corresponding to a region where a fluctuation-induced transparency regime is expected. Indeed, the value of $\bar{\gamma}$ almost reaches zero at ℓ_T, leaving the scaling (6.29) largely visible, in agreement with the prediction of Fig. 6.3.

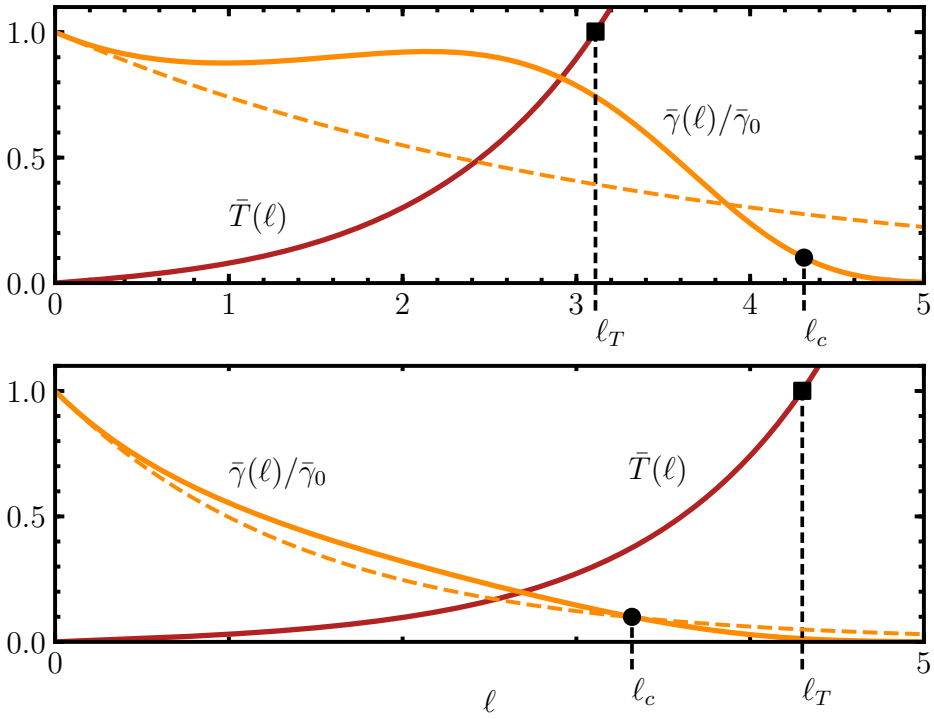

Fig. 6.4. RG flow of $\bar{\gamma}$ and $\bar{T}$ obtained by numerically solving Eq. (6.55) with the initial conditions $\bar{\gamma}(\ell = 0) = \bar{\gamma}_0$ and $T(\ell = 0) = 0$. The dashed lines correspond to the first-order solutions (6.29). Upper (lower) panel: Values of $\bar{\gamma}_0$ and g as indicated by the $+$ ($\times$) symbol in Fig. 6.3.

6.5. Conclusion and outlook

In this chapter, we investigated the effects of a localized loss on a Luttinger liquid within a Keldysh functional description. The approach addresses by construction the effective properties of the loss barrier near the Fermi level. An RG analysis was performed perturbative in the dissipation strength, and in a dual description perturbative in the weak link induced by a strong dissipation. The resulting RG flow at first order entails a strong renormalization of the effective barrier, which can be understood to lead to a suppression of loss near the Fermi level in both cases of repulsive and attractive interactions, either via a fluctuation-induced quantum Zeno effect or a fluctuation-induced transparency. The study of the RG flow within Luttinger liquid theory was then extended to second order in the impurity strength. At second order, the nonlinear impurity term in the actions leads to the generation of a local effective temperature, which effectively provides a cutoff scale for the RG flow. The evaluation of this cutoff scale reveals different regimes characterized by the microscopic parameters of the system where a qualitatively different behavior of the effective impurity is obtained. In a thermal regime, the generation of the effective temperature prevents a significant renormalization of the impurity strength. However, further regimes are identified in which self-thermalization effects take a subleading part and a strong renormalization of the effective loss barrier persists.

We can understand the Luttinger liquid approach pursued in this chapter to provide a coarse-grained description of the renormalization of the scattering properties obtained in Chapter 4 as a result of the interplay with Friedel oscillations. The methods used in both chapters are

indeed complementary in the following sense. The Luttinger liquid incorporates interactions at arbitrary strength, while the analysis proceeds perturbatively in the impurity strength. In contrast, the real-space RG approach is valid for any impurity strength, but the analysis is feasible only perturbative in the interactions. Both approaches predict qualitatively the same results corresponding to the stable fixed points approached by the RG flow. Moreover, for repulsive interactions, the scaling of the RG flow near the stable fixed point coincides in both cases. However, for attractive interactions, a different scaling near the stable fixed point is observed.

Further improvements on the description could be achieved by including the back action of the localized loss on the bulk state of the Luttinger liquid, such as a modified momentum distribution. Moreover, the study of thermalization effects in Luttinger liquids with a finite conductance is desirable due to the presence of currents induced by the localized loss. Further, in the second-order analysis a breakdown of perturbation theory is encountered in domains near the unstable fixed points (cf. Fig. 6.3). Here, e.g., generalized approximation schemes for the low-frequency expansion could provide additional insights into the RG flow [123].

While we mainly focused on fermions, the results are expected to apply also for one-dimensional Bose gases in the strong coupling regime, whose low-energy excitations also behave as a Luttinger liquid (cf. Sec. 2.3.3). In particular, transport across a localized potential barrier was shown to be strongly renormalized by fluctuations [131], suggesting that the effects predicted in this work should also be visible there. A similar experimental setup was considered in Ref. [41]. Finally, a natural extension of the Luttinger liquid approach exists for spinful fermions in the presence of a coherent impurity [80]. Therefore, the study of the interplay of the spin degrees of freedom with a localized loss is desirable, in particular in view of recent experiments [43, 44].

CHAPTER 7

SPECTRAL PROPERTIES OF LOCALIZED DISSIPATION

The numerous works published in recent years in the context of non-Hermitian physics, which is characterized by a non-Hermitian generator of the dynamics, testify the high interest in this field. Examples include the extensive study of parity-time symmetric systems [163, 164], where naturally a phase characterized by a real-valued spectrum connects to the familiar realm of Hermitian physics, the investigation of non-reciprocal effects, widely accessible with non-Hermitian settings [20, 21], and non-Hermitian topology [31, 165] leading to novel effects as the non-Hermitian skin effect. One of the hallmarks of non-Hermitian physics is the occurrence of spectral singularities dubbed exceptional points [135], where two or more eigenvectors of a non-Hermitian Hamiltonian become linearly dependent leading to novel types of phase transitions [166, 167].

The effective non-Hermitian Hamiltonian $\widetilde{H}$ (3.8) discussed in Chapter 3 as the generator of dynamics for correlation functions constitutes a non-Hermitian model. Here, an interplay between the spectral properties of the non-Hermitian Hamiltonian on a lattice and the microscopic quantum Zeno effect is revealed, based on the following expectations. In the limit of weak dissipation, the spectral properties are expected to be similar to the ones in the absence of loss, i.e., delocalized scattering states whose eigenvalues may acquire a small imaginary part. Contrary, in the limit of strong dissipation, as a consequence of the quantum Zeno effect, dissipation is expected to act only locally at the loss site, while the remaining system becomes asymptotically dissipation-free. We show that for intermediate dissipation strength the spectrum exhibits a sharp reorganization, with a localized state emerging at a critical value of γ, associated with a large imaginary eigenvalue. The transition point constitutes an exceptional point of the effective non-Hermitian Hamiltonian.

As a preparation, we discuss several peculiarities of the spectral properties of non-Hermitian generators of dynamics. With this at hand, we study the spectrum and eigenfunctions of the effective non-Hermitian Hamiltonian and associated retarded Green's function in presence of a localized loss, both numerically for a finite size and analytically in the thermodynamic limit. Subsequently, we turn towards the observability of the therein encountered spectral transition. Moreover, the superposition of the localized loss with a real-valued potential reveals an interesting interplay of the localized mode and the bulk spectrum leading to a spectral flow [168, 169] phenomenon.

The main results on the spectral transition in Sec. 7.2 have been published in publication [134].[1] We remark that Ref. [170] appeared during the completion of publication [134], pointing out the same transition described here.

7.1. Non-Hermitian eigenvalue problems

While the Hermicity of a matrix ensures that its eigenvalues are real-valued and its eigenspaces mutually orthogonal, both properties do not apply to non-Hermitian matrices. As a result, new concepts like complex-valued eigenvalues and non-orthogonal eigenvectors occur. This leads to surprising mathematical properties such as the emergence of spectral singularities, so-called exceptional points, where two or more eigenvectors become linearly dependent [135]. Exceptional points emerge in a variety of physical problems thus rendering their mathematical properties physically relevant. We briefly discuss some important properties of non-Hermitian eigensystems to set the stage for the study of the non-Hermitian effective Hamiltonian (3.8) and the associated retarded Green's function in the following sections.

Let us consider the spectral properties of a non-Hermitian matrix M, which in a physical context could be associated, e.g., with an effective non-Hermitian Hamiltonian (cf. Eq. (3.8)) or the dynamical matrix of an equation of motion [166]. The eigenvalues of M are in general complex-valued. In the case of a non-Hermitian Hamiltonian, the real part of an eigenvalue can be associated with the energy of a mode and the imaginary part with its lifetime [171].

Moreover, the eigenvectors are generally not orthogonal, in contrast to the eigenvectors of a Hermitian matrix. In order to diagonalize a non-Hermitian matrix, it is then useful to consider a biorthogonal system, as explained in the following. To this end, we define the left and right eigenvectors, $\widetilde{\psi}$ (a "row-vector") and ψ [135], via

$$\widetilde{\psi} M = \widetilde{\psi}\,\widetilde{\lambda}, \qquad M\psi = \lambda\psi, \tag{7.1}$$

with $\widetilde{\lambda}$ and λ the associated left and right eigenvalues. It can be easily shown that left and right eigenvalues are in fact identical by noting that H^T has the same characteristic polynomial as H, i.e., $\widetilde{\lambda} = \lambda$.

M can then be brought into a diagonal form D by a change of basis, $D = S^{-1}MS$, where the columns of S are given by right eigenvectors of H and the rows of S^{-1} by the left eigenvectors of M (assuming a complete eigenbasis exists). For a Hermitian matrix left and right eigenvectors are trivially connected via $\widetilde{\psi} = \psi^\dagger$, while this identity is no longer true for a non-Hermitian matrix. The set of left and right eigenvectors, instead, forms a biorthogonal system characterized by [171]

$$\widetilde{\psi}_k \cdot \psi_l = \delta_{k,l}, \tag{7.2}$$

where proper normalization is assumed. Note that the use of the identity (7.2) for normalization leads in general to a violation of the familiar relation $\psi_k^\dagger \cdot \psi_k \neq 1$.

We now turn to the concept of exceptional points, which is a consequence of the non-orthogonal eigenspaces. To this end, we consider a non-Hermitian matrix $M(\zeta)$ depending on a complex-valued tuning parameter ζ. In general, singular points ζ_c in the parameter space exist at which

[1] Several paragraphs and sentences in Sec. 7.2 can be found almost identically in publication [134].

two or more eigenvectors of $M(\zeta)$ coalesce, i.e., they become linearly dependent. Consequently, the set of eigenvectors no longer constitutes a complete generating set and $M(\zeta_c)$ is non-diagonalizable. ζ_c is then called an exceptional point of $M(\zeta)$. Consequently, a Hermitian matrix cannot exhibit an exceptional point as an implication of the spectral theorem ensuring its diagonalizability [172]. The number n of coalescing modes defines the order of the exceptional point.

At an exceptional point (of order two), the eigenvalues of the two coalescing modes become necessarily degenerate. Moreover, the spectrum exhibits a square-root branching point for the following reason. The characteristic polynomial contains generally terms of the form $\sim \sqrt{\zeta - \lambda_{1,2}}$, with $\lambda_{1,2}$ the complex eigenvalues of the coalescing modes [135], resulting in an eigenvalue landscape reflecting a complex square-root behavior. This constitutes a Riemannian sheet structure containing a branch cut near the "singular" exceptional point [135]. In particular, this branching behavior is different from the level crossing encountered in Hermitian systems [173]. Moreover, higher-order exceptional points exhibit n-th-root branching points [31].

The mathematical properties of a non-Hermitian matrix result in a variety of physical implications. For example, a novel mechanism of phase transitions was proposed in Ref. [166] where typically the exceptional point appears as the endpoint ("critical point") of a line of first-order phase transition, as a consequence of the Riemannian sheet structure of the eigenvalues. Further, the sensitive dependence of the spectrum on ζ due to the square-root branching at an exceptional point has been proposed to be utilized in sensors [174]. In Ref. [167], critical fluctuations were discussed as a result of the coalescence of massless and massive modes at an exceptional point. In Ref. [175], unidirectional response was experimentally realized in a microtoroid resonator tuned to an exceptional point. Parity-time symmetric non-Hermitian systems were intensively studied [164] where generically an exceptional point occurs at the transition between the parity-time-symmetric and the parity-time-broken phase [135].

7.2. Spectral properties of the Green's function: Localized state

We now discuss the spectral properties of the retarded Green's function and of the associated non-Hermitian Hamiltonian for a non-interacting system on a lattice subject to a localized loss. We show that the spectrum exhibits a transition, with a localized state emerging above a critical value of γ. This localized state acquires an imaginary part significantly larger than the imaginary parts of all other modes. First, we numerically solve the eigenproblem for a finite system with L sites. With these results at hand, we analytically derive localized solutions for the infinitely large lattice.

7.2.1. Spectrum

We consider the retarded Green's function in frequency space $G_{i,j}(\omega)$ for a non-interacting system on a lattice of size L described by the Hamiltonian (3.3) and in the presence of a localized loss γ. The spectrum of $G_{i,j}(\omega)$ is related to the one of the non-Hermitian effective Hamiltonian $\widetilde{H}$ (3.8)

$$\widetilde{H}_{kl} = -J\left(\delta_{k,l+1} + \delta_{k+1,l}\right) - i\gamma\delta_{k,0}\delta_{l,0}, \tag{7.3}$$

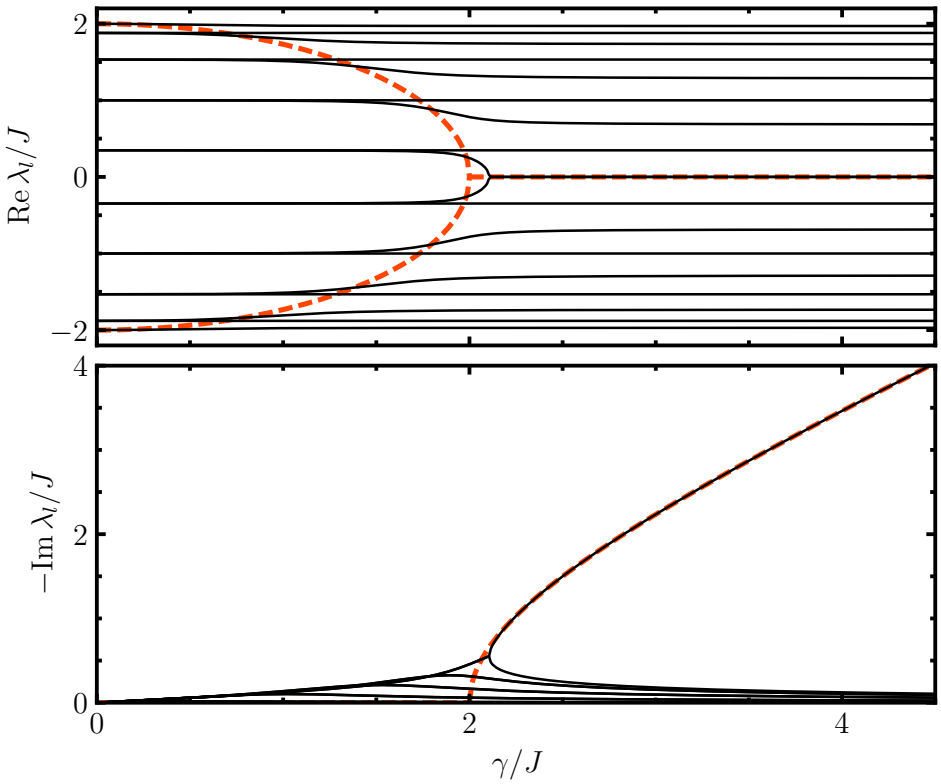

Fig. 7.1. Real (upper panel, black lines) and imaginary part (lower panel, black lines) of the eigenvalues λ_l of the non-Hermitian effective Hamiltonian $\widetilde{H}$ as a function of γ, for $L = 18$ and periodic boundary conditions. The red dashed lines indicate the analytical solutions (7.10), respectively (7.12).

as a consequence of the following relationship:

$$G^{-1}_{i,j}(\omega) = (\omega + i\epsilon)\delta_{ij} - \widetilde{H}_{ij}, \tag{7.4}$$

with ϵ an infinitesimal positive quantity ensuring causality. The eigenvalues of the effective Hamiltonian are poles of the retarded Green's function and are thus expected to be of physical relevance. Since $\widetilde{H}$ is non-Hermitian, its eigenvalues λ_l are complex-valued.

The real and imaginary parts of the spectrum of $\widetilde{H}$ as a function of γ are depicted in Fig. 7.1 for a system of finite size ($L = 18$, periodic boundary conditions). For all γ, the real part of the eigenvalues lies within $-2J$ and $2J$, i.e., in the same energy band as of the system in the absence of the impurity. The values of the imaginary parts are typically of order $\sim \gamma/L$. The spectrum clearly reorganizes at $\gamma_c = 2J$, and for $\gamma > \gamma_c$ a single eigenvalue acquires an imaginary part of order $\sim \gamma$, much larger than the other modes (cf. Fig. 7.1, lower panel). The remaining eigenvalues possess a finite imaginary part, which becomes increasingly small upon increasing γ. Moreover, some eigenvalues have a vanishing imaginary part for any value of γ: these correspond to the dissipationless subspace [51] discussed in Sec. 3.2. In the real part of the spectrum (see Fig. 7.1, upper panel), a successive shift of frequencies takes place upon increasing γ, which ends at $\gamma = \gamma_c$. These shifts follow a semicircle pattern, corresponding to the energies of a specific set of delocalized solutions, as discussed further below. At γ_c, two previously non-degenerate values merge at zero frequency. This value corresponds to the mode with finite imaginary part.

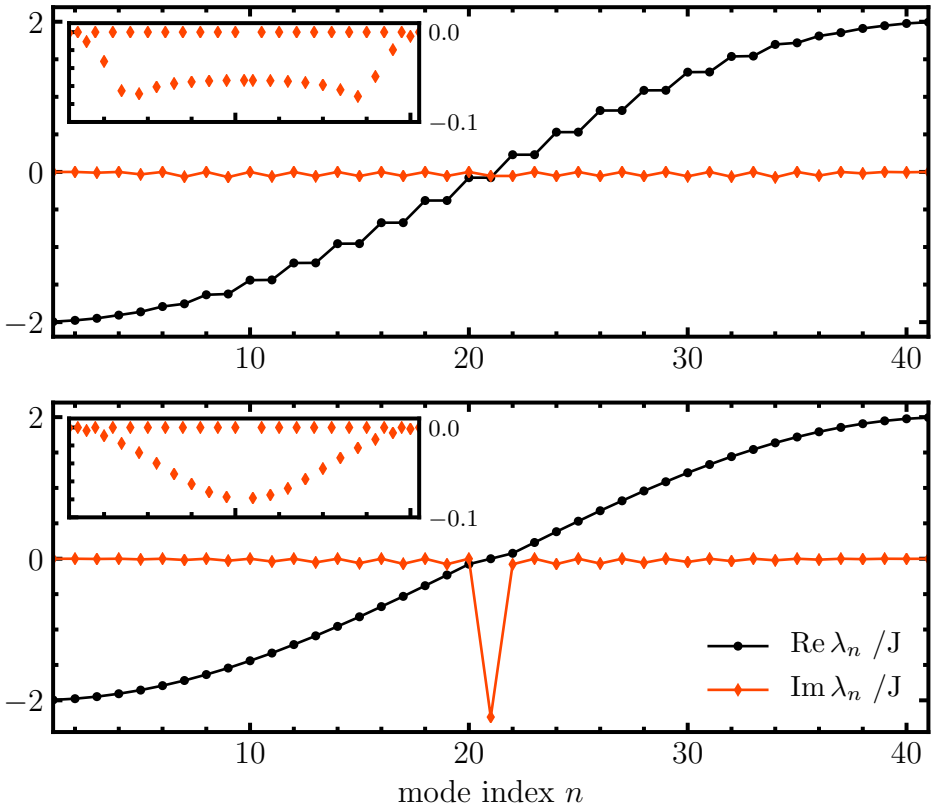

Fig. 7.2. Real (black) and imaginary part (red) of the spectrum of $\widetilde{H}$ for dissipation strengths smaller (upper panel, $\gamma = 1$) and larger than γ_c (lower panel, $\gamma = 3$), for periodic boundary conditions and $L = 41$. The insets show a magnified view of the the respective imaginary parts of the spectrum.

In Fig. 7.2 the real (black) and imaginary parts (red) of the spectrum for a system of finite size ($L = 41$, periodic boundary conditions) are depicted for two different values of the dissipation strength γ, above and below the threshold value $\gamma_c = 2J$, respectively. In the spectrum for $\gamma > \gamma_c$, the eigenvalue of a single distinct mode acquires an imaginary part significantly larger compared to all other modes. In contrast, in the spectrum for $\gamma < \gamma_c$, such a distinct mode does not occur. The insets present a magnified view for the distribution of the smaller imaginary parts, revealing modes with finite or vanishing imaginary part. In addition, in the real part of the spectrum, a shift of frequencies is observed in comparison between the two panels.

For increasing system sizes L, real and imaginary part of the eigenvalue for the single distinct mode approach the red dashed lines in Fig. 7.1. The approach of the imaginary part of the single distinct mode with increasing system size is depicted in Fig. 7.3 (left panel). In contrast, the imaginary parts of all other modes decrease as $\sim 1/L$ upon increasing the system size which is shown in Fig. 7.3 (right panel) exemplary for a single mode. The modes with a finite but small imaginary part of order $\sim \gamma/L$ exhibit a non-monotonic behavior as a function of γ (cf. Fig. 7.1, lower panel, and Fig. 7.3, right panel). The respective maxima are attained for $\gamma < \gamma_c$ and the imaginary parts are monotonously decreasing for $\gamma > \gamma_c$. In fact, the sum of all the eigenvalues must satisfy $\sum_l \lambda_l = -i\gamma$ (the imaginary part of the trace of $\widetilde{H}$ (7.3)), i.e., the imaginary parts of all eigenvalues must add up to $-\gamma$. Therefore, upon increasing L, the number of modes grows, while the contribution of each mode scales as $1/L$ in order to yield a finite sum (except for the

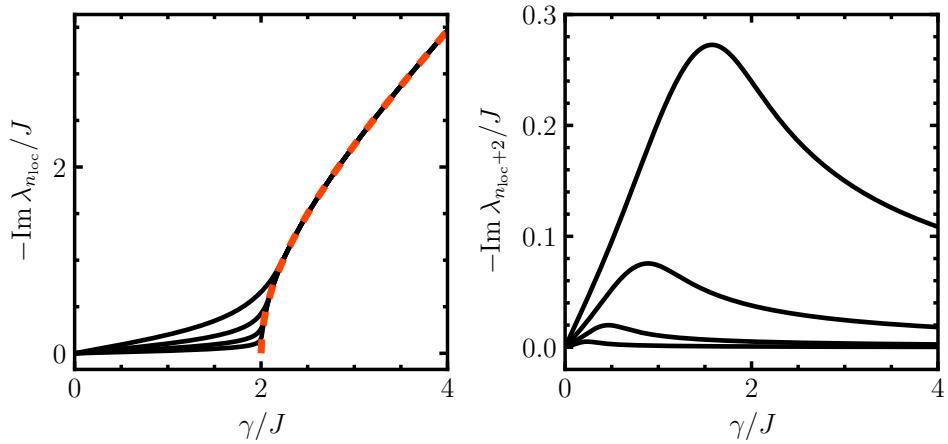

Fig. 7.3. Left panel: Imaginary part of the localized mode (mode index n_{loc}) for different system sizes, $L = 11, 21, 41, 81$ (from top to bottom), and periodic boundary conditions. With increasing system size, the dashed red line is approached which indicates the analytical result (7.10) in the infinite system. Right panel: Typical behavior of the imaginary part of the delocalized modes (here an exemplary mode $n = n_{\mathrm{loc}} + 2$), for the same system sizes as in the left panel. With increasing system size (top to bottom), the imaginary part decreases asymptotically to zero for all γ.

outstanding mode, which contributes with a finite value to the sum). In this respect, the single distinct mode accumulates asymptotically all dissipation in the regime $\gamma/J \gg 1$.

7.2.2. Eigenmodes

In order to further clarify the nature of this transition, we numerically inspect the corresponding eigenvectors. We can identify three different types of modes, corresponding to the three qualitative behaviors found for the eigenvalues. The single mode acquiring a large imaginary eigenvalue turns out to be a localized state, exponentially localized at the loss site and only present for $\gamma > \gamma_c$ (cf. Fig. 7.4, lower panel), while the other modes correspond to delocalized scattering states cf. Fig. 7.4, upper panel). The zero-damping modes which are not affected by the localized loss for all values of γ exhibit a node at the impurity site. Half of the modes show this dissipation-free behavior (see Fig. 7.2, insets). These modes can be understood as the spectral manifestation of the dissipation-free subspace discussed in Sec. 3.8.

The spectral properties described so far can be interpreted as an incarnation of the (microscopic) quantum Zeno effect. In fact, the imaginary part (i.e., the inverse lifetime) of the delocalized modes features a non-monotonic dependence on γ, as shown in Fig. 7.3 (right panel). On the converse, the localized mode is the fastest decaying mode and is related to the emptying of the loss site. Therefore, in the limit of large γ, the dissipation is restricted to the dissipative subspace defined by the loss site (cf. Sec. 2.2).

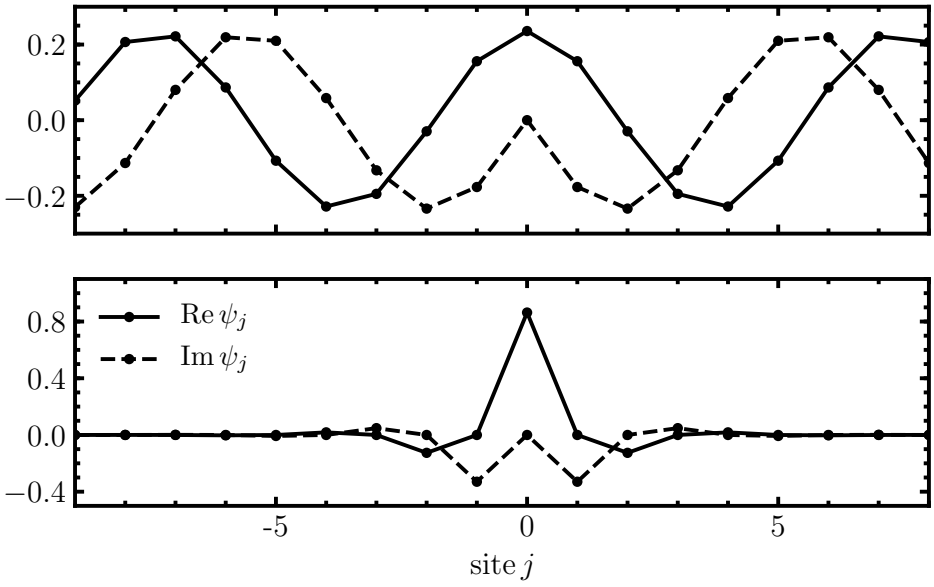

Fig. 7.4. Upper panel: Profile of the delocalized solution (7.9), for $\gamma = 1.5J$. Lower panel: Profile of the localized-state solution (7.11), for $\gamma = 3J$.

7.2.3. Analytical solution: Localized state

We further substantiate the nature of the localized state by solving analytically the scattering problem defined by the non-Hermitian Schrödinger equation

$$i\partial_t \psi_j = \sum_k \widetilde{H}_{jk}\psi_k, \tag{7.5}$$

for an infinitely large ($L = \infty$) system. Exponentially localized solutions are found by using the ansatz

$$\psi_j = A\mathrm{e}^{-\kappa|j|-i\lambda t}, \qquad \kappa, \lambda \in \mathbb{C}. \tag{7.6}$$

By writing $\kappa = \kappa_R + i\kappa_I$, we find the conditions

$$\cosh\kappa_R \, \sin\kappa_I = \frac{\gamma}{2J}, \qquad \sinh\kappa_R \, \cos\kappa_I = 0, \tag{7.7}$$

and the corresponding eigenvalue λ is given by

$$\lambda = -2J\mathrm{e}^{-\kappa} - i\gamma. \tag{7.8}$$

Eqs. (7.7) admit two types of solutions. For $\gamma < \gamma_c = 2J$ two solutions exist, with $\kappa_R = 0$ and

$$\kappa_I^{(1)} = \arcsin\frac{\gamma}{2J}, \qquad \kappa_I^{(2)} = \pi - \kappa_I^{(1)}, \tag{7.9}$$

which corresponds to the eigenvalues

$$\lambda^{(1)} = -\sqrt{\gamma_c^2 - \gamma^2}, \qquad \lambda^{(2)} = \sqrt{\gamma_c^2 - \gamma^2}, \tag{7.10}$$

indicated by the red dashed lines in Fig. 7.1, for $\gamma < \gamma_c$. These solutions are delocalized since $\kappa_R = 0$, and correspond to the ones experimentally investigated in Ref. [42] (cf. discussion below). The solution $\psi^{(1)}$ is shown in Fig. 7.4 (upper panel). The shift of frequencies seen in the real part of the spectrum for $\gamma < \gamma_c$ follows the semicircle described by Eqs. (7.10), see Fig. 7.1 (upper panel).

For $\gamma > \gamma_c$, instead, a single solution is found for which $\kappa_I = \pi/2$ and

$$\kappa_R = \ln\left[\frac{1}{2J}\left(\gamma + \sqrt{\gamma^2 - \gamma_c^2}\right)\right], \tag{7.11}$$

thus describing a localized function, shown in Fig. 7.4 (lower panel), with the localization length κ_R^{-1}, decreasing with γ. The corresponding eigenvalue λ reads

$$\mathrm{Re}\,\lambda = 0, \qquad \mathrm{Im}\,\lambda = -\sqrt{\gamma^2 - \gamma_c^2}, \tag{7.12}$$

as indicated in Figs. 7.1 and 7.3 (left panel) by the red dashed lines (for $\gamma > \gamma_c$). It shows perfect agreement with the finite-size spectrum, reflecting its locality, with corrections being important at $\gamma \sim \gamma_c$. The two solutions of Eq. (7.9) coalesce at γ_c, which therefore constitutes an exceptional point of $\widetilde{H}$ [135]. While in the thermodynamic limit an exceptional point is always present, in the spectrum of a finite-sized system, its presence depends on the geometry. In Fig. 7.1 the geometry (periodic boundary conditions and $L = 2 + 4n, n \in \mathbb{N}$) allows the presence of an exceptional point at a finite size, which corresponds to the sharp branching points of two eigenvalues in the real and imaginary parts of the spectrum, slightly above $\gamma = 2J$. The conditions for the formation of exceptional points in finite-sized spectra have been exhaustively classified in Ref. [170]. However, a single distinct mode with large imaginary eigenvalue is observed independently from these conditions.

We remark that the emergence of a localized solution is unique for the lattice model while the continuum analog of Eq. (7.5) does not support a localized solution, as shown in Sec. 2.5.

7.2.4. Non-Hermitian properties of the retarded Green's function

We briefly discuss some mathematical properties of the non-Hermitian eigenproblem associated with the effective Hamiltonian (7.3) and its consequences for the retarded Green's function (7.4). As can be inferred from Eq. (7.3) the effective Hamiltonian $\widetilde{H}$ is described by a complex symmetric matrix, i.e., $\widetilde{H}^T = \widetilde{H}$. The defining identity (7.1) for left eigenvectors $\widetilde{\psi}$ then implies $\widetilde{H}^T\widetilde{\psi}^T = \widetilde{H}\widetilde{\psi}^T = \lambda\widetilde{\psi}^T$ (cf. Sec. 7.1) and therefore left and right eigenvectors are connected by transposition, i.e., $\widetilde{\psi} = \psi^T$. Consequently, the biorthogonality relation (7.2) reads

$$\psi_k^T \cdot \psi_l = \delta_{k,l}. \tag{7.13}$$

Note the difference in comparison to the orthogonality relation of a Hermitian eigensystem, where Hermitian conjugation appears instead of transposition. As a result of this pseudo-orthogonality, we obtain an expansion of the retarded Green's function (7.4) in a real-space representation as

$$G_{k,l}(\omega) = \sum_n (\psi_n)_k (\psi_n)_l (\omega + i\epsilon - \lambda_n)^{-1}, \tag{7.14}$$

where $(\psi_n)_k$ is the k-th component of the n-th eigenmode. Here, each mode contributes with a complex eigenvalue λ_n and a complex coefficient $(\psi_n)_k(\psi_n)_l$, in contrast to a Hermitian system where the expansion would read

$$G_{i,j}(\omega) = \sum_n (\psi_n)_i^*(\psi_n)_j(\omega + i\epsilon - \lambda_n)^{-1}, \tag{7.15}$$

with real λ_n. In particular, the diagonal part, $k = l$, in the latter case is determined by real coefficients $|(\psi_n)_k|^2$. We discuss further consequences of the expansion (7.14) in Sec. 7.3.1. Finally, we remark that the non-orthogonality of eigenstates is considered in Ref. [176] as a requirement for a non-exponential decay in the presence of a localized loss of a wave function, initially localized remote from the loss site (similar to the constant loss rate in the second regime discussed in Chapter 3.2.2).

7.3. Observability of the spectral transition

We now turn to the observability of the spectral properties discussed in the previous section. In order to gain a first insight into the spectral properties in a real-space representation, we study the local density of states [120] of a fermionic wire with a localized loss. We are particularly interested in probing the spectral transition characterized by the emergence of the single distinct mode with a large imaginary eigenvalue. To this end, we consider a bosonic system with homogeneous losses and a localized pump, leading to similar spectral properties featuring a localized mode with a long lifetime.

7.3.1. Local density of states

Having studied the spectrum and eigenbasis of the effective non-Hermitian Hamiltonian in Sec. 7.2, we now consider the retarded Green's function (7.4) in a real-space basis. To this end, we consider the spectral function $A(\omega)$ [6, 84], which is closely related to the retarded Green's function as

$$A_{i,j}(\omega) = -2 \operatorname{Im} G_{i,j}(\omega). \tag{7.16}$$

The spectral function can be interpreted as the distribution of resonant levels of the system, i.e., as a probability (it holds $A(\omega) > 0$) of hitting a resonance when exciting the system at a frequency ω [6]. Here, we focus on the diagonal part of the spectral function, namely the local density of states (LDoS) defined by [120]

$$\mathrm{LDoS}_j(\omega) = -\frac{1}{\pi} \operatorname{Im} G_{j,j}(\omega). \tag{7.17}$$

In Fig. 7.5 the LDoS (colormap) is depicted as a function of the frequency ω and dissipation strength γ. In particular, we consider its average over all lattice sites j

$$\overline{\mathrm{LDoS}}(\omega) = \frac{1}{L}\sum_j \mathrm{LDoS}_j(\omega), \tag{7.18}$$

in order to smooth away even-odd effects. The comparison to the real part of the spectrum of $\widetilde{H}$ is indicated by the black dashed lines (cf. Fig. 7.1, upper panel), and several features of the

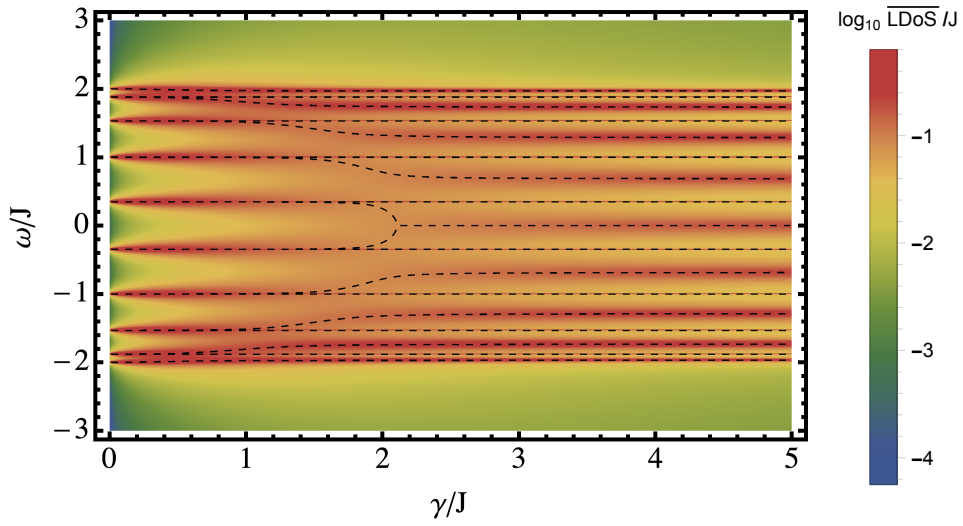

Fig. 7.5. LDoS averaged over all lattice sites j, as a function of γ and ω, for periodic boundary conditions, $L = 18$, and $\epsilon/J = 10^{-4}$. The dashed lines indicate the real part of the spectrum of $\widetilde{H}$ for comparison (cf. Fig. 7.1, upper panel).

spectral properties discussed in Sec. 7.2 are revealed to be evident in the LDoS. First, one can clearly observe the shift of the resonances for $\gamma \lesssim \gamma_c$ in direct correspondence to the real part of the spectrum. Further, the resonant peaks broaden below γ_c before narrowing again with increasing dissipation strength, directly reflecting the imaginary spectrum of the delocalized modes discussed in Sec. 7.2.1 (cf. Fig. 7.3, right panel). Moreover, the zero-dissipation modes are visible as narrow resonances unaffected by the presence of dissipation (we chose a finite ϵ for regularization in Eq. 7.4).

Remarkably, a broad peak emerging at γ_c is absent. We emphasize that this is not an artifact of the spatial average in Eq. (7.18). The emergence of such a feature could be naively expected, since for an orthogonal eigenbasis the expansion in the eigenmodes (7.15) results in $\mathrm{LDoS}_j(\omega) = -1/\pi \ \mathrm{Im} \sum_n |(\psi_n)_j^2| (\omega + i\epsilon - \lambda_n)^{-1}$. Hence, each mode n contributes to the LDoS with a Lorentzian peak centered at $\mathrm{Re}\,\lambda_n$ with a positive coefficient $|(\psi_n)_j^2|$. Thus, one would expect at γ_c a peak emerging centered at $\omega = 0$ and then broadening for increasing γ, which is different from the behavior observed in Fig. 7.5. The absence of this feature can be understood by noting that for the non-Hermitian system under consideration the expansion (7.14) yields

$$\mathrm{LDoS}_j(\omega) = -\frac{1}{\pi} \mathrm{Im} \sum_n (\psi_n)_j^2 (\omega + i\epsilon - \lambda_n)^{-1} \tag{7.19a}$$

$$= \frac{1}{\pi} \sum_n \frac{\mathrm{Re}[(\psi_n)_j^2](|\mathrm{Im}\,\lambda_n| + \epsilon) - \mathrm{Im}[(\psi_n)_j^2](\omega - \mathrm{Re}\,\lambda_n)}{(\omega - \mathrm{Re}\,\lambda_n)^2 + (|\mathrm{Im}\,\lambda_n| + \epsilon)^2}, \tag{7.19b}$$

where both $(\psi_n)_j^2$ and λ_n are complex-valued, and we used $\mathrm{Im}\,\lambda_n < 0$. Here, the first term of the addend describes a Lorentzian distribution centered at $\mathrm{Re}\,\lambda_n$ with a width $|\mathrm{Im}\,\lambda_n| + \epsilon$. The additional second term can lead to negative coefficients in the summation, allowing for a different behavior than obtained by a summation of Lorentzian peaks. As an additional consequence, the spectral line shape of resonances in the LDoS_j is not Lorentzian, and in particular allows one to engineer [177] asymmetric resonance peaks.

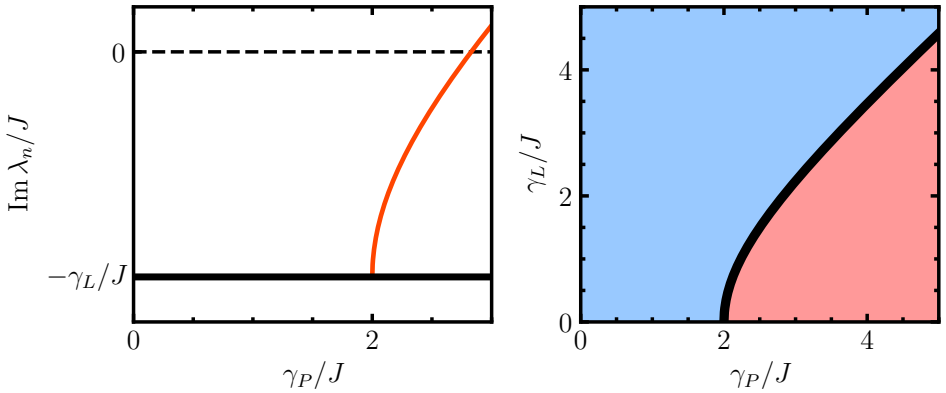

Fig. 7.6. Left panel: Imaginary part of the spectrum of the effective Hamiltonian for a bosonic system with homogeneous losses γ_L and a localized pump γ_P, for $L \to \infty$. At a critical value of $2J$, the eigenvalue of a single mode (red) growths larger than the imaginary parts of the eigenvalues of all other modes (black). Eventually, the single distinct eigenvalue becomes positive (dashed line), signaling an instability of the system. Right panel: Phase diagram associated with the spectral behavior shown in the left panel. The blue-shaded area indicates the stable regime and the red-shaded area the unstable one. The phase boundary (black) reflects the growths of the imaginary part of the single distinct mode until the threshold given by γ_L is overcome.

7.3.2. Bosons with a localized pump: Instability of the localized state

We now give an example of a possible experimental protocol to probe the properties of the localized mode pointed out in Sec. 7.2. To this end, we modify the so far considered model in the following way. First, we consider a bosonic system described by the bosonic analog of the tight-binding Hamiltonian (3.3). Second, we assume the presence of spatially homogeneous losses of strength γ_L. Third, we introduce a localized pump described by a Lindblad operator $\mathrm{L} = \psi^\dagger$ (replacing the localized loss), controlled by a strength γ_P. The non-Hermitian Hamiltonian associated with the quantum master equation (3.2) is then given by

$$\widetilde{H}_{kl} = -J\left(\delta_{k,l+1} + \delta_{k+1,l}\right) + i\gamma_P \delta_{k,0}\delta_{l,0} - i\gamma_L \delta_{k,l}. \tag{7.20}$$

For example, one could realize such a system by an optical cavity array [178] with imperfect cavities resulting in homogeneous losses and a localized pumping. Localized sources in free bosonic systems have been further discussed in Ref. [63].

The reason we consider bosons with a localized pump is the positive sign of the pumping term in Eq. (7.20) (cf. in contrast Eq. (7.3)). The spectral properties are then similar to the ones obtained for a localized loss, with a special mode emerging at a threshold $\gamma_P = 2J$, but now its imaginary part *increases* with increasing dissipation strength. The resulting dependence of the imaginary spectrum on γ_P is illustrated in Fig. 7.6 (left panel), in the thermodynamic limit $L \to \infty$. In the absence of a pump, the homogeneous losses lead to a uniform imaginary part of $-\gamma_L$ for all modes. With increasing pumping strength γ_P, at a critical value $\gamma_P = 2J$, the imaginary part of a single distinct mode acquires an imaginary part much larger than the ones of all other modes (whose change is of order $\sim \gamma_P/L$, cf. Sec. 7.2), thus compensating the losses and signaling a long-lived mode. Upon increasing the pumping strength γ_P further, the imaginary part of the distinct mode eventually overcomes the threshold value given by

γ_L and the system becomes unstable. In Fig. 7.6 (right panel), the resulting regions of stability (blue) and instability (red) are indicated in dependence on γ_L and γ_P, reflecting the square root growth (7.12) of the imaginary eigenvalue until the instability is reached. From this, the critical dissipation strength $\gamma_c = 2J$ can be extracted by the instability transition in the limit $\gamma_L \to 0$.

Moreover, the localized nature of the long-lived mode could, e.g., be observed via the following protocol. The response of the cavity amplitude $\langle b_j \rangle$ to a coherent, homogeneous and time-local pulse $E_j(t) = E_0\delta(t)$ is given by

$$\langle b_j \rangle = \int_{t'} \sum_{j'} G_{j,j'}(t-t')E_{j'}(t') \overset{t\to\infty}{\sim} E_0(\psi_{n_{\mathrm{loc}}})_j \mathrm{e}^{-i\lambda_{n_{\mathrm{loc}}}t}, \tag{7.21}$$

with n_{loc} the mode index of the localized mode. Here, we obtained in the long-time limit the dominating contribution by the distinct long-lived mode with the smallest imaginary eigenvalue, exhibiting a localized profile $\sim (\psi_{n_{\mathrm{loc}}})_j$.

Finally, we remark that similar spectral effects have been described in a recent work [179]. Here, an ensemble of pumped two-level atoms weakly coupled to a resonator is considered. The special mode is induced at the transition frequency of the atoms, without introducing a spatial inhomogeneity in the system. A lasing transition then occurs at the instability point.

7.4. Complex-valued impurity potential

In Sec. 7.2.3 we analytically studied the eigenproblem of the effective non-Hermitian Hamiltonian (7.3), where we focused on localized solutions. Remarkably, a localized solution is only present for large dissipation strengths, exceeding a threshold value γ_c. We now generalize this approach to complex-valued impurity potentials, realized by a localized loss superimposed with a coherent potential part (cf. Sec. 3.9). This extension of the model allows us, first, to compare the limiting cases of either a pure localized loss and a pure potential barrier and, second, to study the interplay of both types of impurities. We obtain a phase diagram that characterizes the existence of a localized state in dependence on the dissipation strength γ and coherent potential strength u. In this parameter space, the exceptional point is situated at the endpoint of a branch cut for the real frequency of the localized state. As a result of this topology, an encircling of the exceptional point on a closed path is found to continuously connect adjacent eigenmodes, leading to a spectral flow phenomenon, similar to the spectral behavior in the case of a Laughlin [168] or Thouless pump [169].

7.4.1. Spectral properties and localized state

We consider a complex impurity potential quantified by a parameter $g = u - i\gamma$ and obtain the corresponding effective non-Hermitian Hamiltonian by replacing $-i\gamma \to g$ in Eq. (7.3). The ansatz (7.6) for a localized solution of the corresponding eigenvalue problem (7.5) yields the eigenvalue

$$\lambda = -2J\mathrm{e}^{-\kappa} + u - i\gamma, \tag{7.22}$$

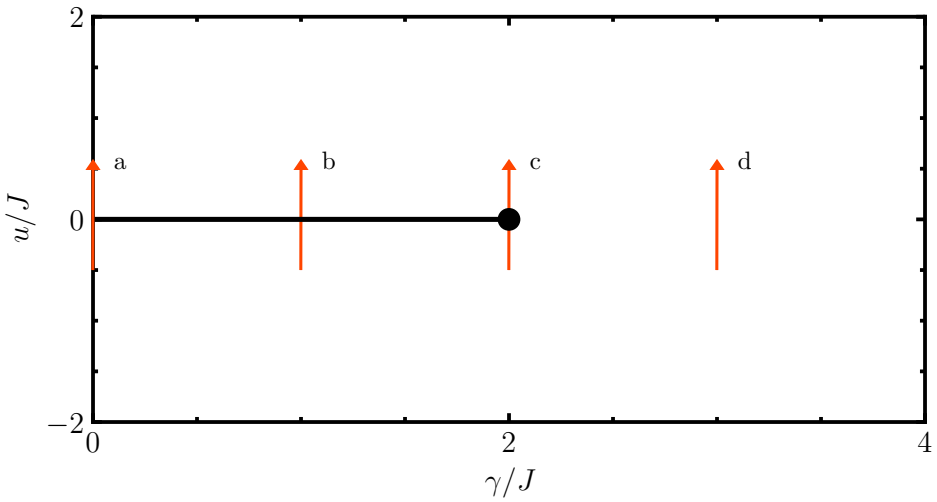

Fig. 7.7. Phase diagram depicting the existence of a localized state for a complex-valued impurity potential, characterized by the dissipation strength γ and coherent part u. A localized state is absent for the parameters indicated by the black line. The position of the exceptional point is marked by a black dot. The red arrows illustrate paths in the parameter space leading to qualitatively different behaviors of the frequency of the localized mode (see main text; cf. Fig. 7.8).

and the conditions for $\kappa = \kappa_R + i\kappa_I$:

$$\cosh\kappa_R \, \sin\kappa_I = \frac{\gamma}{2J}, \qquad \sinh\kappa_R \, \cos\kappa_I = -\frac{u}{2J}. \tag{7.23}$$

Beside the two limiting cases, either $u = 0$ or $\gamma = 0$, Eqs. (7.23) can only be solved numerically. Having already considered the solutions for $\gamma = 0$ in Sec. 7.2.3, we briefly discuss the case of a pure coherent barrier ($\gamma = 0$), where we obtain a closed-form solution

$$\kappa_R = \operatorname{arsinh}\frac{|u|}{2J}, \qquad \kappa_I = \arg(-u) = \begin{cases} \pi & \text{for } u > 0, \\ 0 & \text{for } u < 0, \end{cases} \tag{7.24}$$

with the corresponding eigenvalue

$$\lambda = \operatorname{sgn}(u)\sqrt{u^2 + 4J^2}. \tag{7.25}$$

In this case, for all $u \neq 0$ we find a finite κ_R and consequently a finite localization length κ_R^{-1}, indicating the presence of a localized state. The corresponding real-valued frequency λ is situated outside the band, with $\lambda = 2J$ for $u = 0^+$ and $\lambda = -2J$ for $u = 0^-$. Consequently, the frequency of the localized mode exhibits a discontinuity when the barrier strength u changes its sign.

For a generic impurity with finite γ and u, Eqs. (7.23) always admit a localized solution characterized by $\kappa_R \neq 0$ (note $\kappa_R = 0$ implies $u = 0$). The existence of a localized solution in dependence on γ and u is then summarized in Fig. 7.7. Here, the black horizontal line indicates the *absence* of a localized state for $u = 0$ and $\gamma < \gamma_c$, while for all other parameters a

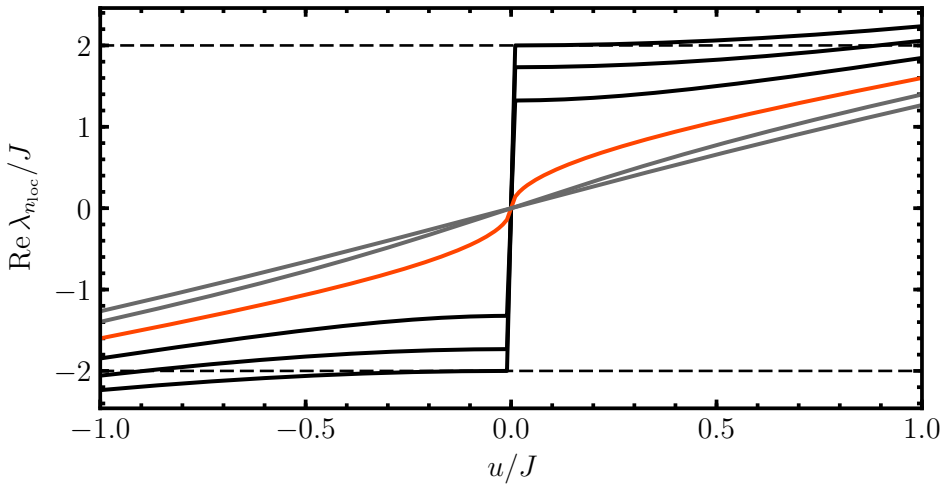

Fig. 7.8. Real part of the eigenvalue of the localized state as a function of the potential u for different dissipation strength $\gamma/J = 0, 1, 1.5, 2.0, 2.5, 3.0$ (outer to inner solid lines). The real part is discontinuous for $\gamma < \gamma_c$ (solid black), continuous for $\gamma > \gamma_c$ (solid gray), and exhibits non-analytical behavior for γ_c (solid red). The black dashed lines indicate the upper and lower band edge, $\pm 2J$.

localized solution is present. The black dot indicates the position of the exceptional point at $(\gamma, u) = (\gamma_c, 0)$.

Upon crossing the black line, the localized solution delocalizes as a mode with an infinite localization length described by Eq. (7.10), before localizing again at a different frequency. Consequently, the frequency of the localized state jumps discontinuously between the two eigenvalues in Eq. (7.10). In Fig. 7.8 the real frequency (Re λ) is shown for different values of γ as a function of u, obtained by numerically solving Eq. (7.23). This variation of the impurity potential corresponds to qualitatively different paths in the (γ, u) plane, indicated in Fig. 7.7 by the red arrows. For $\gamma < \gamma_c$ (solid black), corresponding to paths of type a, b in Fig. 7.7, which cross the black line, the frequency is indeed discontinuous. On the contrary, for $\gamma > \gamma_c$ (solid gray), representing paths of type d in Fig. 7.7, the frequency is continuous. At the critical value γ_c, corresponding to a path c in Fig. 7.7, passing through the exceptional point, the real part is non-analytic at $u = 0$ (solid red).

We remark, that the phase diagram in Fig. 7.7 can be extended to negative γ by simply mirroring it at the $\gamma = 0$ axis. The topology of the extended diagram is then characterized by two exceptional points situated at $\gamma = \pm 2J$, which are connected by a line signaling the absence of a localized state. The region for $\gamma < 0$ is not accessible with fermions, but corresponds to a gain term for bosons, see Sec. 7.3.2.

Finally, we notice that in the additional presence of a finite coherent potential, the imaginary part of the localized mode exhibits similar behavior as shown in Fig. 7.1 (lower panel), i.e., it acquires a large imaginary part with increasing dissipation strength. However, the sharp transition at γ_c is smoothed out, signaling the presence of a localized mode also for $\gamma < \gamma_c$.

7.4.2. Spectral flow

As a forward direction, we consider the following protocol featuring a time-dependent complex-valued impurity (see also preliminary results on fast oscillating impurities in Appendix E). The protocol is based on the results of the previous section, namely the gap in the frequency of the localized state that occurs when the $(u = 0)$-line is crossed below $\gamma < \gamma_c$, while in contrast a gap is absent for $\gamma > \gamma_c$ (cf. Figs. 7.7 and 7.8). As a result, a change of the impurity potential following a closed path in parameter space (γ, u) leads to a shift of the bulk state frequencies resulting in a spectral flow phenomenon, as depicted in Fig. 7.9. Here, the spectral flow of the modes (left panels) is schematically shown for three different closed paths in the parameter space, which are in turn depicted in the right-hand-side panels (two cycles are shown, respectively).

In the upper panel, a path is considered which passes through the origin $(\gamma = 0, u = 0)$ and encircles the exceptional point. Here, all modes participate in the spectral flow described in the following. After the completion of one cycle, the localized state (solid red) continuously connects the two modes at the band edge, i.e., modes with index $n = 1$ and $n = L$. When passing through the origin, its frequency jumps, as indicated by the dashed red arrows. As a result, the frequency of the bulk modes shifts during each cycle (solid black), and a mode n is continuously connected to the mode $n - 1$ for a counterclockwise encircling of the exceptional point ($n + 1$ for a clockwise encircling). In the center panel, the path in parameter space encircles the exceptional point but cuts the $(u = 0)$-line at finite $\gamma < \gamma_c$. As a consequence, only modes whose frequencies lie within the gap of the localized mode are participating in the spectral flow (solid black), while modes with a frequency outside do not flow (dotted black). In the lower panel, a path cutting the $(u = 0)$-line twice for $\gamma < \gamma_c$ is shown, leading to an exclusion of the band center from the spectral flow. Hence, two disconnected spectral flows are observed in the upper and lower half of the band. All complex eigenvalues participating in the spectral flow are found to follow a mutually connected, closed path in the complex plane.

In order to illustrate the observability of the spectral flow, in Fig. 7.10 the LDoS (7.17) is shown (cf. Sec. 7.3.1) as a function of ω and for a varying impurity potential depending on a parametric time τ. The variation of the impurity potential follows a closed path encircling the exceptional point and passing through the origin, similar to the path considered in the upper panel of Fig. 7.9. The spectral flow is clearly observed as a continuous shift of the resonance peaks, following the dashed black lines which indicate the real part of the spectrum of the effective non-Hermitian Hamiltonian. The localized state emerges at the band edge and broadens with increasing dissipation strength. Here, a geometry without dissipation-free modes is considered for illustrative purposes, since these modes are unaffected by the impurity and do not participate in the spectral flow. Similarly, the other types of paths in parameter space considered in Fig. 7.9 translate to the LDoS, which is presented in Appendix D.

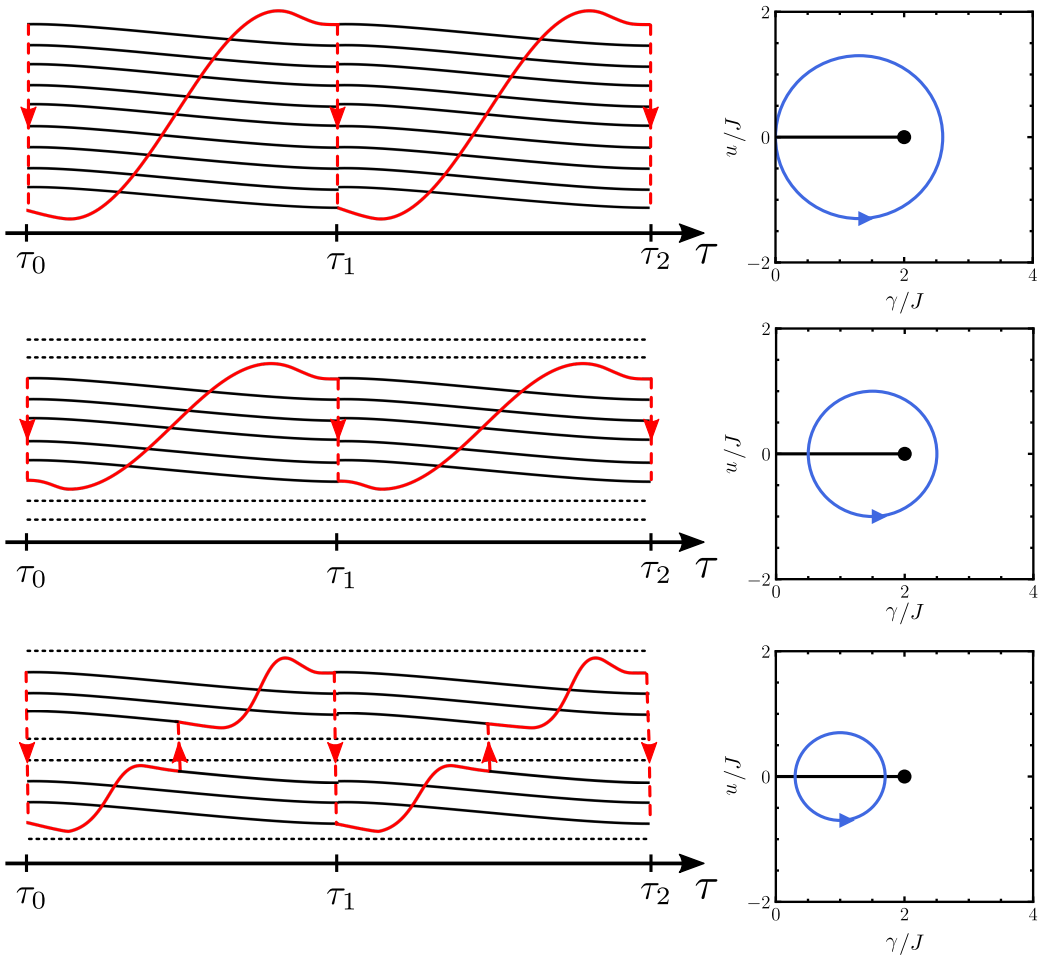

Fig. 7.9. Schematic representation of the real part of the spectrum (left panels) exhibiting a spectral flow for a variation of the complex-valued impurity potential along three different closed paths in parameter space (right panels). The paths are parametrized by a parametric time τ, starting at τ_0, and depicted for two cycles, completed at τ_1, τ_2, respectively. Modes participating in the spectral flow (solid black lines) are encircled by the frequency of the localized mode (red lines) and connect continuously to an adjacent mode after the completion of each cycle. Modes that are not encircled in this way simply connect to themselves (dashed black lines) and thus do not participate in the spectral flow. Dashed red arrows illustrate the jump of the localized mode frequency.

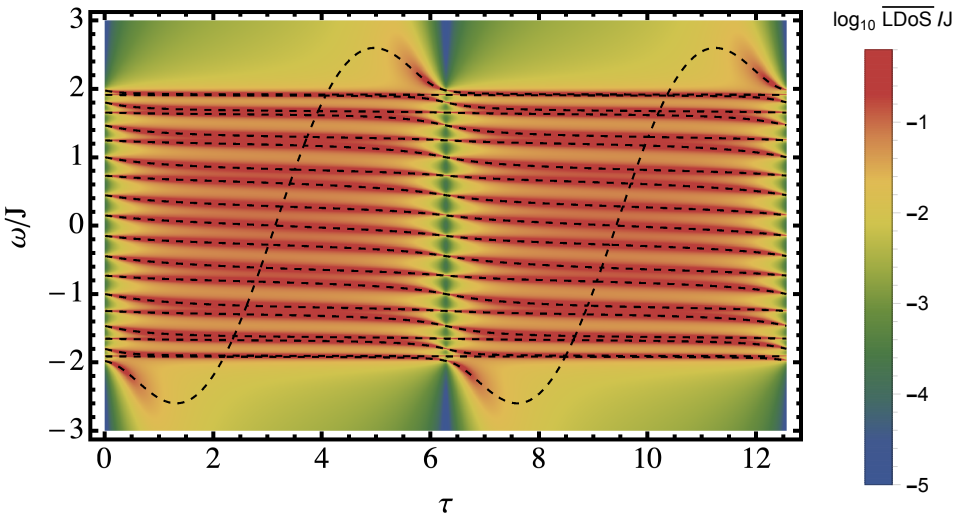

Fig. 7.10. Local density of states LDoS averaged over all lattice sites j as a function of frequency and parametric time τ, for $L = 20$ and open boundary conditions. The black dashed lines indicate the real parts of the corresponding spectrum of the effective Hamiltonian. The impurity potential as a function of parametric time τ is given by $g(\tau) = 2J\sin(\tau) - i2J(1-\cos\tau)$, for $\tau \in [0, 4\pi]$, parameterizing a circle around the exceptional point passing through the origin at $\tau = 0, 2\pi$ (two cycles).

7.5. Conclusion and outlook

We analyzed the spectral properties of the effective non-Hermitian Hamiltonian on a lattice and the associated retarded Green's function in the presence of a localized loss. A reorganization of the spectrum was revealed at a critical dissipation strength γ_c, which constitutes an exceptional point of the effective non-Hermitian Hamiltonian. Above the transition, a single mode localized at the loss site acquires an imaginary part much larger than all other modes. Below the transition, instead, two solutions with an infinite localization length are encountered. The reorganization of the spectrum can be observed in the spectral function $A(\omega)$ in a real-space representation. In a related setup for a bosonic system with a localized pump, the appearance of a single long-loved mode leads to an instability transition when a threshold pumping strength is exceeded. Moreover, the interplay of the localized loss with a localized coherent potential leads to remarkable spectral effects such as a spectral flow phenomenon for time-dependent impurities. We supplement the analysis with a collection of preliminary results on rapidly oscillating dissipative impurities, which is presented in Appendix E.

The spectral properties discussed in this chapter connect to several previous works on systems subject to a localized loss. In Ref. [42] similar homogeneous solutions as in Eq. (7.9) are found and shown to be related to the emergence of coherent perfect absorption, which was experimentally realized in a BEC. In Ref. [180], this spectral transition for the two-site model ($L = 2$ in Eq. (7.3)) has been experimentally observed in a Fermi gas. In Ref. [181] the spectral reorganization of systems coupled locally to external modes has been discussed for a general case, in particular pointing out the emergence of exceptional points and the relation of these features to phase transitions. Here, a distinct mode similar to the localized mode is regarded as a collective mode with respect to the delocalized eigenfunctions of the unperturbed system [181]. Moreover, a similar phase transition has been also described in Ref. [56] for a one-dimensional

BEC with a localized loss. Further, for a localized pump of bosons on a lattice, a qualitative change in the growth rate at a critical value has been reported in Ref. [63].

We briefly comment on the robustness of the sharp transition observed in the spectrum in the presence of interactions. Within a Hartree-Fock approximation (cf. Chapter 5), interactions lead to an effective coherent potential superimposed to the localized loss (cf. Sec. 7.4). As a consequence, the sharp transition, e.g., seen in the imaginary part of the spectrum in Fig. 7.3 (left panel) is smeared out. Nevertheless, the feature of a single localized mode acquiring a large imaginary part for large γ is expected to persist.

The analysis in this chapter can be extended to impurities with an additional intrinsic structure. For example, two asymmetric impurities are found to exhibit spectral properties such as a hybridization of localized states in the domain where the two dissipation strengths are comparable. An interesting question concerns the observability of the spectral flow beyond response, e.g., for adiabatic protocols. However, due to the presence of dissipation, e.g., a quantized transport as for a Laughlin [168] or Thouless pump [169] is not expected. Possible extensions of the model including gain could balance the loss of particles within an adiabatic cycle. Moreover, the spectral flow phenomenon exhibits a topological structure, since only the crossing point of the branch cut and the position of the exceptional point are relevant. Therefore, the interplay with non-Hermitian topology [31, 165] and models featuring topologically protected bound states can be considered an interesting field of study.

CHAPTER 8

CONCLUSION

In this work, we discussed fermionic quantum wires driven out of equilibrium by the presence of a localized dissipation. We investigated the dynamics of the system after switching on a localized loss and showed the emergence of a non-equilibrium steady state. A far-reaching theoretical description of its properties was obtained by the identification of the loss probability η_k, which enabled the energy-resolved description of depletion processes in observables. The momentum distribution in the non-equilibrium steady state was found to be a depleted remnant of the initial Fermi distribution, preserving a step at the original Fermi momentum. The resulting non-thermal descendant of the Fermi surface gives rise to coherent phenomena such as Friedel oscillations, despite the non-equilibrium nature of the state. The Friedel oscillations dress the bare localized loss, resulting in the formation of an effective dissipative impurity with strongly modified properties, reflecting the interplay of many-body and non-equilibrium effects. In particular, the precise wavenumber of $2k_F$ of the Friedel oscillations leads to energy-dependent scattering and loss properties of the effective barrier. As a result, the loss probability η_k was shown to be strongly renormalized for $k \sim k_F$, being completely suppressed at k_F, thus restoring unitarity at the Fermi level. Moreover, the transmission and reflection probabilities are drastically modified for modes in the vicinity of the Fermi level, entailing perfect reflection for repulsive, and perfect transmission for attractive interactions. These results were consistently derived by the application of several complementary methods. A connection between the microscopic descriptions, corresponding to the real-space renormalization group (RG) and dynamical Hartree-Fock approaches, and the effective Luttinger liquid approach could be achieved via a renormalization scheme of the dissipation strength. This led to an overarching picture, where a fluctuation-induced quantum Zeno effect is established for repulsive interactions, and a fluctuation-induced transparency for attractive ones. While the transport properties at the fixed points are analogous to the one of a coherent barrier, the RG scaling in the approach to the stable fixed point for attractive interactions shows a novel scaling behavior. Moreover, in the spectrum of the non-Hermitian Hamiltonian associated with a localized loss on a lattice, a sharp reorganization of the spectrum was found at a critical dissipation strength, as a spectral incarnation of the quantum Zeno effect. By the inclusion of an additional real-valued potential, we obtained a phase diagram for the occurrence of a localized mode. Upon varying the complex impurity potential, a spectral flow of the bulk modes could be induced.

Furthermore, we considered the observability of the renormalized depletion properties. We showed that the momentum-resolved loss rate directly reflects the renormalization of the loss probability η_k. In turn, the suppression of losses results in an increased occupation in the wire for modes near the Fermi level, which was observed numerically within a Hartree-Fock approximation of the dynamics. Additionally, the RG scaling in the approach to the fixed points is reflected by the renormalization of η_k for modes in the vicinity of k_F. A non-monotonic RG flow could be achieved depending on the microscopic parameters, leading to intermediate regimes, $k \neq k_F$, where an increased loss probability is experienced. Moreover, we considered the effects of cutoff scales due to a finite size and temperature of the wire and found that sizable renormalization effects can be expected within current experimental setups. The consideration of self-thermalization effects allowed the characterization of regimes where renormalization effects are prominent despite the generation of a cutoff scale for the RG flow, which was demonstrated within a second-order perturbative analysis of the Luttinger model with localized losses.

We conclude with a discussion of possible generalizations and new avenues based on the methods and effects demonstrated in this thesis. Further experimental platforms are conceivable where the interplay between collective behavior and localized dissipation can lead to a drastic modification of the dynamics, such as many-body instances of the quantum Zeno effect. While we have largely focused on fermionic systems, the low-energy properties of one-dimensional interacting bosons are likewise covered by the Luttinger liquid model [84]. Accordingly, in previous studies [131], strong effects in interacting bosonic systems induced by coherent impurities have been revealed. Hence, the investigation of the fate of a fluctuation-induced quantum Zeno effect or transparency for strongly interacting bosons seems promising. The consideration of further condensed matter platforms with localized dissipation is desirable, e.g., wire junctions in Luttinger liquids [57, 124–128], where the loss channel is mimicked by a quantum wire. Moreover, the definition of a momentum-resolved loss rate raises the question of how information about the quantum state of the wire could be directly harvested from the stream of emitted particles in an energy-resolved way.

While we already investigated the problem with a variety of complementary approaches, the application of additional methods, such as the functional renormalization group (FRG), could yield supplementary insights. In studies of interacting quantum wires with coherent impurities, the FRG was shown to capture, e.g., exponents of power laws reflecting the Luttinger liquid behavior [118–121]. Possible modifications of these exponents due to non-equilibrium effects would provide valuable insights for the identification of novel non-equilibrium universality classes.

Furthermore, already within the applications of the methods used in this thesis, various generalizations of the here considered instances of localized dissipation are conceivable. An overarching goal of such generalizations could be the development of new tools for engineering quantum states by localized dissipation. To this end, the study of dissipative barriers with additional intrinsic structure appears as a promising forward direction. For example, localized losses with an engineered spatial profile and the superposition with coherent potentials enable additional control. Here, interesting perspectives appear in view of the spectral properties obtained by a variation of a complex impurity potential and the possibilities for the interplay between localized dissipation and quantum interference. In addition, the novel universal scaling found in the real-space RG approach for attractive interactions encourages further investigations of

whether similar scaling can be achieved in other dissipative problems, where a competition between coherent and incoherent effects occurs. Moreover, the enriched fixed point structure due to variations of the loss profile calls for a connection to effective field-theoretic descriptions. Further perspectives include the study of transport properties in the presence of a finite voltage bias due to the coupling to external reservoirs. In particular, the possible interplay with non-reciprocal effects in non-Hermitian quantum systems [20, 21] represents an interesting direction.

While we focused in this work on spin-polarized fermions, the consideration of spin degrees of freedom is known to yield novel effects in the case of coherent impurities [80, 85]. This fact originates in the decoupling of the spin and charge degrees of freedom in a Luttinger liquid and the possible interplay with magnetic fields. In particular, spin-dependent dissipative barriers were realized in recent experiments with ultracold atoms [43, 44], rendering the discussion of strong interactions in this context an interesting future direction. Moreover, the consideration of spin degrees of freedom establishes a connection to the study of dissipative impurities in the context of the Kondo problem [84]. Finally, given the high level of control which can be achieved in the implementation of localized dissipation, the extension to time-dependent impurities appears as a promising field of study [177, 182–186]. In particular, the interplay between inelastic scattering effects for a periodically-driven impurity and the rich landscape of localized states for complex impurity potentials could provide a source of novel effects [183–185]. This calls for an investigation of driven complex impurities within the Floquet scattering theory [139, 187].

APPENDIX A

NON-INTERACTING FERMIONS

A.1. Density profile for different fillings

In order to complement the discussion in Sec. 3.2 we report in Fig. A.1 for different initial fillings the density profiles after the quench of a localized loss. One can observe smaller density

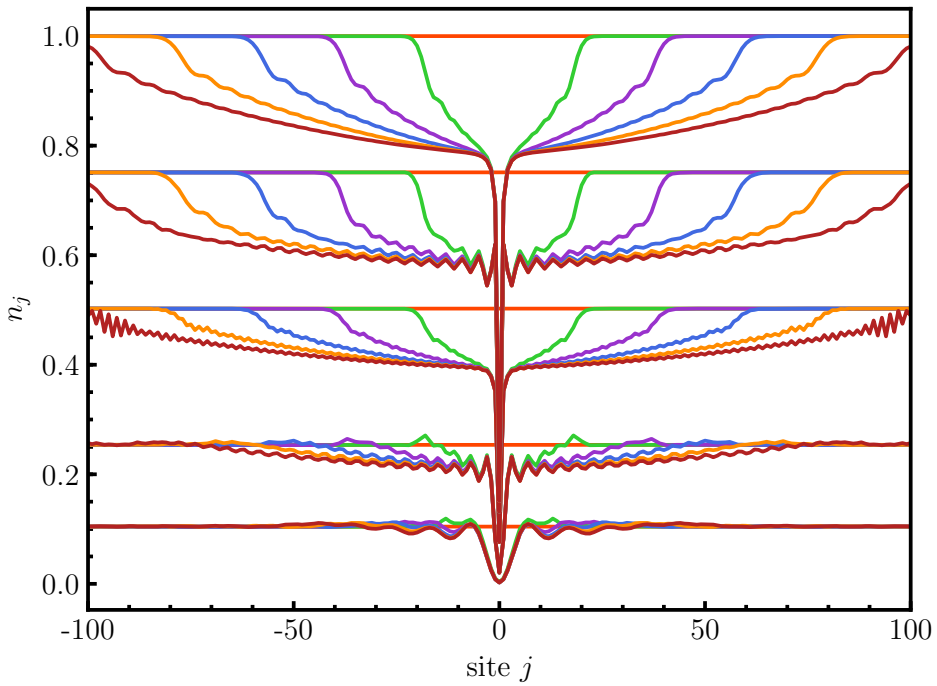

Fig. A.1. Density profile for different filling levels $v = 0.1, 0.25, 0.5, 0.75, 1.0$ (combined in a single figure, bottom to top) at different times elapsed from the quench in the second temporal regime, $tJ = 0, 10, 20, 30, 40, 50$. For all curves $L = 201, \gamma = 2J$.

modifications traveling ahead of the depleted region for initial fillings below half-filling, while this effect is absent for larger fillings. Moreover, the light-cone speed is clearly filling-dependent below half-filling and constant above half-filling, as discussed in Sec. 3.2.4.

A.2. Computation of the density profile

We report here the integrals required in the derivation of the closed-form expressions in Sec. 3.4, corresponding to

$$\int_0^x \frac{y^2}{(ay+b)^2}\,dy = \frac{ax(2b+ax)}{b+ax} + \frac{2b}{a^3}\ln\left(\frac{b}{b+ax}\right), \tag{A.1}$$

for n_{imp} (3.62) and

$$\int_0^x \frac{y}{(ay+b)^2}dy = \frac{1}{a^2}\left(\frac{b}{b+ax} - 1 - \ln\frac{b}{b+ay}\right), \tag{A.2}$$

for n_{bg} (3.63).

A.3. Computation of the current

In this appendix, we provide additional details of the derivation of the current in Sec. 3.5. To this end, we evaluate

$$\mathrm{Im}\partial_y C(x,y)|_{y=x} = \mathrm{Im}\partial_y \int_{-k_F}^{k_F} \frac{dq}{2\pi} f^*(\epsilon_q,q,x) f(\epsilon_q,q,y)|_{y=x}, \tag{A.3}$$

where we used the two-point correlations $C(x,y) \equiv C(x,y,t,t)$ in the stationary regime (3.32). First, we expand

$$\begin{aligned}\mathrm{Im}\partial_y C(x,y)|_{y=x} &= \mathrm{Im}\int_{-k_F}^{k_F}\frac{dq}{2\pi}\big[-iq + i|q|\mathrm{sgn}(x)|r_q|^2 - iqr_q^* e^{-i|q||x|-iqx} \\ &\qquad + i|q|\mathrm{sgn}(x) r_q e^{i|q||x|+iqx}\big] \qquad (A.4)\\ &= \mathrm{Im}\int_0^{k_F}\frac{dq}{\pi} q\big[i\,\mathrm{sgn}(x)|r_q|^2 - r_q^* e^{-iq|x|}\sin(qx) \\ &\qquad + i\mathrm{sgn}(x) r_q e^{\,iq|x|}\cos(qx)\big]. \qquad (A.5)\end{aligned}$$

Here, we separate the expression into its real and imaginary parts and obtain

$$\begin{aligned}\mathrm{Im}\partial_y C(x,y)|_{y=x} &= \int_0^{k_F}\frac{dq}{\pi} q\big[\mathrm{sgn}(x)|r_q|^2 - \sin(qx)\mathrm{Im}(r_q^* e^{-iq|x|}) \\ &\qquad + \mathrm{sgn}(x)\cos(qx)\mathrm{Re}(r_q e^{iq|x|})\big] \qquad (A.6)\\ &= \mathrm{sgn}(x)\int_0^{k_F}\frac{dq}{\pi} q\big[|r_q|^2 + \sin^2(qx)\mathrm{Re}(r_q^*) - \sin(qx)\cos(qx)\mathrm{Im}(r_q^*) \\ &\qquad + \cos^2(qx)\mathrm{Re}(r_q) - \cos(qx)\sin(qx)\mathrm{Im}(r_q)\big], \qquad (A.7)\end{aligned}$$

where we used $\sin(q|x|) = \mathrm{sgn}(x)\sin(qx)$. By noticing $\mathrm{Im}(r_q^*) = -\mathrm{Im}(r_q)$, we finally arrive at

$$\mathrm{Im}\partial_y C(x,y)|_{y=x} = \mathrm{sgn}(x)\int_0^{k_F}\frac{dq}{\pi} q\big[|r_q|^2 + \mathrm{Re}(r_q)\big], \tag{A.8}$$

as reported in Eq. (3.67) in the main text.

A.4. Third temporal regime

This appendix supplements the discussion of the momentum distribution dynamics in the third temporal regime in Sec. 3.8.2. In Fig. A.2 the momentum distribution $n_k(t)$ is shown for the remaining geometries introduced in Sec. 3.8.1 (cf. Fig 3.13). In both cases, a dissipation-free

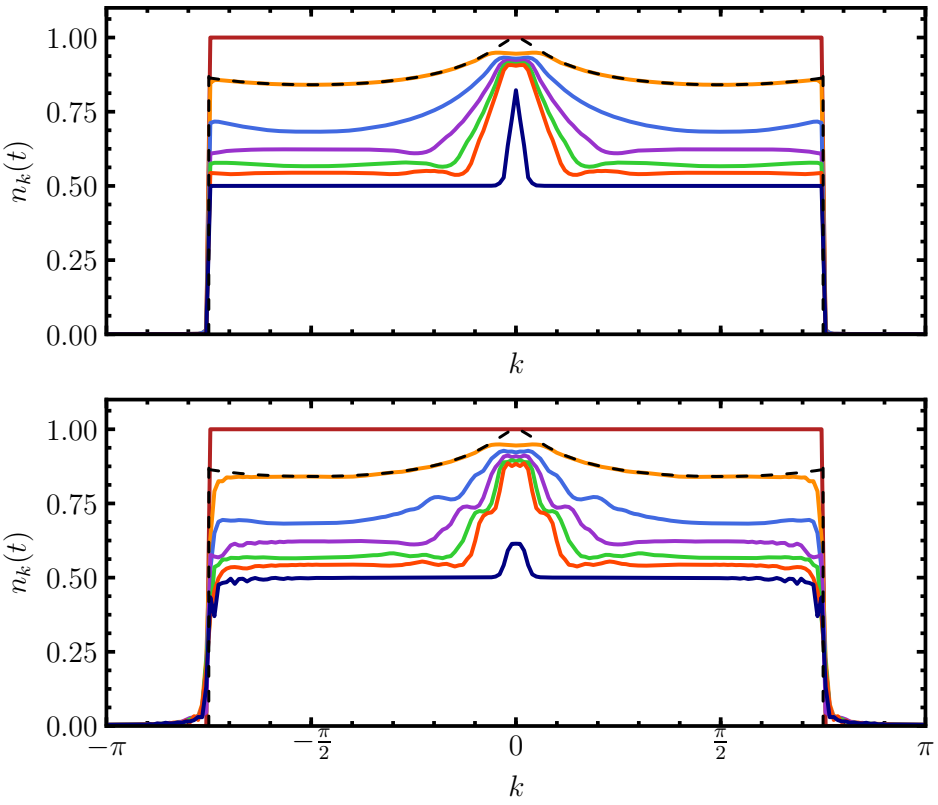

Fig. A.2. Momentum distribution $n_k(t)$ from the numerical simulations (solid) for different geometries of the system. The distribution is shown for different times after the quench in the second and third temporal regime, $tJ = 0, 50, 100, 150, 200, 250, 2000$. Upper Panel: Periodic boundary conditions and even number of sites, $L = 200$. Lower panel: Open boundary conditions and odd number of sites, $L = 201$. For all curves $\gamma = 0.5J, v = 0.75$. The dashed lines show the comparison with the analytical results in the second temporal regime which lasts up to time $t_{II} = 50$.

subspace is absent and the dynamics is similar to the one in the left panel of Fig. 3.14. Within the second temporal regime, all the momentum distributions in Figs. A.2 and 3.14 deplete in the same way, aside from finite size effects at $k \approx 0$ and $k \approx \pm k_F$ (cf. Sec. 3.6.2), as indicated by the dashed lines representing analytical results. In contrast, in the third temporal regime, the dynamics of $n_k(t)$ exhibits non-universal features for the different boundary conditions. This highlights the universality of the second temporal regime as opposed to the non-universality of the third temporal regime.

In addition, we report in Fig. A.3 the density profile within the third temporal regime for periodic boundary conditions. As discussed in Sec. 3.8.2 of the main text, the exact antipodal point (respectively, two antipodal points for an even number of sites) of the loss site depletes beyond the mean value of the density. Moreover, density oscillations are observed in its vicinity.

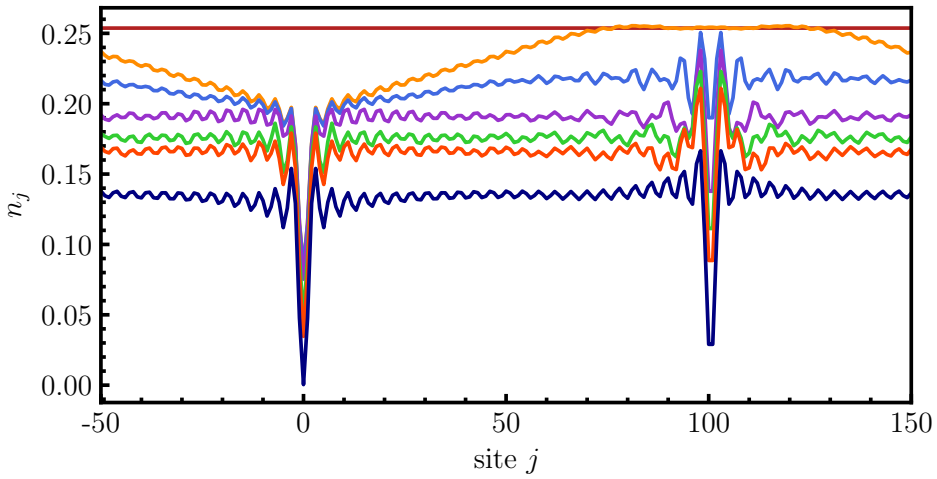

Fig. A.3. Density profile in the third temporal regime at times $tJ = 0, 50, 100, 150, 200, 250, 2000$. The localized loss is situated at $j = 0$. For all curves $L = 201, \gamma = 0.5J, \nu = 0.25$.

APPENDIX B

REAL-SPACE RENORMALIZATION GROUP

B.1. Non-logarithmically divergent terms

We discuss the additional non-oscillating contributions in the perturbative corrections considered in Sec. (4.2.1). These contributions do not entail logarithmic divergences and do not lead to momentum-specific corrections. For the Hartree corrections (4.12), we find additional terms which are given for δt_k^H by a term $2t_k n_0 C_H$, and for δr_k^H by a term $2r_k n_0 C_H$, with (cf. Sec. 4.2.1)

$$C_H = \frac{1}{iv_k}\int_{x'>d}\int_{x''>d}\int_0^{k_F}\frac{dq}{2\pi}V(x'-x'') = \frac{\widetilde{V}(0)}{2iv_k}\int_{X>d}\int_0^{k_F}1. \tag{B.1}$$

Hence, these terms diverge as the system size $\sim L$. These contributions are thus not sensitive to the limit $k \to k_F$ and can be understood as a redefinition of the chemical potential due to the switching on of interactions. Similar terms occur also for a coherent barrier [85, 86].

Similarly, also for the exchange contribution (4.22), non-oscillating terms appear in addition to the $C^+_{<,>}$ contributions discussed in the main text. These additional terms originate from the $C^-_{<,>}$ part of the exchange potential. For completeness, we briefly discuss their form in this appendix. In the case of the corrections to the reflection we find

$$\begin{aligned}\delta r_k^{ex,-} \sim \int_{x'>d}\int_{x''>d} V(x'-x'')\Big(&\left[e^{-ikx'}+r_k e^{ikx'}\right]\left[e^{-ikx''}+r_k e^{ikx''}\right]\\ &+ t_k^2 e^{ik(x'+x'')}]\Big)C^-_>(x'',x'),\end{aligned} \tag{B.2}$$

with the correlation function $C^-_>$ given in Eq. (4.21). By following the argumentation of Sec. 4.2.1, i.e., to drop terms with and integrand oscillating even for $k = q$, we are left with a single contribution $r_k C_{\rm ex}$, with

$$C_{\rm ex} = -\frac{r_k}{iv_k}\int_{x'>0}\int_{x''>0}\int_0^{k_F}\frac{dq}{2\pi}\,(1+2r_q+2r_q^2)V(x'-x'')e^{i(k-q)(x'-x'')}. \tag{B.3}$$

Notice the different structure in the exponent compared to the terms (4.25) which give rise to logarithmic divergences. Indeed, with the usual transformations of the integration domain (cf. Sec. 4.2.1), we obtain

$$C_{\mathrm{ex}} \sim \int_{X>d} \int_{-X}^{X} d\chi \int_{0}^{k_F} dq\, V(\chi) \mathrm{e}^{i\chi(k-q)} \simeq \widetilde{V}(0) \int_{X>d} \int_{0}^{k_F} dq\, 1. \tag{B.4}$$

This yields, as for the Hartree contribution, a term divergent with the system size, not entailing any momentum-specific corrections, originating from the shift of the chemical potential due to the switching on of interactions. For the exchange corrections to the transmission (4.26), one similarly obtains a non-logarithmically divergent contribution given by $t_k C_{\mathrm{ex}}$.

APPENDIX C

LUTTINGER LIQUID DESCRIPTION

C.1. Evaluation of $G_R + G_A$

We show explicitly the vanishing of the expression $\langle \phi_q \theta_c \rangle + \langle \theta_c \phi_q \rangle$, relevant for the computation of the correlation functions in Eq. (6.18) of the main text. The equal time correlations are understood as the limit of a vanishing time difference at which both fields are evaluated. Thus, the fields do not commute inside the average as they carry an infinitesimally different time index, and the advanced and retarded equal time correlators are indeed different from each other and add up to zero. This can be explicitly shown by evaluating

$$\begin{aligned} \langle \phi_q \theta_c \rangle_{(t)} + \langle \theta_c \phi_q \rangle_{(t)} &\sim \int_\omega \left[G^R_{\phi\theta}(\omega) + G^A_{\theta\phi}(\omega) \right] \\ &= -\frac{\pi}{k} \int_\omega \left[\frac{\omega}{(\omega - i\epsilon)^2 - \omega_0^2} + \frac{\omega}{(\omega + i\epsilon)^2 - \omega_0^2} \right], \end{aligned} \tag{C.1}$$

with $\omega_0^2 = v^2 k^2$, as obtained from Eq. (6.4). The evaluation can be conveniently achieved by means of a contour integration. To compute Eq. (C.1), we include an infinitesimal convergence factor originating from the equal time limit discussed above. This allows one to close the contour at infinity. For, e.g., the advanced Green's function, this factor is implemented by

$$\frac{\omega e^{-i\omega 0_-}}{(\omega - i\epsilon)^2 - \omega_0^2} = \frac{\omega e^{-i\omega 0_-}}{(\omega - i\epsilon + \omega_0^2)(\omega - i\epsilon - \omega_0^2)}. \tag{C.2}$$

The poles are situated in the upper complex plane at $\omega^\pm = i\epsilon \pm \omega_0$. In turn, the contour can be closed in the upper plane. The residues are obtained by $\mathrm{res}_{\omega^\pm} f(\omega) = \lim_{\omega \to \omega^\pm} (\omega - \omega^\pm) f(\omega) = \frac{1}{2}$, with $f(\omega)$ given by Eq. (C.2). In fact, the residues of the retarded Green function in the lower complex plane yield the same value. Therefore, due to the opposite orientation of the contours, the sum of both vanishes, in accordance with the Keldysh causality structure.

C.2. Irrelevance of terms in the bosonic mapping

We consider the irrelevance in the RG sense of additional terms to the backscattering contribution (6.13a) possibly originating from the representation of the fermionic operator (2.84). For the leading harmonics, additional terms to the ones considered in the main text (cf. Sec. 6.2) can originate from the factor $\sqrt{\rho_0 - \frac{1}{\pi}\partial_x\theta}$. For the equal contour terms $L_\pm^* L_\pm$ in the impurity action (6.13a), we obtain a factor

$$\rho_0 - \frac{1}{\pi}\partial_x\theta_\pm = \rho_0 - \frac{1}{\sqrt{2}\pi}\left(\partial_x\theta_c \pm \partial_x\theta_q\right). \tag{C.3}$$

The contour mixing terms $L_-^* L_+$ can be expanded in the density fluctuations $\partial_x\theta/\rho_0$, since θ changes slowly in space, yielding

$$\begin{aligned}\sqrt{\rho_0 - \frac{1}{\pi}\partial_x\theta_-}\sqrt{\rho_0 - \frac{1}{\pi}\partial_x\theta_+} &= \rho_0 - \frac{1}{2\pi}\left(\partial_x\theta_+ + \partial_x\theta_-\right) + \mathcal{O}\left(\left(\partial_x\theta_\pm\right)^2\right)\\ &= \rho_0 - \frac{1}{\sqrt{2}\pi}\partial_x\theta_c + \mathcal{O}\left(\left(\partial_x\theta_\pm\right)^2\right).\end{aligned} \tag{C.4}$$

In the discussion in Sec. (6.2), we considered the zero-order contribution from these factors. The gradient terms are indeed irrelevant, as the additional derivative reduces the canonical scaling dimension of the corresponding rate $\widetilde{\gamma}$ by one, as shown below. Higher-order terms in the field derivatives are even less relevant for this reason. We show explicitly that no additional relevant contributions are generated. From the impurity part of the action (6.10), we obtain to first order in the gradient terms (cf. Eqs. (C.3) and (C.4)) the two backscattering contributions

$$\widetilde{S}_{\mathrm{b}}^{(1)} = i\frac{\sqrt{2}}{\pi}\widetilde{\gamma}\int dtdx\;\delta(x)\partial_x\theta_c\left[\cos(\sqrt{2}\theta_c)\left(\mathrm{e}^{i\sqrt{2}\phi_q} - \cos(\sqrt{2}\theta_q)\right)\right], \tag{C.5a}$$

$$\widetilde{S}_{\mathrm{b}}^{(2)} = i\frac{\sqrt{2}}{\pi}\widetilde{\gamma}\int dtdx\;\delta(x)\partial_x\theta_q\left[\cos(\sqrt{2}\theta_c)\sin(\sqrt{2}\theta_q)\right]. \tag{C.5b}$$

We notice the canonical scaling dimension $[\widetilde{\gamma}] = 0$. $\widetilde{S}_{\mathrm{b}}^{(1,2)}$ then acquire the same fluctuation contribution as S_{b}, originating from the factor $\cos(\sqrt{2}\theta_c)$. Here, the decomposition into slow and fast mode does not generate additional terms as the fast momenta average vanishes due the odd factor of k introduced by the gradient. Hence, we obtain the RG scaling $\mathrm{d}\widetilde{\gamma}/\mathrm{d}\ell = -g\widetilde{\gamma}$. Since $g > 0$, both contributions (C.5) are thus irrelevant in the RG sense.

APPENDIX D

SPECTRAL FLOW: SPECTRAL FUNCTION

We report in this appendix the LDoS for a variation of the complex impurity potential corresponding to the two other types of paths in parameter space discussed in Sec. 7.4.2 in the context of Fig. 7.9. In Fig. D.1, the LDoS (7.17) is shown for a path corresponding to the one in the central panel of Fig. 7.9, revealing a spectral flow for modes in the center of the band, while modes at the band edge do not participate (cf. Sec. 7.4.2). In Fig. D.2, the LDoS is shown for a path corresponding to the one in the lower panel of Fig. 7.9, revealing a spectral flow in two separate regions within the band, while the band center does not participate (cf. Sec. 7.4.2).

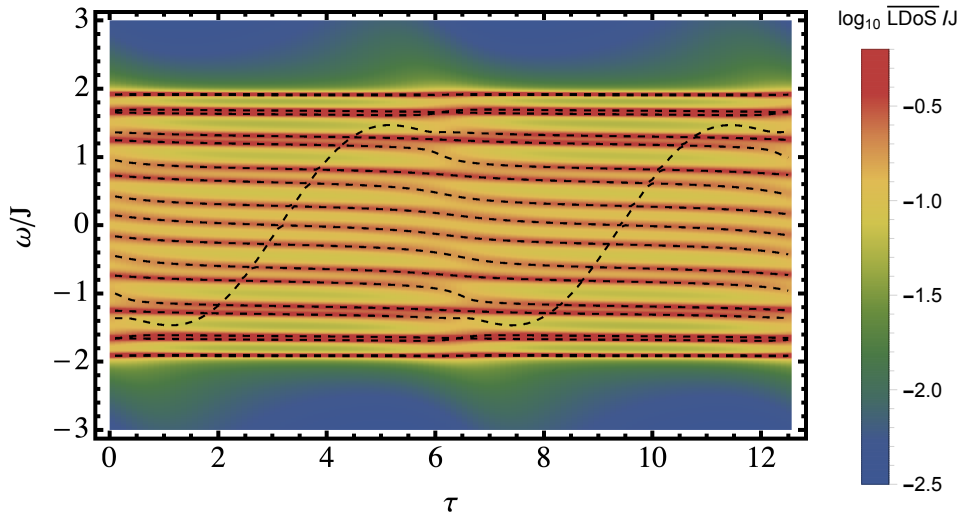

Fig. D.1. Local density of states $\overline{\text{LDoS}}$ averaged over all lattice sites j as a function of frequency and parametric time τ, for $L = 20$ and open boundary conditions. The black dashed lines indicate the real parts of the corresponding spectrum of the effective Hamiltonian. The impurity potential as a function of parametric time τ is given by $g(\tau) = J\sin(\tau) - iJ[1.5 + (1 - \cos\tau)]$, for $\tau \in [0, 4\pi]$, parameterizing a circle enclosing the exceptional point and crossing the $(u = 0)$-line at a finite $\gamma = 1.5J$ for $\tau = 0, 2\pi$ (two cycles shown).

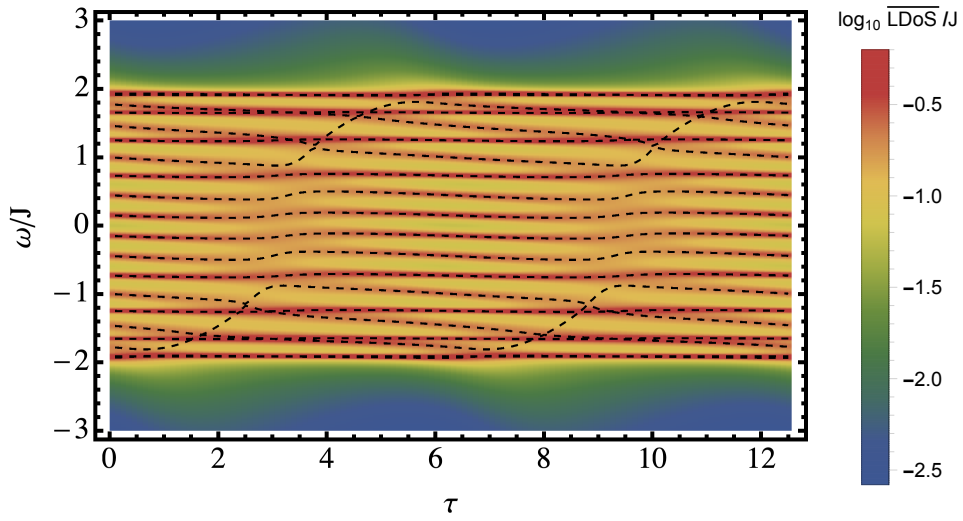

Fig. D.2. Local density of states $\overline{\text{LDoS}}$ averaged over all lattice sites j as a function of frequency and parametric time τ, for $L = 20$ and open boundary conditions. The black dashed lines indicate the real parts of the corresponding spectrum of the effective Hamiltonian. The impurity potential as a function of parametric time τ is given by $g(\tau) = 0.5J\sin(\tau) - iJ[0.8 + 0.5(1 - \cos\tau)]$, for $\tau \in [0, 4\pi]$, parameterizing a circle which crosses the $(u = 0)$-line twice in each cycle at $\gamma = 0.8J$ and $\gamma = 1.8J$ (two cycles shown).

APPENDIX E

TIME-DEPENDENT LOSS IMPURITIES

Oscillating impurities in quantum wires have been studied for coherent [177, 182–186] as well as dissipative impurities [139]. In the absence of interactions, observables such as the transmission and conductance in the wires have been investigated. Typically, a rich interplay between localized states and the transmission properties is encountered due to the possibility to form so-called bound states in the continuum (BIC) [183, 185]. As a result, both perfect reflection and transmission can be achieved [177, 182–185]. Here, different types of localized states are encountered, which either emerge from the static part of the impurity (cf. Sec. 7.2) or from the Floquet spectrum, originating from inelastic scattering processes [177, 182]. In particular, an oscillating dissipative impurity entailing loss and pump in a bosonic wire was studied in Ref. [139]. The system can be fine-tuned to a state where perfect transmission is achieved over the full energy range of the band. Moreover, interacting systems have been considered. A current enhancement due to inelastic backscattering within a Tomonaga-Luttinger model approach was predicted in Ref. [188] and a power-law behavior of the energy deposition rate in a Luttinger liquid was described in Ref. [189].

In this appendix, we present several preliminary results for oscillating dissipative impurities, obtained by generalizing the study of correlations in the non-interacting lattice model in Sec. 3.2.1. This can be conveniently achieved by integrating Eq. (3.7) with a generic time-dependent impurity potential. We consider non-adiabatically-driven impurities where the most general complex impurity potential (cf. Sec. 3.9.1) can be written as

$$g(t) = u_s + u_0 \sin(\Omega t) - i[\gamma_s - \gamma_0 \cos(\Omega t + \phi)], \tag{E.1}$$

with $\gamma_s - \gamma_0 \geq 0$. Hence, Ω corresponds to the frequency of the drive.

As a prominent feature in these systems, we encounter a sharp transition at a driving frequency $\Omega_c = 4J$, corresponding to the finite bandwidth of the lattice model. This transition is, e.g., observed in the particle loss rate and can be quantified by the roughness of the current profile in the wire. As a consequence, a dephasing of Friedel oscillations is obtained below Ω_c, while a stable profile is obtained above the transition. In addition, the competition between heating effects by the periodic drive and depletion provides new tools for engineering the momentum distribution n_k.

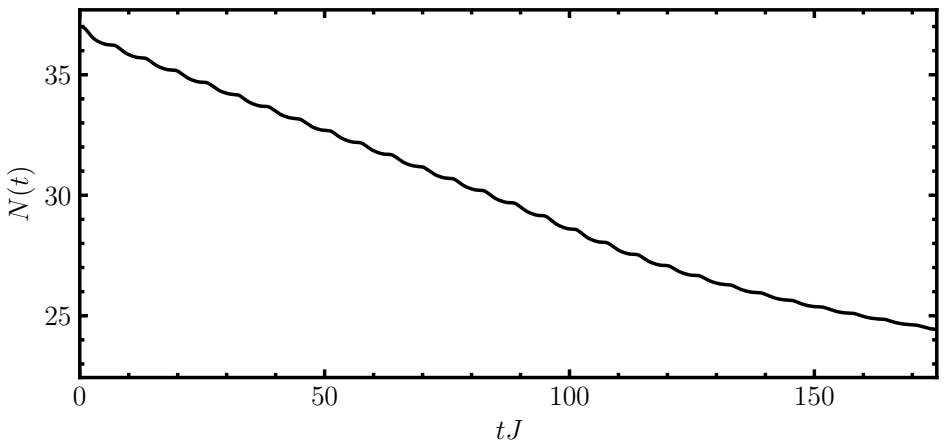

Fig. E.1. Occupation number $N(t)$ as a function of time elapsed from the quench for $\gamma_0 = J, \nu = 0.25, L = 151, \Omega = J$.

First, we consider a purely lossy impurity given by $g(t) = -i\gamma(t)$ with

$$\gamma(t) = \gamma_0(1 - \cos(\Omega t)), \tag{E.2}$$

entailing that the loss is switched on continuously at $t = 0$, and oscillates between $\gamma = 0$ and $\gamma = 2\gamma_0$, such that γ_0 describes the mean value of the dissipation strength.

The second temporal regime remains well-defined, as can be inferred from Fig. E.1, where the occupation number $N(t)$ is depicted as a function of time. Within the second regime, the loss rate (i.e., the slope of $N(t)$) is constant on average. The oscillations of the impurity are seen as small oscillations on top of the mean value of the loss rate. Therefore, the loss rate averaged over the period $T = 2\pi/\Omega$ of the drive is suitable to quantify the loss rate in the second temporal regime:

$$\overline{\mathrm{d}N/\mathrm{d}t} = (N(t+T) - N(t))/T. \tag{E.3}$$

In Fig. E.2, the average loss rate in the second regime is shown for different values of the initial filling ν and the mean dissipation strength γ_0. Regimes of decreased or increased loss rate are observed, depending on ν and γ_0, as compared to the loss rate obtained by the average dissipation strength γ_0, which is indicated by the dashed line. Moreover, the dashed line corresponds to the loss rate in the limit $\Omega \to \infty$ and is asymptotically approached. The opposite limit of small Ω is not accessible since in this case the period T of a single oscillation cycle exceeds the duration of the second regime, $T > t_{II}$. The different behaviors depending on ν and γ_0 can be understood as an interplay with the non-monotonic behavior of η_k as a function of $\gamma(t)$.

As a prominent feature, a sharp change in the behavior of the average loss rate is obtained at a value $\Omega_c = 4J$ of the driving frequency. This corresponds to a drive with a frequency faster than the scale set by the bandwidth of the lattice model. The exact form of the feature at Ω_c in the average loss rate depends on both ν and γ_0, exhibiting a step-like behavior for small ν and γ_0, which changes to a kink for larger ν and γ_0, suggesting a further investigation of the contribution of individual modes.

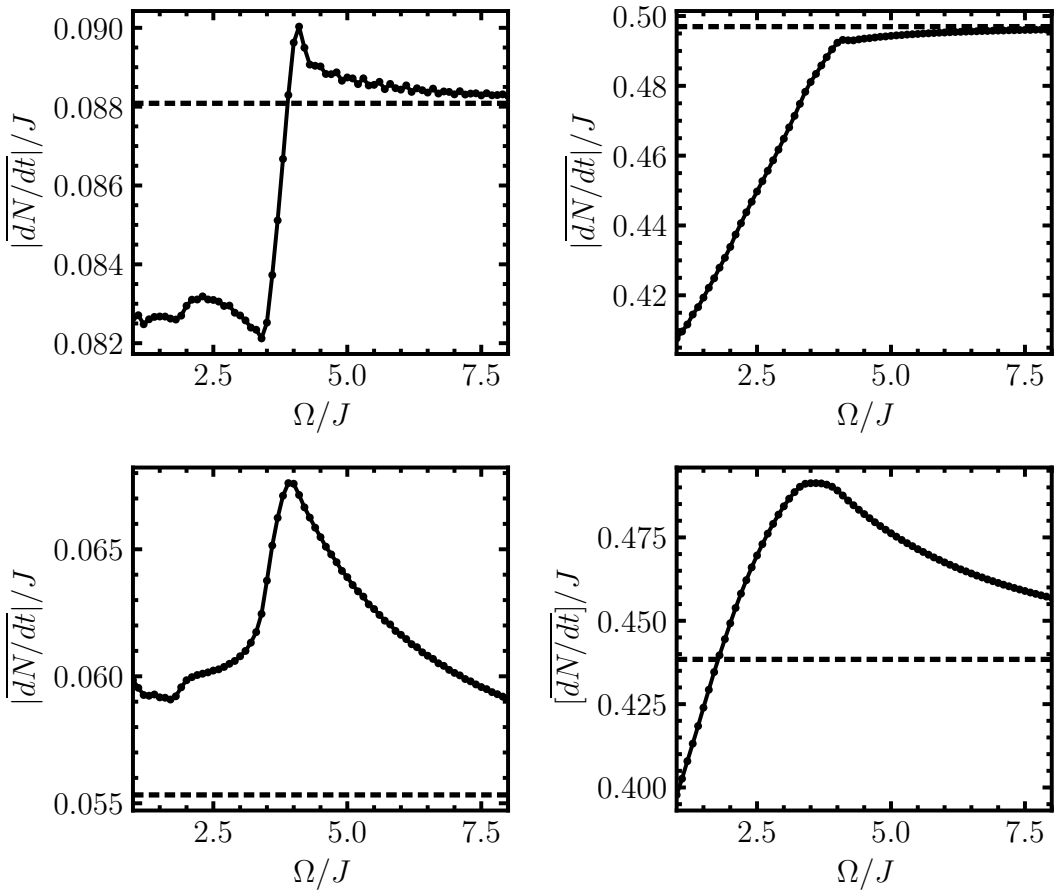

Fig. E.2. Average total particle loss rate $\overline{\mathrm{d}N/\mathrm{d}t}$ in the second regime as a function of the driving frequency Ω, for $(\gamma_0 = J, \nu = 0.25)$ (upper left panel), for $(\gamma_0 = J, \nu = 0.75)$ (upper right panel), for $(\gamma_0 = 5J, \nu = 0.25)$ (lower left panel), and for $(\gamma_0 = 5J, \nu = 0.75)$ (lower right panel). The average loss rate was obtained by averaging over two periods of the drive within the second regime. For all curves $L = 101$.

The nature of the transition observed in the average loss rate can be further rationalized by considering the profiles of the current j in the wire, which is shown in Fig. E.3 (upper panels). For driving frequencies $\Omega < \Omega_c$ (left panel), the current profile exhibits strong oscillations, while for $\Omega > \Omega_c$ (right panel) the oscillations of the impurity potential average out, as expected, leading to a smooth current profile. Remarkably, a sharp transition between both behaviors occurs at Ω_c. The latter fact can be made precise in the following way. We quantify the roughness of the current profile by its variance. Here, we compute the variance in a region next to the loss site, where at finite times the current profile has approximately relaxed to its stationary value. The in this way defined roughness of the current profile is shown in Fig. E.3 (lower panel), revealing a sharp transition at Ω_c.

Furthermore, the oscillating current profile affects the Friedel oscillations. For $\Omega > \Omega_c$, stationary spatial oscillations of the density profile are obtained. Contrary, for $\Omega < \Omega_c$ the current oscillations modify the local amplitude of the Friedel oscillations, leading to their dephasing. In the latter case, the density profile shows oscillations in time. In addition, the consideration of an oscillating complex impurity potential enables increased control of the Friedel oscillations. In particular, the asymptotic amplitude of the Friedel oscillations $\sim r_{k_F}$ (cf. Eq. (3.59)) exhibits a

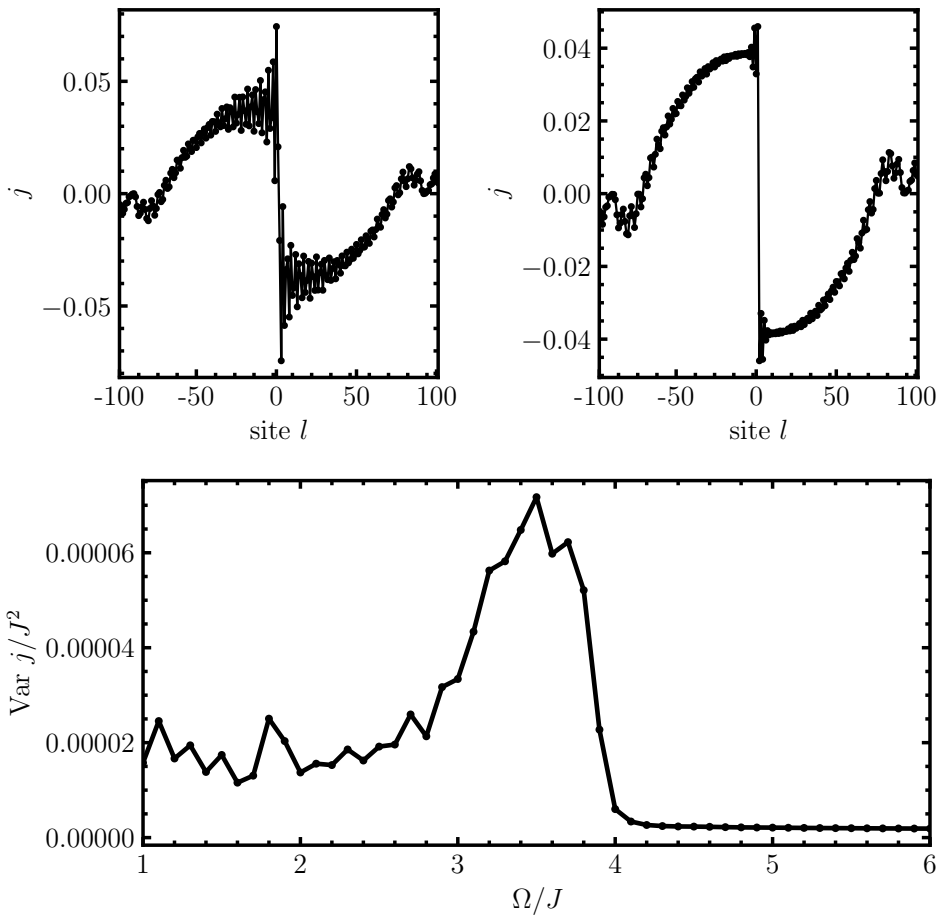

Fig. E.3. Upper panel: Current profiles for $\Omega = 3.7J$ (left) and $\Omega = 4.3J$ (right), for $\gamma_0 = 3, \nu = 0.25, L = 201$. Lower panel: Variance of the current profile as a measure of its roughness, computed in the segment $j \in [5, 30]$, for $\gamma_0 = 3J, \nu = 0.25, L = 201$.

phase, $\arg r_{k_F}$, whose control is enhanced by adding a dissipative part compared to a coherent impurity, i.e., $g = u - i\gamma$, according to

$$\arg r_k = \begin{cases} \arctan(f) + \pi, & u \leq 0, \\ \arctan(f) - \pi, & u > 0, \end{cases} \qquad f(u, \gamma, v_k) = \frac{u v_k}{\gamma^2 + u^2 + \gamma v_k}. \tag{E.4}$$

Further observables accessible for oscillating impurities include the energy transfer rate. Here, a competition between the energy dissipated by particle losses and deposited due to the periodic drive is encountered. As an example of how this fact can be utilized to engineer the momentum distribution of the wire, we report in Fig. E.4 the momentum distribution for two different driving frequencies for an impurity potential $g(t) = J\sin(\Omega t) - iJ(1 - \cos(\Omega t))$. Here, the periodic drive leads to excitations of initially unoccupied states for $\Omega < \Omega_c$. On the contrary, for $\Omega > \Omega_c$, this effect is absent, reflecting the competition between heating and depletion effects. Further, the relative phase between the coherent and incoherent parts of the oscillating impurity potential is found to affect this competition.

As an additional forward direction, the study of the Floquet spectrum and Floquet scattering theory [187] for many-body systems with lossy impurities appears promising. This can be

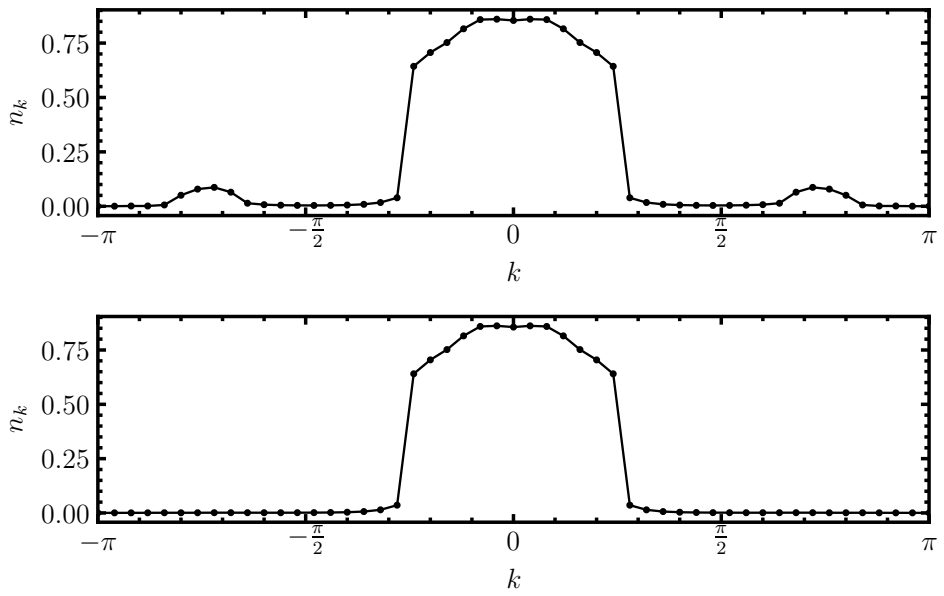

Fig. E.4. Momentum distribution for a complex oscillating impurity potential $g(t) = J\sin(\Omega t) - iJ(1-\cos(\Omega t))$ near the end of the second regime for $\Omega = 3J$ (upper panel), $\Omega = 6J$ (lower panel). For all curves $L = 51, \nu = 0.25$.

motivated in view of the findings on localized states in Sec. 7.4 and the results obtained in Ref. [190] for the Floquet spectrum of a two-level system with oscillating losses.

BIBLIOGRAPHY

[1] A. Altland and B. Simons, *Condensed Matter Field Theory* (Cambridge University Press, 2006).

[2] H.-P. Breuer and F. Petruccione, *The Theory of Open Quantum Systems* (Oxford University Press, Jan. 2007).

[3] J. Schwinger, 'Brownian Motion of a Quantum Oscillator', J. Math. Phys. **2**, 407 (1961).

[4] A. Kamenev, *Field Theory of Non-Equilibrium Systems* (Cambridge University Press, 2011).

[5] C. Gardiner and P. Zoller, *Quantum Noise*, Springer Series in Synergetics (Springer, 2004).

[6] L. M. Sieberer, M. Buchhold and S. Diehl, 'Keldysh field theory for driven open quantum systems', Rep. Prog. Phys. **79**, 096001, 096001 (2016).

[7] S. Diehl, A. Micheli, A. Kantian, B. Kraus, H. P. Büchler and P. Zoller, 'Quantum states and phases in driven open quantum systems with cold atoms', Nat. Phys. **4**, 878 (2008).

[8] R. Landauer, 'The noise is the signal', Nature **392**, 658 (1998).

[9] A. Mitra and T. Giamarchi, 'Thermalization and dissipation in out-of-equilibrium quantum systems: A perturbative renormalization group approach', Phys. Rev. B **85**, 075117 (2012).

[10] D. M. Kennes and V. Meden, 'Luttinger liquid properties of the steady state after a quantum quench', Phys. Rev. B **88** (2013).

[11] M. Schiró and A. Mitra, 'Transient Orthogonality Catastrophe in a Time-Dependent Nonequilibrium Environment', Phys. Rev. Lett. **112**, 246401 (2014).

[12] M. Schiró and A. Mitra, 'Transport across an impurity in one-dimensional quantum liquids far from equilibrium', Phys. Rev. B **91**, 235126 (2015).

[13] M. A. Cazalilla and M.-C. Chung, 'Quantum quenches in the Luttinger model and its close relatives', J. Stat. Mech.: Theory Exp. **2016**, 064004 (2016).

[14] E. G. D. Torre, S. Diehl, M. D. Lukin, S. Sachdev and P. Strack, 'Keldysh approach for nonequilibrium phase transitions in quantum optics: Beyond the Dicke model in optical cavities', Phys. Rev. A **87**, 023831 (2013).

[15] M. Rigol, V. Dunjko, V. Yurovsky and M. Olshanii, 'Relaxation in a Completely Integrable Many-Body Quantum System: An Ab Initio Study of the Dynamics of the Highly Excited States of 1D Lattice Hard-Core Bosons', Phys. Rev. Lett. **98**, 050405 (2007).

[16] L. M. Sieberer, A. Chiocchetta, A. Gambassi, U. C. Täuber and S. Diehl, 'Thermodynamic equilibrium as a symmetry of the Schwinger-Keldysh action', Phys. Rev. B **92**, 134307 (2015).

[17] S. Diehl, A. Tomadin, A. Micheli, R. Fazio and P. Zoller, 'Dynamical Phase Transitions and Instabilities in Open Atomic Many-Body Systems', Phys. Rev. Lett. **105** (2010).

[18] S. Diehl, E. Rico, M. A. Baranov and P. Zoller, 'Topology by dissipation in atomic quantum wires', Nat. Phys. **7**, 971 (2011).

[19] C.-E. Bardyn, M. A. Baranov, C. V. Kraus, E. Rico, A. İmamoğlu, P. Zoller and S. Diehl, 'Topology by dissipation', New J. Phys. **15**, 085001 (2013).

[20] A. Metelmann and A. A. Clerk, 'Nonreciprocal Photon Transmission and Amplification via Reservoir Engineering', Phys. Rev. X **5**, 021025 (2015).

[21] A. Metelmann and A. A. Clerk, 'Nonreciprocal quantum interactions and devices via autonomous feedforward', Phys. Rev. A **95**, 013837 (2017).

[22] Y. Yanay and A. A. Clerk, 'Reservoir engineering of bosonic lattices using chiral symmetry and localized dissipation', Phys. Rev. A **98**, 043615 (2018).

[23] M. Schiro and O. Scarlatella, 'Quantum impurity models coupled to Markovian and non-Markovian baths', J. Chem. Phys. **151**, 044102 (2019).

[24] S. Lapp, J. Ang'ong'a, F. A. An and B. Gadway, 'Engineering tunable local loss in a synthetic lattice of momentum states', New J. Phys. **21**, 045006 (2019).

[25] S. Wolff, A. Sheikhan, S. Diehl and C. Kollath, 'Nonequilibrium metastable state in a chain of interacting spinless fermions with localized loss', Phys. Rev. B **101**, 075139 (2020).

[26] A. Polkovnikov, K. Sengupta, A. Silva and M. Vengalattore, 'Colloquium: Nonequilibrium dynamics of closed interacting quantum systems', Rev. Mod. Phys. **83**, 863 (2011).

[27] L. M. Sieberer, S. D. Huber, E. Altman and S. Diehl, 'Dynamical Critical Phenomena in Driven-Dissipative Systems', Phys. Rev. Lett. **110**, 195301 (2013).

[28] P. C. Hohenberg and B. I. Halperin, 'Theory of dynamic critical phenomena', Rev. Mod. Phys. **49**, 435 (1977).

[29] M. Kardar, G. Parisi and Y.-C. Zhang, 'Dynamic Scaling of Growing Interfaces', Phys. Rev. Lett. **56**, 889 (1986).

[30] S. Mathey and S. Diehl, 'Activating critical exponent spectra with a slow drive', Phys. Rev. Research **2**, 013150 (2020).

[31] F. K. Kunst and V. Dwivedi, 'Non-Hermitian systems and topology: A transfer-matrix perspective', Phys. Rev. B **99**, 245116 (2019).

[32] M. Müller, S. Diehl, G. Pupillo and P. Zoller, in *Advances In Atomic, Molecular, and Optical Physics* (Elsevier, 2012), pp. 1–80.

[33] F. Brennecke, R. Mottl, K. Baumann, R. Landig, T. Donner and T. Esslinger, 'Real-time observation of fluctuations at the driven-dissipative Dicke phase transition', Proc. Natl. Acad. Sci. U.S.A. **110**, 11763 (2013).

[34] T. Tomita, S. Nakajima, I. Danshita, Y. Takasu and Y. Takahashi, 'Observation of the Mott insulator to superfluid crossover of a driven-dissipative Bose-Hubbard system', Sci. Adv. **3**, e1701513 (2017).

[35] T. Fink, A. Schade, S. Höfling, C. Schneider and A. Imamoglu, 'Signatures of a dissipative phase transition in photon correlation measurements', Nat. Phys. **14**, 365 (2018).

[36] R. Ma, B. Saxberg, C. Owens, N. Leung, Y. Lu, J. Simon and D. I. Schuster, 'A dissipatively stabilized Mott insulator of photons', Nature **566**, 51 (2019).

[37] R. H. Dicke, 'Coherence in Spontaneous Radiation Processes', Phys. Rev. **93**, 99 (1954).

[38] J. Berges, S. Borsányi and C. Wetterich, 'Prethermalization', Phys. Rev. Lett. **93**, 142002 (2004).

[39] M. Heyl, 'Dynamical quantum phase transitions: a review', Rep. Prog. Phys. **81**, 054001 (2018).

[40] G. Barontini, R. Labouvie, F. Stubenrauch, A. Vogler, V. Guarrera and H. Ott, 'Controlling the Dynamics of an Open Many-Body Quantum System with Localized Dissipation', Phys. Rev. Lett. **110**, 035302 (2013).

[41] R. Labouvie, B. Santra, S. Heun and H. Ott, 'Bistability in a Driven-Dissipative Superfluid', Phys. Rev. Lett. **116**, 235302 (2016).

[42] A. Müllers, B. Santra, C. Baals, J. Jiang, J. Benary, R. Labouvie, D. A. Zezyulin, V. V. Konotop and H. Ott, 'Coherent perfect absorption of nonlinear matter waves', Sci. Adv. **4**, eaat6539 (2018).

[43] M. Lebrat, S. Häusler, P. Fabritius, D. Husmann, L. Corman and T. Esslinger, 'Quantized Conductance through a Spin-Selective Atomic Point Contact', Phys. Rev. Lett. **123**, 193605 (2019).

[44] L. Corman, P. Fabritius, S. Häusler, J. Mohan, L. H. Dogra, D. Husmann, M. Lebrat and T. Esslinger, 'Quantized conductance through a dissipative atomic point contact', Phys. Rev. A **100**, 053605 (2019).

[45] V. A. Brazhnyi, V. V. Konotop, V. M. Pérez-García and H. Ott, 'Dissipation-Induced Coherent Structures in Bose-Einstein Condensates', Phys. Rev. Lett. **102**, 144101 (2009).

[46] V. S. Shchesnovich and V. V. Konotop, 'Control of a Bose-Einstein condensate by dissipation: Nonlinear Zeno effect', Phys. Rev. A **81**, 053611 (2010).

[47] V. S. Shchesnovich and D. S. Mogilevtsev, 'Three-site Bose-Hubbard model subject to atom losses: Boson-pair dissipation channel and failure of the mean-field approach', Phys. Rev. A **82**, 043621 (2010).

[48] P. Barmettler and C. Kollath, 'Controllable manipulation and detection of local densities and bipartite entanglement in a quantum gas by a dissipative defect', Phys. Rev. A **84**, 041606 (2011).

[49] D. Witthaut, F. Trimborn, H. Hennig, G. Kordas, T. Geisel and S. Wimberger, 'Beyond mean-field dynamics in open Bose-Hubbard chains', Phys. Rev. A **83**, 063608 (2011).

[50] D. A. Zezyulin, V. V. Konotop, G. Barontini and H. Ott, 'Macroscopic Zeno Effect and Stationary Flows in Nonlinear Waveguides with Localized Dissipation', Phys. Rev. Lett. **109**, 020405 (2012).

[51] K. V. Kepesidis and M. J. Hartmann, 'Bose-Hubbard model with localized particle losses', Phys. Rev. A **85**, 063620 (2012).

[52] G. Kordas, S. Wimberger and D. Witthaut, 'Decay and fragmentation in an open Bose-Hubbard chain', Phys. Rev. A **87**, 043618 (2013).

[53] I. Vidanović, D. Cocks and W. Hofstetter, 'Dissipation through localized loss in bosonic systems with long-range interactions', Phys. Rev. A **89**, 053614 (2014).

[54] A. Schnell, D. Vorberg, R. Ketzmerick and A. Eckardt, 'High-Temperature Nonequilibrium Bose Condensation Induced by a Hot Needle', Phys. Rev. Lett. **119**, 140602 (2017).

[55] M. Kiefer-Emmanouilidis and J. Sirker, 'Current reversals and metastable states in the infinite Bose-Hubbard chain with local particle loss', Phys. Rev. A **96**, 063625 (2017).

[56] D. Sels and E. Demler, 'Thermal radiation and dissipative phase transition in a BEC with local loss', Ann. Phys. **412**, 168021 (2020).

[57] A. Roy and K. Saha, 'Interacting bosons in two-dimensional lattices with localized dissipation', New J. Phys. **21**, 103050 (2019).

[58] M. Kunimi and I. Danshita, 'Nonequilibrium steady states of Bose-Einstein condensates with a local particle loss in double potential barriers', Phys. Rev. A **100** (2019).

[59] A. R. Kolovsky and D. L. Shepelyansky, 'Evaporative Cooling and Self-Thermalization in an Open System of Interacting Fermions', Ann. Phys. (Berl.) **531**, 1900231 (2019).

[60] A. A. Bychek, P. S. Muraev and A. R. Kolovsky, 'Probing quantum chaos in many-body quantum systems by the induced dissipation', Phys. Rev. A **100**, 013610 (2019).

[61] F. Tonielli, R. Fazio, S. Diehl and J. Marino, 'Orthogonality Catastrophe in Dissipative Quantum Many-Body Systems', Phys. Rev. Lett. **122**, 040604 (2019).

[62] P. L. Krapivsky, K. Mallick and D. Sels, 'Free fermions with a localized source', J. Stat. Mech.: Theory Exp. **2019**, 113108 (2019).

[63] P. L. Krapivsky, K. Mallick and D. Sels, 'Free Bosons with a Localized Source', arXiv:1911.08617 (2019).

[64] F. Tonielli, N. Chakraborty, F. Grusdt and J. Marino, 'Ramsey interferometry of non-Hermitian quantum impurities', arXiv:2003.07378 (2020).

[65] Y. Yanay and A. A. Clerk, 'Reservoir engineering with localized dissipation: dynamics and pre-thermalization', arXiv:2001.05409 (2020).

[66] D. H. Smith and A. G. Volosniev, 'Engineering momentum profiles of cold-atom beams', Phys. Rev. A **100**, 033604 (2019).

[67] B. Misra and E. C. G. Sudarshan, 'The Zeno's paradox in quantum theory', J. Math. Phys. **18**, 756 (1977).

[68] W. M. Itano, D. J. Heinzen, J. J. Bollinger and D. J. Wineland, 'Quantum Zeno effect', Phys. Rev. A **41**, 2295 (1990).

[69] P. Facchi and S. Pascazio, 'Quantum Zeno Subspaces', Phys. Rev. Lett. **89**, 080401 (2002).

[70] P. Facchi and S. Pascazio, 'Quantum Zeno dynamics: mathematical and physical aspects', J. Phys. A **41**, 493001 (2008).

[71] S. Pascazio, 'All You Ever Wanted to Know About the Quantum Zeno Effect in 70 Minutes', Open Syst. Inf. Dyn. **21**, 1440007 (2014).

[72] I. Bloch, 'Ultracold quantum gases in optical lattices', Nat. Phys. **1**, 23 (2005).

[73] I. Bloch, J. Dalibard and W. Zwerger, 'Many-body physics with ultracold gases', Rev. Mod. Phys. **80**, 885 (2008).

[74] C. Gross and I. Bloch, 'Quantum simulations with ultracold atoms in optical lattices', Science **357**, 995 (2017).

[75] A. G. Kofman and G. Kurizki, 'Acceleration of quantum decay processes by frequent observations', Nature **405**, 546 (2000).

[76] L. S. Schulman, 'Continuous and pulsed observations in the quantum Zeno effect', Phys. Rev. A **57**, 1509 (1998).

[77] N. Syassen, D. M. Bauer, M. Lettner, T. Volz, D. Dietze, J. J. García-Ripoll, J. I. Cirac, G. Rempe and S. Dürr, 'Strong Dissipation Inhibits Losses and Induces Correlations in Cold Molecular Gases', Science **320**, 1329 (2008).

[78] J. J. Garcia-Ripoll, S. Dürr, N. Syassen, D. M. Bauer, M. Lettner, G. Rempe and J. I. Cirac, 'Dissipation-induced hard-core boson gas in an optical lattice', New J. Phys. **11**, 013053 (2009).

[79] C. L. Kane and M. P. A. Fisher, 'Transport in a one-channel Luttinger liquid', Phys. Rev. Lett. **68**, 1220 (1992).

[80] C. L. Kane and M. P. A. Fisher, 'Transmission through barriers and resonant tunneling in an interacting one-dimensional electron gas', Phys. Rev. B **46**, 15233 (1992).

[81] M. P. A. Fisher and L. I. Glazman, in *Mesoscopic Electron Transport*, edited by L. L. Sohn, L. P. Kouwenhoven and G. Schön (Springer Netherlands, 1997).

[82] A. Anthore, D. M. Kennes, E. Boulat, S. Andergassen, F. Pierre and V. Meden, 'Universality at work – the local sine-Gordon model, lattice fermions, and quantum circuits', Eur. Phys. J. ST **229**, 663 (2020).

[83] F. D. M. Haldane, 'General Relation of Correlation Exponents and Spectral Properties of One-Dimensional Fermi Systems', Phys. Rev. Lett. **45**, 1358 (1980).

[84] T. Giamarchi, *Quantum Physics in One Dimension*, International Series of Monographs on Physics (Clarendon Press, 2003).

[85] K. A. Matveev, D. Yue and L. I. Glazman, 'Tunneling in one-dimensional non-Luttinger electron liquid', Phys. Rev. Lett. **71**, 3351 (1993).

[86] D. Yue, L. I. Glazman and K. A. Matveev, 'Conduction of a weakly interacting one-dimensional electron gas through a single barrier', Phys. Rev. B **49**, 1966 (1994).

[87] J. Friedel, 'XIV. The distribution of electrons round impurities in monovalent metals', Philos. Mag. **43**, 153 (1952).

[88] J. Friedel, 'Metallic alloys', Il Nuovo Cimento (1955-1965) **7**, 287 (1958).

[89] R. Egger and H. Grabert, 'Friedel Oscillations for Interacting Fermions in One Dimension', Phys. Rev. Lett. **75**, 3505 (1995).

[90] R. Egger and H. Grabert, 'Friedel Oscillations in Luttinger Liquids', in *Quantum Transport in Semiconductor Submicron Structures*, edited by B. Kramer (Springer Netherlands, Dordrecht, 1996), pp. 133–158.

[91] A. J. Daley, 'Quantum trajectories and open many-body quantum systems', Adv. Phys. **63**, 77 (2014).

[92] M. O. Scully and M. S. Zubairy, *Quantum Optics* (Cambridge University Press, Sept. 1997).

[93] D. A. Steck, 'Quantum and Atom Optics', available online at http://steck.us/teaching (revision 0.12.6, 23 April 2019) (2007).

[94] A. Kamenev, in *Nanophysics: Coherence and Transport, École d'été de Physique des Houches Session LXXXI* (Elsevier, 2005), pp. 177–246.

[95] M. F. Maghrebi and A. V. Gorshkov, 'Nonequilibrium many-body steady states via Keldysh formalism', Phys. Rev. B **93** (2016).

[96] L. M. Sieberer, S. D. Huber, E. Altman and S. Diehl, 'Nonequilibrium functional renormalization for driven-dissipative Bose-Einstein condensation', Phys. Rev. B **89** (2014).

[97] M. Buchhold, 'Thermalization and Out-of-Equilibrium Dynamics in Open Quantum Many-Body Systems', PhD thesis (Technische Universität Dresden, 2015).

[98] F. Tonielli, 'Keldysh Field Theory for dissipation-induced states of Fermions', MA thesis (University of Pisa, 2016).

[99] J. Barnes, ed., *Complete Works of Aristotle, Volume 1: The Revised Oxford Translation* (Princeton University Press, 1984).

[100] M. C. Fischer, B. Gutiérrez-Medina and M. G. Raizen, 'Observation of the Quantum Zeno and Anti-Zeno Effects in an Unstable System', Phys. Rev. Lett. **87**, 040402 (2001).

[101] E. Fradkin, *Field Theories of Condensed Matter Physics* (Cambridge University Press, 2013).

[102] F. D. M. Haldane, 'Luttinger liquid theory of one-dimensional quantum fluids', J. Phys. Condens. Matter **14**, 2585 (1981).

[103] Z. Yao, H. W. C. Postma, L. Balents and C. Dekker, 'Carbon nanotube intramolecular junctions', Nature **402**, 273 (1999).

[104] P. Fendley, A. W. W. Ludwig and H. Saleur, 'Exact Conductance through Point Contacts in the $\nu = 1/3$ Fractional Quantum Hall Effect', Phys. Rev. Lett. **74**, 3005 (1995).

[105] D. C. Mattis and E. H. Lieb, 'Exact Solution of a Many-Fermion System and Its Associated Boson Field', J. Math. Phys. **6**, 304 (1965).

[106] S. Eggert, 'One-dimensional quantum wires: A pedestrian approach to bosonization', arXiv:0708.0003 (2007).

[107] J. von Delft and H. Schoeller, 'Bosonization for beginners - refermionization for experts', Ann. Phys. (Berl.) **7**, 225 (1998).

[108] S. Tomonaga, 'Remarks on Bloch's Method of Sound Waves applied to Many-Fermion Problems', Prog. Theor. Phys. **5**, 544 (1950).

[109] J. M. Luttinger, 'An Exactly Soluble Model of a Many-Fermion System', J. Math. Phys. **4**, 1154 (1963).

[110] J. Sirker, 'The Luttinger Liquid and Integrable Models', Int. J. Mod. Phys. B **26**, 1244009 (2012).

[111] K. Schönhammer, in *Physics and Chemistry of Materials with Low-Dimens* (Springer Netherlands), pp. 93–136.

[112] J. Voit, 'One-dimensional Fermi liquids', Rep. Prog. Phys. **58**, 977 (1995).

[113] D. L. Maslov and M. Stone, 'Landauer conductance of Luttinger liquids with leads', Phys. Rev. B **52**, R5539 (1995).

[114] I. Safi and H. J. Schulz, 'Transport in an inhomogeneous interacting one-dimensional system', Phys. Rev. B **52**, R17040 (1995).

[115] C. Schenke, A. Minguzzi and F. W. J. Hekking, 'Probing superfluidity of a mesoscopic Tonks-Girardeau gas', Phys. Rev. A **85**, 053627 (2012).

[116] E. H. Lieb and W. Liniger, 'Exact Analysis of an Interacting Bose Gas', Phys. Rev. **130**, 1605 (1963).

[117] M. D. Girardeau and A. Minguzzi, 'Motion of an impurity particle in an ultracold quasi-one-dimensional gas of hard-core bosons', Phys. Rev. A **79**, 033610 (2009).

[118] V. Meden, W. Metzner, U. Schollwöck and K. Schönhammer, 'Scaling behavior of impurities in mesoscopic Luttinger liquids', Phys. Rev. B **65**, 045318 (2002).

[119] V. Meden, W. Metzner, U. Schollwöck and K. Schönhammer, 'A Single Impurity in a Luttinger Liquid: How It "Cuts" the Chain', J. Low Temp. Phys. **126**, 1147 (2002).

[120] S. Andergassen, T. Enss, V. Meden, W. Metzner, U. Schollwöck and K. Schönhammer, 'Functional renormalization group for Luttinger liquids with impurities', Phys. Rev. B **70**, 075102 (2004).

[121] W. Metzner, M. Salmhofer, C. Honerkamp, V. Meden and K. Schönhammer, 'Functional renormalization group approach to correlated fermion systems', Rev. Mod. Phys. **84**, 299 (2012).

[122] A. Mitra, S. Takei, Y. B. Kim and A. J. Millis, 'Nonequilibrium Quantum Criticality in Open Electronic Systems', Phys. Rev. Lett. **97**, 236808 (2006).

[123] E. G. Dalla Torre, E. Demler, T. Giamarchi and E. Altman, 'Dynamics and universality in noise-driven dissipative systems', Phys. Rev. B **85**, 184302 (2012).

[124] S. Lal, S. Rao and D. Sen, 'Junction of several weakly interacting quantum wires: A renormalization group study', Phys. Rev. B **66**, 165327 (2002).

[125] S. Das, S. Rao and D. Sen, 'Renormalization group study of the conductances of interacting quantum wire systems with different geometries', Phys. Rev. B **70**, 085318 (2004).

[126] D. N. Aristov, A. P. Dmitriev, I. V. Gornyi, V. Y. Kachorovskii, D. G. Polyakov and P. Wölfle, 'Tunneling into a Luttinger Liquid Revisited', Phys. Rev. Lett. **105**, 266404 (2010).

[127] D. N. Aristov, I. V. Gornyi, D. G. Polyakov and P. Wölfle, 'Y junction of Luttinger liquid wires out of equilibrium', Phys. Rev. B **95**, 155447 (2017).

[128] D. N. Aristov, I. V. Gornyi, D. G. Polyakov and P. Wölfle, 'Emergent chirality in multilead Luttinger-liquid junctions out of equilibrium', Phys. Rev. B **100**, 165410 (2019).

[129] A. Schmid, 'Diffusion and Localization in a Dissipative Quantum System', Phys. Rev. Lett. **51**, 1506 (1983).

[130] H. P. Büchler, V. B. Geshkenbein and G. Blatter, 'Superfluidity versus Bloch Oscillations in Confined Atomic Gases', Phys. Rev. Lett. **87**, 100403 (2001).

[131] M. Cominotti, D. Rossini, M. Rizzi, F. Hekking and A. Minguzzi, 'Optimal Persistent Currents for Interacting Bosons on a Ring with a Gauge Field', Phys. Rev. Lett. **113**, 025301 (2014).

[132] T. Gericke, P. Würtz, D. Reitz, C. Utfeld and H. Ott, 'All-optical formation of a Bose–Einstein condensate for applications in scanning electron microscopy', Appl. Phys. B **89**, 447 (2007).

[133] H. Fröml, A. Chiocchetta, C. Kollath and S. Diehl, 'Fluctuation-Induced Quantum Zeno Effect', Phys. Rev. Lett. **122**, 040402 (2019).

[134] H. Fröml, C. Muckel, C. Kollath, A. Chiocchetta and S. Diehl, 'Ultracold quantum wires with localized losses: Many-body quantum Zeno effect', Phys. Rev. B **101**, 144301 (2020).

[135] W. D. Heiss, 'The physics of exceptional points', J. Phys. A **45**, 444016 (2012).

[136] J. Muga, J. Palao, B. Navarro and I. Egusquiza, 'Complex absorbing potentials', Phys. Rep. **395**, 357 (2004).

[137] T. Müller, MA thesis (University of Cologne, in preparation).

[138] V. Obst, 'Dissipative structures and quantum Zeno effect in ultracold atoms', Bachelor's Thesis (University of Cologne, 2019).

[139] S. Longhi, 'Non-Hermitian Floquet invisibility', EPL **117**, 10005 (2017).

[140] M. Abramowitz and I. A. Stegun, *Handbook of Mathematical Functions* (National Bureau of Standards, 1972).

[141] P. W. Anderson, 'A poor man's derivation of scaling laws for the Kondo problem', J. Phys. C: Solid State Phys. **3**, 2436 (1970).

[142] M. Lebrat, Gri šins, D. Husmann, S. Häusler, L. Corman, T. Giamarchi, J.-P. Brantut and T. Esslinger, 'Band and Correlated Insulators of Cold Fermions in a Mesoscopic Lattice', Phys. Rev. X **8**, 011053 (2018).

[143] S. Krinner, T. Esslinger and J.-P. Brantut, 'Two-terminal transport measurements with cold atoms', J. Phys. Condens. Matter **29**, 343003 (2017).

[144] C. Wetterich, 'Exact evolution equation for the effective potential', Phys. Lett. B **301**, 90 (1993).

[145] R. Gezzi, T. Pruschke and V. Meden, 'Functional renormalization group for nonequilibrium quantum many-body problems', Phys. Rev. B **75**, 045324 (2007).

[146] M. Gievers, MA thesis (University of Cologne, in preparation).

[147] Y. V. Nazarov and L. I. Glazman, 'Resonant Tunneling of Interacting Electrons in a One-Dimensional Wire', Phys. Rev. Lett. **91**, 126804 (2003).

[148] H. Kato and D. Yoshioka, 'Suppression of persistent currents in one-dimensional disordered rings by the Coulomb interaction', Phys. Rev. B **50**, 4943 (1994).

[149] P. Schmitteckert and U. Eckern, 'Phase coherence in a random one-dimensional system of interacting fermions: A density-matrix renormalization-group study', Phys. Rev. B **53**, 15397 (1996).

[150] A. Cohen, K. Richter and R. Berkovits, 'Spin and interaction effects on charge distribution and currents in one-dimensional conductors and rings within the Hartree-Fock approximation', Phys. Rev. B **57**, 6223 (1998).

[151] V. Meden, W. Metzner, U. Schollwöck, O. Schneider, T. Stauber and K. Schönhammer, 'Luttinger liquids with boundaries: Power-laws and energy scales', Eur. Phys. J. B **16**, 631 (2000).

[152] V. Meden and U. Schollwöck, 'Persistent currents in mesoscopic rings: A numerical and renormalization group study', Phys. Rev. B **67**, 035106 (2003).

[153] A. Gendiar, M. Moško, P. Vagner and R. Németh, 'Tunneling of Interacting Fermions in 1D Systems', Acta Phys. Pol. **108**, 661 (2005).

[154] A. Gendiar, M. Moško, P. Vagner and R. Németh, 'Tunneling of interacting one-dimensional electrons through a single scatterer: Luttinger liquid behavior in the Hartree–Fock model', Physica E **34**, 596 (2006).

[155] M. Moško, P. Vagner, A. Gendiar and R. Németh, 'Coherent transport of interacting electrons through a single scatterer', Physica B **378-380**, 908 (2006).

[156] D. J. Thouless, *The quantum mechanics of many-body systems* (Courier Corporation, 2014).

[157] M. Fowler, 'Bosonisation, cut-offs and the spin wave velocity for the Heisenberg-Ising chain', J. Phys. Condens. Matter **13**, 1459 (1980).

[158] R. Nemeth and M. Mosko, 'Spinless Hartree-Fock model of persistent current in rings with single scatterer: Comparison with correlated models', arXiv:cond-mat/0503146 (2005).

[159] A. O. Gogolin, A. A. Nersesyan and A. M. Tsvelik, *Bosonization and strongly correlated systems* (Cambridge University Press, 2004).

[160] A. Mitra and T. Giamarchi, 'Mode-Coupling-Induced Dissipative and Thermal Effects at Long Times after a Quantum Quench', Phys. Rev. Lett. **107**, 150602 (2011).

[161] M. Buchhold and S. Diehl, 'Nonequilibrium universality in the heating dynamics of interacting Luttinger liquids', Phys. Rev. A **92**, 013603 (2015).

[162] M. Buchhold and S. Diehl, 'Kinetic theory for interacting Luttinger liquids', Eur. Phys. J. D **69** (2015).

[163] T. Prosen, 'PT-Symmetric Quantum Liouvillean Dynamics', Phys. Rev. Lett. **109** (2012).

[164] R. El-Ganainy, K. G. Makris, M. Khajavikhan, Z. H. Musslimani, S. Rotter and D. N. Christodoulides, 'Non-Hermitian physics and PT symmetry', Nat. Phys. **14**, 11 (2018).

[165] Z. Gong, Y. Ashida, K. Kawabata, K. Takasan, S. Higashikawa and M. Ueda, 'Topological Phases of Non-Hermitian Systems', Phys. Rev. X **8**, 031079 (2018).

[166] R. Hanai, A. Edelman, Y. Ohashi and P. B. Littlewood, 'Non-Hermitian Phase Transition from a Polariton Bose-Einstein Condensate to a Photon Laser', Phys. Rev. Lett. **122**, 185301 (2019).

[167] R. Hanai and P. B. Littlewood, 'Critical fluctuations at a many-body exceptional point', arXiv:1908.03243 (2019).

[168] R. B. Laughlin, 'Quantized Hall conductivity in two dimensions', Phys. Rev. B **23**, 5632 (1981).

[169] D. J. Thouless, 'Quantization of particle transport', Phys. Rev. B **27**, 6083 (1983).

[170] P. C. Burke, J. Wiersig and M. Haque, 'Non-Hermitian scattering on a tight-binding lattice', arXiv:1910.07439 (2019).

[171] U. C. Tauber, *Critical Dynamics* (Cambridge University Press, 2009).

[172] D. Werner, *Funktionalanalysis* (Springer Berlin Heidelberg, 2018).

[173] S. Sachdev, *Quantum Phase Transitions* (Cambridge University Press, 2009).

[174] W. Chen, Ş. K. Özdemir, G. Zhao, J. Wiersig and L. Yang, 'Exceptional points enhance sensing in an optical microcavity', Nature **548**, 192 (2017).

[175] B. Peng, Ş. K. Özdemir, M. Liertzer, W. Chen, J. Kramer, H. Yılmaz, J. Wiersig, S. Rotter and L. Yang, 'Chiral modes and directional lasing at exceptional points', Proc. Natl. Acad. Sci. U.S.A. (2016).

[176] J. Wiersig, 'Role of nonorthogonality of energy eigenstates in quantum systems with localized losses', Phys. Rev. A **98** (2018).

[177] S. Longhi, 'Tunable dynamic Fano resonances in coupled-resonator optical waveguides', Phys. Rev. A **91** (2015).

[178] M. Hartmann, F. Brandão and M. Plenio, 'Quantum many-body phenomena in coupled cavity arrays', Laser Photonics Rev. **2**, 527 (2008).

[179] A. A. Zyablovsky, I. V. Doronin, E. S. Andrianov, A. A. Pukhov, Y. E. Lozovik, A. P. Vinogradov and A. A. Lisyansky, 'Exceptional points as lasing pre-thresholds in open-cavity lasers', arXiv:2002.03254 (2020).

[180] J. Li, A. K. Harter, J. Liu, L. de Melo, Y. N. Joglekar and L. Luo, 'Observation of parity-time symmetry breaking transitions in a dissipative Floquet system of ultracold atoms', Nat. Commun. **10** (2019).

[181] C. Jung, M. Müller and I. Rotter, 'Phase transitions in open quantum systems', Phys. Rev. E **60**, 114 (1999).

[182] M. V. Entin and M. M. Mahmoodian, 'High-frequency blockade in tight-binding one-dimensional lattice with single vibrating site', EPL **84**, 47008 (2008).

[183] D. Thuberg, S. A. Reyes and S. Eggert, 'Quantum resonance catastrophe for conductance through a periodically driven barrier', Phys. Rev. B **93** (2016).

[184] S. A. Reyes, D. Thuberg, D. Pérez, C. Dauer and S. Eggert, 'Transport through an AC-driven impurity: Fano interference and bound states in the continuum', New J. Phys. **19**, 043029 (2017).

[185] A. Agarwala and D. Sen, 'Effects of local periodic driving on transport and generation of bound states', Phys. Rev. B **96** (2017).

[186] A. Tanaka, T. Nakamura and T. Cheon, 'Generating nonequilibrium stationary state from ground state condensate through an almost-adiabatic cycle', arXiv:1912.04434 (2019).

[187] W. Li and L. E. Reichl, 'Floquet scattering through a time-periodic potential', Phys. Rev. B **60**, 15732 (1999).

[188] D. E. Feldman and Y. Gefen, 'Backscattering off a point impurity: Current enhancement and conductance greater than e^2/h per channel', Phys. Rev. B **67**, 115337 (2003).

[189] N. A. Kamar and T. Giamarchi, 'Time-dependent local potential in a Tomonaga-Luttinger liquid', Phys. Rev. A **96** (2017).

[190] J. A. De Marco, *Dissipatively driven waveguides*, Bachelor's thesis (University of Bonn), 2019.

ACKNOWLEDGMENTS

I would like to express my deep gratitude to my supervisor Prof. Dr. Sebastian Diehl for the opportunity to participate in the research of his group. I am grateful for the uncountable number of discussions, his guidance, and constant support, and would like to thank for his effort and donated time.
I owe Dr. Alessio Chiocchetta my deepest thanks for the constant inflow of knowledge and support he provided to me as my office mate, supervisor, and colleague. His invaluable methodical input and insights paved the way for this thesis.
I would like to thank Prof. Dr. Achim Rosch for taking over the second assessment and Prof. Dr. Paul van Loosdrecht for taking over the chair of the thesis defense committee.
I thank Prof. Dr. Corinna Kollath and Christopher Muckel for the successful collaboration. Moreover, I am grateful to many other physicists for the interesting and insightful discussions on physics and their valuable feedback on my projects. In particular, I thank Dr. Alessio Chiocchetta, Oriana Dießel, and Marcel Zimmer for the careful reading of the manuscript.
I thank Mariela Boevska for her friendly and dedicated administrative support. Furthermore, I thank all members of the research groups Diehl and Scherer for the many inspiring discussions on physics and the pleasant social environment they provided.
I am grateful for the support I received from the Bonn-Cologne Graduate School of Physics and Astronomy and Dr. Petra Neubauer-Guenther.
Finally, I would like to acknowledge the constructive way in which the Institute for Theoretical Physics and the University of Cologne dealt with the difficulties of the coronavirus pandemic, during which this thesis was finalized, for the benefit of the students.

STATEMENT OF AUTHORSHIP

Erklärung

Ich versichere, dass ich die von mir vorgelegte Dissertation selbständig angefertigt, die benutzten Quellen und Hilfsmittel vollständig angegeben und die Stellen der Arbeit – einschließlich Tabellen, Karten und Abbildungen –, die anderen Werken im Wortlaut oder dem Sinn nach entnommen sind, in jedem Einzelfall als Entlehnung kenntlich gemacht habe; dass diese Dissertation noch keiner anderen Fakultät oder Universität zur Prüfung vorgelegen hat; dass sie – abgesehen von unten angegebenen Teilpublikationen – noch nicht veröffentlicht worden ist, sowie, dass ich eine solche Veröffentlichung vor Abschluss des Promotionsverfahrens nicht vornehmen werde. Die Bestimmungen der Promotionsordnung sind mir bekannt. Die von mir vorgelegte Dissertation ist von Prof. Dr. Sebastian Diehl betreut worden.

Heinrich Fröml

Teilpublikationen

- H. Fröml, A. Chiocchetta, C. Kollath, and S. Diehl, *'Fluctuation-Induced Quantum Zeno Effect'*, Phys. Rev. Lett. 122, 040402 (2019).
- H. Fröml, C. Muckel, C. Kollath, A. Chiocchetta, and S. Diehl, *'Ultracold quantum wires with localized losses: Many-body quantum Zeno effect'*, Phys. Rev. B 101, 144301 (2020)